

August 2017

# Quantum and Classical Optics of Plasmonic Systems: 3d/2d Materials and Photonic Topological Insulators

Seyyed Ali Hassani gangaraj  
*University of Wisconsin-Milwaukee*

Follow this and additional works at: <https://dc.uwm.edu/etd>

 Part of the [Electrical and Electronics Commons](#), and the [Electromagnetics and Photonics Commons](#)

---

## Recommended Citation

Hassani gangaraj, Seyyed Ali, "Quantum and Classical Optics of Plasmonic Systems: 3d/2d Materials and Photonic Topological Insulators" (2017). *Theses and Dissertations*. 1637.  
<https://dc.uwm.edu/etd/1637>

This Dissertation is brought to you for free and open access by UWM Digital Commons. It has been accepted for inclusion in Theses and Dissertations by an authorized administrator of UWM Digital Commons. For more information, please contact [open-access@uwm.edu](mailto:open-access@uwm.edu).

QUANTUM AND CLASSICAL OPTICS OF PLASMONIC SYSTEMS: 3D/2D  
MATERIALS AND PHOTONIC TOPOLOGICAL INSULATORS

by

Seyyed Ali Hassani Gangaraj

A Dissertation Submitted in  
Partial Fulfillment of the  
Requirements for the Degree of

Doctor of Philosophy  
in Engineering

at

The University of Wisconsin-Milwaukee

August 2017

ABSTRACT  
QUANTUM AND CLASSICAL OPTICS OF PLASMONIC SYSTEMS: 3D/2D MATERIALS  
AND PHOTONIC TOPOLOGICAL INSULATORS

by

Seyyed Ali Hassani Gangaraj

The University of Wisconsin-Milwaukee, 2017  
Under the Supervision of Professor George W. Hanson

At the interface of two different media such as metal and vacuum, light can couple to the electrons of the metal to form a wave that is bound to the interface. This wave is called a surface plasmon-polariton (SPP), generally characterized by intense fields that decay quickly away from the interface. Due to their unique properties, SPPs have found a broad range of applications in various areas of science, including light harvesting, medical science, energy transfer and imaging. In addition to the widely studied classical plasmonics, quantum plasmonics is also attracting considerable interest in the electromagnetics and quantum optics communities. In this thesis several new areas of investigation into quantum plasmonics is presented, focusing on entanglement mediated by SPPs in several different environments: 3D waveguides, 2D surfaces and on photonic topological insulators.

Entanglement is an experimentally verified property of nature where pairs of quantum systems are connected in some manner such that the quantum state of each system cannot be described independently. Generating, preserving, and controlling entanglement is necessary for many quantum computer implementations. It is highly desirable to control entanglement between two multi-level emitters such as quantum dots via a macroscopic, easily-adjusted external parameter. SPPs guided by the medium, as a coupling agent between quantum dots, are highly tunable and offer a promising way to achieve having control over a SPP mediated entanglement.

We first consider two quantum dots placed above 3D finite length waveguides. We have restricted our consideration to two waveguides types, i.e. a metal nanowire and a groove waveguide. Our main results in this work are to show that realistic finite-length nanowire and groove waveguides, with their associated discontinuities, play a crucial role in the engineering of highly entangled states. It is demonstrated that proper positioning of the emitters with respect to the waveguide edges can lead to a significant increase in entanglement compared to the case of the emitter coupled to an infinite plasmonic waveguide. Moreover, even for the infinite-length case, discontinuities in the waveguides do not always play a detrimental role, to be more specific, an increase in entanglement compared to the unperturbed waveguides can be achieved by introducing coupling slots (engineered perturbations) into the structure.

In addition to 3D environments, two dimensional (2D) materials are of intense interest due to their extraordinary capabilities to manipulate reflection and transmission characteristics, and beam-

forming. Some notable examples of 2D layered crystals include graphene, black phosphorus (BP) and boron nitride. Graphene in particular has received considerable attention as a promising 2D surface for many applications relating to its integrability and electronic tune-ability. Black phosphorus is also a layered material that has recently been exfoliated into its multilayers, showing good electrical transport properties and promising optical characteristics.

Most of the previous studies of the electromagnetic response of 2D surfaces and metallic surface plasmons have considered isotropic structures with omnidirectional plasmonic surface wave propagation on the plane of these materials. Such an omnidirectional surface wave propagation does not allow for launching energy from electromagnetic source to a specific target on the surface, which is a desirable characteristic. However, an appropriate structured anisotropic surface can provide such a capability, such as an array of graphene strips. In addition, by tuning of the graphene doping it is possible to have a hyperbolic surface response. Working in this regime of surface conductivity, it is possible to launch SPPs along a specific direction, which is tunable via doping of the graphene. In this work, the electromagnetic response of anisotropic 2D surfaces has been investigated based on the analysis of the Greens function for the surface plasmonic wave contribution of the Sommerfeld integral. The Sommerfeld integral form of the Greens function can be time-consuming to evaluate, and here, it has been shown that for the surface waves, this integral can be evaluated efficiently as a mixture of continuous and discrete spectrums associated to the radiation of the source into the ambient space and energy coupled to the SPPs. Graphene strip arrays provide directive surface waves in the low THz regime, and unperturbed black phosphorus provides a similar response for higher frequency ranges.

All plasmonic devices are impacted by SPP diffraction at surface defects and discontinuities. In particular, for reciprocal materials a surface defect/discontinuity can both scatter a forward mode into a backward mode (and vice versa) and cause significant radiation/diffraction of the SPP. The presence of a backward state comes from time reversal (TR) symmetry; when broken, a backward state may be absent, and reflection at a discontinuity can be suppressed. As a result, surface energy becomes unidirectional and follows the contour of the interface. This type of system can be broadly classified as a photonic topological insulators (PTIs). The properties of PTIs are quantified by the Berry phase, Berry connection, and an invariant known as the Chern number. Also the physical meaning of the Berry phase, connection, and curvature, how these quantities arise in electromagnetic problems, and the significance of Chern numbers for unidirectional, scattering-immune surface wave propagation are discussed. The Chern numbers for the electromagnetic modes supported by a biased plasma have been calculated. It has been demonstrated that the modes supported by biased plasmas indeed possess non-trivial Chern numbers, which leads to the propagation of a topologically protected and unidirectional surface modes (energy) at the interface between the biased plasma and topologically trivial material.

The ability to guide the energy from one quantum dot to another one is a great advantage to achieve highly entangled states. Here, in this thesis for the first time, we investigated the unidirectional surface wave assisted entanglement in PTIs. We have investigated spontaneous and pumped entanglement of two level systems (quantum dots) in the vicinity of a photonic topological insulator interface, which supports a unidirectional SPP in the common bandgap of the bulk materials. We also have derived a master equation for quantum dots interactions in a general three-dimensional, nonreciprocal, inhomogeneous and lossy environment. The resulting entanglement is shown to be extremely robust to defects occurring in the material system.

© Copyright by Seyyed Ali Hassani Gangaraj, 2017  
All Rights Reserved

# TABLE OF CONTENTS

LIST OF FIGURES . . . . .	ix
LIST OF TABLES . . . . .	xvii
<b>1 Introduction</b>	<b>1</b>
1.1 Background . . . . .	1
1.2 Dyadic Green Functions . . . . .	2
1.2.1 Mathematical Basis of Dyadic Green Function . . . . .	2
1.2.2 Derivation of the Electric Field Dyadic Green Functions . . . . .	4
1.3 Heisenberg Equations of Motion (HEM) . . . . .	6
1.3.1 Field Quantization in Lossy Inhomogeneous Media . . . . .	6
1.3.2 Non-Pumped Concurrence of Two Quantum Dots Interacting Through lossy Inhomogeneous Medium . . . . .	8
1.4 Density Operator and Quantum Master Equation (ME) . . . . .	11
1.4.1 The Density Operator . . . . .	11
1.4.2 Interaction Picture . . . . .	13
1.4.3 Master Equations For Quantum Dots Interacting in a Lossy Inhomogeneous Reciprocal Medium . . . . .	14
1.4.4 Master Equation in the Symmetric Basis . . . . .	18
1.4.5 Single Excited Emitter . . . . .	19
1.4.6 Single Excited Emitter With Pure Dephasing . . . . .	20
1.4.7 Steady-State Concurrence Between Two Quantum Dots . . . . .	21
<b>2 3D Plasmonic Systems Mediated Entanglement</b>	<b>23</b>
2.1 Introduction . . . . .	23
2.2 3D Plasmonic Waveguide Geometries (Nano-Wires, Groove Waveguides) . . . . .	25
2.2.1 Dissipative Decay Rate and Coherent Coupling Term . . . . .	25
2.2.2 Transient Entanglement Mediated by Surface Waves Supported by Nano-Wire and Groove Waveguides . . . . .	29
2.2.3 Steady State Entanglement Under External Pumping . . . . .	31
2.3 Summary . . . . .	34

<b>3</b>	<b>Hyperbolic and Isotropic 2D Plasmonic Systems Mediated Entanglement</b>	<b>36</b>
3.1	Introduction . . . . .	36
3.2	Infinite 2D Graphene Sheet . . . . .	37
3.2.1	Green Function Analysis . . . . .	37
3.2.2	Controllable Entanglement Using Gate Voltage . . . . .	39
3.3	2D Hyperbolic Surface (Black Phosphorus and Graphene Stripes) . . . . .	41
3.3.1	Green Function Analysis and Directive Surface Waves . . . . .	41
3.3.2	Directional Properties of SPPs on 2D Surfaces . . . . .	44
3.3.3	Complex-Plane Analysis in the $q_x$ -Plane . . . . .	45
3.3.4	Approximation of the Outer Integral Using Stationary Phase, and Exact Evaluation Using the Continuous Spectrum . . . . .	49
3.3.5	Stationary Phase Evaluation of the Outer Integral . . . . .	49
3.3.6	Complex-Plane Analysis in the $q_z$ – Plane . . . . .	50
3.3.7	P-type Branch Point in the $q_z$ -Plane . . . . .	51
3.3.8	Type-0 Branch Point in the $q_z$ -Plane . . . . .	51
3.3.9	Type-1 Branch Point in the $q_z$ -Plane . . . . .	52
3.3.10	Branch Cut Analysis in the $q_z$ -Plane . . . . .	52
3.3.11	Conductivity and Its Effect on Branch Points and SPP Confinement . . . . .	55
3.3.12	Anisotropic Hyperbolic Layer (Graphene Strip Array) . . . . .	56
3.3.13	Anisotropic Non-Hyperbolic Layer (Black Phosphorus) . . . . .	59
3.4	Tunable Directed Surface Plasmon-Polariton (SPP) Mediated Entanglement . . . . .	61
3.5	Summary . . . . .	63
<b>4</b>	<b>Photonic Topological Insulators</b>	<b>65</b>
4.1	Review of Theory . . . . .	65
4.1.1	Motivation- Backscattering-Immune One-Way SPP Propagation . . . . .	65
4.1.2	Origin of the Berry Phase . . . . .	67
4.1.3	Berry Curvature, Flux, and Tensor, and Chern Number . . . . .	72
4.1.4	Chern Number, Bulk-Edge Correspondence, and Topologically Protected Edge States . . . . .	75
4.2	Electromagnetic Description - Berry quantities for photons . . . . .	80
4.2.1	Some electromagnetic material classes that posses non-trivial Chern numbers . . . . .	82
4.2.2	Berry quantities for continuum media . . . . .	83
4.3	Continuum Photonic Example . . . . .	84
4.3.1	Low Frequency Band of the TM-Mode, Material Model (4.78) . . . . .	88
4.3.2	High Frequency Band of the TM-Mode, Material Model (4.78) . . . . .	89
4.3.3	TE-Mode . . . . .	90



4.3.4	Integer Chern Numbers and Wave Vector Cutoff for Magneto-Optic Material Response . . . . .	91
4.3.5	Full-Wave Simulation of One-Way Propagation . . . . .	94
4.3.6	Numerical Computation of the Chern Number . . . . .	97
4.4	Summary . . . . .	99
<b>5</b>	<b>Quantum Master Equation for General Non-Reciprocal Inhomogeneous Lossy Medium</b>	<b>101</b>
5.1	Introduction . . . . .	101
5.2	Master Equation for General 3D Nonreciprocal Environments . . . . .	102
5.3	Robust Entanglement with 3D Non-Reciprocal Photonic Topological Insulator . . . . .	106
5.3.1	Transient Entanglement: Unidirectional SPP-Assisted Qubit Communication . . . . .	106
5.3.2	Continuum Photonic Topological Insulator Realization of a Nonreciprocal Surface Plasmon Polariton Environment . . . . .	108
5.3.3	Entanglement Evaluation in Different Environments . . . . .	108
5.3.4	Topological Aspect of Entanglement . . . . .	110
5.3.5	Preserving Entanglement in the Presence of Large Defects . . . . .	111
5.3.6	Finite-Width Waveguide . . . . .	111
5.3.7	Effect of Different Initial State Preparations . . . . .	112
5.3.8	Lossy Biased Plasma . . . . .	115
5.4	Summary . . . . .	115
	<b>Appendices</b>	<b>117</b>
.1	Appendix I: Non-Reciprocal Green Function . . . . .	118
.2	Appendix II: Master Equation Approximations . . . . .	120
.3	Appendix III: Comparison With Previous 1D Chiral Theory . . . . .	121
.4	Appendix IV: Concurrence in the Unidirectional Case . . . . .	126
	<b>Curriculum Vitae</b>	<b>142</b>

## LIST OF FIGURES

2.1	Two identical two-level emitters (e.g., atoms or quantum dots) placed next to (a) a metal nanowire (insert shows geometry of the nanowire with coupling slots; the slot opening angle and width are $95^\circ$ and 15 nm, respectively) and (b) a V-shaped channel cut in a flat metal plane (if coupling slots are present, their length, width and depth are 70 nm, 15 nm, and 138 nm, respectively). We consider both infinite- and finite-length waveguides. . . . .	24
2.2	Normalized coupling strength $g_{ab}$ and decay rate $\Gamma_{ab}$ as a function of distance between emitters above an infinite-length silver nanowire with and without coupling slots (based on scattered Green function). $\Gamma_{ab}$ is proportional to the Purcell factor when $z=0$ (i.e. $\mathbf{r}_\alpha = \mathbf{r}_\beta$ ). The position of one emitter is fixed at $z = 0$ and the second emitter position is changing with $z$ . Slot are located at $z = -40$ nm and $z = 1.5\lambda_{\text{spp}} + 40$ nm = 677.5 nm. . . . .	27
2.3	(a) Absolute value of plasmon electric field intensity on a finite nanowire of length $1.5\lambda_{\text{spp}}$ . The plasmon mode is excited by the emitter positioned at $z = 0$ nm at a distance 20 nm above the nanowire surface. (b) geometry, (c)-(d) Normalized coupling strength $g_{ab}$ and decay rate $\Gamma_{ab}$ as a function of a distance between emitters above the nanowire with and without coupling slots (based on scattered Green function). Slots are located at $z = 27$ nm and $z = 1.5\lambda_{\text{spp}} - 27$ nm=610.5 nm. . . . .	28
2.4	(a) Time dependence of transient concurrence between two emitters laterally separated by $1.5\lambda_{\text{spp}} = 637.5$ nm. We assume that the emitters are in vacuum (solid green line), near an infinite wire with (dashed brown line) and without (solid brown line) coupling slots, near a finite wire of length of $1.5\lambda_{\text{spp}}$ with (solid red) and without (dashed blue line) coupling slots. In the case of the finite wire, qubits are placed above the nanowire ends, and slots are located 27 nm from each end. The normalization constant $\Gamma_{aa}$ is the decay rate of the emitter (Eq. (2.1)) for the given geometry. (b) Time dependence of the population of the emitter initially in the excited, $\rho_{eg}$ , and ground, $\rho_{ge}$ , states, for the case of a finite nanowire with coupling slots. . . . .	29

2.5	(a) Concurrence of two qubits separated by $1.5\lambda_{\text{spp}}$ . Vacuum case (dashed green line), infinite groove (dotted black line), infinite groove with coupling slots (dashed blue line) 40 nm laterally away from the qubits (outside the space between them), and finite groove of length $2\lambda_{\text{spp}}$ (solid red line). (b) Time dependence of the population of the emitter initially in the excited, $\rho_{eg}$ , and ground, $\rho_{ge}$ , states. . . . .	30
2.6	Time dependence of the concurrence between two qubits including the effect of pure dephasing (see 1.121). Qubits are placed either above the ends of a finite-length nanowire (Fig. 5.7(a)) or finite-length groove (Fig. 5.9(a)). The emitter coupling rates for the case of the nanowire are $\Gamma_{aa} = 6.5\mu\text{eV}$ , $\Gamma_{ab} = -1.2\mu\text{eV}$ , $g_{ab} = 2.85\mu\text{eV}$ , while for the case of the groove waveguide $\Gamma_{aa} = 11.38\mu\text{eV}$ , $\Gamma_{ab} = -6.48\mu\text{eV}$ , $g_{ab} = 5.8\mu\text{eV}$ . The QD pure dephasing rate, $\gamma'$ , is equal to $1\mu\text{eV}$ . . . . .	30
2.7	Time dependence of the concurrence between two qubits pumped by external electromagnetic fields. Qubits are placed above either a nanowire (left panel) or groove (right panel). Qubit separation is $1.5\lambda_{\text{spp}}$ . The system geometry is the same as in Figs. 2.4,2.5.	32
2.8	Steady state concurrence, $C_\infty$ , as function of qubit separation normalized by the modal wavelength, $\lambda_{\text{spp}}$ . Qubits are placed either above a finite nanowire (right) or a finite groove (left). The geometry is the same as in Figs. 2.4,2.5. Asymmetric, antisymmetric and symmetric pumping have been considered. . . . .	33
2.9	Dynamics of the density matrix elements for qubits under external pumping. Qubits are above a finite groove with qubit separation $1.5\lambda_{\text{spp}} = 634.5$ (see Fig. 2.5 for details of the geometry). Two different regimes of pumping have been considered, symmetric pumping (two field pumping) and asymmetric pumping (single field pumping). . . . .	34
3.1	Schematic representation of two two-level-atom (TLA) above an infinite graphene sheet. TLAs are pumped by two independent laser fields with intensities $E_a$ and $E_b$ . The graphene is suspended in vacuum. . . . .	39
3.2	Transient and steady state concurrence of two QDs above graphene sheet. . . . .	40
3.3	Steady state concurrence as a function of height above graphene $y$ , and QDs spacing $x$ .	41
3.4	Anisotropic surface with conductivity tensor $\sigma$ at the interface of two isotropic materials.	42
3.5	Equifrequency surfaces for metasurface having $\sigma_{xx} = 0.003 + 0.25i$ mS and $\sigma_{zz} = 0.03 - 0.76i$ mS (blue hyperbola; see also Fig. 3.14b), and $\sigma_{xx} = 1.3 + 16.9i$ mS and $\sigma_{zz} = 0.4 - 9.2i$ mS (green hyperbola; see also Fig. 3.14c). For comparison, the isotropic case for $\sigma_{xx} = \sigma_{zz} = 0.03 - 0.76i$ mS (black circle) is also shown. The red dashed line merely denotes 45 degrees with respect to the $x$ axis for guidance. . . . .	45
3.6	Real and imaginary parts of $f_{yy}(q_z)$ obtained numerically, (4.62), and using the residue term (3.27) for an array of graphene strips at $f = 10$ THz. The source is $\lambda/50$ above the surface, and $x = 0.2\lambda$ . . . . .	47

3.7	Ratio of the branch cut and residue terms in (3.25), $\sigma_{xx} = \alpha\sigma_0(0.01 + i)$ , $\sigma_{zz} = 0.1\sigma_{xx}^*$ , $\sigma_0 = e^2/4\hbar$ . Source is positioned $\lambda/50$ above the surface, $f = 10$ THz, and $x = 0.2\lambda$ . . . . .	48
3.8	The electric field $E_y$ obtained by stationary phase result (3.32) (red) and numerical integration (3.23) (blue) for (a) $\sigma_{xx} = 0.02 + 0.57i$ mS, $\sigma_{zz} = 0.02 - 0.57i$ mS and (b) $\sigma_{xx} = 0.003 + 0.25i$ mS, $\sigma_{zz} = 0.03 - 0.76i$ mS, $\rho = 0.4\lambda$ , $\rho/(y + y') = 80$ , $f = 10$ THz.	50
3.9	a,b: Branch cut contours $\text{Im}(q_{xp}) = 0$ determined from a plot of the absolute value of $\text{Im}(q_{xp})$ for a lossless model of a graphene strip array at 10 THz ( $\sigma'_{xx} = \sigma'_{zz} = 0$ , $\sigma''_{xx} = 0.57i$ mS, $\sigma''_{zz} = -0.57i$ mS). The branch point locations are $q_z^{\text{TE}}/k = 1.005$ , $q_z^{\text{TM}}/k = 9.3$ , $q_z^{(-1)}/k = -3.22i$ . c. Integration contour in the $q_z -$ plane showing branch points (dots) and branch cuts (thick lines). . . . .	53
3.10	Branch cut contours $\text{Im}(q_{xp}) = 0$ determined from a plot of the absolute value of $\text{Im}(q_{xp})$ for a lossy model of a graphene strip array at 10 THz with $\sigma_{xx} = 0.02 + 0.57i$ mS and $\sigma_{zz} = 0.02 - 0.57i$ mS. . . . .	54
3.11	Branch cut contour $\text{Im}(q_{xp}) = 0$ determined from a plot of the absolute value of $\text{Im}(q_{xp})$ for graphene with $\mu_c = 0.5$ eV at $T = 0$ K and $f = 20$ THz. . . . .	54
3.12	Branch cut contours $\text{Im}(q_{xp}) = 0$ determined from a plot of the absolute value of $\text{Im}(q_{xp})$ for a lossy model of multi-layer graphene strip at 10 THz, $\sigma_{xx} = 1.3 + 16.9i$ mS and $\sigma_{zz} = 0.4 - 9.2i$ mS. . . . .	56
3.13	a: Array of graphene strips. b: Imaginary parts of $\sigma_{xx}$ and $\sigma_{zz}$ and c: real parts of $\sigma_{xx}$ and $\sigma_{zz}$ normalized to $\sigma_0 = e^2/4\hbar$ for a graphene strip array with $\tau = 0.35$ ps, $\mu_c = 0.33$ eV, $W = 59$ nm and $L = 64$ nm. Region 1 is hyperbolic and region 2 is simply anisotropic . . . . .	57
3.14	Electric field $E_y$ excited by a $y$ -directed dipole current above a graphene strip array. a: graphene with $\mu_c = 0.45$ eV and $\mu_c = 0.33$ eV, $W = 59$ nm, $L = 64$ nm, $\sigma_{xx} = 0.02 + 0.57i$ mS and $\sigma_{zz} = 0.02 - 0.57i$ mS. b: $\mu_c = 0.45$ eV, $W = 56.1$ nm, $L = 62.4$ nm, $\sigma_{xx} = 0.003 + 0.25i$ mS and $\sigma_{zz} = 0.03 - 0.76i$ mS. c: Strip array with a 5-layer graphene, $\mu_c = 1$ eV, $W = 196$ nm and $L = 200$ nm, $\sigma_{xx} = 1.3 + 16.9i$ mS and $\sigma_{zz} = 0.4 - 9.2i$ mS. Blue line is for the integration along the real axis (3.39) and dashed red line is for integration along the branch cuts (4.102). $f = 10$ THz, $\rho = 0.2\lambda$ , and $y = 0.005\lambda$ . . . . .	58

3.15	a, b. Real and imaginary parts of $\sigma_{xx}$ and $\sigma_{zz}$ ( $x$ and $z$ are in-plane crystal axes of BP, with $x$ along the small effective mass direction, or commonly called the armchair direction) obtained at doping level $10 \times 10^{13}/\text{cm}^2$ and c,d. $5 \times 10^{12}/\text{cm}^2$ normalized to $\sigma_0 = e^2/4\hbar$ with a 10 nm thickness. Regions 1 and 3 show anisotropic inductive and capacitive responses, respectively, and region 2 shows the hyperbolic regime. T=300 K and damping is 2 meV. . . . .	59
3.16	a: Branch cut contours for $\text{Im}(q_{xp}) = 0$ determined from the absolute value of $\text{Im}(q_{xp})$ in the $q_z -$ plane. b. Absolute value of $E_y$ excited by a $y$ -directed dipole current source above black phosphorus with doping level $10 \times 10^{13}/\text{cm}^2$ at $f = 92.6$ THz. The blue line is for the integration along the real axis (3.39) and the dashed red line is for the integration along the branch cuts (4.102). $\rho = 0.2\lambda$ and $y = 0.005\lambda$ . c: SPP field in-plane distribution in logarithmic scale calculated by FDTD. d: SPP field vertical variation in logarithmic scale calculated by FDTD. . . . .	60
3.17	A 2D hyperbolic material located in the $x - z$ plane with conductivity components $\sigma_{xx}$ and $\sigma_{zz}$ . Quantum dot 'a' is located at the center, and two other quantum dots are at two different angles. The dipole polarization is along $y$ , normal to the surface. . . . .	61
3.18	Steady-state entanglement for various pairs of QDs. The height of the dots above the hyperbolic surface is $h = \lambda/60$ , and frequency is 10 THz. The distance between each pair (QD <sub>a</sub> - QD <sub>b</sub> and QD <sub>a</sub> - QD <sub>c</sub> ) is $d = \lambda/2$ . Optical dipole moment of the dot at the center is 30 D, and the two other dots have moment 30 D. The dot at the center is illuminated by a pump with intensity $\Omega_{aa} = 0.35\Gamma_{aa}$ . Solid blue line is the steady state entanglement between pairs QD <sub>a</sub> at center and QD <sub>b</sub> at $\phi = 50^\circ$ . Solid red is the steady state entanglement between pair QD <sub>a</sub> at the center and QD <sub>c</sub> at $\phi = 235^\circ$ . Horizontal axis, R, is the ratio of conductivity tensor components that yield these conductivity values. . . . .	62
3.19	Time-evolution of entanglement. The QDs are $h = \lambda/60$ above the surface, and frequency is 10 THz. The distance between the dots is $d = \lambda/2$ . Optical dipole moment of the dot at the center is 30 D, and same thing for the other two dots. The dot at the center is illuminated by a pump with $\Omega_{aa} = 0.35\Gamma_{aa}$ . The ratio $R = 1.42$ ( $\phi = 50^\circ$ ) corresponds to $\sigma_{xx} = 0.001 - 3.87i$ mS, $\sigma_{zz} = 0.0010 + 5.5080i$ mS and $R = 2$ ( $\phi = 235^\circ$ ) corresponds to $\sigma_{xx} = 0.001 - 2.9i$ mS, $\sigma_{zz} = 0.001 + 5.9i$ mS. . . . .	63
3.20	SPP propagation due to a dipole located at $h = \lambda/60$ above the surface made by graphene strips array with $\tau = 1$ pS, $W = 97$ nm and $L = 100$ nm. a: Solid blue for $\mu_c = 0.8$ eV and solid red is for $\mu_c = 1.01$ eV. QDs are indicated by red dots. b: Driven concurrence by a pump with intensity $\Omega = 0.4\Gamma_{aa}$ between pair QD <sub>a</sub> , QD <sub>b</sub> and QD <sub>a</sub> , QD <sub>c</sub> when beam is in a different direction. . . . .	63

4.1	a. Dispersion of reciprocal SPP. Upper-left insert shows SPP power flow excited by a vertical dipole source near a step change in height at the interface between a reciprocal medium (below) and a different reciprocal medium (above), b. nonreciprocal SPP; shaded region depicts frequency range of uni-directional propagation. Upper-right insert is the same as upper-left insert, except that the lower medium is now non-reciprocal and we operate in the gap, ensuring one-way propagation. . . . .	66
4.2	a. Parallel transport around a sphere. b. Parallel transport about a closed contour on a sphere and solid angle subtended. . . . .	70
4.3	Depiction of electron orbits in an insulator in the presence of a magnetic field, and interrupted orbits at the edge. . . . .	79
4.4	Bulk-edge correspondence. Materials with common bandgap and different Chern numbers share an interface where a uni-directional edge state closes the gap. . . . .	80
4.5	Interface between a magnetic-field biased plasma (bottom) and a simple material (top).	85
4.6	Band diagram and Chern numbers (TM modes) for a magneto-optic material; blue: TM mode, no spatial cut-off, green: TM mode, with spatial cut-off, red: TE mode, purple: gap. Left: magneto-optic material (4.78) with $\omega_e/\omega_0 = 5.6$ and $k_{\max} = 10$ ( $\omega_0/c$ ), right: magneto-optic material (4.77) with $\omega_p/2\pi = 9.7$ THz, $\omega_c/2\pi = 1.73$ THz ( $\omega_p/\omega_c = 5.6$ ), and $k_{\max} = 10$ ( $\omega_c/c$ ), black: SPP dispersion. . . . .	86
4.7	Electric field due to a 2D vertical dipole and $\omega_p/2\pi = 9.7$ THz for three cases: left: unbiased (reciprocal) case that respects TR symmetry, $\omega_c = 0$ , at 10 THz ( $\lambda = 30\mu$ m), center: biased with $\omega_c/2\pi = 1.73$ THz at 12 THz, outside of the band gap ( $\omega/\omega_c = 6.93$ ), and right: biased with $\omega_c/2\pi = 1.73$ THz inside the bandgap at 10 THz, ( $\omega/\omega_c = 5.78$ ). . . . .	94
4.8	Electric field at 10 THz for a 3D vertical dipole at a magnetoplasma–plasma interface (top interface is between the magnetoplasma and the $\varepsilon = -5$ simple plasma, all other interfaces are between the magnetoplasma and vacuum). Top: unbiased ( $\omega_c = 0$ , reciprocal) case. Bottom: non-reciprocal case when $\omega_c/2\pi = 1.73$ THz inside the bandgap ( $\omega/\omega_c = 5.78$ ). . . . .	95
4.9	Electric field near a magnetoplasma–plasma interface, as in Fig. 4.8, in the non-reciprocal case when a large ( $1\lambda$ ) spherical vacuum obstacle is placed in the SPP path.	95
4.10	Side view of power density due to a vertical point dipole source at the interface between a magnetoplasma–plasma interface (top surface, all other sides interface with vacuum). a. Power density in the reciprocal case. b. Non-reciprocal case. . . . .	96
4.11	Side view of power density due to a vertical point dipole source at the interface between a magnetoplasma–plasma interface. a. Power density in the reciprocal case. b. Non-reciprocal case. . . . .	96

5.1	Two qubits at the interface of a PTI and topologically trivial medium. The resulting unidirectional SPP provides a strongly non-reciprocal environment for qubit entanglement. . . . .	101
5.2	Left panel: Concurrence between two qubits for a reciprocal system. For the dissipative regime $\text{Im}(\mathbf{G}(\mathbf{r}_1, \mathbf{r}_2)) = \text{Im}(\mathbf{G}(\mathbf{r}_2, \mathbf{r}_1)) = 0.9$ and $\text{Re}(\mathbf{G}(\mathbf{r}_1, \mathbf{r}_2)) = 0$ and for the coherent regime $\text{Re}(\mathbf{G}(\mathbf{r}_1, \mathbf{r}_2)) = \text{Re}(\mathbf{G}(\mathbf{r}_2, \mathbf{r}_1)) = 0.9$ and $\text{Im}(\mathbf{G}(\mathbf{r}_1, \mathbf{r}_2)) = 0$ . Right panel: Concurrence between two qubits for a unidirectional system. For the dissipative regime $\text{Im}(\mathbf{G}(\mathbf{r}_2, \mathbf{r}_1)) = 0.9$ , $\text{Re}(\mathbf{G}(\mathbf{r}_2, \mathbf{r}_1)) = 0$ and for the coherent case $\text{Im}(\mathbf{G}(\mathbf{r}_2, \mathbf{r}_1)) = 0$ , $\text{Re}(\mathbf{G}(\mathbf{r}_2, \mathbf{r}_1)) = 0.9$ . In all cases the Green function quantity is normalized by $\text{Im}(\mathbf{G}(\mathbf{r}_1, \mathbf{r}_1))$ . . . . .	107
5.3	a. Transient concurrence for two interacting qubits in different environments; 1) vacuum, 2) at the interface of a gold half-space ( $\varepsilon = -91.6 - 3i$ ) and vacuum, 3) at the interface of a magnetized plasma ( $\omega_p/\omega = 0.95$ , $\omega_c/\omega = 0.21$ ) and vacuum, and 4) at the interface of the magnetized plasma and an opaque medium (non-biased plasma with $\omega_p/\omega = \sqrt{3}$ , such that $\varepsilon = -2$ ). b. One way SPP at the interface of the biased plasma and the opaque medium at $\omega/2\pi = 200$ THz. c. Driven concurrence of two qubits in the same environments as in panel a. d. Steady states concurrence versus pumping intensities for the case of the biased plasma and opaque medium interface. The qubit separation is $2.4 \mu\text{m}$ ( $1.6\lambda_0$ ). . . . .	109
5.4	Reciprocal bulk bands (solid blue) for the biased plasma ( $\omega_p/\omega = 0.95$ ), and the unidirectional gap-crossing SPP (dashed red) dispersion for a biased-plasma/opaque medium ( $\varepsilon = -2$ ) interface, for different values of bias at $\omega/2\pi = 200$ THz. . . . .	110
5.5	Concurrence mediated by a unidirectional SPP at the interface of biased plasma ( $\omega_p/\omega = 0.95$ ) and an opaque medium ( $\varepsilon = -2$ ) when the left dot has an initial excitation (state $ 4\rangle =  e_1, g_2\rangle$ ). For $\omega_c < 0$ , the same three absolute values are considered as for positive bias, i.e., $\omega_c/\omega_0 = - 0.27 , - 0.21 $ , and $- 0.11 $ . The qubit separation is $2.4 \mu\text{m}$ ( $1.6\lambda_0$ ). . . . .	111
5.6	Left panel: Transient concurrence of two qubits interacting through a flat interface made of an opaque medium ( $\varepsilon = -2$ ) and both an unbiased plasma ( $\omega_p/\omega = 0.95$ , $\omega_c/\omega = 0$ ) and a biased plasma ( $\omega_p/\omega = 0.95$ , $\omega_c/\omega = 0.21$ ). Insert shows shows the electric field $E_y$ excited by a vertical electric dipole. Right panel: Same thing for the case of a defected interface, where the defect contour length is of the order of a free-space wavelength. The system of qubits is initially prepared in the state $ 4\rangle =  e_1, g_2\rangle$ . The qubit separation is $1.7 \mu\text{m}$ ( $1.13\lambda_0$ ). . . . .	112

5.7	a. Finite-width waveguide formed by an opaque medium and biased plasma. b. Transient and driven concurrence of two qubits interacting through the finite-width waveguide. For the biased plasma, $\omega_p/\omega = 0.95$ and $\omega_c/\omega = 0.21$ , and for the opaque medium, $\varepsilon = -2$ . c. Dynamics of the qubits under external pumping. d. Steady state concurrence for different pump values. Waveguide width is $1.8 \mu\text{m}$ ( $1.2\lambda_0$ ) and qubit separation is $2.4 \mu\text{m}$ ( $1.6\lambda_0$ ) . . . . .	113
5.8	Transient concurrence of two qubits interacting in a finite-width waveguide (see Fig. 5.7a) consisting of an opaque medium ( $\varepsilon = -2$ ) and a biased plasma ( $\omega_p/\omega = 0.95$ , $\omega_c/\omega = 0.21$ ). The defect contour length is of the order of a free-space wavelength, and spans the width of the waveguide, $W = 1.8 \mu\text{m}$ ( $1.2\lambda_0$ ). Qubit spacing for the flat interface is $2.4 \mu\text{m}$ ( $1.6\lambda_0$ ), and for the interface with defect, the line-of-sight spacing is $2.4 \mu\text{m}$ . The system of qubits is initially prepared in the state $ 4\rangle =  e_1, g_2\rangle$ . . . . .	113
5.9	Left panel: Transient and driven concurrence for a system of qubits interacting through a right going unidirectional SPP while the initial excitation is in the right qubit. Right panel: Dynamics of the qubit system for the transient case. For the biased plasma $\omega_p/\omega = 0.95$ and $\omega_c/\omega = 0.21$ , and for the opaque medium $\varepsilon = -2$ . The waveguide geometry is shown in Fig. 5.7a, and qubit separation is $2.4 \mu\text{m}$ ( $1.6\lambda_0$ ) . . . . .	114
5.10	Left panel: Transient and driven concurrence for a system of qubits initially prepared in the Bell state. Right panel: Dynamics of the qubits system under external pumping. For the biased plasma, $\omega_p/\omega = 0.95$ and $\omega_c/\omega = 0.21$ , and for the opaque medium $\varepsilon = -2$ . The waveguide geometry is shown in Fig. 5.7a with $W = 1.8 \mu\text{m}$ ( $1.2\lambda_0$ ), and qubit separation is $2.4 \mu\text{m}$ ( $1.6\lambda_0$ ). . . . .	114
5.11	Left panel: Transient concurrence of two qubits interacting through an infinite interface between a biased plasma ( $\omega_p/\omega = 0.95$ and $\omega_c/\omega = 0.21$ ) and an opaque medium ( $\varepsilon = -2$ ) for different values of the collision frequency. Right panel: Steady state concurrence for different pump values in the lossy case. Qubit separation is $2.4 \mu\text{m}$ ( $1.6\lambda_0$ ) . . . . .	115
12	a. Magnetic current source (black dot, $z$ -directed and $z$ -invariant) located at $x = 0, y = d$ inside a biased plasma region, with an opaque half space occupying $y < 0$ . b. Magnetic field $H_z(x)$ at the interface of an $\varepsilon = -2$ half-space ( $x$ ) and a magnetized plasma having $\omega_p/\omega = 0.95$ and $\omega_c/\omega = 0.21$ , at $\omega_0/2\pi = 200$ THz. The magnetic line source is located $\lambda_0/10$ above the interface in the plasma region, and the field is evaluated at $(x, y = \lambda_0/10, z = 0)$ . c. Field behavior in the vicinity of the source showing the discontinuity of the residue component. d. Same as (b) for the unbiased (reciprocal) case, $\omega_c/\omega = 0$ . . . . .	124



13	a. Magnetic field $H_z(x)$ at the interface of an $\varepsilon = -0.47$ half-space and a magnetized plasma having $\omega_p/\omega = 0.95$ and $\omega_c/\omega = 0.20$ , at $\omega_0/2\pi = 230$ THz. The magnetic line source is located $\lambda_0/10$ above the interface in the plasma region, and the field is evaluated at $(x, y = \lambda_0/10, z = 0)$ . b. Field behavior in the vicinity of the source showing the discontinuity of the residue component. . . . .	125
14	a. Dissipative decay (solid blue) and coherent (dashed red) rates at the interface of a biased plasma ( $\omega_p/\omega = 0.95$ , $\omega_c/\omega = 0.21$ ) and an opaque medium ( $\varepsilon = -2$ ) at $\omega/2\pi = 200$ THz. b. The same as a. but for 207 THz. The black circle demonstrate the point dipole source, and the dipole moment is $d = 60$ D. c. The normalized rates as a function of the height of the two qubits above the interface for a fixed separation of $2.1 \mu\text{m}$ . . . . .	125

## LIST OF TABLES

1.1	Qubits Pauli operators and their acts on the atomic states. . . . .	19
-----	---	----

## LIST OF ABBREVIATIONS

$\epsilon_0$ .....	vacuum permittivity
$\mu_0$ .....	vacuum permeability
<b>J</b> .....	volume current density
<b>E</b> .....	electric field intensity
<b>H</b> .....	magnetic field intensity
<b>D</b> .....	electric flux density
<b>B</b> .....	magnetic flux density
$c$ .....	vacuum speed of light
<b>SPP</b> .....	surface plasmon polariton
<b>THz</b> .....	terahertz
<b>HEM</b> .....	Heisenberg equation of motion
<b>ME</b> .....	master equation
<b>BP</b> .....	black phosphorus
<b>GA</b> .....	genetic algorithm
<b>PTI</b> .....	photonic topological insulator
<b>TR</b> .....	time reversal
<b>I</b> .....	inversion

# ACKNOWLEDGEMENTS

I would like to thank my Ph.D. adviser, Professor George W. Hanson, for all his tireless efforts, continuous support, advising me throughout this project and for the valuable life lessons he imparted with his attitude and knowledge. Throughout these years, he has been very inspirational to me and has been a great mentor. Without his guidance and persistent help this dissertation would not have been possible for me. I can truly claim the years I have been working under his supervision as the most progressive years of my life so far.

From a long view of the history of mankind - seen from, say, ten thousand years from now - there can be little doubt that the most significant event of the 19th century will be judged as Maxwell's discovery of the laws of electrodynamics.

*Richard P. Feynman*

# Chapter 1

## Introduction

### 1.1 Background

Surface plasmon-polaritons (SPPs) are electromagnetic waves that are confined to material interfaces, and allow sub-wavelength confinement of light [1]. Extensive research has been carried out in this field due to their technological potential. Applications of SPPs in electronics and optics are numerous and include light harvesting [2], medical sciences [3], plasmon focusing [4], and waveguiding and interferometry [5]. These applications and their rapid development have been made possible by the large array of experimental tools that have become available in recent years for nanoscale fabrication and theoretical tools in the form of powerful electromagnetic simulation methods. At the same time, and completely parallel to this remarkable progress, there has been a growing excitement about the prospects for exploring quantum properties of surface plasmons and building plasmonic devices that operate faithfully at the quantum level [6].

In this basis, many efforts have been made to control the coupling between quantum emitters, atoms or generally qubits and the electromagnetic field. One major force driving the interest in this research area lies in quantum information science, which often requires the generation of entangled states between qubits and transfer of quantum states between matter and light degrees of freedom [7]. One of the necessary elements in this context is coupling of qubits provided by the interchange of fermions or bosons [8, 9]. Electromagnetic field establishes the factor needed to prepare or maintain an entangled state or to couple two prepared entangled systems. This can be accomplished by coupling the quantum system (system of atoms) to cavity modes or in the case of very large separation, by coupling to the waveguide modes [10, 11].

Photonic crystal cavities [12] and waveguides [13], nano-wire structures [14] and dielectric slot waveguides [15] are examples of plasmonic and non-plasmonic electromagnetic structures proposed in the literature for tailoring the light-matter interaction. Enhancement of electromagnetic modes in these structures is the most important aspect, given by the Purcell factor, which is the decay

rate of the quantum dot in the presence of the medium normalized by that of vacuum. Surface waves, which are supported at the interface of a metallic structure and a dielectric, display strong field concentration, and so are great candidates to be exploited for quantum optics. Along with 3D plasmonic systems, 2D plasmonic structures have also attracted a great attention for quantum optics applications and controlling the atom-field and atom-atom coupling due to their potential to support and control plasmonic waves using a gate voltage in graphene [16, 17] or doping in single/multi-layer black phosphorus [18].

In order to have strong and robust communication and entangled states in a system of qubits interacting through a medium, we have to focus the energy from the excited qubit toward other qubit in the system. However, all 2D or 3D plasmonic devices are impacted by SPP reflection, radiation, and diffraction at surface defects and discontinuities, which leads to losing the atomic coupling. In particular, for reciprocal materials, for each forward propagating mode there is a corresponding backward mode with identical propagation constant and modal distribution, and a surface defect/discontinuity can both scatter a forward mode into a backward mode (and vice versa) and cause significant radiation/diffraction of the SPP into the bulk materials. In order to control this effect we have to 1) eliminate one of the modes (forward or backward), and 2) ensure that energy is not radiated into the bulk materials. The presence of a backward state comes from time-reversal (TR) symmetry; when the symmetry is broken, a backward state may be absent, and reflection at a discontinuity can be suppressed. Furthermore, if the surface mode appears in a common bandgap of both bulk materials, then at a surface discontinuity radiation/diffraction into the bulk is suppressed. As a result, surface energy is unidirectional and must follow the contour of the interface, even in the presence of strong discontinuities. As it will be discussed in the later chapters, this interesting behavior of scattering-immune surface wave can lead to a focused unidirectional energy transfer and so robust entanglement. This type of system can be broadly classified as a photonic topological insulator (PTI) [19], which is an electromagnetic insulator in its bulk with conducting states on its surface. The first PTIs were considered in [20] as analogs to electronic topological insulators (TIs), in which surface electron transport occurs without dissipation, even in the presence of impurities.

The rest of this chapter is devoted to a brief introduction to the mathematical aspects of dyadic Green functions, and the electric field dyadic Green function derivation for electromagnetic systems. Then the two methods of Heisenberg equation of motion (HEM) and quantum master equation (ME) are described, which are used to describe different 2D/3D quantum system evolution in later chapters.

## 1.2 Dyadic Green Functions

### 1.2.1 Mathematical Basis of Dyadic Green Function

Let us consider the following general inhomogeneous equation

$$\mathcal{L}\mathbf{A}(\mathbf{r}) = \mathbf{B}(\mathbf{r}) \quad (1.1)$$

where  $\mathbf{A}(\mathbf{r})$  is a general unknown vectorial field,  $\mathbf{B}(\mathbf{r})$  is the known source term and  $\mathcal{L}$  is a linear operator which acts on the unknown field. The general solution of the above equation consists of a homogeneous solution ( $\mathbf{B}(\mathbf{r}) = 0$ ) and particular inhomogeneous solution. It is usually difficult to find the solution of 1.1 while it is easier to consider the special source term  $\delta(\mathbf{r} - \mathbf{r}')$  which is zero everywhere except at the point  $\mathbf{r} - \mathbf{r}' = 0$ . Therefore 1.1 becomes

$$\mathcal{L}\mathbf{G}_i(\mathbf{r}, \mathbf{r}') = n_i\delta(\mathbf{r} - \mathbf{r}') \quad (1.2)$$

where  $n_i$ ,  $i = x, y, z$  denotes an arbitrary unit vector. As can be seen the unknown vector  $\mathbf{G}_i$  depends on the location of delta function inhomogeneity. In a general form, 1.2 can be written as

$$\mathcal{L}\mathbf{G}(\mathbf{r}, \mathbf{r}') = \mathbf{I}\delta(\mathbf{r} - \mathbf{r}') \quad (1.3)$$

where  $\mathbf{I}$  is the unit dyad and  $\mathbf{G}$  is a dyadic function known as the dyadic Green function. By having the known dyadic Green function of 1.1, one can find the unknown vector field  $\mathbf{A}(\mathbf{r})$  by post-multiplying both sides of 1.3 with  $\mathbf{B}(\mathbf{r}')$  and integrating over the volume where  $\mathbf{B}(\mathbf{r}) \neq 0$ . This process gives

$$\int_V \mathcal{L}\mathbf{G}(\mathbf{r}, \mathbf{r}')\mathbf{B}(\mathbf{r}')dV' = \int_V \mathbf{B}(\mathbf{r}')\delta(\mathbf{r} - \mathbf{r}')dV', \quad (1.4)$$

and the right hand side of above equation reduces to  $\mathbf{B}(\mathbf{r})$ , and with 1.1 it follows that

$$\mathbf{A}(\mathbf{r}) = \int_V \mathbf{G}(\mathbf{r}, \mathbf{r}')\mathbf{B}(\mathbf{r}')dV'. \quad (1.5)$$

Thus the solution of the original equation can be found by integrating the product of the dyadic Green function and the source term over the volume where the source is non zero.

The assumption that the operator  $\mathcal{L}$  and  $\int dV'$  can be interchanged is not strictly valid and special care must be applied if the integrand is not well behaved. Most often the dyadic Green function  $\mathbf{G}$  is singular at  $\mathbf{r} = \mathbf{r}'$  and an infinitesimal exclusion volume surrounding  $\mathbf{r} = \mathbf{r}'$  has to be introduced [21, 22]. Depolarization of the principal volume must be treated separately resulting in the depolarization term,  $\mathbf{L}$ , which depends only on the geometrical shape of the exclusion volume. Furthermore, in most numerical schemes, the principal volume has a finite size giving rise to an additional correction term labeled as the self term  $\mathbf{M}$ . However, as the exclusion volume shrinks the self term reduces to zero. As long as we consider field points outside of the source volume  $V$  we do not need to consider these issues. In the next section we briefly bring the derivation of the dyadic Green function for electric field.



### 1.2.2 Derivation of the Electric Field Dyadic Green Functions

The Maxwell Equations, in a generalized medium, where we have assumed time-harmonic fields with an  $e^{-i\omega t}$  dependence, can be written as

$$\begin{aligned}
\nabla \times \mathbf{E}(\mathbf{r}, \omega) &= i\omega \mathbf{B}(\mathbf{r}, \omega) \\
\nabla \times \mathbf{H}(\mathbf{r}, \omega) &= -i\omega \mathbf{D}(\mathbf{r}, \omega) + \mathbf{j}(\mathbf{r}, \omega) \\
\nabla \cdot \mathbf{D}(\mathbf{r}, \omega) &= \rho(\mathbf{r}, \omega) \\
\nabla \cdot \mathbf{B}(\mathbf{r}, \omega) &= 0
\end{aligned} \tag{1.6}$$

where  $\mathbf{E}$  is the electric field,  $\mathbf{D}$  is the electric displacement,  $\mathbf{H}$  is the magnetic field,  $\mathbf{B}$  is the magnetic induction,  $\mathbf{j}$  is the current density and  $\rho$  is the charge density. The  $\mathbf{E}/\mathbf{B}$  fields can be related to the  $\mathbf{D}/\mathbf{H}$  fields through the constitutive relations, assuming simple isotropic, local, media,

$$\begin{aligned}
\mathbf{D}(\mathbf{r}, \omega) &= \epsilon_0 \epsilon(\mathbf{r}, \omega) \mathbf{E}(\mathbf{r}, \omega) \\
\mathbf{H}(\mathbf{r}, \omega) &= \frac{1}{\mu_0 \mu(\mathbf{r}, \omega)} \mathbf{B}(\mathbf{r}, \omega)
\end{aligned} \tag{1.7}$$

where  $\epsilon$  and  $\mu$  are the relative material permittivity and permeability and  $\epsilon_0$  and  $\mu_0$  are the permittivity and permeability of the free space. To determine the dyadic Green function for the electric field we start with the wave equation for the electric field. For an inhomogeneous medium,

$$\nabla \times \nabla \times \mathbf{E}(\mathbf{r}) - k^2 \mathbf{E}(\mathbf{r}) = i\omega \mu_0 \mu(\mathbf{r}) \mathbf{j}(\mathbf{r}), \tag{1.8}$$

where we can define for each component of  $\mathbf{j}$  a corresponding Green function. For instance, for  $\mathbf{j}_x$  we have

$$\nabla \times \nabla \times \mathbf{G}_x(\mathbf{r}, \mathbf{r}') - k^2 \mathbf{G}_x(\mathbf{r}, \mathbf{r}') = \mathbf{n}_x \delta(\mathbf{r} - \mathbf{r}'). \tag{1.9}$$

A similar equation can be formulated for a point source polarized along the other directions  $y$  and  $z$ . In order to account for all orientations we write as the general definition of the dyadic Green function for the electric field

$$\nabla \times \nabla \times \mathbf{G}(\mathbf{r}, \mathbf{r}') - k^2 \mathbf{G}(\mathbf{r}, \mathbf{r}') = \mathbf{I} \delta(\mathbf{r} - \mathbf{r}'), \tag{1.10}$$

where as what we had before,  $\mathbf{I}$  is the unit tensor. The first column of the tensor  $\mathbf{G}$  corresponds to the field due to a point source polarized along  $x$ , the second column to the field due to a point source along  $y$  direction and the third column is the field due a point source polarized along the  $z$  direction. Therefore the dyadic Green function is a compact notation for three vectorial Green functions.

The source current  $\mathbf{j}(\mathbf{r})$  can be viewed as a superposition of point currents, so if we know the

Green function we can find the particular solution of the electric field in 1.8 as

$$\mathbf{E}(\mathbf{r}) = i\omega\mu_0 \int_V \mathbf{G}(\mathbf{r}, \mathbf{r}') \mu(\mathbf{r}') \mathbf{j}(\mathbf{r}') dV'. \quad (1.11)$$

The above equation is the particular solution and we need to add any homogeneous solution  $\mathbf{E}_0$ . Therefore the general solution has the following form

$$\mathbf{E}(\mathbf{r}) = \mathbf{E}_0 + i\omega\mu_0 \int_V \mathbf{G}(\mathbf{r}, \mathbf{r}') \mu(\mathbf{r}') \mathbf{j}(\mathbf{r}') dV' \quad (1.12)$$

and the corresponding magnetic field is

$$\mathbf{H}(\mathbf{r}) = \mathbf{H}_0 + \int_V [\nabla \times \mathbf{G}(\mathbf{r}, \mathbf{r}')] \mathbf{j}(\mathbf{r}') dV'. \quad (1.13)$$

The above equations lead to volume integral equations. They form the basis for various theoretical and numerical formalisms such as the method of moments, the Lippmann-Schwinger equation, or the coupled dipole method.

Some common relations valid for reciprocal dyadic Green functions are [23]

$$\begin{aligned} \mathbf{G}_{ij}^*(\mathbf{r}, \mathbf{r}', \omega) &= \mathbf{G}_{ij}(\mathbf{r}, \mathbf{r}', -\omega) \\ \mathbf{G}_{ji}(\mathbf{r}', \mathbf{r}, \omega) &= \mathbf{G}_{ij}(\mathbf{r}, \mathbf{r}', \omega) \end{aligned} \quad (1.14)$$

and the most important one for our use is

$$\begin{aligned} &\text{Im}(\mathbf{G}(\mathbf{r}, \mathbf{r}', \omega)) \\ &= \int d^3\mathbf{s} (\text{Im}(\epsilon(\mathbf{s}, \omega)) \mathbf{G}(\mathbf{r}, \mathbf{s}, \omega) \mathbf{G}^*(\mathbf{s}, \mathbf{r}', \omega) - \text{Im}(\mu^{-1}(\mathbf{s}, \omega)) [\mathbf{G}(\mathbf{r}, \mathbf{s}, \omega) \times \nabla_{\mathbf{s}}] \cdot [\nabla_{\mathbf{s}} \times \mathbf{G}^*(\mathbf{s}, \mathbf{r}', \omega)]). \end{aligned} \quad (1.15)$$

As an example, the Green dyadic for electric field in free space is

$$\mathbf{G}^0(\mathbf{r}, \mathbf{r}', \omega) = \left( \mathbf{I} + \frac{1}{k^2} \nabla \nabla \right) \frac{e^{ikR}}{4\pi R} = \left[ \frac{(kR)^2 + ikR - 1}{(kR)^2} \mathbf{I} + \frac{3 - 3ikR - (kR)^2}{(kR)^2} \frac{\mathbf{R} \otimes \mathbf{R}}{R^2} \right] \frac{e^{ikR}}{4\pi R}, \quad (1.16)$$

where  $\mathbf{R} = \mathbf{r} - \mathbf{r}'$ . The imaginary part of the Green dyadic is  $\text{Im}\mathbf{G}^0(\mathbf{r}, \mathbf{r}', \omega) = k/6\pi$ .

Although the dyadic Green function is a classical quantity, it plays a crucial role in the methods of describing the evolution of quantum systems. In what follows, two of them are discussed; the Heisenberg equations of motion (HEM) and master equation (ME).

### 1.3 Heisenberg Equations of Motion (HEM)

We introduce the quantum theoretical formalism developed by Welsch and colleagues [24, 28, 26, 27] which describes the quantization of the electromagnetic field for lossy, inhomogeneous media. Using this approach, we define a Hamiltonian that describes the coupling between an atom or quantum dot (QD) and the general field to calculate the dynamics of the system and other quantum properties such as entanglement. We shall solve these equations self-consistently and non-perturbatively, thus making them applicable in both the weak and strong coupling regimes. Although in this formalism the whole process is non-classical and requires quantum operator description of the quantities, the coupling between emitter and medium can be rigorously incorporated into the formalism through the dyadic Green function.

#### 1.3.1 Field Quantization in Lossy Inhomogeneous Media

We begin with the sourceless quantized form of Maxwell's equation

$$\begin{aligned}
\nabla \times \hat{\mathbf{E}}(\mathbf{r}, \omega) &= i\omega \hat{\mathbf{B}}(\mathbf{r}, \omega) \\
\nabla \times \hat{\mathbf{H}}(\mathbf{r}, \omega) &= -i\omega \hat{\mathbf{D}}(\mathbf{r}, \omega) \\
\nabla \cdot \hat{\mathbf{D}}(\mathbf{r}, \omega) &= 0 \\
\nabla \cdot \hat{\mathbf{B}}(\mathbf{r}, \omega) &= 0.
\end{aligned} \tag{1.17}$$

where the fields have been elevated to operator level. Similarly the constitutive relations become

$$\begin{aligned}
\hat{\mathbf{D}}(\mathbf{r}, \omega) &= \epsilon_0 \epsilon(\mathbf{r}, \omega) \hat{\mathbf{E}}(\mathbf{r}, \omega) + \hat{\mathbf{P}}_N(\mathbf{r}, \omega) \\
\hat{\mathbf{H}}(\mathbf{r}, \omega) &= \frac{1}{\mu_0 \mu(\mathbf{r}, \omega)} \hat{\mathbf{B}}(\mathbf{r}, \omega) + \hat{\mathbf{M}}_N(\mathbf{r}, \omega)
\end{aligned} \tag{1.18}$$

As can be seen in the above equations, in order to consider the material loss, two additional noise terms  $\hat{\mathbf{P}}_N(\mathbf{r}, \omega)$  and  $\hat{\mathbf{M}}_N(\mathbf{r}, \omega)$  have been added, which are associated with electric and magnetic losses respectively. Using the above sets of equations we can obtain the electric field wave equation

$$\nabla \times \mu^{-1}(\mathbf{r}, \omega) \nabla \times \hat{\mathbf{E}}(\mathbf{r}, \omega) - \frac{\omega_\lambda^2}{c^2} \epsilon(\mathbf{r}, \omega) \hat{\mathbf{E}}(\mathbf{r}, \omega) = i\omega_\lambda \mu_0 \hat{\mathbf{j}}_N(\mathbf{r}, \omega) \tag{1.19}$$

where

$$\hat{\mathbf{j}}_N(\mathbf{r}, \omega) = -i\omega_\lambda \hat{\mathbf{P}}_N(\mathbf{r}, \omega) + \nabla \times \hat{\mathbf{M}}_N(\mathbf{r}, \omega) \tag{1.20}$$

is the noise current and  $\omega_\lambda$  is the eigen frequency of a single continuous mode. From this we can obtain the total electric field operator as

$$\hat{\mathbf{E}}(\mathbf{r}, \omega_\lambda) = \int \left[ \mathbf{G}(\mathbf{r}, \mathbf{r}', \omega_\lambda) \cdot \hat{\mathbf{P}}_N(\mathbf{r}', \omega_\lambda) + \frac{i}{\omega_\lambda} \mathbf{G}(\mathbf{r}, \mathbf{r}', \omega_\lambda) \cdot \nabla \times \hat{\mathbf{M}}_N(\mathbf{r}', \omega_\lambda) \right] d\mathbf{r}' \quad (1.21)$$

where  $\mathbf{G}$  is the classical Green function given by

$$\nabla \times \mu^{-1}(\mathbf{r}, \omega_\lambda) \nabla \times \mathbf{G}(\mathbf{r}, \mathbf{r}', \omega_\lambda) - \frac{\omega_\lambda^2}{c^2} \epsilon(\mathbf{r}, \omega_\lambda) \mathbf{G}(\mathbf{r}, \mathbf{r}', \omega_\lambda) = \frac{\omega_\lambda^2}{c^2} \mathbf{I} \delta(\mathbf{r} - \mathbf{r}'). \quad (1.22)$$

Working in the Heisenberg picture, operators become time dependent so we can write the total electric field operator as

$$\hat{\mathbf{E}}(\mathbf{r}, \omega_\lambda, t) = \int \left[ \mathbf{G}(\mathbf{r}, \mathbf{r}', \omega_\lambda) \cdot \hat{\mathbf{P}}_N(\mathbf{r}', \omega_\lambda, t) + \frac{i}{\omega_\lambda} \mathbf{G}(\mathbf{r}, \mathbf{r}', \omega_\lambda) \cdot \nabla \times \hat{\mathbf{M}}_N(\mathbf{r}', \omega_\lambda, t) \right] d\mathbf{r}'. \quad (1.23)$$

Considering the noise polarization and the noise magnetization, we introduce a set of continuous bosonic vector fields  $\hat{\mathbf{b}}_e(\mathbf{r}, \omega_\lambda, t)$  and  $\hat{\mathbf{b}}_m(\mathbf{r}, \omega_\lambda, t)$  which are responsible for the excitation of noises [27, 28]

$$\begin{aligned} \hat{\mathbf{P}}_N(\mathbf{r}, \omega_\lambda, t) &= i \sqrt{\frac{\hbar \text{Im}(\epsilon(\mathbf{r}, \omega_\lambda))}{\pi \epsilon_0}} \hat{\mathbf{b}}_e(\mathbf{r}, \omega_\lambda, t) \\ \hat{\mathbf{M}}_N(\mathbf{r}, \omega_\lambda, t) &= \sqrt{\frac{-\hbar \text{Im}(\mu^{-1}(\mathbf{r}, \omega_\lambda))}{\pi \mu_0 \epsilon_0^2}} \hat{\mathbf{b}}_m(\mathbf{r}, \omega_\lambda, t) \end{aligned} \quad (1.24)$$

such that the bosonic field operators satisfy  $[\hat{b}_{\nu,i}, \hat{b}_{\nu',j}^\dagger] = \delta_{\nu\nu'} \delta_{ij}(\mathbf{r} - \mathbf{r}') \delta(\omega_\lambda - \omega'_\lambda)$  and  $[\hat{b}_{\nu,i}, \hat{b}_{\nu',j}] = 0$  where  $\nu, \nu' = e, m$  and  $i, j = x, y, z$ . At this point it should be noted that the mode frequency  $\omega_\lambda$  is not the same as the Fourier transform variable,  $\omega$ , of the time variable  $t$ . Substituting 1.24 into 1.21 one can find the quantum electric field operator of the mode  $\omega_\lambda$  in term of classical Green function and bosonic field operators and then the total time dependent electric field from all modes may can be written as the sum of the positive and negative frequency components

$$\begin{aligned} \hat{\mathbf{E}}(\mathbf{r}, t) &= \int_0^\infty \hat{\mathbf{E}}(\mathbf{r}, \omega_\lambda, t) d\omega_\lambda + \text{H.C.} = i \sqrt{\frac{\hbar}{\pi \epsilon_0}} \times \\ &\int_0^\infty d\omega_\lambda \int \mathbf{G}(\mathbf{r}, \mathbf{r}', \omega_\lambda) \cdot \left[ \sqrt{\text{Im}(\epsilon(\mathbf{r}', \omega_\lambda))} \hat{\mathbf{b}}_e(\mathbf{r}', \omega_\lambda, t) + \frac{c}{\omega_\lambda} \nabla \times \sqrt{-\text{Im}(\mu^{-1}(\mathbf{r}', \omega_\lambda))} \hat{\mathbf{b}}_m(\mathbf{r}', \omega_\lambda, t) \right] d\mathbf{r}' \\ &+ \text{H.C.} \end{aligned} \quad (1.25)$$

where H.C. denoted Hermitian conjugate. At first sight, it looks like for materials with vanishing loss the electric field relating to the bosonic noise operators would become zero. However, if we are careful in taking the limits then we arrive at a finite answer for the electric field operator [24].

### 1.3.2 Non-Pumped Concurrence of Two Quantum Dots Interacting Through lossy Inhomogeneous Medium

We consider two quantum dots interacting through a lossy inhomogeneous reservoir with an arbitrary  $\epsilon(\mathbf{r}, \omega)$  and  $\mu(\mathbf{r}, \omega)$ . In the Heisenberg picture the total Hamiltonian of the system is

$$\begin{aligned} H_{\text{total}} = & \sum_{\nu=e,m} \int d\mathbf{r} \int_0^{+\infty} d\omega_\lambda \hbar\omega_\lambda \mathbf{b}_\nu^\dagger(\mathbf{r}, \omega_\lambda, t) \cdot \mathbf{b}_\nu(\mathbf{r}, \omega_\lambda, t) + \sum_{m=a,b} \hbar\omega_m \sigma_m^\dagger(t) \sigma_m(t) \\ & - \sum_{m=a,b} (\sigma_m^\dagger(t) + \sigma_m(t)) \mathbf{d}_m \cdot \mathbf{E}(\mathbf{r}_m, t) \end{aligned} \quad (1.26)$$

where the first term describes the bosonic field modes (photons and plasmons) and the sum  $\nu = e, m$  is over the electric/magnetic modes, the second term describes the qubit (spin 1/2) Pauli operators where  $\hat{\sigma}^\dagger/\hat{\sigma}$  are the Pauli raising/lowering operators of the QD exciton, and the last term represents the interaction between field and quantum dots. Furthermore,  $\omega_m$  is the QDs transition frequency,  $\mathbf{d}_m$  is the optical dipole moment of the  $m$ th QD and the electric field operator has been found in the previous sub-section, 1.25 with  $\mathbf{G}(\mathbf{r}, \mathbf{r}', \omega_\lambda)$  as the classical Green function that propagates the field from a dipole source at  $\mathbf{r}'$  to  $\mathbf{r}$ .

Before going further, let us take a brief look on the most important terms of the total Hamiltonian expression, interaction and qubit terms.

We consider  $|j\rangle$  as states describing the atomic system, then the Schrodinger equation gives  $H_a |j\rangle = E_j |j\rangle$  where  $E_j$  is the energy associated with each state. Multiplying both sides of this equation with bra  $\langle j|$  from right and summing over all states gives

$$\sum_j H_a |j\rangle \langle j| = \sum_j E_j |j\rangle \langle j| \rightarrow H = \sum_j E_j |j\rangle \langle j|. \quad (1.27)$$

Considering a two-level atom as our system with  $|e\rangle$  as excited state and  $|g\rangle$  as the ground state then we have  $H_a = E_e |e\rangle \langle e| + E_g |g\rangle \langle g|$ . If we choose the reference of energy to be at the middle of excited and ground states energies then we need to re-scale the atom Hamiltonian by the averages of the energies  $E_{ave} = \mathbf{I}(E_e + E_g)/2$  which gives

$$H_a = E_e |e\rangle \langle e| + E_g |g\rangle \langle g| - \mathbf{I}\left(\frac{E_e + E_g}{2}\right) = \frac{1}{2} (E_e - E_g) \hat{\sigma}_z \quad (1.28)$$

where  $\hat{\sigma}_z = \hat{\sigma}^\dagger \hat{\sigma} - \hat{\sigma} \hat{\sigma}^\dagger$  is the inversion operator. Another representation could be choosing the ground state as the energy reference. In this case we have to re-scale by  $E_g |g\rangle \langle g|$  which yields

$$H_a = E_e |e\rangle \langle e| + E_g |g\rangle \langle g| - E_g |g\rangle \langle g| = \hbar\omega_a \hat{\sigma}^\dagger \sigma \quad (1.29)$$

where  $\omega_a = E_e/\hbar$  is the atomic transition frequency.

The interaction Hamiltonian can be considered as  $H_{int} = -\hat{\mathbf{p}} \cdot \hat{\mathbf{E}}$  where  $\hat{\mathbf{p}} = q\mathbf{r}_\delta$  is the general dipole operator. Using dipole approximation we assume  $\mathbf{r}_\delta \ll 2\pi c/\omega_a$ . Considering  $\sum_j |j\rangle \langle j| = \mathbf{I}$  we have  $q\mathbf{r}_\delta = \sum_{i,j} |i\rangle \langle i| q\mathbf{r}_\delta \sum_j |j\rangle \langle j| = \sum_{i,j} \mathbf{d}_{ij} |i\rangle \langle j|$  where  $\mathbf{d}_{ij} = \langle i| q\mathbf{r}_\delta |j\rangle$  is the electric dipole transition matrix and  $q = -e$  is the charge of electron. Assuming the diagonal elements of  $\mathbf{d}_{ij}$  vanish it follows that

$$\hat{\mathbf{p}} \equiv q\mathbf{r}_\delta = \mathbf{d}_{eg} |e\rangle \langle g| + \mathbf{d}_{ge} |g\rangle \langle e| = (\hat{\sigma}^\dagger + \hat{\sigma})\mathbf{d} \quad (1.30)$$

where we have supposed  $\mathbf{d}_{eg} = \mathbf{d}_{ge} = \mathbf{d}$ . Therefore for the interaction term of the total Hamiltonian we have  $H_{int} = -(\hat{\sigma}^\dagger + \hat{\sigma})\mathbf{d} \cdot \hat{\mathbf{E}}$ .

Let us come back to the total Hamiltonian expression. By using the Heisenberg equation of motion  $\partial_t \hat{A}(t) = -i\hbar^{-1}[\hat{A}(t), H_{total}]$  we can find the dynamics of the operators  $\mathbf{b}$ ,  $\mathbf{b}^\dagger$  and  $\sigma_m^{+/-}$ . After carrying out the first derivative of the operators with respect to time we have

$$\begin{aligned} \partial_t \hat{\sigma}_m &= -i\omega_m \hat{\sigma} + i\hbar^{-1} \mathbf{d}_m \cdot \hat{\mathbf{E}}(\mathbf{r}_m) \\ \partial_t \hat{\sigma}_m^\dagger &= i\omega_m \hat{\sigma} - i\hbar^{-1} \mathbf{d}_m \cdot \hat{\mathbf{E}}(\mathbf{r}_m) \\ \partial_t \hat{\mathbf{b}}_e(\mathbf{r}, \omega_\lambda) &= -i\omega_\lambda \hat{\mathbf{b}}_e(\mathbf{r}, \omega_\lambda) + \sqrt{\frac{\text{Im}(\epsilon(\mathbf{r}, \omega_\lambda))}{\pi\hbar\epsilon_0}} \sum_{m=a,b} \mathbf{G}^*(\mathbf{r}, \mathbf{r}_m, \omega_\lambda) \cdot \mathbf{d}_m [\sigma_m + \sigma_m^\dagger] \\ \partial_t \hat{\mathbf{b}}_m(\mathbf{r}, \omega_\lambda) &= -i\omega_\lambda \hat{\mathbf{b}}_m(\mathbf{r}, \omega_\lambda) + \sqrt{\frac{-\text{Im}(\mu^{-1}(\mathbf{r}, \omega_\lambda))}{\pi\hbar\epsilon_0}} \frac{c}{\omega_\lambda} \sum_{m=a,b} [\mathbf{G}^*(\mathbf{r}, \mathbf{r}_m, \omega_\lambda) \times \nabla_r] \cdot \mathbf{d}_m [\sigma_m + \sigma_m^\dagger] \end{aligned} \quad (1.31)$$

where the relations  $\sigma_m \sigma_m^\dagger \sigma_m = \sigma_m$ ,  $\sigma_m^\dagger \sigma_m \sigma_m^\dagger = \sigma_m^\dagger$  and  $\sigma_m^\dagger \sigma_m^\dagger \sigma_m = \sigma_m \sigma_m \sigma_m^\dagger = 0$  are used. The equations in 1.31 do not form a closed set unless we make the weak excitation approximation, which ignores higher order photon correlations (i.e. multiphoton correlations). The result of truncating the number of excitations in the system to a single excitation is that  $\sigma_{m,z} = \sigma_m^\dagger \sigma_m - \sigma_m \sigma_m^\dagger = -1$ . If we consider our initial field to be the vacuum field, this approximation is exact. Next we take a one-sided Fourier transform  $\int_0^\infty e^{i\omega t} \partial_t A(t) dt = -i\omega A(\omega) - A(t=0)$  which leads to

$$\begin{aligned} \hat{\sigma}_m(\omega) &= \frac{i\hat{\sigma}(t=0)}{\omega - \omega_m} - i \frac{\hbar^{-1} \mathbf{d}_m \cdot \hat{\mathbf{E}}(\mathbf{r}_m, \omega)}{\omega - \omega_m} \\ \hat{\sigma}_m^\dagger(\omega) &= \frac{i\hat{\sigma}^\dagger(t=0)}{\omega + \omega_m} + i \frac{\hbar^{-1} \mathbf{d}_m \cdot \hat{\mathbf{E}}(\mathbf{r}_m, \omega)}{\omega + \omega_m} \\ \hat{\mathbf{b}}_e(\mathbf{r}, \omega_\lambda, \omega) &= \hat{\mathbf{b}}_e^0(\mathbf{r}, \omega_\lambda, \omega) + i \sqrt{\frac{\text{Im}(\epsilon(\mathbf{r}, \omega_\lambda))}{\pi\hbar\epsilon_0}} \sum_{m=a,b} \mathbf{G}^*(\mathbf{r}, \mathbf{r}_m, \omega_\lambda) \cdot \mathbf{d}_m \frac{[\sigma_m(\omega) + \sigma_m^\dagger(\omega)]}{\omega - \omega_\lambda} \\ \hat{\mathbf{b}}_m(\mathbf{r}, \omega_\lambda, \omega) &= \hat{\mathbf{b}}_m^0(\mathbf{r}, \omega_\lambda, \omega) + i \sqrt{\frac{-\text{Im}(\mu^{-1}(\mathbf{r}, \omega_\lambda))}{\pi\hbar\epsilon_0}} \frac{c}{\omega_\lambda} \sum_{m=a,b} [\mathbf{G}^*(\mathbf{r}, \mathbf{r}_m, \omega_\lambda) \times \nabla_r] \cdot \mathbf{d}_m \frac{[\sigma_m + \sigma_m^\dagger]}{\omega - \omega_\lambda} \end{aligned} \quad (1.32)$$

where  $\hat{\mathbf{b}}^0$  is the free field solution without an emitter (the QD) [29]. In the previous section we had

found the quantized form of the time dependent electric field operator in 1.25. If we take a Fourier transform

$$\begin{aligned} \mathcal{F.T} [\hat{\mathbf{E}}(\mathbf{r}, t)] &= \hat{\mathbf{E}}(\mathbf{r}, \omega) = i\sqrt{\frac{\hbar}{\pi\epsilon_0}} \times \\ &\int_0^\infty d\omega_\lambda \int \mathbf{G}(\mathbf{r}, \mathbf{r}', \omega_\lambda) \cdot \left[ \sqrt{\text{Im}(\epsilon(\mathbf{r}', \omega_\lambda))} \hat{\mathbf{b}}_e(\mathbf{r}', \omega_\lambda, \omega) + \frac{c}{\omega_\lambda} \nabla \times \sqrt{-\text{Im}(\mu^{-1}(\mathbf{r}', \omega_\lambda))} \hat{\mathbf{b}}_m(\mathbf{r}', \omega_\lambda, \omega) \right] d\mathbf{r}' \\ &+ \text{H.C.} \end{aligned} \quad (1.33)$$

inserting  $\hat{\mathbf{b}}_e/m$  from 1.32 in 1.33 then considering the fact that the Green function is analytical in the upper portion of the complex plane and using the following relation

$$\lim_{y \rightarrow 0^+} \int_a^b \frac{f(x)}{x + iy} = -i\pi \int_a^b f(x) \delta(x) dx + \mathcal{P} \int_a^b \frac{f(x)}{x} \quad (1.34)$$

along with 1.15 for reciprocal Green functions it is straightforward to show (the computational details are omitted for conciseness) that the electric field can be written as

$$\hat{\mathbf{E}}(\mathbf{r}, \omega) = \hat{\mathbf{E}}^0(\mathbf{r}, \omega) + \sum_{m=a,b} \frac{1}{\epsilon_0} \mathbf{G}(\mathbf{r}, \mathbf{r}_m; \omega) \cdot \mathbf{d}_m (\sigma_m^\dagger(\omega) + \sigma_m(\omega)) \quad (1.35)$$

where the first term on the right hand side is the initial vacuum field which does not contribute in the dynamics of the system and can be ignored. If we plug-in  $\sigma_m^\dagger(\omega) + \sigma_m(\omega)$  from 1.32 into 1.35 we obtain

$$\hat{\mathbf{E}}(\mathbf{r}, \omega) = \sum_{m=a,b} \frac{1}{\epsilon_0} \mathbf{G}(\mathbf{r}, \mathbf{r}_m; \omega) \cdot \hat{\mathbf{S}}_m(\omega) + \sum_{m=a,b} \alpha_m(\omega) \mathbf{G}(\mathbf{r}, \mathbf{r}_m; \omega) \cdot \hat{\mathbf{E}}(\mathbf{r}_m, \omega) \quad (1.36)$$

considering equal transition frequency for QDs,  $\omega_a = \omega_b = \omega_d$ , where  $\alpha_m(\omega) = \frac{2\omega_d d_m^2}{\hbar \epsilon_0 (\omega_d^2 - \omega^2)}$  is the bare polarizability,  $\hat{\mathbf{S}}_m = i\mathbf{d}_m \left( \frac{\sigma_m^+(t=0)}{\omega + \omega_d} + \frac{\sigma_m^-(t=0)}{\omega - \omega_d} \right)$  is the quantum dipole source and  $\hat{\mathbf{E}}(\mathbf{r}_m, \omega)$  is the total electric field at the position of  $m$ th quantum dot. Using 1.36 the total electric field at the position of the quantum dots,  $\mathbf{E}(\mathbf{r}_{a/b})$ , can be found and then using the first equation in 1.32 one can find  $\hat{\sigma}_{a/b}$  in the frequency domain. The quantum dynamics of the spatially separated qubits can be obtained from the inverse Fourier transform of the qubit operators

$$\hat{\sigma}_{a/b}(\omega) = \frac{i\hat{\sigma}_{a/b}(t=0)}{(\omega - \omega_d)} - \frac{\hbar^{-1} \mathbf{d}_{a/b} \cdot \mathbf{E}(\mathbf{r}_{a/b}, \omega)}{(\omega - \omega_d)}. \quad (1.37)$$

Writing the wave function as

$$|\psi(t)\rangle = \sum_{m=a,b} C_m^u(t) |a_m^e, 0\rangle + C_m^g(t) |a_m^g, \lambda\rangle. \quad (1.38)$$

where the first entry denoted the state of the atoms and second stands for the state of reservoir. The amplitude coefficient of the qubit upper excited state is  $C_{a/b}^u = \int_{-\infty}^{+\infty} \langle 0 | \hat{\sigma}_{a/b}(\omega) | \psi(t=0) \rangle e^{i\omega t} dt$ ,

with  $|0\rangle$  the lower level eigenstate of the qubits. The upper state population of each qubit is then obtained from  $|C_m^u|^2$  [6]. The entanglement between the two qubits are related to the concurrence between them,  $C(t)$ , which can be obtained from the excited state populations as  $C(t) = 2C_a^u(t)C_b^u(t)$ . A concurrence value of 0 indicates no quantum entanglement, whereas a value of 1 is a maximally-entangled state [30].

## 1.4 Density Operator and Quantum Master Equation (ME)

### 1.4.1 The Density Operator

The density matrix describes a quantum system in a mixed state (a statistical ensemble, statistical mixture of multiple quantum states: for a two state system, it is either in state 1 or state 2, but we don't know which one it is), rather than a pure state, described by a single state vector, or a quantum superposition (it is in both states 1 and 2 at the same time- a quantum superposition of pure states is another pure state, for example  $|\psi\rangle = (|\psi_1\rangle + |\psi_2\rangle)/\sqrt{2}$ ).

If a quantum system may be found in state  $|\psi_1\rangle$  with probability  $p_1$ , or it may be found in state  $|\psi_2\rangle$  with probability  $p_2$ , etc., the density operator (Hermitian,  $\hat{\rho} = \hat{\rho}^\dagger$ ) is

$$\hat{\rho} = \sum_i p_i |\psi_i\rangle \langle \psi_i|, \quad (1.39)$$

where  $p_i$  is the probability of the system being in the  $i$ th state  $|\psi_i\rangle$  of the ensemble, where  $\langle \psi_i|\psi_i\rangle = 1$ . Why: If a quantum system may be found in state  $|\psi_1\rangle$  with probability  $p_1$ , or it may be found in state  $|\psi_2\rangle$  with probability  $p_2$ , then the probability of measuring outcome  $p$  associated with state  $|\psi_p\rangle$  is the probability of measuring  $p$  given that the system is in  $|\psi_1\rangle$ ,  $|\langle \psi_p|\psi_1\rangle|^2$  times the probability that the system is in state  $|\psi_1\rangle$ , plus the probability of measuring  $p$  given that the system is in  $|\psi_2\rangle$ ,  $|\langle \psi_p|\psi_2\rangle|^2$  times the probability that the system is in state  $|\psi_2\rangle$ . Thus,

$$P(p) = p_1 |\langle \psi_p|\psi_1\rangle|^2 + p_2 |\langle \psi_p|\psi_2\rangle|^2 \quad (1.40)$$

$$= p_1 \langle \psi_p|\psi_1\rangle \langle \psi_1|\psi_p\rangle + p_2 \langle \psi_p|\psi_2\rangle \langle \psi_2|\psi_p\rangle \quad (1.41)$$

$$= \langle \psi_p| (p_1 |\psi_1\rangle \langle \psi_1| + p_2 |\psi_2\rangle \langle \psi_2|) |\psi_p\rangle \quad (1.42)$$

$$= \langle \psi_p|\hat{\rho}|\psi_p\rangle. \quad (1.43)$$

The probabilities satisfy

$$0 \leq p_i \leq 1, \quad Tr(\hat{\rho}) = \sum_i p_i = 1, \quad \sum_i p_i^2 \leq 1. \quad (1.44)$$

For a pure state, all  $p_i$  vanish except one (say, the  $j$ th one), and  $\hat{\rho} = |\psi_j\rangle \langle \psi_j|$ . Like the wavefunction, the density operator in the Schrödinger representation is explicitly time-dependent, unlike the usual



Schrödinger picture where operators are not explicitly time dependent,

$$\hat{\rho}(t) = \sum_i p_i |\psi_i(t)\rangle \langle \psi_i(t)|. \quad (1.45)$$

Mixed states arise in situations where one does not know which particular states are being manipulated, such as a system in thermal equilibrium, or a system with an uncertain preparation history (so one does not know which pure state the system is in). As an example, say there is a 50% probability that the system is in state 1  $|\psi_1\rangle$ , and a 50% probability that the state vector is state 2,  $|\psi_2\rangle$ . Then, the system is in a mixed state with the density matrix

$$\hat{\rho} = \frac{1}{2} |\psi_1\rangle \langle \psi_1| + \frac{1}{2} |\psi_2\rangle \langle \psi_2|. \quad (1.46)$$

As another example, assume that there is a 50% chance that a system is in state  $|\psi_1\rangle$ , and a 50% chance it is in the superposition state  $(|\psi_1\rangle + |\psi_2\rangle)/\sqrt{2}$ . Then,

$$\hat{\rho} = \frac{1}{2} |\psi_1\rangle \langle \psi_1| + \frac{1}{2} \frac{|\psi_1\rangle + |\psi_2\rangle}{\sqrt{2}} \frac{\langle \psi_1| + \langle \psi_2|}{\sqrt{2}} \quad (1.47)$$

$$= \frac{1}{2} |\psi_1\rangle \langle \psi_1| + \frac{1}{4} |\psi_1\rangle \langle \psi_1| + \frac{1}{4} |\psi_1\rangle \langle \psi_2| + \frac{1}{4} |\psi_2\rangle \langle \psi_1| + \frac{1}{4} |\psi_2\rangle \langle \psi_2| \quad (1.48)$$

$$= \frac{3}{4} |\psi_1\rangle \langle \psi_1| + \frac{1}{4} |\psi_1\rangle \langle \psi_2| + \frac{1}{4} |\psi_2\rangle \langle \psi_1| + \frac{1}{4} |\psi_2\rangle \langle \psi_2|. \quad (1.49)$$

This state is partially mixed,

$$\rho = \begin{bmatrix} \frac{3}{4} & \frac{1}{4} \\ \frac{1}{4} & \frac{1}{4} \end{bmatrix}, \quad \text{partially mixed, eigenvalues are } \frac{1}{2} - \frac{1}{4}\sqrt{2}, \frac{1}{4}\sqrt{2} + \frac{1}{2}. \quad (1.50)$$

An important difference between statistical mixtures and coherent superpositions is the presence of off-diagonal terms in the density matrix. For a statistical mixture (mixed state) the off-diagonal terms are zero (each atom in the mixture will either be in a state such that  $\rho_{11} = 1$  and  $\rho_{22} = 0$ , or in a state such that  $\rho_{11} = 0$  and  $\rho_{22} = 1$ , and so  $\rho_{12} = \rho_{21} = 0$ ). In contrast, systems in coherent superpositions are such that both  $\rho_{11}$  and  $\rho_{22}$  are nonzero, *resulting in non-zero off-diagonal elements*. For example, assume that the system is in the superposition state  $(|\psi_1\rangle + |\psi_2\rangle)/\sqrt{2}$ . Then,

$$\hat{\rho} = \frac{|\psi_1\rangle + |\psi_2\rangle}{\sqrt{2}} \frac{\langle \psi_1| + \langle \psi_2|}{\sqrt{2}} \quad (1.51)$$

$$= \frac{1}{2} |\psi_1\rangle \langle \psi_1| + \frac{1}{2} |\psi_1\rangle \langle \psi_2| + \frac{1}{2} |\psi_2\rangle \langle \psi_1| + \frac{1}{2} |\psi_2\rangle \langle \psi_2|, \quad (1.52)$$

such that

$$\rho = \begin{bmatrix} \frac{1}{2} & \frac{1}{2} \\ \frac{1}{2} & \frac{1}{2} \end{bmatrix}, \quad \text{pure state, eigenvalues are } 0, 1. \quad (1.53)$$

So, pure states can have non-zero off-diagonal elements (but need not), and mixed states do not have off-diagonal elements.

Before moving on to the master equation derivation we briefly discuss about the interaction picture.

### 1.4.2 Interaction Picture

The interaction picture (also known as the Dirac picture) is an intermediate representation between the Schrödinger and the Heisenberg pictures. Whereas in the other two pictures either the state vector or the operators carry time dependence, in the interaction picture both carry part of the time dependence of observables. The interaction picture is useful in dealing with the changes to the wave functions and observable due to the interactions.

Consider a Hamiltonian in the Schrödinger picture

$$H_S = H_{0,S} + H_{i,S}, \quad (1.54)$$

where  $H_{0,S}$  is exactly solvable and  $H_{i,S}$  is a time-dependent perturbation. Then, in the interaction picture state vectors are

$$|\psi_I(t)\rangle = e^{+iH_{0,S}t/\hbar} |\psi_S(t)\rangle \quad (1.55)$$

(note the plus sign in the exponential), where  $|\psi_S\rangle$  is the state vector in the Schrödinger picture. Operators in the interaction picture are

$$\hat{A}_I(t) = e^{iH_{0,S}t/\hbar} \hat{A}_S e^{-iH_{0,S}t/\hbar}. \quad (1.56)$$

thus

$$H_{0,I}(t) = e^{iH_{0,S}t/\hbar} H_{0,S} e^{-iH_{0,S}t/\hbar} = H_{0,S} \quad (1.57)$$

and

$$H_{i,I}(t) = e^{iH_{0,S}t/\hbar} H_{i,S} e^{-iH_{0,S}t/\hbar}. \quad (1.58)$$

In the interaction picture, states evolve as

$$\frac{d}{dt} |\psi_I(t)\rangle = \frac{d}{dt} e^{iH_0, st/\hbar} |\psi_S(t)\rangle = \frac{i}{\hbar} H_{0,S} |\psi_I(t)\rangle + e^{iH_0, st/\hbar} \frac{d}{dt} |\psi_S(t)\rangle \quad (1.59)$$

$$= \frac{i}{\hbar} H_{0,S} |\psi_I(t)\rangle + e^{iH_0, st/\hbar} \frac{d}{dt} \left( e^{-iH_S t/\hbar} |\psi_S(0)\rangle \right) \quad (1.60)$$

$$= \frac{i}{\hbar} H_{0,S} |\psi_I(t)\rangle + e^{iH_0, st/\hbar} \left( -\frac{i}{\hbar} H_S \right) |\psi_S(t)\rangle \quad (1.61)$$

$$= \frac{i}{\hbar} H_{0,S} |\psi_I(t)\rangle + \left( -\frac{i}{\hbar} \left( H_{0,S} |\psi_I(t)\rangle + e^{iH_0, st/\hbar} H_{i,S} \right) |\psi_S(t)\rangle \right) \quad (1.62)$$

$$= -\frac{i}{\hbar} \left( e^{iH_0, st/\hbar} H_{i,S} \right) |\psi_S(t)\rangle = -\frac{i}{\hbar} e^{iH_0, st/\hbar} H_{i,S} e^{-iH_0, st/\hbar} |\psi_I(t)\rangle \quad (1.63)$$

$$= -\frac{i}{\hbar} H_{i,I} |\psi_I(t)\rangle. \quad (1.64)$$

This is like in the Schrödinger picture,

$$\frac{d}{dt} |\psi_S(t)\rangle = -\frac{i}{\hbar} H_S |\psi_S(t)\rangle, \quad (1.65)$$

but only the interaction term is involved.

### 1.4.3 Master Equations For Quantum Dots Interacting in a Lossy Inhomogeneous Reciprocal Medium

We suppose that the total Hamiltonian of the system can be written as

$$H = H_0 + V, \quad (1.66)$$

where

$$H_0 = H_F + H_A = \int d^3\mathbf{r} \int_0^\infty d\omega \hbar\omega \hat{f}_\omega^\dagger(\mathbf{r}) \hat{f}_\omega(\mathbf{r}) + \frac{\hbar\omega_0}{2} (\hat{\sigma}_{z1} + \hat{\sigma}_{z2}), \quad (1.67)$$

is the Hamiltonian of the reservoir and quantum dots and

$$V = - \sum_{i=1,2} \left( \hat{\sigma}_i^\dagger \hat{\mathbf{E}}(\mathbf{r}_i) \cdot \mathbf{d}_i + \hat{\sigma}_i \hat{\mathbf{E}}^\dagger(\mathbf{r}_i) \cdot \mathbf{d}_i \right). \quad (1.68)$$

is the interaction Hamiltonian. As was discussed earlier, operators in the interaction picture are related to operators in the Schroedinger picture by 1.56, thus in the interaction picture

$$\begin{aligned}
e^{iH_0t/\hbar} \hat{\sigma}_i^\dagger \hat{\mathbf{E}}(\mathbf{r}_i, \omega) e^{-iH_0t/\hbar} &= e^{iH_A t/\hbar} \hat{\sigma}_i^\dagger e^{-iH_A t/\hbar} e^{iH_F t/\hbar} \hat{\mathbf{E}}(\mathbf{r}_i, \omega) e^{-iH_F t/\hbar} \\
e^{iH_A t/\hbar} \hat{\sigma}_i^\dagger e^{-iH_A t/\hbar} &= e^{i\omega_0 t} \hat{\sigma}_i^\dagger \\
e^{iH_A t/\hbar} \hat{\sigma}_i e^{-iH_A t/\hbar} &= e^{-i\omega_0 t} \hat{\sigma}_i, \\
e^{\alpha \hat{f}^\dagger \hat{f}} \hat{f} e^{-\alpha \hat{f}^\dagger \hat{f}} &= e^{-\alpha} \hat{f} \\
e^{\alpha \hat{f}^\dagger \hat{f}} \hat{f}^\dagger e^{-\alpha \hat{f}^\dagger \hat{f}} &= e^{\alpha} \hat{f}^\dagger \\
e^{i\hat{H}_F t/\hbar} \hat{\mathbf{E}}(\mathbf{r}_i, \omega) e^{-i\hat{H}_F t/\hbar} &= e^{-i\omega t} \hat{\mathbf{E}}(\mathbf{r}_i, \omega), \quad e^{iH_F t/\hbar} \hat{\mathbf{E}}^\dagger(\mathbf{r}_i, \omega) e^{-iH_F t/\hbar} = e^{i\omega t} \hat{\mathbf{E}}^\dagger(\mathbf{r}_i, \omega). \quad (1.69)
\end{aligned}$$

and thus

$$\begin{aligned}
e^{iH_0t/\hbar} \hat{\sigma}_i^\dagger \hat{\mathbf{E}}(\mathbf{r}_i, \omega) e^{-iH_0t/\hbar} &= e^{i(\omega_0 - \omega)t} \hat{\sigma}_i^\dagger \hat{\mathbf{E}}(\mathbf{r}_i, \omega), \\
e^{i\hat{H}_0 t/\hbar} \hat{\sigma}_i \hat{\mathbf{E}}^\dagger(\mathbf{r}_i, \omega) e^{-i\hat{H}_0 t/\hbar} &= e^{-i(\omega_0 - \omega)t} \hat{\sigma}_i \hat{\mathbf{E}}^\dagger(\mathbf{r}_i, \omega),
\end{aligned}$$

and also

$$\tilde{V} = - \int_0^\infty d\omega \sum_{i=1,2} \left( e^{i(\omega_0 - \omega)t} \hat{\sigma}_i^\dagger \hat{\mathbf{E}}(\mathbf{r}_i, \omega) \cdot \mathbf{d}_i + e^{-i(\omega_0 - \omega)t} \hat{\sigma}_i \hat{\mathbf{E}}^\dagger(\mathbf{r}_i, \omega) \cdot \mathbf{d}_i \right). \quad (1.70)$$

Starting from the equation of motion for the density

$$\frac{\partial \hat{\rho}}{\partial t} = -\frac{i}{\hbar} [\mathbf{H}, \hat{\rho}] = -\frac{i}{\hbar} [\mathbf{H}_0 + \mathbf{V}, \hat{\rho}] \quad (1.71)$$

where H is the total Hamiltonian of the system and V is the interaction Hamiltonian. We will work in interaction picture so the equation for density matrix reduces to

$$\frac{\partial \tilde{\rho}(t)}{\partial t} = -\frac{i}{\hbar} [\tilde{V}(t), \tilde{\rho}(t)]. \quad (1.72)$$

We can write the formal solution of the above equation as

$$\tilde{\rho}(t) = \tilde{\rho}(0) - \frac{i}{\hbar} \int_0^t dt' [\tilde{V}(t'), \tilde{\rho}(t')]. \quad (1.73)$$

substituting (1.73) back into (1.72), we obtain

$$\frac{\partial \tilde{\rho}(t)}{\partial t} = -\frac{i}{\hbar} [\tilde{V}(t), \tilde{\rho}(0)] - \frac{1}{\hbar^2} \int_0^t dt' [\tilde{V}(t), [\tilde{V}(t'), \tilde{\rho}(t')]], \quad (1.74)$$

and tracing out the reservoir degrees of freedom,

$$\frac{\partial \tilde{\rho}_S(t)}{\partial t} = -\frac{i}{\hbar} \text{Tr}_R \left[ \tilde{V}(t), \tilde{\rho}(0) \right] - \frac{1}{\hbar^2} \int_0^t dt' \text{Tr}_R \left[ \tilde{V}(t), \left[ \tilde{V}(t'), \tilde{\rho}(t') \right] \right]. \quad (1.75)$$

We now assume that due to the weakness of interaction between reservoir and the system density matrix can be separated, i.e.  $\tilde{\rho}(t) = \tilde{\rho}_S(t) \otimes \tilde{\rho}_R(0)$  (Born approximation). We assume also that, even though system may cause excitations in the reservoir, all such excitations decay very fast. We also assume that the reservoir density matrix is diagonal. Then,

$$\text{Tr}_R \left[ \tilde{V}(t), \tilde{\rho}(0) \right] \sim \sum_R \langle \mathbf{R} | \left[ \tilde{V}(t), \tilde{\rho}(0) \right] | \mathbf{R} \rangle \sim \sum_R \langle \mathbf{R} | \left[ b_R, f(b_R^\dagger b_R) \right] | \mathbf{R} \rangle \sim \sum_R \langle \mathbf{R} | b_R | \mathbf{R} \rangle = 0,$$

and thus

$$\frac{\partial \tilde{\rho}_S(t)}{\partial t} = -\frac{1}{\hbar^2} \int_0^t dt' \text{Tr}_R \left[ \tilde{V}(t), \left[ \tilde{V}(t'), \tilde{\rho}_s(t') \otimes \tilde{\rho}_R(0) \right] \right]. \quad (1.76)$$

Finally, we use the Markov approximation

$$\frac{\partial \tilde{\rho}_S(t)}{\partial t} = -\frac{1}{\hbar^2} \int_0^\infty dt' \text{Tr}_R \left[ \tilde{V}(t), \left[ \tilde{V}(t-t'), \tilde{\rho}_s(t) \otimes \tilde{\rho}_R(0) \right] \right]. \quad (1.77)$$

Let us consider the commutator in the master equations in more details,

$$\begin{aligned} \text{Tr}_R \left[ \tilde{V}(t), \left[ \tilde{V}(t-t'), \tilde{\rho}_s(t) \otimes \tilde{\rho}_R(0) \right] \right] &= \text{Tr}_R \left[ \tilde{V}(t), \tilde{V}(t-t') \tilde{\rho}_s(t) \otimes \tilde{\rho}_R(0) - \tilde{\rho}_s(t) \otimes \tilde{\rho}_R(0) \tilde{V}(t-t') \right] \\ &= \text{Tr}_R \left( \tilde{V}(t) \tilde{V}(t-t') \tilde{\rho}_s(t) \tilde{\rho}_R - \tilde{V}(t-t') \tilde{\rho}_s(t) \tilde{\rho}_R \tilde{V}(t) + \text{H.c.} \right). \end{aligned} \quad (1.78)$$

The first term in 1.78 is

$$\begin{aligned} \text{Tr}_R \left( \tilde{V}(t) \tilde{V}(t-t') \tilde{\rho}_s(t) \tilde{\rho}_R \right) &= \iint_0^\infty d\omega d\omega' \sum_{i,j=1,2} \text{Tr}_R \left( e^{i(\omega_0-\omega)t} \hat{\sigma}_i^\dagger \hat{\mathbf{E}}(\mathbf{r}_i, \omega) \cdot \mathbf{d}_i + e^{-i(\omega_0-\omega)t} \hat{\sigma}_i \hat{\mathbf{E}}^\dagger(\mathbf{r}_i, \omega) \cdot \mathbf{d}_i \right) \\ &\times \left( e^{i(\omega_0-\omega')(t-t')} \hat{\sigma}_j^\dagger \hat{\mathbf{E}}(\mathbf{r}_j, \omega') \cdot \mathbf{d}_j + e^{-i(\omega_0-\omega')(t-t')} \hat{\sigma}_j \hat{\mathbf{E}}^\dagger(\mathbf{r}_j, \omega') \cdot \mathbf{d}_j \right) \tilde{\rho}_s(t) \tilde{\rho}_R. \end{aligned} \quad (1.79)$$

and once again we need to take into account that density matrix of reservoir is diagonal. In this case,

$$\begin{aligned} \text{Tr}_R \left( \hat{\mathbf{E}}(\mathbf{r}_i, \omega) \hat{\mathbf{E}}(\mathbf{r}_j, \omega') \tilde{\rho}_R \right) &\sim \sum_R \langle \mathbf{R} | \hat{f}^2 | \mathbf{R} \rangle = 0, \\ \text{Tr}_R \left( \hat{\mathbf{E}}^\dagger(\mathbf{r}_i, \omega) \hat{\mathbf{E}}(\mathbf{r}_j, \omega') \tilde{\rho}_R \right) &\sim \sum_R \langle \mathbf{R} | \hat{f}^\dagger \hat{f} | \mathbf{R} \rangle = \overline{n(\omega)} \approx 0, \\ \text{Tr}_R \left( \hat{\mathbf{E}}(\mathbf{r}_i, \omega) \hat{\mathbf{E}}^\dagger(\mathbf{r}_j, \omega') \tilde{\rho}_R \right) &\sim \sum_R \langle \mathbf{R} | \hat{f} \hat{f}^\dagger | \mathbf{R} \rangle \sim \sum_R \langle \mathbf{R} | 1 + \hat{f}^\dagger \hat{f} | \mathbf{R} \rangle \delta(\omega - \omega'). \end{aligned} \quad (1.80)$$

Here we took into account that the average number of thermal photons  $\overline{n(\omega)}$  is negligible. Thus

only the last term is nonzero,

$$\mathrm{Tr}_R \left( \tilde{V}(t) \tilde{V}(t-t') \tilde{\rho}_s(t) \tilde{\rho}_R \right) = \sum_{i,j=1,2} d_{\alpha i} d_{\beta j} \int_0^\infty d\omega e^{i(\omega_0 - \omega)t'} \hat{\sigma}_i^\dagger \hat{\sigma}_j \tilde{\rho}_s(t) \mathrm{Tr}_R \left( \hat{E}_\alpha(\mathbf{r}_i, \omega) \hat{E}_\beta^\dagger(\mathbf{r}_j, \omega) \tilde{\rho}_R \right), \quad (1.81)$$

and so,

$$\begin{aligned} \mathrm{Tr}_R \left( \hat{E}_\alpha(\mathbf{r}_i, \omega) \hat{E}_\beta^\dagger(\mathbf{r}_j, \omega) \tilde{\rho}_R \right) &= \\ \frac{\hbar}{\pi \varepsilon_0} \frac{\omega^4}{c^4} \iint d^3 \mathbf{r} d^3 \mathbf{r}' \sqrt{\varepsilon''(\mathbf{r}, \omega)} \sqrt{\varepsilon''(\mathbf{r}', \omega)} G_{\alpha \delta}(\mathbf{r}_i, \mathbf{r}, \omega) G_{\beta \gamma}^*(\mathbf{r}_j, \mathbf{r}', \omega) \mathrm{Tr}_R \left( \hat{f}_\delta(\mathbf{r}, \omega) \hat{f}_\gamma^\dagger(\mathbf{r}', \omega) \tilde{\rho}_R \right) &= \\ \frac{\hbar}{\pi \varepsilon_0} \frac{\omega^4}{c^4} \int d^3 \mathbf{r} \varepsilon''(\mathbf{r}, \omega) G_{\alpha \gamma}(\mathbf{r}_i, \mathbf{r}, \omega) G_{\beta \gamma}^*(\mathbf{r}_j, \mathbf{r}, \omega) &= \frac{\hbar}{\pi \varepsilon_0} \frac{\omega^2}{c^2} \mathrm{Im} G_{\alpha \beta}(\mathbf{r}_i, \mathbf{r}_j, \omega) \end{aligned} \quad (1.82)$$

and therefore,

$$\mathrm{Tr}_R \left( \tilde{V}(t) \tilde{V}(t-t') \tilde{\rho}_s(t) \tilde{\rho}_R \right) = \sum_{i,j=1,2} \hat{\sigma}_i^\dagger \hat{\sigma}_j \tilde{\rho}_s(t) \int_0^\infty d\omega e^{i(\omega_0 - \omega)t'} \tilde{\Gamma}_{ij}(\omega), \quad (1.83)$$

$$\tilde{\Gamma}_{ij}(\omega) = \frac{\hbar \omega^2}{\pi \varepsilon_0 c^2} \sum_{\alpha, \beta=x,y,z} d_{\alpha i} \mathrm{Im}(G_{\alpha \beta})(\mathbf{r}_i, \mathbf{r}_j, \omega) d_{\beta j} \quad (1.84)$$

thus

$$\begin{aligned} -\frac{1}{\hbar^2} \int_0^\infty dt' \mathrm{Tr}_R \left( \tilde{V}(t) \tilde{V}(t-t') \tilde{\rho}_s(t) \tilde{\rho}_R \right) &= -\frac{1}{\hbar^2} \sum_{i,j=1,2} \hat{\sigma}_i^\dagger \hat{\sigma}_j \tilde{\rho}_s(t) \int_0^\infty d\omega \tilde{\Gamma}_{ij}(\omega) \int_0^\infty dt' e^{i(\omega_0 - \omega)t'} \\ &= -\sum_{i,j=1,2} \frac{\Gamma_{ij}(\omega_0)}{2} \hat{\sigma}_i^\dagger \hat{\sigma}_j \tilde{\rho}_s(t) + i \sum_{i,j=1,2} g_{ij}(\omega_0) \hat{\sigma}_i^\dagger \hat{\sigma}_j \tilde{\rho}_s(t), \end{aligned} \quad (1.85)$$

$$\begin{aligned} g_{ij}(\omega_0) &= \frac{1}{\pi \hbar \varepsilon_0 c^2} \mathcal{P} \int_0^\infty d\omega \frac{\omega^2}{\omega - \omega_0} \sum_{\alpha, \beta=x,y,z} d_{\alpha i} \mathrm{Im}(G_{\alpha \beta})(\mathbf{r}_i, \mathbf{r}_j, \omega) d_{\beta j} \\ &= \frac{\omega_0^2}{\varepsilon_0 \hbar c^2} \sum_{\alpha, \beta=x,y,z} d_{\alpha i} \mathrm{Re}(G_{\alpha \beta})(\mathbf{r}_i, \mathbf{r}_j, \omega_0) d_{\beta j} \end{aligned} \quad (1.86)$$

Finally, we neglect the Lamb shift,  $g_{ii}(\omega_0)$ , i.e.

$$\begin{aligned} -\frac{1}{\hbar^2} \int_0^\infty dt' \mathrm{Tr}_R \left( \tilde{V}(t) \tilde{V}(t-t') \tilde{\rho}_s(t) \tilde{\rho}_R \right) &= -\sum_{i,j=1,2} \frac{\Gamma_{ij}(\omega_0)}{2} \hat{\sigma}_i^\dagger \hat{\sigma}_j \tilde{\rho}_s(t) \\ &\quad + i \left( g_{12}(\omega_0) \hat{\sigma}_1^\dagger \hat{\sigma}_2 + g_{21}(\omega_0) \hat{\sigma}_2^\dagger \hat{\sigma}_1 \right) \tilde{\rho}_s(t) \end{aligned} \quad (1.87)$$

Next, we present a detailed calculation of the second term in 1.78,

$$\begin{aligned}
& \text{Tr}_R \tilde{V}(t-t') \tilde{\rho}_s(t) \tilde{\rho}_R \tilde{V}(t) = \\
& \iint_0^\infty d\omega d\omega' \sum_{i,j=1,2} \text{Tr}_R \left( e^{i(\omega_0-\omega')(t-t')} \hat{\sigma}_j^\dagger \hat{\mathbf{E}}(\mathbf{r}_j, \omega') \cdot \mathbf{d}_j + e^{-i(\omega_0-\omega')(t-t')} \hat{\sigma}_j \hat{\mathbf{E}}^\dagger(\mathbf{r}_j, \omega') \cdot \mathbf{d}_j \right) \tilde{\rho}_s(t) \tilde{\rho}_R \\
& \times \left( e^{i(\omega_0-\omega)t} \hat{\sigma}_i^\dagger \hat{\mathbf{E}}(\mathbf{r}_i, \omega) \cdot \mathbf{d}_i + e^{-i(\omega_0-\omega)t} \hat{\sigma}_i \hat{\mathbf{E}}^\dagger(\mathbf{r}_i, \omega) \cdot \mathbf{d}_i \right). \tag{1.88}
\end{aligned}$$

In contrast to the above case, the only non-zero term is

$$\text{Tr}_R \left( \hat{\mathbf{E}}^\dagger(\mathbf{r}_j, \omega') \tilde{\rho}_R \hat{\mathbf{E}}(\mathbf{r}_i, \omega) \right) \sim \text{Tr}_R \left( \hat{\mathbf{E}}(\mathbf{r}_i, \omega) \hat{\mathbf{E}}^\dagger(\mathbf{r}_j, \omega') \tilde{\rho}_R \right), \tag{1.89}$$

thus

$$\begin{aligned}
& -\frac{1}{\hbar^2} \int_0^\infty dt' \text{Tr}_R \left( \tilde{V}(t-t') \tilde{\rho}_s(t) \tilde{\rho}_R \tilde{V}(t) \right) = \\
& -\frac{1}{\hbar^2} \int_0^\infty dt' \sum_{i,j=1,2} d_{\alpha j} d_{\beta i} \int_0^\infty d\omega e^{i(\omega_0-\omega)t'} \hat{\sigma}_j \tilde{\rho}_s(t) \hat{\sigma}_i^\dagger \text{Tr}_R \left( \hat{E}_\beta(\mathbf{r}_i, \omega) \hat{E}_\alpha^\dagger(\mathbf{r}_j, \omega) \tilde{\rho}_R \right) = \\
& -\frac{1}{\hbar^2} \sum_{i,j=1,2} \hat{\sigma}_i \tilde{\rho}_s(t) \hat{\sigma}_j^\dagger \int_0^\infty d\omega \tilde{\Gamma}_{ij}(\omega) \left( \pi \delta(\omega - \omega_0) - i\mathcal{P} \left( \frac{1}{\omega - \omega_0} \right) \right) = \\
& -\sum_{i,j=1,2} \frac{\Gamma_{ij}(\omega_0)}{2} \hat{\sigma}_i \tilde{\rho}_s(t) \hat{\sigma}_j^\dagger + i \sum_{i,j=1,2} g_{ij}(\omega_0) \hat{\sigma}_i \tilde{\rho}_s(t) \hat{\sigma}_j^\dagger. \tag{1.90}
\end{aligned}$$

Using the first and second term in 1.78, for a reciprocal medium,  $\Gamma_{ij}(\omega_0) = \Gamma_{ji}(\omega_0)$ , and  $g_{ij}(\omega_0) = g_{ji}(\omega_0)$  and the Lindblad operator in the Master equation takes the form

$$\frac{\partial \tilde{\rho}_S(t)}{\partial t} = \sum_{i,j=1,2} \frac{\Gamma_{ij}(\omega_0)}{2} \left( 2\hat{\sigma}_i \tilde{\rho}_s(t) \hat{\sigma}_j^\dagger - \hat{\sigma}_i^\dagger \hat{\sigma}_j \tilde{\rho}_s(t) - \tilde{\rho}_s(t) \hat{\sigma}_i^\dagger \hat{\sigma}_j \right) + i \left[ g_{12}(\omega_0) \hat{\sigma}_1^\dagger \hat{\sigma}_2 + g_{21}(\omega_0) \hat{\sigma}_2^\dagger \hat{\sigma}_1, \tilde{\rho}_s(t) \right]. \tag{1.91}$$

#### 1.4.4 Master Equation in the Symmetric Basis

Having formed the operator-level ME, we need to project it onto a basis in order to solve it using scalar (non-operator) mathematics. Let us define the basis

$$|3\rangle = |e_1\rangle \otimes |e_2\rangle = |e_1, e_2\rangle, \quad |0\rangle = |g_1\rangle \otimes |g_2\rangle = |g_1, g_2\rangle, \quad |\pm\rangle = \frac{1}{\sqrt{2}} (|e_1, g_2\rangle \pm |g_1, e_2\rangle). \tag{1.92}$$

The following tables show how qubit operators act on basis vectors.

	$ 3\rangle$	$ 0\rangle$	$ +\rangle$	$ -\rangle$		$\langle 3 $	$\langle 0 $	$\langle + $	$\langle - $
$\hat{\sigma}_1$	$ g_1, e_2\rangle$	0	$ 0\rangle/\sqrt{2}$	$ 0\rangle/\sqrt{2}$	$\hat{\sigma}_1$	0	$\langle e_1, g_2 $	$\langle 3 /\sqrt{2}$	$-\langle 3 /\sqrt{2}$
$\hat{\sigma}_1^\dagger$	0	$ e_1, g_2\rangle$	$ 3\rangle/\sqrt{2}$	$- 3\rangle/\sqrt{2}$	$\hat{\sigma}_1^\dagger$	$\langle g_1, e_2 $	0	$\langle 0 /\sqrt{2}$	$\langle 0 /\sqrt{2}$
$\hat{\sigma}_2$	$ e_1, g_2\rangle$	0	$ 0\rangle/\sqrt{2}$	$- 0\rangle/\sqrt{2}$	$\hat{\sigma}_2$	0	$\langle g_1, e_2 $	$\langle 3 /\sqrt{2}$	$\langle 3 /\sqrt{2}$
$\hat{\sigma}_2^\dagger$	0	$ g_1, e_2\rangle$	$ 3\rangle/\sqrt{2}$	$ 3\rangle/\sqrt{2}$	$\hat{\sigma}_2^\dagger$	$\langle e_1, g_2 $	0	$\langle 0 /\sqrt{2}$	$-\langle 0 /\sqrt{2}$

	$ 3\rangle$	$ 0\rangle$	$ +\rangle$	$ -\rangle$		$\langle 3 $	$\langle 0 $	$\langle + $	$\langle - $
$\hat{\sigma}_1^\dagger \hat{\sigma}_1$	$ 3\rangle$	0	$ e_1, g_2\rangle/\sqrt{2}$	$ e_1, g_2\rangle/\sqrt{2}$	$\hat{\sigma}_1^\dagger \hat{\sigma}_1$	$\langle 3 $	0	$\langle e_1, g_2 /\sqrt{2}$	$\langle e_1, g_2 /\sqrt{2}$
$\hat{\sigma}_1^\dagger \hat{\sigma}_2$	0	0	$ e_1, g_2\rangle/\sqrt{2}$	$- e_1, g_2\rangle/\sqrt{2}$	$\hat{\sigma}_1^\dagger \hat{\sigma}_2$	0	0	$\langle g_1, e_2 /\sqrt{2}$	$\langle g_1, e_2 /\sqrt{2}$
$\hat{\sigma}_2^\dagger \hat{\sigma}_1$	0	0	$ g_1, e_2\rangle/\sqrt{2}$	$ g_1, e_2\rangle/\sqrt{2}$	$\hat{\sigma}_2^\dagger \hat{\sigma}_1$	0	0	$\langle e_1, g_2 /\sqrt{2}$	$-\langle e_1, g_2 /\sqrt{2}$
$\hat{\sigma}_2^\dagger \hat{\sigma}_2$	$ 3\rangle$	0	$ g_1, e_2\rangle/\sqrt{2}$	$- g_1, e_2\rangle/\sqrt{2}$	$\hat{\sigma}_2^\dagger \hat{\sigma}_2$	$\langle 3 $	0	$\langle g_1, e_2 /\sqrt{2}$	$-\langle g_1, e_2 /\sqrt{2}$

Table 1.1: Qubits Pauli operators and their acts on the atomic states.

If we take into account that  $\Gamma_{12}(\omega_0) = \Gamma_{21}(\omega_0)$ , and  $g_{12}(\omega_0) = g_{21}(\omega_0)$ , we obtain

$$\begin{aligned}
\frac{\partial \tilde{\rho}_S(t)}{\partial t} &= \frac{\Gamma_{11}(\omega_0)}{2} \left( 2\hat{\sigma}_1 \tilde{\rho}_s(t) \hat{\sigma}_1^\dagger - \hat{\sigma}_1^\dagger \hat{\sigma}_1 \tilde{\rho}_s(t) - \tilde{\rho}_s(t) \hat{\sigma}_1^\dagger \hat{\sigma}_1 \right) + \frac{\Gamma_{22}(\omega_0)}{2} \left( 2\hat{\sigma}_2 \tilde{\rho}_s(t) \hat{\sigma}_2^\dagger - \hat{\sigma}_2^\dagger \hat{\sigma}_2 \tilde{\rho}_s(t) - \tilde{\rho}_s(t) \hat{\sigma}_2^\dagger \hat{\sigma}_2 \right) \\
&+ \frac{\Gamma_{12}(\omega_0)}{2} \left( 2\hat{\sigma}_1 \tilde{\rho}_s(t) \hat{\sigma}_2^\dagger - \hat{\sigma}_1^\dagger \hat{\sigma}_2 \tilde{\rho}_s(t) - \tilde{\rho}_s(t) \hat{\sigma}_1^\dagger \hat{\sigma}_2 + 2\hat{\sigma}_2 \tilde{\rho}_s(t) \hat{\sigma}_1^\dagger - \hat{\sigma}_2^\dagger \hat{\sigma}_1 \tilde{\rho}_s(t) - \tilde{\rho}_s(t) \hat{\sigma}_2^\dagger \hat{\sigma}_1 \right) \\
&+ ig_{12}(\omega_0) \left( \hat{\sigma}_1^\dagger \hat{\sigma}_2 \tilde{\rho}_s(t) + \hat{\sigma}_2^\dagger \hat{\sigma}_1 \tilde{\rho}_s(t) - \tilde{\rho}_s(t) \hat{\sigma}_1^\dagger \hat{\sigma}_2 - \tilde{\rho}_s(t) \hat{\sigma}_2^\dagger \hat{\sigma}_1 \right). \tag{1.93}
\end{aligned}$$

A further simplification is possible if we assume that the emitters are identical and that LDOS at the positions of emitters is the same, i.e.  $\Gamma_{11} = \Gamma_{22}$ ,

$$\frac{\partial \tilde{\rho}_{33}(t)}{\partial t} = -2\Gamma_{11} \tilde{\rho}_{33}(t), \tag{1.94}$$

$$\frac{\partial \tilde{\rho}_{++}(t)}{\partial t} = (\Gamma_{11} + \Gamma_{12}) \tilde{\rho}_{33}(t) - (\Gamma_{11} + \Gamma_{12}) \tilde{\rho}_{++}(t), \tag{1.95}$$

$$\frac{\partial \tilde{\rho}_{--}(t)}{\partial t} = (\Gamma_{11} - \Gamma_{12}) \tilde{\rho}_{33}(t) - (\Gamma_{11} - \Gamma_{12}) \tilde{\rho}_{--}(t), \tag{1.96}$$

$$\frac{\partial \tilde{\rho}_{00}(t)}{\partial t} = (\Gamma_{11} + \Gamma_{12}) \tilde{\rho}_{++}(t) + (\Gamma_{11} - \Gamma_{12}) \tilde{\rho}_{--}(t), \tag{1.97}$$

$$\frac{\partial \tilde{\rho}_{+-}(t)}{\partial t} = -(\Gamma_{11} - 2ig_{12}) \tilde{\rho}_{+-}(t), \tag{1.98}$$

$$\frac{\partial \tilde{\rho}_{30}(t)}{\partial t} = -\Gamma_{11} \tilde{\rho}_{30}(t), \tag{1.99}$$

$$\frac{\partial \tilde{\rho}_{-+}(t)}{\partial t} = -(\Gamma_{11} + 2ig_{12}) \tilde{\rho}_{-+}(t). \tag{1.100}$$

### 1.4.5 Single Excited Emitter

Let us assume that only one emitter is in the excited state:  $|\Psi\rangle = |e_1, g_2\rangle$ . The density matrix of system is

$$\rho_0 = |\Psi\rangle \langle \Psi| = |e_1, g_2\rangle \langle e_1, g_2|. \tag{1.101}$$

we switch to the basis defined in 1.92. It yields

$$|e_1, g_2\rangle = \sum_{i=0,3,\pm} C_i |i\rangle. \tag{1.102}$$



expansion coefficients are  $C_{0,3} = 0$ , and  $C_{\pm} = 1/\sqrt{2}$ . Thus in a symmetric basis,

$$\Psi_S = \frac{1}{\sqrt{2}} (|+\rangle + |-\rangle), \quad (1.103)$$

and the only non-zero components of the density matrix are  $\rho_{++}(0) = \rho_{+-}(0) = \rho_{-+}(0) = \rho_{--}(0) = 1/2$ . Then the system of equations are

$$\rho_{33}(t) = 0, \quad \rho_{00}(t) = 0, \quad (1.104)$$

$$\frac{\partial \rho_{++}(t)}{\partial t} = -(\Gamma_{11} + \Gamma_{12}) \rho_{++}(t), \quad \Rightarrow \quad \rho_{++}(t) = \frac{1}{2} e^{-(\Gamma_{11} + \Gamma_{12})t}, \quad (1.105)$$

$$\frac{\partial \rho_{--}(t)}{\partial t} = -(\Gamma_{11} - \Gamma_{12}) \rho_{--}(t), \quad \Rightarrow \quad \rho_{--}(t) = \frac{1}{2} e^{-(\Gamma_{11} - \Gamma_{12})t}, \quad (1.106)$$

$$\frac{\partial \rho_{+-}(t)}{\partial t} = -(\Gamma_{11} - 2ig_{12}) \rho_{+-}(t), \quad \Rightarrow \quad \rho_{+-}(t) = \frac{1}{2} e^{-(\Gamma_{11} - 2ig_{12})t}, \quad (1.107)$$

$$\frac{\partial \rho_{-+}(t)}{\partial t} = -(\Gamma_{11} + 2ig_{12}) \rho_{-+}(t), \quad \Rightarrow \quad \rho_{-+}(t) = \frac{1}{2} e^{-(\Gamma_{11} + 2ig_{12})t}. \quad (1.108)$$

In order to characterize entanglement between two emitters we use the concept of concurrence [32, 33], which is defined as

$$C = \max(0, \sqrt{u_1} - \sqrt{u_2} - \sqrt{u_3} - \sqrt{u_4}), \quad (1.109)$$

where  $u_i$  are arranged in descending order of the eigenvalues of the matrix  $\rho_s \tilde{\rho}_s$ , where  $\tilde{\rho}_s = \sigma_y \otimes \sigma_y \rho_s^* \sigma_y \otimes \sigma_y$  is the spin-flip density matrix with  $\sigma_y$  being the Pauli matrix. Concurrence may vary in the range between 0 (unentangled state) and 1 (completely entangled), such that values between 0 and 1 correspond to different degrees of entanglement. If only non-zero elements of the density matrix are considered then

$$\begin{aligned} C(t) &= \sqrt{[\rho_{++}(t) - \rho_{--}(t)]^2 + 4\text{Im}[\rho_{+-}(t)]^2} \\ &= \frac{1}{2} \sqrt{[e^{-(\Gamma_{11} + \Gamma_{12})t} - e^{-(\Gamma_{11} - \Gamma_{12})t}]^2 + 4e^{-2\Gamma_{11}t} \sin^2(2g_{12}t)}. \end{aligned} \quad (1.110)$$

#### 1.4.6 Single Excited Emitter With Pure Dephasing

Another decay channel for quantum systems is some internal interactions (electron-phonon interaction in QDs), which can be accounted by a pure dephasing term. Pure dephasing through phonon interactions forms the dominant non-radiative loss mechanism. This effect can be taken into account in the Master equation via the standard Lindbladian superoperator  $\mathcal{L}\hat{O} = \hat{O}\tilde{\rho}_s(t)\hat{O}^\dagger - 1/2[\hat{O}^\dagger\hat{O}, \tilde{\rho}_s(t)]$  as follows [30]

$$\mathcal{L}(\sigma_\alpha^\dagger \sigma_\alpha) = \mathcal{L}(|e_\alpha\rangle \langle e_\alpha|) = \frac{\gamma_\alpha}{2} [2|e_\alpha\rangle \langle e_\alpha| \rho |e_\alpha\rangle \langle e_\alpha| - |e_\alpha\rangle \langle e_\alpha| \rho - \rho |e_\alpha\rangle \langle e_\alpha|], \quad (1.111)$$

where  $\gamma_1 = \gamma_2 = \gamma$  as the pure dephasing rate of the  $\alpha$ th QD. Considering this extra term in the master equation, the differential equations governing the density operator elements become

$$\frac{\partial \rho_{++}}{\partial t} = - \left( \Gamma_{11} + \Gamma_{12} + \frac{\gamma}{2} \right) \rho_{++} + \frac{\gamma}{2} \rho_{--} \quad (1.112)$$

$$\frac{\partial \rho_{--}}{\partial t} = - \left( \Gamma_{11} - \Gamma_{12} + \frac{\gamma}{2} \right) \rho_{--} + \frac{\gamma}{2} \rho_{++} \quad (1.113)$$

$$\frac{\partial \rho_{+-}}{\partial t} = - \left( \Gamma_{11} + \frac{\gamma}{2} - 2ig_{12} \right) \rho_{+-} + \frac{\gamma}{2} \rho_{-+} \quad (1.114)$$

$$\frac{\partial \rho_{-+}}{\partial t} = - \left( \Gamma_{11} + \frac{\gamma}{2} + 2ig_{12} \right) \rho_{-+} + \frac{\gamma}{2} \rho_{+-}. \quad (1.115)$$

The solution of these equation takes the form

$$\rho_{++} = \frac{e^{-(\Gamma_{11}+\gamma/2)t}}{2} \left[ \cosh \left( \sqrt{\Gamma'_{12}}t \right) - \frac{\Gamma_{12} - \gamma/2}{\Gamma'_{12}} \sinh \left( \sqrt{\Gamma'_{12}}t \right) \right] \quad (1.116)$$

$$\rho_{--} = \frac{e^{-(\Gamma_{11}+\gamma/2)t}}{2} \left[ \cosh \left( \sqrt{\Gamma'_{12}}t \right) + \frac{\Gamma_{12} + \gamma/2}{\Gamma'_{12}} \sinh \left( \sqrt{\Gamma'_{12}}t \right) \right] \quad (1.117)$$

$$\rho_{+-} = \frac{e^{-(\Gamma_{11}+\gamma/2)t}}{2} \left[ \cos \left( 2\sqrt{g'_{12}}t \right) + \frac{ig_{12} + \gamma/4}{g'_{12}} \sin \left( 2\sqrt{g'_{12}}t \right) \right] \quad (1.118)$$

where  $\Gamma'_{12} = \sqrt{\Gamma_{12}^2 + \gamma^2/4}$ ,  $g'_{12} = \sqrt{g_{12}^2 - \gamma^2/16}$ . Thus,

$$\rho_{++} - \rho_{--} = -\frac{\Gamma_{12}}{2\Gamma'_{12}} e^{-(\Gamma_{11}+\gamma/2)t} \left( e^{\sqrt{\Gamma'_{12}}t} - e^{-\sqrt{\Gamma'_{12}}t} \right), \quad (1.119)$$

$$\text{Im} [\rho_{+-}] = \frac{g_{12}}{2g'_{12}} e^{-(\Gamma_{11}+\gamma/2)t} \sin \left( 2\sqrt{g'_{12}}t \right), \quad (1.120)$$

and therefore the concurrence in presence of dephasing is

$$C(t) = \frac{e^{-(\Gamma_{11}+\gamma/2)t}}{2} \sqrt{(\Gamma_{12}/\Gamma'_{12})^2 \left( e^{\sqrt{\Gamma'_{12}}t} - e^{-\sqrt{\Gamma'_{12}}t} \right)^2 + 4(g_{12}/g'_{12})^2 \sin^2 \left( 2\sqrt{g'_{12}}t \right)}. \quad (1.121)$$

It can be easily shown that in the limit of  $\gamma \rightarrow 0$ , 1.121 reduces to 1.110.

#### 1.4.7 Steady-State Concurrence Between Two Quantum Dots

As one can see from 1.110 or 1.121, the concurrence between two emitters interacting through a lossy inhomogeneous environment decays with time. In order to obtain a steady entangled state we need to compensate for the depopulation of the emitters excited states (via coupling to the environment) by pumping with an external laser field. Here we restrict our consideration to the case when the external pumps are modeled by classical monochromatic waves of frequency  $\omega_L$ ,  $\mathbf{E}_\alpha = \mathbf{E}_{0\alpha} e^{-i\omega_L t} + \text{c.c.}$ , and assume that each of the emitters can be pumped individually (i.e., using focused beams). In this case, the master equation takes the form

$$\partial_t \rho_s(t) = -(i/\hbar) [\mathbf{V}_p, \rho_s(t)] + \mathcal{L} \rho_s(t), \quad (1.122)$$

where

$$V_p = -\hbar \sum_{\alpha=a,b} (\Omega_\alpha e^{-i\Delta_\alpha t} \sigma_\alpha^\dagger + \Omega_\alpha^* e^{i\Delta_\alpha t} \sigma_\alpha), \quad (1.123)$$

accounts for the interaction between the classical pump field and qubits,  $\Omega_\alpha = \mathbf{d} \cdot \mathbf{E}_{0\alpha}/\hbar$  is the effective Rabi frequency of the pump, and  $\Delta_\alpha = \omega_\alpha - \omega_L$  is a detuning parameter. Here we assume that  $\mathbf{E}_{0\alpha}$  is the full field at the dipole position, i.e. it is the sum of the external pump field and field scattered by the medium. In the basis defined in 1.92 we obtain a system of 16 coupled differential equations for the density matrix, which we solve numerically.

## Chapter 2

# 3D Plasmonic Systems Mediated Entanglement

### 2.1 Introduction

Generating, preserving and controlling entanglement between quantum systems is of great importance for quantum communications, teleportation, metrology, cryptology, computing and other operations involving quantum bits (qubits) [32]. A fundamental problem facing practical applications of entanglement is environment-induced dissipation of the quantum system. The traditional view [34] holds that dissipation is necessarily detrimental as it leads to decoherence, and thus to entanglement decay. However, recently it has been realized that dissipation may have a positive effect as well. In particular, it has been demonstrated that by engineering dissipation of the environment, quantum systems can be driven into the desired entangled steady state (SS), encoding the outcome of quantum computations [35, 36, 37]. In this case, the depopulation of the quantum system is compensated by constant pumping with an external electromagnetic field, and properties of the final states depend on the environment to which the systems are coupled. Therefore, engineering of the environment seen by qubits is of crucial importance for applications in quantum optics.

Of particular interest are structured photonic reservoirs, i.e. structures that have strongly inhomogeneous spatial or spectral distributions of their photonic density of states, as they offer an unprecedented level of control over emitter decay dynamics [38, 39, 40, 41, 75]. The efficient dissipative generation of entanglement has been theoretically predicted and experimentally demonstrated for qubits in optical cavities [43, 44, 45] and photonic crystal systems [46, 47, 48]. In particular, it was reported [43] that dissipative preparation of entanglement between qubits in high-finesse optical cavities offers significant advantages for fidelity improvement over the protocols based on unitary dynamics; decreasing the error by an order of magnitude requires only an order of magnitude increase of the cavity finesse in the former case, compared to a two order of magnitude increase of the finesse

required in the latter case. Preparation of entangled states with fidelity (with respect to the Bell state  $\Psi^+$ ) exceeding 91.9% was experimentally demonstrated [44]. Though offering strong potential for creating highly-entangled states, the small size of optical cavities is a disadvantage when it comes to transferring quantum states over long distances, which is important for applications in quantum communications. For long distance entanglement, coupling of the qubits to reservoirs supporting propagating photonic modes, such as photonic crystals, is useful. In particular, efficient transfer of entanglement between two quantum dots (QDs) placed inside a photonic crystal over a distance 100 times the wavelength of vacuum radiation has been theoretically predicted [46].

Despite the success of using all-dielectric photonic reservoirs for preparation and transfer of entanglement, the large size of such structures is a drawback for their use in nanophotonic integrated circuits. In order to overcome this difficulty, significant attention has been recently devoted to plasmonic waveguides as intermediaries for quantum state transfer. Nanoscale localization of plasmonic modes, as well as their relatively long propagation lengths, makes them good candidates for photonic circuits [49]. Efficient plasmon-mediated entanglement has been predicted for emitters coupled to a metal or metamaterial slab [50], infinitely long V-shaped waveguides cut in a flat metal plane [51, 74], infinitely long nanowires [53, 74, 54, 55], and arrays of metallic nanospheres [56]. Transfer of entanglement over distances far-exceeding the radiation wavelength was reported [74].

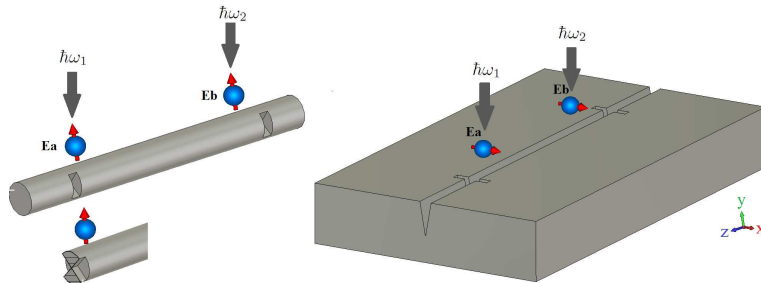


Figure 2.1: Two identical two-level emitters (e.g., atoms or quantum dots) placed next to (a) a metal nanowire (insert shows geometry of the nanowire with coupling slots; the slot opening angle and width are  $95^\circ$  and 15 nm, respectively) and (b) a V-shaped channel cut in a flat metal plane (if coupling slots are present, their length, width and depth are 70 nm, 15 nm, and 138 nm, respectively). We consider both infinite- and finite-length waveguides.

One can ask if it is possible to optimize the geometry of a plasmonic waveguide in order to achieve stronger plasmon mediated entanglement between qubits. Moreover, realistic waveguides are never infinite, and can have discontinuities, accidental or by design. Therefore, it is important to understand what role waveguide edges and inhomogeneities can play in entanglement transfer.

We consider two quantum emitters (modeled as two-level systems) placed above 3D waveguides. Since there are a multitude of possible plasmonic waveguide geometries that one can envision, here we

restrict our consideration to two waveguides that have been extensively studied in the literature, i.e. a metal nanowire and a V-shaped channel cut in a flat metal plane (see Fig. 2.1). Regarding long-distance entanglement, these waveguide geometries have been studied assuming that the nanowire and groove are infinite in their axial directions [74, 51]. The main result of this chapter is to show that realistic finite-length nanowire and groove waveguides, with their associated discontinuities, play a crucial role in the engineering of highly entangled states. We demonstrate that proper positioning of the emitters with respect to the waveguide edges can lead to a significant increase in entanglement compared to the case of the emitter coupled to an infinite plasmonic waveguide. Moreover, even for the infinite-length case, discontinuities in the waveguides do not always play a detrimental role; an increase in entanglement compared to the unperturbed case can be achieved by introducing coupling slots into the structure (which aid in qubit-waveguide coupling).

## 2.2 3D Plasmonic Waveguide Geometries (Nano-Wires, Groove Waveguides)

### 2.2.1 Dissipative Decay Rate and Coherent Coupling Term

As discussed in 1.4, the importance of the classical dyadic Green function is that it leads to the dissipative decay rate and coherent coupling terms

$$\begin{aligned}\Gamma_{\alpha\beta}(\omega_\alpha) &= \frac{2}{\varepsilon_0\hbar} \text{Im} \mathbf{d} \cdot \mathbf{G}(\mathbf{r}_\alpha, \mathbf{r}_\beta, \omega_\alpha) \cdot \mathbf{d}, \\ g_{\alpha\beta}(\omega_\alpha) &= \frac{1}{\varepsilon_0\hbar} \text{Re} \mathbf{d} \cdot \mathbf{G}(\mathbf{r}_\alpha, \mathbf{r}_\beta, \omega_\alpha) \cdot \mathbf{d},\end{aligned}\tag{2.1}$$

where it is supposed the Green function is multiplied by  $k_0^2 = \omega^2/c^2$ . Here  $\mathbf{d}$  is the emitter transition dipole moment,  $\Gamma_{\alpha\alpha}$  and  $\Gamma_{\alpha\beta}(\alpha \neq \beta)$  are the decay rates of the emitter  $\alpha$  due to its interaction with the reservoir (which includes the plasmonic system), and plasmon mediated interactions with the emitter  $\beta$ , respectively. When the emitter itself is in a lossless region of space (such as the space above the waveguide),  $\text{Im}\mathbf{G}(\mathbf{r}_\alpha, \mathbf{r}_\alpha, \omega_\alpha)$  does not have any singularity and thus the decay rate is always finite. The emitters transition frequency shift induced by dipole-dipole coupling is given by  $g_{\alpha\beta}(\alpha \neq \beta)$ . We assume that the emitter transition frequency  $\omega_\alpha$  already accounts for the photonic Lamb shift which is defined by  $g_{\alpha\alpha}$ . In [74] it was shown that for an infinite waveguide the best entanglement was obtained when  $\Gamma_{\alpha\beta}$  was large and  $g_{\alpha\beta}$  was small (forming the dissipative regime). For the finite waveguide case this classification does not hold exactly, which is discussed below.

In the following we consider two identical emitters located near one of the plasmonic waveguides shown in Fig. 2.1 and assume that the waveguide material is silver, which is a relatively low loss metal. We choose the dipole transition frequency of the emitters to be  $\omega_a/2\pi = \omega_b/2\pi = 500$  THz (emission wavelength  $\lambda = 600$  nm). The relative permittivity of silver at the dipole transition frequency is

$-13.9 + i0.92$  [60], and we fully account for the dispersive properties of the metal. For the nanowire waveguide we choose the radius to be  $R = 35$  nm, such that the surface plasmon wavelength in the nanowire is  $\lambda_{\text{spp}} = 425$  nm, and the propagation length is  $l = 1.7 \mu\text{m}$ , calculated analytically [61]. For the groove waveguide, the depth of the groove is 138 nm and its opening angle is  $20^\circ$ ; these dimensions were chosen in [74] to yield almost identical plasmonic wavelengths and propagation lengths for the rod and groove structures (for the groove  $\lambda_{\text{spp}} = 423$  nm and  $l = 1.7 \mu\text{m}$ ), facilitating comparison between the waveguides.

The total emitter decay rate can be expressed as  $\Gamma_{aa} = \Gamma_{\text{rad}} + \Gamma_{\text{Joule}} + \Gamma_{\text{pl}}$ , in terms of the following emitter decay channels: (a) free-space radiation,  $\Gamma_{\text{rad}}$ , (b) Joule losses in the metal,  $\Gamma_{\text{Joule}}$ , and (c) excitation of surface plasmons,  $\Gamma_{\text{pl}}$ . Since radiative decay is not helpful for long-distance entanglement, and Ohmic decay is obviously deleterious, it is clear that we want to maximize the plasmon decay channel, which enhances qubit-qubit interaction. This requires careful positioning of the emitter above the nanowire surface; if the emitter is too close to the nanowire surface, Joule losses dominate the emitter decay (quenching). On the other hand, if the emitter is too far away than it mostly radiates into free space. This problem was studied in [74] where it was demonstrated that at  $\lambda = 600$  nm the optimum distance between the surface of an  $R = 35$  nm infinitely-long silver nanowire and a tuned emitter is 20 nm (which maximizes  $\Gamma_{\text{pl}}$ ), with dipole moment perpendicular to the wire, and for the groove structure the optimum emitter height is 12 nm above the surface of the metal, positioned over the central line of the groove and polarized horizontally.

For the finite nanowire, the problem is more complicated and a unique definition of  $\Gamma_{\text{pl}}$  is difficult (since plasmons reflect and refract from the nanowire edges). We expect that the optimum distance should not be considerably different from the infinite-nanowire case, and we here choose the separation between the emitter and waveguide to be the same as the optimum height for the infinite structure, 20 nm for the nanowire and 12 nm for the groove. Although not shown here, slight improvement in entanglement can be obtained by adjusting the qubit height by a few nm.

Although a primary aim of this work is to examine the effect of a finite plasmonic waveguide structure on entanglement, we first show that introducing discontinuities on an infinite waveguide can enhance qubit-waveguide coupling (i.e., in the following we refer to these discontinuities as coupling slots), thereby enhancing entanglement. Results of calculation of  $\Gamma_{ab}$  and  $g_{ab}$  for emitters placed above an infinite-length nanowire are presented in Fig. 2.2. Here  $z$  is the lateral separation between emitters, and

$$\Gamma_0 = \frac{2}{\varepsilon_0 \hbar} \text{Im} \mathbf{d} \cdot \mathbf{G}^{(0)}(\mathbf{r}_\alpha, \mathbf{r}_\alpha, \omega_\alpha) \cdot \mathbf{d} = \frac{\omega_0^3 d^2}{3\pi \varepsilon_0 \hbar c^3} \quad (2.2)$$

is a decay rate of the emitter in the vacuum. The Purcell factor (PF), the ratio between emitter decay rates in the vicinity of nanowire and in the vacuum, is equal to  $\Gamma_{ab}/\Gamma_0$  when  $z = 0$ . Thus, presence of coupling slots increases the PF (see Fig. 2.2(b)). In Fig. 2 one emitter is located at  $z = 0$ , and the position of the other emitter varies from  $z = 0$  to  $z = 1.5\lambda_{\text{spp}} = 637.5$  nm. Note that here, and in

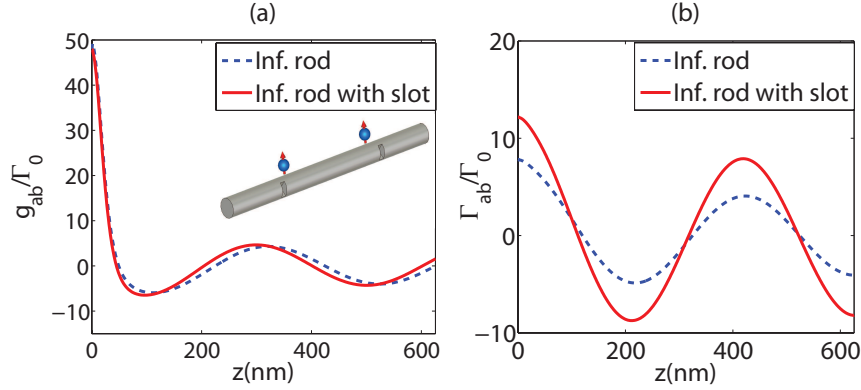


Figure 2.2: Normalized coupling strength  $g_{ab}$  and decay rate  $\Gamma_{ab}$  as a function of distance between emitters above an infinite-length silver nanowire with and without coupling slots (based on scattered Green function).  $\Gamma_{ab}$  is proportional to the Purcell factor when  $z=0$  (i.e.  $\mathbf{r}_\alpha = \mathbf{r}_\beta$ ). The position of one emitter is fixed at  $z = 0$  and the second emitter position is changing with  $z$ . Slots are located at  $z = -40$  nm and  $z = 1.5\lambda_{\text{spp}} + 40$  nm = 677.5 nm.

Fig. 2.3 below, we plot the rates based on the scattered Green function; this term is dominant over the vacuum Green function for all cases of interest (otherwise the plasmonic system would not affect the qubits much, such as, e.g., if the height of the qubits was increased considerably), and it avoids the singularity in  $g_{aa}$  associated with the vacuum Lamb shift. However, in computing entanglement we use the full (scattered plus vacuum) Green function.

Oscillatory behavior of  $\Gamma_{ab}$  and  $g_{ab}$  as a function of qubit separation distance is evident in Fig. 2.2, with the period of oscillation being approximately equal to the plasmon wavelength. Moreover, the positions of the  $\Gamma_{ab}$  maxima correspond to positions of  $g_{ab}$  minima. Thus coherent and dissipative regimes become dominant at different separations between emitters [74]. For the case of a nanowire with coupling slots, the slots are fixed at  $z = -40$  nm and  $z = 1.5\lambda_{\text{spp}} + 40$  nm = 677.5 nm (one slot is to the right of the right emitter, and the other to the left of the left emitter;  $z$  refers to emitter-emitter separation). Coupling slots can lead to enhancement of entanglement between the emitters by increasing the dissipative decay rate at the emitter positions, as shown in the figure (for the effect of coupling slots on entanglement, see Fig. 5.7 below). By adding judiciously-chosen coupling slots to the infinitely long nanowire we are increasing emitter-waveguide coupling, similar to the improved field-plasmon coupling in the case of a grating, and thereby increasing emitter decay rates  $\Gamma_{aa}$  and  $\Gamma_{ab}$  into the plasmon channel. It should be noted that coupling slots seem to affect only the dissipative regime, as the slot induced modification of the coherent exchange rate seems to be insignificant (Fig. 2.2(a)). Also note that the ratios  $\Gamma_{ab}/\Gamma_0$  and  $g_{ab}/\Gamma_0$  do not depend on the emitter dipole moment  $\mathbf{d}$ , since we are in the weak coupling regime.



It is likely that further improvement in emitter-plasmon coupling (and, subsequently, entanglement) can be made by optimizing the slot geometry. In fact, qubit entanglement depends on many parameters even if the dipole transition frequency and nanowire diameter are fixed. In the case of an infinitely-long nanowire these parameters are the distance between emitters and the nanowire surface, separation between emitters, and position and geometry of the coupling slots. In the case of a finite-length nanowire we also have to consider the nanowire length, and positions of the emitters and coupling slots relative to the nanowire ends. In theory, optimal values of these parameters could be found through multi-variable optimization. However, in this work we make no attempt to find optimal values; we merely show that reasonably-positioned qubits and coupling slots can improve entanglement.

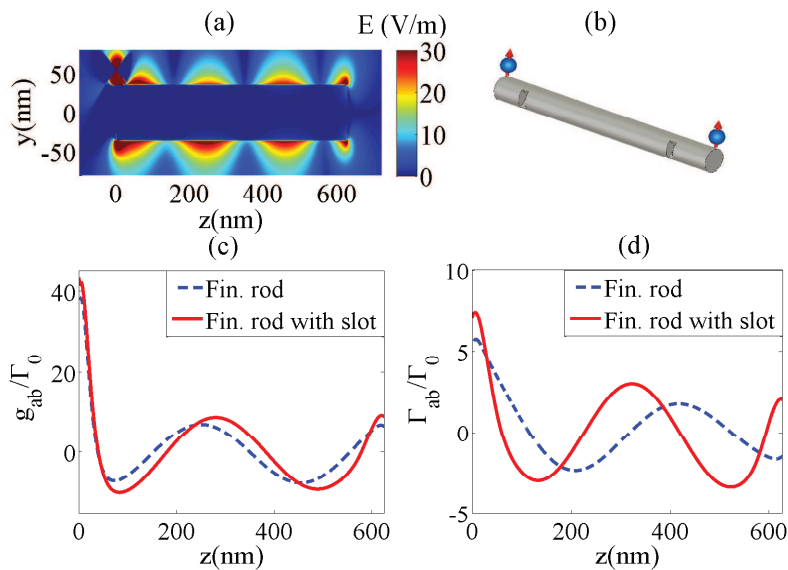


Figure 2.3: (a) Absolute value of plasmon electric field intensity on a finite nanowire of length  $1.5\lambda_{\text{spp}}$ . The plasmon mode is excited by the emitter positioned at  $z = 0$  nm at a distance 20 nm above the nanowire surface. (b) geometry, (c)-(d) Normalized coupling strength  $g_{ab}$  and decay rate  $\Gamma_{ab}$  as a function of a distance between emitters above the nanowire with and without coupling slots (based on scattered Green function). Slots are located at  $z = 27$  nm and  $z = 1.5\lambda_{\text{spp}} - 27$  nm = 610.5 nm.

For the finite-length nanowire we choose the nanowire length to be  $1.5\lambda_{\text{spp}} = 637.5$  nm. We assume one emitter is located above one end of the nanowire ( $z = 0$  nm). If coupling slots are present, they are placed 27 nm away from each end of the nanowire (this location leads to enhanced  $\Gamma_{ab}$  when qubits are at the nanowire ends). The spatial distribution of the electric field intensity of the plasmon mode is shown in Fig. 2.3(a). In order to calculate this distribution we assume a classical electric dipole at the first emitter's position. We can see that the positioned emitters experience maximum intensity of the plasmon electric field.

Figures. 2.3(b) and 2.3(c) show the dissipative and coherent rates as a function of emitter-emitter separation for the finite-length nanowire. We can see that due to plasmon reflections from the nanowire edges, positions of maximums of  $g_{ab}$  and  $\Gamma_{ab}$  almost coincide with each other. Thus

we can not clearly separate the dissipative and coherent regimes in the emitter dynamics anymore, unlike for the infinite-waveguide case. For emitters positioned over the nanowire ends, the addition of coupling slots leads to an increase of coupling between emitters and surface plasmons. Moreover, in this case we observe a shift in the position of the maximums of the emitter coupling rates (which does not occur for the infinite-length structure), as the slots change the effective length of the nanowire. Although not shown, similar results and conclusions are obtained for the groove waveguide.

## 2.2.2 Transient Entanglement Mediated by Surface Waves Supported by Nano-Wire and Groove Waveguides

In order to calculate the transient concurrence we use the analytic equation in 1.110. Steady-state concurrence is calculated using (1.109) and density matrix elements are obtained by solving numerically the system of 16 differential equations. Unless specified otherwise, the pure dephasing rate of the emitters,  $\gamma_a$ , is equal to zero.

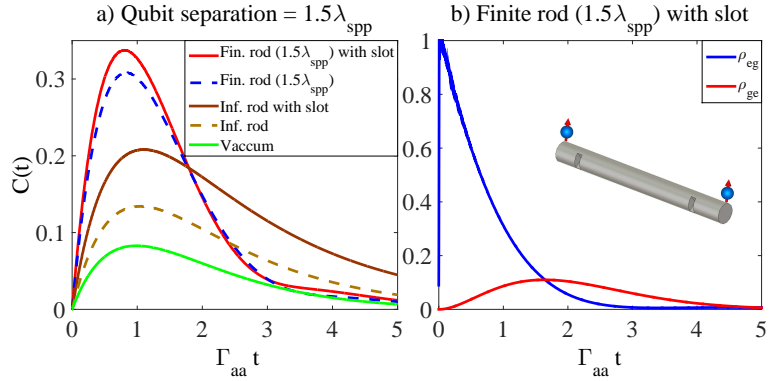


Figure 2.4: (a) Time dependence of transient concurrence between two emitters laterally separated by  $1.5\lambda_{spp} = 637.5\text{nm}$ . We assume that the emitters are in vacuum (solid green line), near an infinite wire with (dashed brown line) and without (solid brown line) coupling slots, near a finite wire of length of  $1.5\lambda_{spp}$  with (solid red) and without (dashed blue line) coupling slots. In the case of the finite wire, qubits are placed above the nanowire ends, and slots are located 27 nm from each end. The normalization constant  $\Gamma_{aa}$  is the decay rate of the emitter (Eq. (2.1)) for the given geometry. (b) Time dependence of the population of the emitter initially in the excited,  $\rho_{eg}$ , and ground,  $\rho_{ge}$ , states, for the case of a finite nanowire with coupling slots.

It was reported in [74], that entanglement between emitters coupled to an infinite length plasmonic nanowire exceeds that between emitters in vacuum. As one can see from Fig. 2.4(a), entanglement can be improved even further by introducing discontinuities (coupling slots) in the nanowire, as described in Sec. 2.2.1. In particular, using an infinite nanowire with coupling slots (see Fig. 2.1 and Sec. 2.2.1 for the details of the slot geometry) can considerably increase concurrence compared to the case with no slots, due to improved emitter-nanowire coupling.

Figure 2.4(a) also shows results for the concurrence of two qubits near a finite-length nanowire,

with length equal to  $1.5\lambda_{\text{spp}}$ , forming a Fabry-Pérot (FP) cavity, with the qubits positioned above the ends of the wire. It can be seen that by coupling into the FP nanowire resonances, we can considerably improve entanglement compared to the infinite-length case. Fig. 2.4(b) shows evolution of the emitters excited state population for the case of a finite nanowire with coupling slots. Here  $\rho_{eg}$  is the probability of the first qubit to be in the excited state and the second qubit to be in ground state, and  $\rho_{ge}$  is similarly defined. The initial state is  $\rho_{eg} = 1$ . We can see that decay of the emitter initially in the excited state leads to excitations of the emitter initially in the ground state, creating a transient entangled state, which is decaying with time.

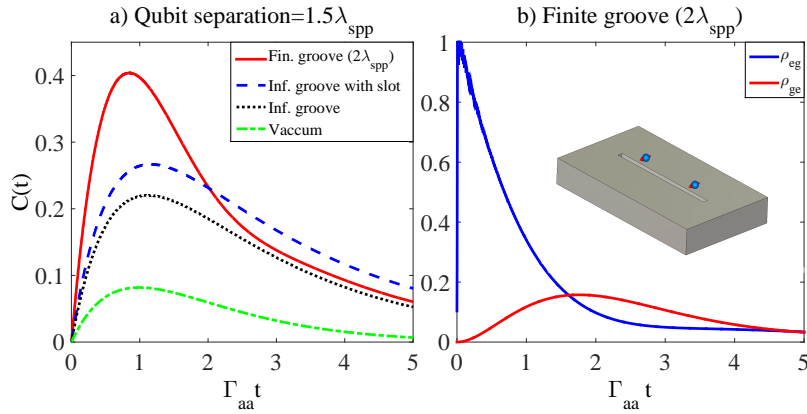


Figure 2.5: (a) Concurrence of two qubits separated by  $1.5\lambda_{\text{spp}}$ . Vacuum case (dashed green line), infinite groove (dotted black line), infinite groove with coupling slots (dashed blue line) 40 nm laterally away from the qubits (outside the space between them), and finite groove of length  $2\lambda_{\text{spp}}$  (solid red line). (b) Time dependence of the population of the emitter initially in the excited,  $\rho_{eg}$ , and ground,  $\rho_{ge}$ , states.

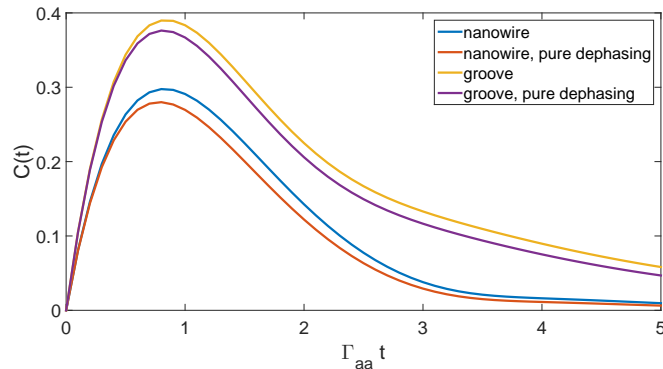


Figure 2.6: Time dependence of the concurrence between two qubits including the effect of pure dephasing (see 1.121). Qubits are placed either above the ends of a finite-length nanowire (Fig. 5.7(a)) or finite-length groove (Fig. 5.9(a)). The emitter coupling rates for the case of the nanowire are  $\Gamma_{aa} = 6.5\mu\text{eV}$ ,  $\Gamma_{ab} = -1.2\mu\text{eV}$ ,  $g_{ab} = 2.85\mu\text{eV}$ , while for the case of the groove waveguide  $\Gamma_{aa} = 11.38\mu\text{eV}$ ,  $\Gamma_{ab} = -6.48\mu\text{eV}$ ,  $g_{ab} = 5.8\mu\text{eV}$ . The QD pure dephasing rate,  $\gamma'$ , is equal to  $1\mu\text{eV}$ .

The concurrence of two qubits separated by a distance  $1.5\lambda_{\text{spp}} = 634.5\text{ nm}$  is shown in Fig. 2.5(a)

for an infinite groove, an infinite groove with coupling slots (slots are positioned as in the nanowire case), and a  $2\lambda_{\text{spp}}$  groove. Although the finite nanowire considered above had length  $1.5\lambda_{\text{spp}}$ , for the finite groove the length is  $2\lambda_{\text{spp}}$  because for the groove the modal field is not strong at the groove ends (although not shown, the modal field distribution in the groove is more cavity-like, with a node at the groove end-wall), and so a  $2\lambda_{\text{spp}}$  groove allows the qubits to be separated by  $1.5\lambda_{\text{spp}}$  and also to be at the modal antinodes. Results for the finite-length groove are shown without slots since for this case coupling slots did not improve concurrence considerably; for the nanowire the modal field is strong at the wire ends (Fig. 2.3), but it is not exactly a modal antinode because of strong end-diffraction. In this case, coupling slots serve to shift the mode pattern slightly, enhancing qubit-plasmon coupling. If the qubits are positioned exactly at a modal antinode, which is better defined away from the wire ends, coupling slots have a weaker effect on improving concurrence. It can be seen that for the infinite groove, the addition of coupling slots leads to improved concurrence, and the FP resonances of the finite-length groove leads to further improvement. As reported in [74], for the chosen geometry the groove waveguide leads to stronger entanglement compared to the nanowire (although this conclusion is likely dependent on metal absorption and geometry). The population dynamics of the qubits are also shown for the finite groove case in Fig. 2.5(b).

In order to study the effect of pure dephasing, we considered a QD with dipole moment 30 D as our model system. It was reported [48] that the dephasing rate,  $\gamma_a$  of the QD is equal to  $1 \mu\text{eV}$ . We considered emitters placed either above a finite nanowire (Fig. 2.4(a)) or a finite groove (Fig. 5.9(a)) without coupling slots. The emitter coupling rates for the case of the nanowire are  $\Gamma_{aa} = 6.5\mu\text{eV}$ ,  $\Gamma_{ab} = -1.2\mu\text{eV}$ ,  $g_{ab} = 2.85\mu\text{eV}$ , while for the case of the groove waveguide  $\Gamma_{aa} = 11.38\mu\text{eV}$ ,  $\Gamma_{ab} = -6.48\mu\text{eV}$ ,  $g_{ab} = 5.8\mu\text{eV}$ . We can see that in general the pure dephasing decay rate is smaller than the radiative decay rate. Even though it affects entanglement detrimentally, the decrease in concurrence is rather small (see Fig. 2.6). Thus we otherwise ignore pure dephasing in our results, although the validity of this assumption depends on the QD system under consideration and the temperature.

### 2.2.3 Steady State Entanglement Under External Pumping

Up to this point we have considered spontaneous (or vacuum-induced) decay which leads to transient entanglement between two coupled qubits. Transient entanglement does not persist due to depopulation of the excited state of the qubits. Thus, in order to obtain a steady entangled state, depopulation has to be compensated by pumping qubits with an external laser pump in resonance with the frequency of the qubits' dipole transition. We assume the pump interacts only with the qubits. In this case, the concurrence reaches a final, steady state (SS) value.

Figure 2.7 shows the externally driven concurrence of qubits in the presence of a finite nanowire with length  $1.5\lambda_{\text{spp}}$  with qubits located at the nanowire ends (the same geometry as in Fig. 2.4), a finite groove with length  $2\lambda_{\text{spp}}$ , qubits located symmetrically above its surface separated by  $1.5\lambda_{\text{spp}}$

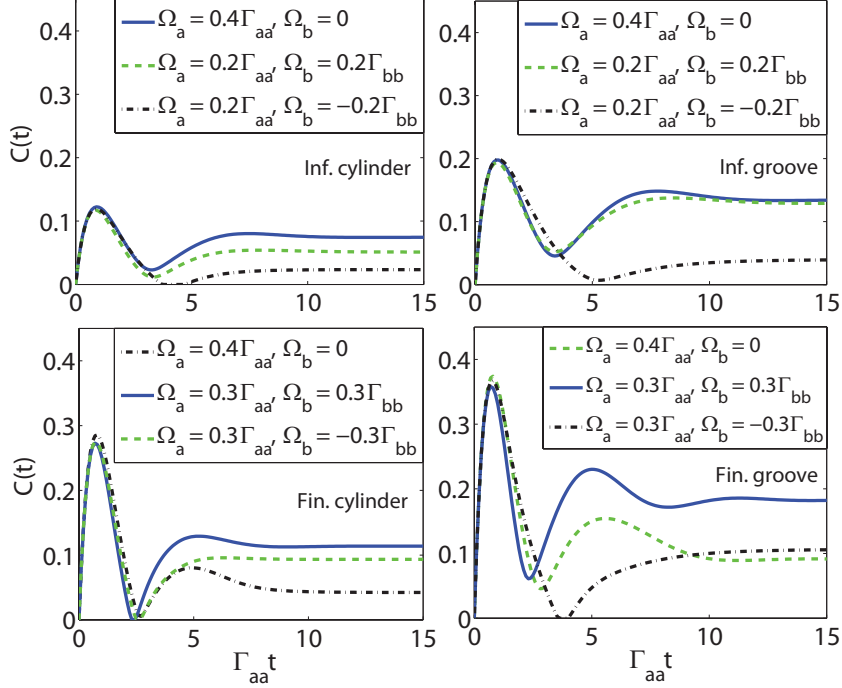


Figure 2.7: Time dependence of the concurrence between two qubits pumped by external electromagnetic fields. Qubits are placed above either a nanowire (left panel) or groove (right panel). Qubit separation is  $1.5\lambda_{\text{spp}}$ . The system geometry is the same as in Figs. 2.4,2.5.

(the same geometry as in Fig. 2.5), and the infinite-length cases with the same qubit spacings as in the finite case. Three different coherent pumps differing in the relative phase of the laser field on qubit 1 and 2 have been considered: symmetric pumping indicates identical Rabi frequencies,  $\Omega_1 = \Omega_2$ , antisymmetric pumping corresponds to  $\Omega_1 = -\Omega_2$  and asymmetric pumping means  $\Omega_1 \neq 0$ ,  $\Omega_2 = 0$ .

From Fig. 2.7, it is clear that the transient portion of the concurrence is intensity independent, and that the infinite groove has a higher transient peak compared to the infinite nanowire for all pumping regimes. Numerical experimentation shows that larger values of  $g_{ab}$  and  $\Gamma_{ab}$  at the positions of the qubits lead to larger transient concurrence peaks. For the geometries studied, these mutual rates are larger for the infinite groove than for the infinite nanowire, which facilitates photon exchange between the qubits for the groove guide. We can also see that the main advantage of a finite waveguide relative to an infinite one is significant improvement in the transient concurrence peak, with more modest improvement in the final, steady-state value.

The panels in Fig. 2.8 shows the SS value of concurrence,  $C_\infty$ , corresponding to different types of pumping as a function of qubit separation normalized to the plasmon wavelength,  $\lambda_{\text{spp}}$  for the finite nanowire (left panels) and finite groove (right panels). Numerical experimentation indicates that for steady state concurrence the preferred case is when we have large  $\Gamma_{ab}$  and small  $g_{ab}$ , in agreement with [74] for the case of infinite waveguides. Therefore, the dissipative regime leads to larger transient entanglement peaks for infinite-length waveguides, and larger values of  $C_\infty$  in general, and it is only for transient entanglement on finite-length waveguides that the dissipative and coherent regimes

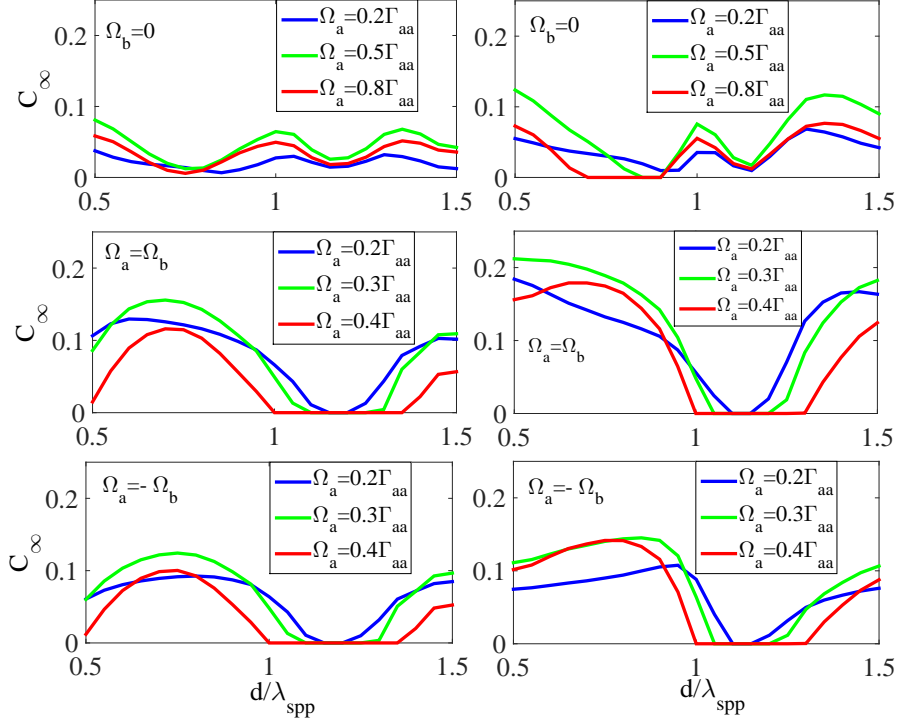


Figure 2.8: Steady state concurrence,  $C_\infty$ , as function of qubit separation normalized by the modal wavelength,  $\lambda_{\text{spp}}$ . Qubits are placed either above a finite nanowire (right) or a finite groove (left). The geometry is the same as in Figs. 2.4,2.5. Asymmetric, antisymmetric and symmetric pumping have been considered.

becomes similar. Here, we can have steady state concurrence close to the peak of the transient value for relatively weak pumping. For steady state concurrence, large  $g_{ab}$  and  $\Gamma_{ab}$  are less ideal, because of the tendency to decrease SS concurrence. Furthermore, pump strength can not be too large otherwise the qubits will interact mostly with the pump and become decoupled from each other. Ideally, the pump should be strong enough to keep the system interacting, but small enough for the qubit interaction to dominate the dynamics. As made clear in Fig. 2.8, pumping one qubit strongly (asymmetric pumping) is possible, but pumping both qubits strongly (symmetric or antisymmetric pumping) reduces concurrence.

Population dynamics of the qubits are shown in Fig. 2.9 for the case when qubits are separated by  $1.5\lambda_{\text{spp}}$  and pumped either symmetrically, or only one qubit was pumped, for different intensities. Four density matrix elements are  $\rho_{gg}$ ,  $\rho_{ee}$ ,  $\rho_{ge}$ , and  $\rho_{eg}$  which are respectively the probability of both qubits to be in ground state, both qubits to be in excited state, the first qubit to be in the ground state and the second to be in the excited state, vice versa. Moreover we have assumed that initial state is a state when  $\rho_{eg} = 1$ .

The qubits dynamics is different for one-field and two-field pumping. For the case of two-field pumping, in the steady state we have  $\rho_{eg} = \rho_{ge}$  which is reasonable as we are pumping both systems identically. We can see that these elements first grow rather fast with the growth of the pump intensity, but then slow down around  $\Omega_{aa} = \Omega_{bb} = 0.3\Gamma_{aa}$ . We can also see that the element  $\rho_{ee}$

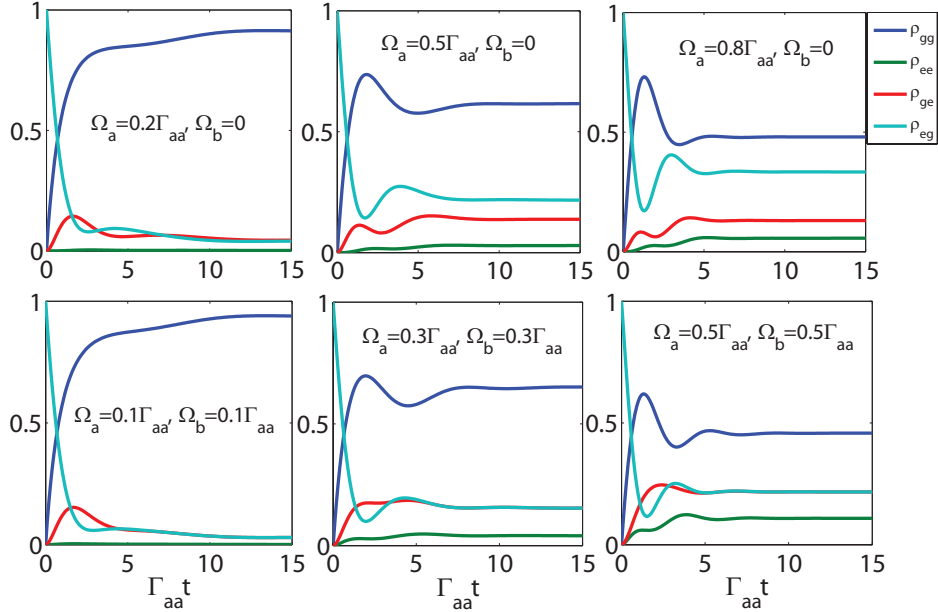


Figure 2.9: Dynamics of the density matrix elements for qubits under external pumping. Qubits are above a finite groove with qubit separation  $1.5\lambda_{\text{spp}} = 634.5$  (see Fig. 2.5 for details of the geometry). Two different regimes of pumping have been considered, symmetric pumping (two field pumping) and asymmetric pumping (single field pumping).

also grows under the influence of the pump. But it first grows slower and then starts growing faster around  $\Omega_{aa} = \Omega_{bb} = 0.3\Gamma_{aa}$ . Therefore, this indicates that under such strong pumping the dynamics of both emitters is mostly defined by external pumps, and not by the qubit-qubit interactions, which is detrimental for entanglement. Under the single field illumination the density matrix elements evolve similarly to the previous case. However,  $\rho_{eg} > \rho_{ge}$ , because the first qubit that is pumped in this case. We can see that with the intensity increase all elements grow, however, when the intensity becomes too strong the growth freezes and only  $\rho_{eg}$  grows, indicating that dynamics of first emitter is entirely defined by the pump field, which is also detrimental for entanglement.

## 2.3 Summary

In this chapter we considered two quantum dots placed above 3D waveguides. Since there are a multitude of possible plasmonic waveguide geometries that one can envision, we restricted our consideration to two waveguides that have been extensively studied in the literature, i.e. a metal nanowire and a V-shaped waveguide which is a channel cut in a flat metal plane (groove waveguide). Our main results in this chapter are to show that realistic finite-length nanowire and groove waveguides, with their associated discontinuities, play a crucial role in the engineering of highly entangled states. Here, we demonstrated that proper positioning of the emitters with respect to the waveguide edges can lead to a significant increase in entanglement compared to the case of the emitter coupled to an infinite

plasmonic waveguide. Moreover, even for the infinite-length case, discontinuities in the waveguides do not always play a detrimental role, to be more specific, an increase in entanglement compared to the unperturbed waveguides can be achieved by introducing coupling slots (engineered perturbations) into the structure which aid in quantum dot-waveguide coupling.



## Chapter 3

# Hyperbolic and Isotropic 2D Plasmonic Systems Mediated Entanglement

### 3.1 Introduction

The development of nano-fabrication technologies has made it possible to fabricate artificial materials exhibiting a hyperbolic regime - hyperbolic metamaterials (HMTMs) [63, 64]. Hyperbolic metamaterials are uniaxial structures with extreme anisotropy, whose reactive effective material tensor components have opposite signs for orthogonal electric field polarizations [65]. Hyperbolic materials exhibit hyperbolic, as opposed to the usual elliptic, dispersion, and combine the properties of transparent dielectrics and reflective metals [63]. These exotic properties have led to new physical phenomena and to the proposal for optical devices for a wide range of applications, such as far-field subwavelength imaging, nanolithography, emission engineering [63], negative index waveguides [66], subdiffraction photonic funnels [67], and nanoscale resonators [68].

The complexity of bulk fabrication of metamaterials has hindered the impact of this technology, especially in the optical regime, and volumetric effects may be detrimental to the associated losses [65]. Metasurfaces [69, 70], sheets of material with extreme sub-wavelength thickness, might address many of the present challenges and allow integration with planarized systems compatible with integrated circuits. Many high frequency electronics applications are envisioned for metasurfaces due to their ability to support and guide highly confined surface plasmons. The class of two dimensional (2D) atomic crystals [71] represents the ultimate embodiment of a meta-surface in terms of thinness, and often performance (e.g. tunability, flexibility, quality factor). Some notable examples of 2D layered crystals include graphene, transition metal dichalcogenides, trichalcogenides, black phosphorus, boron

nitride, and many more.

Graphene in particular has received considerable attention as a promising two-dimensional surface for many applications relating to large enhancement in Purcell emission, integrability, electronic tunability and transformation optics [72, 77]. In addition to graphene, black phosphorus (BP) is also a layered material, with each layer forming a puckered surface due to sp<sup>3</sup> hybridization. It is one of the thermodynamically more stable phases of phosphorus, at ambient temperature and pressure [78]. BP has recently been exfoliated into its multilayers [79, 82], showing good electrical transport properties. In particular, the optical absorption spectra of BP vary sensitively with thickness, doping, and light polarization, especially across the technologically relevant mid- to near-infrared spectrum [83, 85]. Hence, it has also received considerable attention for optoelectronics, such as hyperspectral imaging and detection [86, 89], photodetectors in silicon photonics [90], photo-luminescence due to excitonic effects [91], among many others.

Both natural materials and metasurfaces can be isotropic or anisotropic, and, e.g., isotropic graphene can be employed to form an effective anisotropic metasurface by modulating its conductivity [65, 75]. And, both natural materials and metasurfaces may exhibit a hyperbolic regime. Basic properties of plasmons on 2D hyperbolic surfaces have been recently studied; for metasurfaces comprised of anisotropic plasmonic particles in [92], for graphene strips in [65], and for general continuum 2D materials including black phosphorus in [93]. In the following we consider a brief derivation of the Green function for a 2D sheet with graphene conductivity model.

## 3.2 Infinite 2D Graphene Sheet

### 3.2.1 Green Function Analysis

The graphene is modeled as an infinitesimally thin, local two-sided surface characterized by a surface conductivity  $\sigma(\omega, \mu_c, \Gamma, \gamma, T)$  where  $\omega$  is the radiation frequency,  $\mu_c$  is the graphene chemical potential,  $\gamma$  and  $\Gamma$  are phenomenological intraband and interband scattering rates, respectively that are assumed to be independent of energy  $\varepsilon$  and  $T$  is temperature. The conductivity of graphene has been considered in several recent works [97, 98] and here we use the expression resulting from the Kubo formula [99] (time convention  $\exp(-i\omega t)$ )

$$\sigma(\omega) = \frac{ie^2 K_B T}{\pi^2 (\omega + i\gamma)} \left( \frac{\mu_c}{K_B T} + 2 \ln \left( e^{-\frac{\mu_c}{K_B T}} + 1 \right) \right) + \frac{ie^2 (\omega + i\Gamma)}{\pi^2} \int_0^\infty \frac{f_d(-\varepsilon) - f_d(\varepsilon)}{(\omega + i\Gamma)^2 - 4(\varepsilon/)^2} d\varepsilon, \quad (3.1)$$

in the above equation  $\tau = 1/\gamma$  is the scattering time,  $e$  is the charge of an electron, and  $f_d(\varepsilon) = (e^{(\varepsilon - \mu_c)/K_B T} + 1)^{-1}$  is the Fermi-Dirac distribution. The first and second terms in the conductivity

are due to intraband and interband contributions, respectively. For  $K_B T \ll |\mu_c|, \hbar\omega$  [99]

$$\sigma(\omega) = \frac{ie^2 |\mu_c|}{\pi(\omega + i\gamma)} + \frac{ie^2}{4\pi} \ln \left( \frac{2|\mu_c| - (\omega + i\Gamma)}{2|\mu_c| + (\omega + i\Gamma)} \right). \quad (3.2)$$

We assume laterally-infinite graphene modeled as an infinitesimally-thin, local, two-sided surface characterized by a surface conductivity  $\sigma$ . The Green functions for a graphene sheet at the interface between two dielectrics are given in [16] for graphene on a finite-thickness dielectric support. Considering the graphene sheet in the plane  $y = 0$ , with material described by  $\varepsilon_1$  for  $y > 0$  and  $\varepsilon_2$  for  $y < 0$ , the Green tensor for points in region  $n$  is

$$\mathbf{G}(\mathbf{r}, \mathbf{r}') = (\mathbf{I}k_n^2 + \nabla\nabla\cdot) \{ \mathbf{g}^p(\mathbf{r}, \mathbf{r}') + \mathbf{g}^s(\mathbf{r}, \mathbf{r}') \}, \quad (3.3)$$

where  $k_n = \omega\sqrt{\mu_0\varepsilon_n}$ ,  $n = 1, 2$  is the wavenumber in each half spaces. The principle (p) and scattered (s) Green's function components are

$$\mathbf{g}^p(\mathbf{r}, \mathbf{r}') = \mathbf{I} \frac{e^{ik_1 R}}{4\pi R}, \quad \mathbf{g}^s(\mathbf{r}, \mathbf{r}') = \hat{\mathbf{y}}\hat{\mathbf{y}} g_n^s(\mathbf{r}, \mathbf{r}') + \left( \hat{\mathbf{y}}\hat{\mathbf{x}} \frac{\partial}{\partial x} + \hat{\mathbf{y}}\hat{\mathbf{z}} \frac{\partial}{\partial z} \right) g_c^s(\mathbf{r}, \mathbf{r}') + (\hat{\mathbf{x}}\hat{\mathbf{x}} + \hat{\mathbf{z}}\hat{\mathbf{z}}) g_t^s(\mathbf{r}, \mathbf{r}'), \quad (3.4)$$

where  $\mathbf{I}$  is the unit dyadic,  $k_\rho$  is a radial wavenumber,  $p_n^2 = k_\rho^2 - k_n^2$ ,  $r = \sqrt{(x - x')^2 + (z - z')^2}$ , and  $R = |\mathbf{r} - \mathbf{r}'| = \sqrt{(y - y')^2 + r^2}$ . The Sommerfeld integrals are

$$g_\beta^s(\mathbf{r}, \mathbf{r}') = \frac{1}{2\pi} \int_{-\infty}^{\infty} C_\beta \frac{H_0^{(1)}(k_\rho r) e^{-p(y+y')}}{4p} k_\rho dk_\rho, \quad (3.5)$$

where  $\beta = t, n, c$  depends on the graphene and dielectric support layers. For a pump polarized perpendicular to the graphene surface we only need  $G_{yy}$  and  $\beta = n$ , with

$$C_n = \frac{\left( \frac{\varepsilon_2}{\varepsilon_1} p_1 - p_2 \right) i\omega\varepsilon_1 - \sigma p_1 p_2}{\left( \frac{\varepsilon_2}{\varepsilon_1} p_1 + p_2 \right) i\omega\varepsilon_1 - \sigma p_1 p_2}. \quad (3.6)$$

For more complex geometries, such as graphene on a multi-layered dielectric, only the coefficient  $C_n$  changes. The wave parameter  $p_n = \sqrt{k_\rho^2 - k_n^2}$ , leads to branch points at  $k_\rho = \pm k_n$ , and thus the  $k_\rho$ -plane is a four-sheeted Riemann surface. The standard hyperbolic branch cuts [100] that separate the proper sheet (where  $\text{Re}(p_n) > 0$ , such that the radiation condition as  $|y| \rightarrow \infty$  is satisfied) and the improper sheet are the same as in the absence of surface conductivity  $\sigma$ . The zeros of the denominators of  $C_\beta$  lead to pole singularities in the spectral plane associated with surface plasmon polaritons (SPPs).

Using complex-plane analysis, the scattered Green's function can be written as discrete pole (SPP) contributions plus a branch cut integral over the continuum of radiation modes. For  $\varepsilon_1 = \varepsilon_2 = \varepsilon$ ,

setting the denominator of (3.6) to zero leads to the (TM) SPP wavenumber

$$k_\rho = k \sqrt{1 - \left(\frac{2}{\sigma\eta}\right)^2}, \quad (3.7)$$

where  $\eta = \sqrt{\mu_0/\varepsilon}$  and  $k = \sqrt{\varepsilon}k_0$ . In this case, the vertical wavenumber parameter in the Sommerfeld integrals becomes  $p = \sqrt{k_\rho^2 - k^2} = i2\omega\varepsilon/\sigma$  and if  $\sigma$  is real-valued then  $\text{Re}(p) > 0$  is violated and the TM mode is on the improper Riemann sheet. Assuming complex-valued conductivity  $\sigma = \sigma' + i\sigma''$ ,

$$p = \frac{i2\omega\varepsilon}{\sigma} = \frac{2\omega\varepsilon}{|\sigma|^2} (\sigma'' + i\sigma') \quad (3.8)$$

and therefore if  $\sigma'' > 0$  (as shown below, when the intraband conductivity dominates) the mode is a surface wave on the proper sheet, whereas if  $\sigma'' < 0$  (interband conductivity dominates) the mode is on the improper sheet, assuming an  $\exp(-i\omega t)$  reference [16]. Assuming the dipole moment is perpendicular to the graphene surface, only TM SPPs can be excited.

### 3.2.2 Controllable Entanglement Using Gate Voltage

Regarding to section 3.2.1, the conductivity of the graphene and so its Green function can be controlled using a the graphene chemical potential or its gate voltage. High tunability of the surface plasmon polariton on the surface of graphene sheet makes it a promising environment for SPP assisted entanglement between two quantum dots.

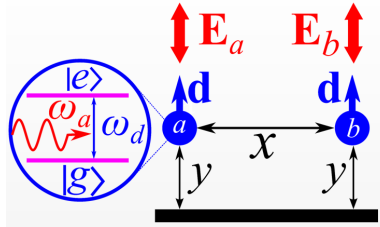


Figure 3.1: Schematic representation of two two-level-atom (TLA) above an infinite graphene sheet. TLAs are pumped by two independent laser fields with intensities  $E_a$  and  $E_b$ . The graphene is suspended in vacuum.

As depicted in fig. 3.1, we consider two identical quantum dots placed at height  $y$  above a freely suspended infinite graphene sheet and horizontal distance  $x$ . It is supposed that their dipole moment  $\mathbf{d}$  is polarized normal to the graphene. The two QDs are externally pumped by two laser beams with electric fields  $\mathbf{E}_j = E_{0,j}e^{-i\omega_j t} + c.c.$ ,  $j = a, b$ . In order to have maximum interaction between the external electromagnetic field and the atoms we assume the field frequency is equal to the atomic transition frequency of the QDS,  $\omega_j = \omega_d$  (zero detuning parameter  $\Delta_j = \omega_j - \omega_d$ ).

Initially we suppose one of the QDs are excited and the other one is in its ground state. The initially excited QD will communicate to the other one through two different channels, excited surface

wave on the graphene and free space radiation. If the QDs are put at a proper distance above the graphene then they can get coupled strongly to the SPPs and so their communication occurs mainly through the supported SPP on the graphene. Based on this, the dynamic of the QDs system and so their entangled state can be controlled by controlling the surface conductivity of the graphene. We use the master equation formulation presented in section 1.4.3 to calculate the transient and steady state entanglement.

We suppose two QDs are placed at  $y = 20$  nm above graphene with distance  $x = 100$  nm. QDs are pumped with fields with Rabi frequency  $\Omega_j = \mathbf{d} \cdot \mathbf{E}_j / \hbar$ . The frequency of the laser and atomic transition frequency are synced at  $\hbar\omega_d = 165$  meV. The concurrence  $C(t)$  between these two emitters is calculated in Fig. 3.2 at three different chemical potentials  $\mu_c = 10, 100$  and  $1000$  meV. Fig. 3.2 shows the transient and steady state concurrence between the emitters at different chemical potentials and the level of external pumping. As can be seen clearly, using  $\mu$  of graphene and  $\Omega_j$  it is possible to control the transient and steady state value of concurrence. From different panels of Fig. 3.2 it can be seen that in order to keep the dynamics of the QDs system the laser intensity should not be very strong, because in this case the emitters mainly get coupled to the external field and so we loose the entanglement. Also the laser intensity should be very weak because it cannot compensate the depopulation of the initial QDs excitations.

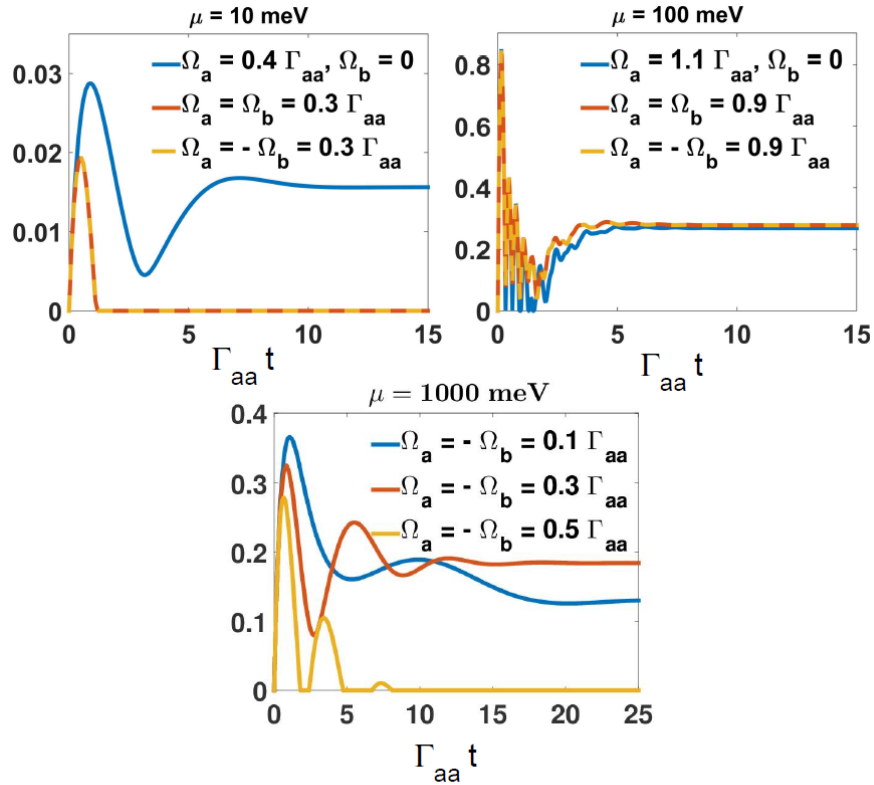


Figure 3.2: Transient and steady state concurrence of two QDs above graphene sheet.

The dependence of the steady state concurrence  $C_\infty$  on height and horizontal distances of the QDs are investigated in Fig. 3.3. As can be seen closer distance necessarily does not mean better  $C_\infty$ . For both height and distance there is an optimum value to get higher steady state concurrence.

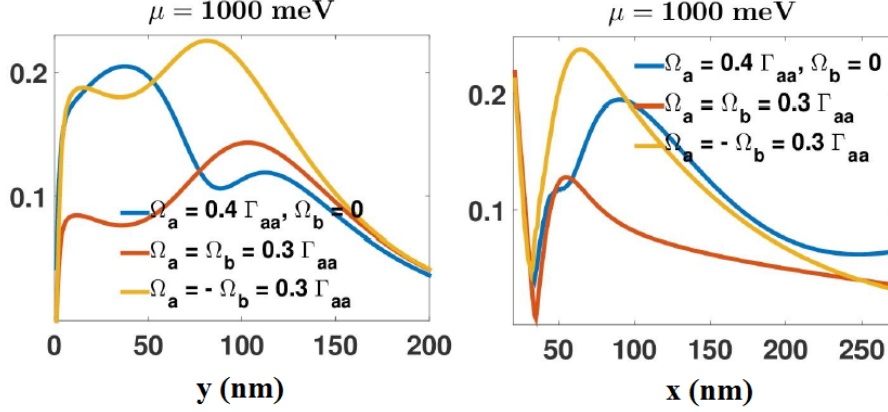


Figure 3.3: Steady state concurrence as a function of height above graphene  $y$ , and QDs spacing  $x$ .

It can be generally concluded that entanglement between two emitters can be substantially tuned by varying the chemical potential of graphene. The degree of entanglement can be further adjusted by changing the emitter and pumping scheme. Proper positioning of the emitters above a graphene layer, as well as choice of the separation distance and substrate material is crucial for entanglement optimization.

As was discussed, graphene sheet is a 2D plane which has isotropic conductivity in case of zero magnetic biasing field. Due to the isotropy of its electrical properties, the supported SPP propagates omnidirectionally in the plane of graphene, and so it is not possible to channelize the energy from source to observation spot. In contrast to the isotropic case, anisotropic 2D surfaces are capable to launch an SPP along specific directions and so stronger and controllable entanglement is achievable. In the next section we discuss about this class of surfaces.

### 3.3 2D Hyperbolic Surface (Black Phosphorus and Graphene Stripes)

#### 3.3.1 Green Function Analysis and Directive Surface Waves

Among the possible anisotropic surfaces, we can name hyperbolic 2D materials for which the diagonal elements of their conductivity tensor have different signs. In this section we study the dyadic Green function derivation of SPP supported by this kind of anisotropic 2D materials.

The geometry under consideration is shown in Fig. 3.4. We consider an anisotropic layer with conductivity tensor  $\sigma = \text{diag}\{\sigma_{xx}, \sigma_{yy}\}$ , embedded at the interface of two isotropic different materials

with electrical properties  $\epsilon_1, \mu_1$  and  $\epsilon_2, \mu_2$ .

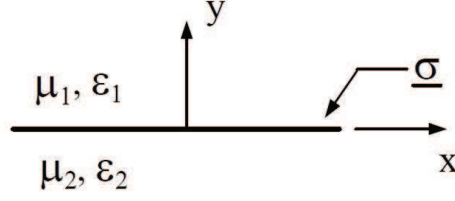


Figure 3.4: Anisotropic surface with conductivity tensor  $\sigma$  at the interface of two isotropic materials.

For any planarly layered, piecewise-constant medium, the electric and magnetic fields in region  $n$  due to an electric current in any region are

$$\mathbf{E}^{(n)}(\mathbf{r}) = (k_n^2 + \nabla \nabla \cdot) \boldsymbol{\pi}^{(n)}(\mathbf{r}) \quad (3.9)$$

$$\mathbf{H}^{(n)}(\mathbf{r}) = i\omega\epsilon_n \nabla \times \boldsymbol{\pi}^{(n)}(\mathbf{r}) \quad (3.10)$$

where  $k_n = \omega\sqrt{\mu_n\epsilon_n}$  and  $\boldsymbol{\pi}^{(n)}(\mathbf{r})$  are the wavenumber and electric Hertzian potential in region  $n$ , respectively. The suppressed time convention is  $e^{i\omega t}$ . Assuming that the current source is in region 1,  $\mathbf{J}^{(1)}$ , then

$$\begin{aligned} \boldsymbol{\pi}^{(1)}(\mathbf{r}) &= \boldsymbol{\pi}_1^p(\mathbf{r}) + \boldsymbol{\pi}_1^s(\mathbf{r}) = \int_{\Omega} \{ \underline{\mathbf{g}}^p(\mathbf{r}, \mathbf{r}') + \underline{\mathbf{g}}^r(\mathbf{r}, \mathbf{r}') \} \cdot \frac{\mathbf{J}^{(1)}(\mathbf{r}')}{i\omega\epsilon_1} d\Omega' \\ \boldsymbol{\pi}^{(2)}(\mathbf{r}) &= \boldsymbol{\pi}_2^s(\mathbf{r}) = \int_{\Omega} \underline{\mathbf{g}}^t(\mathbf{r}, \mathbf{r}') \cdot \frac{\mathbf{J}^{(1)}(\mathbf{r}')}{i\omega\epsilon_1} d\Omega' \end{aligned} \quad (3.11)$$

In the above equation, the underscore indicates dyadic quantities,  $\underline{\mathbf{g}}^p$  is the principal (free space) dyadic Green's function,  $\underline{\mathbf{g}}^r$  is the reflected dyadic Green's function responsible for the fields in the region containing the source,  $\underline{\mathbf{g}}^t$  is the transmitted dyadic Green's function responsible for the fields in the non-source region (here we assume a source in one region or the other, but not in both regions) and  $\Omega$  is the support of the current. With  $y$  parallel to the interface normal, the principle Green's dyadic can be written as

$$\begin{aligned} \underline{\mathbf{g}}^p(\mathbf{r}, \mathbf{r}') &= \mathbf{I} \frac{e^{-ik_1 R}}{4\pi R} \\ &= \mathbf{I} \frac{1}{(2\pi)^2} \int_{-\infty}^{\infty} \int_{-\infty}^{\infty} \frac{e^{-p_1 |y-y'|}}{2p_1} e^{-i\mathbf{q} \cdot (\mathbf{r}-\mathbf{r}')} dq_x dq_y \end{aligned} \quad (3.12)$$

where  $\mathbf{q} = \hat{\mathbf{x}}q_x + \hat{\mathbf{z}}q_z$ ,  $|\mathbf{q}| = q = \sqrt{q_x^2 + q_z^2}$ ,  $p_n^2 = |\mathbf{q}|^2 - k_n^2$ ,  $\rho = \sqrt{(x-x')^2 + (z-z')^2}$ ,  $R = |\mathbf{r} - \mathbf{r}'| = \sqrt{\rho^2 + (y-y')^2}$  and  $\mathbf{I}$  is the unit dyadic.

The scattered (reflected or transmitted) Green's dyadics can be obtained by enforcing the bound-

ary conditions

$$\begin{aligned}\hat{\mathbf{z}} \times (\mathbf{H}_1 - \mathbf{H}_2) &= \mathbf{J}_e^s \\ \hat{\mathbf{z}} \times (\mathbf{E}_1 - \mathbf{E}_2) &= -\mathbf{J}_m^s\end{aligned}\quad (3.13)$$

where  $\mathbf{J}_e^s$  (A/m) and  $\mathbf{J}_m^s$  (V/m) are electric and magnetic surface currents on the boundary. In our case,  $\mathbf{J}_m^s = \mathbf{0}$ , and  $\mathbf{J}_e^s = \boldsymbol{\sigma} \cdot \mathbf{E}$ . Using only an electric Hertzian potential, we can satisfy Maxwell's equations and the relevant boundary conditions. Introducing the two-dimensional Fourier transform

$$\mathbf{a}(\mathbf{q}, y) = \int_{-\infty}^{\infty} \int_{-\infty}^{\infty} \mathbf{a}(\mathbf{r}) e^{i\mathbf{q}\cdot\mathbf{r}} dx dz \quad (3.14)$$

$$\mathbf{a}(\mathbf{r}) = \frac{1}{(2\pi)^2} \int_{-\infty}^{\infty} \int_{-\infty}^{\infty} \mathbf{a}(\mathbf{q}, y) e^{-i\mathbf{q}\cdot\mathbf{r}} dq_x dq_z \quad (3.15)$$

and enforcing the boundary conditions, the scattered Green's dyadic is found to have the form

$$\underline{\mathbf{g}}^{r,t} = \begin{pmatrix} g_{xx}^{r,t} & g_{xy}^{r,t} & 0 \\ g_{yx}^{r,t} & g_{yy}^{r,t} & g_{yz}^{r,t} \\ 0 & g_{zy}^{r,t} & g_{zz}^{r,t} \end{pmatrix} \quad (3.16)$$

where the Sommerfeld integrals are

$$g_{\alpha\beta}^r(\mathbf{r}, \mathbf{r}') = \frac{1}{(2\pi)^2} \int_{-\infty}^{\infty} \int_{-\infty}^{\infty} w_{\alpha\beta}^r(q_x, q_z) \frac{e^{-p_1(y+y')}}{2p_1} e^{-i\mathbf{q}\cdot(\mathbf{r}-\mathbf{r}')} dq_x dq_z. \quad (3.17)$$

The Green's dyadic for region 2,  $\underline{\mathbf{g}}^t(\mathbf{r}, \mathbf{r}')$ , has the same form as for region 1, although in (3.17) the replacement  $w_{\alpha\beta}^r e^{-p_1(y+y')} \rightarrow w_{\alpha\beta}^t e^{p_2 y} e^{-p_1 y'}$  must be made.

The coefficients  $w_{\alpha\beta}^{r,t}$  are complicated for the inhomogeneous case, and so for simplicity in the following we assume the sheet is in a homogeneous space  $\varepsilon_2 = \varepsilon_1 = \varepsilon$ ,  $\mu_2 = \mu_1 = \mu$ . When region 2 differs from region 1, the only change is in the functions (3.18)-(3.19) provided below. Concentrating on the field in the upper-half space,  $w_{\alpha\beta}^r = N_{\alpha\beta}(q_x, q_z)/D(q_x, q_z)$ , where

$$D(q_x, q_z) = 2\sigma_{xx}(k^2 - q_x^2) + 2\sigma_{zz}(k^2 - q_z^2) - i4\frac{k}{\eta}p \left( 1 + \frac{1}{4}\eta^2\sigma_{xx}\sigma_{zz} \right), \quad (3.18)$$

and

$$\begin{aligned}N_{yy}(q_x, q_z) &= -p^2(\sigma_{xx} + \sigma_{zz}) - ipk\eta\sigma_{xx}\sigma_{zz}, \\ N_{xy}(q_x, q_z) &= iq_x p(\sigma_{xx} - \sigma_{zz}), \\ N_{zy}(q_x, q_z) &= -iq_z p(\sigma_{xx} - \sigma_{zz}),\end{aligned}\quad (3.19)$$



where  $p = \sqrt{q_x^2 + q_z^2 - k^2}$ , and  $\eta = \sqrt{\mu/\epsilon}$ . Then, e.g., for the vertical field in the upper half-space,

$$E_y = \frac{1}{i\omega\epsilon} \left( k^2 + \frac{\partial^2}{\partial y^2} \right) (g_{yy}^p(\mathbf{r}, \mathbf{r}') + g_{yy}^r(\mathbf{r}, \mathbf{r}')) + \frac{1}{i\omega\epsilon} \left( \frac{\partial^2}{\partial x \partial y} g_{xy}^r(\mathbf{r}, \mathbf{r}') + \frac{\partial^2}{\partial z \partial y} g_{zy}^r(\mathbf{r}, \mathbf{r}') \right). \quad (3.20)$$

and other field components are obtained from (3.9).

### 3.3.2 Directional Properties of SPPs on 2D Surfaces

Before considering complex-plane evaluation of the Green's functions, we describe some basic properties of SPPs on hyperbolic 2D surfaces [65], [92]-[93]. In order to understand the behavior of surface waves it is instructive to inspect the plasmon dispersion relation  $D(q_x, q_z) = 0$  arising from (3.18), the denominator of the Green's function. As we show later, in the general case SPPs are obtained as a mixture of TE and TM modes, and, moreover, it is not possible to solve for the wavevector eigenmodes  $q_x$  and  $q_z$  from the single complex-valued equation (3.18). Furthermore, unlike for isotropic surfaces, for an anisotropic medium the direction of energy transfer is defined by the group velocity in the medium [94],  $\nabla_{\mathbf{q}}\omega(\mathbf{q})$ , and does not coincide with the direction of the plasmon wavevector  $\mathbf{q}$ . In our case, the dispersion relation for surface plasmons is complicated and the group velocity can not be calculated analytically. However, we can estimate the direction of plasmon propagation geometrically by examining the plasmon's equifrequency contours,  $\omega(\mathbf{q}) = \text{const}$ . As the group velocity is a gradient of frequency with respect to wavevector, the direction of plasmon energy flow is necessary orthogonal to the equifrequency contours.

Assuming that the conductivity is purely imaginary and lossless,  $\sigma_{jj} = i\sigma''_{jj}$ ,  $j = x, z$ , and that  $q_x, q_z \gg k$ , the zeros of (3.18) can be approximated as the solution of

$$\frac{q_x^2}{\sigma''_{zz}} + \frac{q_z^2}{\sigma''_{xx}} = 2p\omega \left( \frac{\epsilon_0}{\sigma''_{xx}\sigma''_{zz}} - \frac{\mu_0}{4} \right). \quad (3.21)$$

Although the right side varies with  $\mathbf{q}$ , because of the square-root  $p$  the variation is less than the left side, and we can approximate the right side as being constant in wavenumber. Then, in the hyperbolic case ( $\sigma''_{xx} \cdot \sigma''_{zz} < 0$ ) the EFS is a hyperbola, as shown in Fig. 3.5 for two values of surface conductivity (blue lines:  $\sigma_{xx} = 0.003 + 0.25i$  mS and  $\sigma_{zz} = 0.03 - 0.76i$  mS; see also Fig. 3.14b, and green lines:  $\sigma_{xx} = 1.3 + 16.9i$  mS and  $\sigma_{zz} = 0.4 - 9.2i$  mS; results in Fig. 3.5 were obtained by solution of the full dispersion relation (3.18).

The hyperbola asymptotes are defined by  $q_z = \pm q_x \sqrt{|\sigma''_{xx}/\sigma''_{zz}|}$ . Taking into account that a dipole excites many plasmons with different  $\mathbf{q}$ , and that the normal to all the points on the hyperbola point in the same direction for a given sign of  $q_x$ , we expect a narrow plasmon beam in the direction of energy flow on a hyperbolic metasurface. For example, the asymptotes of the blue hyperbola in Fig. 3.5 have an angle 30 degrees with respect to the  $x$  axis, and thus the normal to the hyperbola, i.e., the group velocity, is 60 degrees with respect to the  $x$  axis, as indicated in the figure, which is in very good

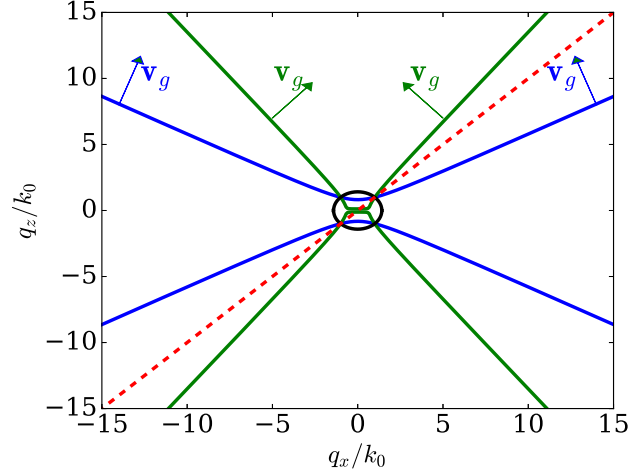


Figure 3.5: Equifrequency surfaces for metasurface having  $\sigma_{xx} = 0.003 + 0.25i$  mS and  $\sigma_{zz} = 0.03 - 0.76i$  mS (blue hyperbola; see also Fig. 3.14b), and  $\sigma_{xx} = 1.3 + 16.9i$  mS and  $\sigma_{zz} = 0.4 - 9.2i$  mS (green hyperbola; see also Fig. 3.14c). For comparison, the isotropic case for  $\sigma_{xx} = \sigma_{zz} = 0.03 - 0.76i$  mS (black circle) is also shown. The red dashed line merely denotes 45 degrees with respect to the  $x$  axis for guidance.

agreement with the numerical results presented in Fig. 3.14b. Similar comments apply to the green hyperbola and Fig. 3.14c. For comparison, in Fig. 3.5 we also presented the hypothetical isotropic case for which the equifrequency contour is a circle, and thus energy does not have a preferential direction.

In the non-hyperbolic (purely anisotropic) case ( $\sigma''_{xx}, \sigma''_{zz} > 0$ ), (3.21) is the equation for an ellipse in  $\mathbf{q}$ -space with the axis oriented along  $q_x$  and  $q_z$ . The length of the ellipse's principal axes along  $q_x$  and  $q_z$  is proportional to  $\sigma''_{zz}$  and  $\sigma''_{xx}$ , respectively. Thus, the EFS has a quasi-elliptic form elongated along the direction of the smallest component of the conductivity tensor, the degree of elongation being set by the ratio of  $\sigma''_{xx}$  and  $\sigma''_{zz}$ . Later, in Fig. 3.16 we consider black phosphorous having  $\sigma_{xx} = 0.0008 - 0.2923i$  mS and  $\sigma_{zz} = 0.0002 - 0.0658i$  mS. Due to the strong elongation of the EFS along the  $q_z$ -axis, the group velocity points approximately along the  $q_x$  axis, such that the SPP carries energy along the  $x$  crystallographic axis (see, e.g., Fig. 3.16).

### 3.3.3 Complex-Plane Analysis in the $q_x$ -Plane

In the case of an isotropic material the coefficients  $w_{\alpha\beta}$  only depend on  $q^2 = q_x^2 + q_z^2$ , leading to

$$g_{\alpha\beta}^r(\mathbf{r}, \mathbf{r}') = \frac{1}{2\pi} \int_0^\infty w_{\alpha\beta}(q) \frac{e^{-p(y+y')}}{2p} J_0(q\rho) q dq = \frac{1}{2\pi} \int_{-\infty}^\infty w_{\alpha\beta}(q) \frac{e^{-p(y+y')}}{4p} H_0^{(2)}(q\rho) q dq \quad (3.22)$$

where  $J_0$  and  $H_0^{(2)}$  are the usual zeroth-order Bessel and Hankel functions, respectively. These two forms can be converted one to another using the relation  $J_0(\alpha) = \frac{1}{2} [H_0^{(1)}(\alpha) + H_0^{(2)}(\alpha)]$ ,  $H_0^{(2)}(-\alpha) = -H_0^{(1)}(\alpha)$ . In this case, such as occurs for graphene without a magnetic bias, the pole of  $w_{\alpha\beta}$  leads to a simple analytical form for the SPP field [16]. However, this is not the case for an anisotropic

surface. Since the two-dimensional Sommerfeld integral can be time-consuming to evaluate, writing

$$g_{\alpha\beta}^r(\mathbf{r}, \mathbf{r}') = \frac{1}{(2\pi)} \int_{-\infty}^{\infty} dq_z e^{-iq_z(z-z')} f_{\alpha\beta}(q_z) \quad (3.23)$$

where

$$f_{\alpha\beta}(q_z) = \frac{1}{(2\pi)} \int_{-\infty}^{\infty} w_{\alpha\beta}(q_x, q_z) \frac{e^{-p(y+y')}}{2p} e^{-iq_x(x-x')} dq_x \quad (3.24)$$

the ‘‘inner’’ integral  $f_{\alpha\beta}(q_z)$  can be evaluated as an SPP residue term (discrete spectral component) and branch cut integral representing the radiation continuum into space (note that the choice of ‘‘inner’’ and ‘‘outer’’ integrals is arbitrary). The branch cut in the  $q_x$  plane is the usual hyperbolic branch cut associated with the branch point due to  $p = \sqrt{q_x^2 + q_z^2 - k^2}$ , occurring at  $q_x = \pm\sqrt{k^2 - q_z^2}$  [100]. Then,

$$f_{\alpha\beta}(q_z) = -iw_{\alpha\beta}^{spp}(q_{xp}, q_z) \frac{e^{-p(q_{xp})(y+y')}}{2p(q_{xp})} e^{-iq_{xp}(x-x')} + \frac{1}{2\pi} \int_{bc} w_{\alpha\beta}(q_x, q_z) \frac{e^{-p(y+y')}}{2p} e^{-iq_x(x-x')} dq_x \quad (3.25)$$

where the first term is the residue contribution and ‘‘bc’’ indicates the hyperbolic branch-cut contour. In (3.25),  $w^{spp}(q_{xp}, q_z) = N(q_{xp}, q_z)/D'(q_{xp}, q_z)$ ,  $D'(q_x, q_z) = \frac{\partial}{\partial q_x} D(q_x, q_z)$ , and where  $q_{xp}$  is the root of  $D(q_x, q_z) = 0$  for a given  $q_z$ ,

$$q_{xp}(q_z) = \pm \sqrt{\frac{-B \pm \sqrt{B^2 - 4AC}}{2A}} \quad (3.26)$$

where  $A = \sigma_{xx}^2$ ,  $B = \frac{1}{4}\alpha^2 - 2k^2\sigma_{xx}^2 + 2(q_z^2 - k^2)\sigma_{xx}\sigma_{zz}$ ,  $C = k^4(\sigma_{xx} + \sigma_{zz})^2 + q_z^2(q_z^2 - 2k^2)\sigma_{zz}^2 - 2k^2q_z^2\sigma_{xx}\sigma_{zz} + \frac{1}{4}\alpha^2(q_z^2 - k^2)$ , and  $\alpha = (4k/\eta)(1 + \frac{1}{4}\eta^2\sigma_{xx}\sigma_{zz})$ . When the SPP field is the dominant contribution to the response, which is the usual regime for plasmonics where the field close to the interface,  $(y, y' \ll \lambda)$  is of interest, the branch cut term can be ignored and the residue term suffices for the calculation of  $f(q_z)$ ,

$$f_{\alpha\beta}^{SPP}(q_z) \approx -iw_{\alpha\beta}^{spp}(q_{xp}, q_z) \frac{e^{-p(q_{xp})(y+y')}}{2p(q_{xp})} e^{-iq_{xp}(x-x')}, \quad (3.27)$$

which considerably speeds up evaluation of the Green’s function (rendering it one-dimensional). Since  $q_{xp}$  is the propagation constant along the  $x$ -axis, the  $\mp$  outside the square root in (4.28) indicates forward/backward propagation, whereas the inner  $\pm$  sign choice governs propagation of different modes (only one of which will propagate). Assuming  $(x - x') > 0$ , the term  $e^{-iq_{xp}(x-x')}$  necessitates that  $\text{Im}(q_{xp}) < 0$  to have a decaying wave traveling away from the source along the  $x$ -axis.

As an example, we consider an anisotropic surface with  $\sigma_{xx} = 0.02 + 0.57i$  mS and  $\sigma_{zz} = 0.02 - 0.57i$  mS. As discussed later in this chapter, such a conductivity tensor can be physically realized by an array of densely packed graphene strips at terahertz and near infrared frequencies. Fig. 3.6 compares

$f_{yy}(q_z)$  obtained numerically by performing the integral (3.23) and obtained by using the residue term only, (3.27). The source is located at  $y' = \lambda/50$ , very near the surface, and radiating at frequency 10 THz. Clearly, in the SPP regime the residue provides the dominant component of the response, and the branch cut integral can be ignored. Although not shown, for source or observation points relatively far from the surface, the branch cut integral is important, and can be the dominant contribution to the scattered field.

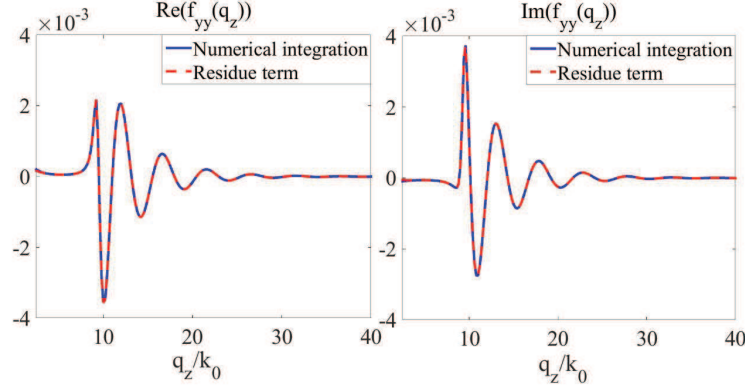


Figure 3.6: Real and imaginary parts of  $f_{yy}(q_z)$  obtained numerically, (4.62), and using the residue term (3.27) for an array of graphene strips at  $f = 10$  THz. The source is  $\lambda/50$  above the surface, and  $x = 0.2\lambda$ .

In the following we are interested in surfaces that provide a strong reactive and low-loss response,  $\text{Im}(\sigma_{\alpha\alpha}) \gg \text{Re}(\sigma_{\alpha\alpha})$ . In addition to this inequality,  $\text{Im}(\sigma_{\alpha\alpha})$  must not be too small [101]. The ability of a surface to support a strong SPP depends on the ratio of the branch cut term (space radiation spectra) to the residue (SPP) term in the inner integral (3.25). In Fig. 3.7 we assume a general hyperbolic form  $\sigma_{xx} = \alpha\sigma_0(0.01 + i)$  and  $\sigma_{zz} = 0.1\sigma_{xx}^*$  where  $\sigma_0 = e^2/4\hbar$  is the conductance quantum,  $e$  is the electron charge, and  $*$  indicates complex conjugation. We assume that losses are relatively small, and use  $\alpha$  in order to vary the magnitude of the conductivity.

It is clearly shown in Fig. 3.7 that for conductivity values smaller than the conductance quantum, the radiation spectra is dominant (in the limit that  $|\sigma| \rightarrow 0$ , the surface vanishes and the entire response is the radiation continuum produced by a source in free space). We have found that conductivity values on the order of the conductance quantum are somewhat borderline; an SPP can exist, although it may not be strongly dominant over the branch cut continuum for small  $q_z$ . Conductivities an order of magnitude or more above the conductance quantum provide a very strong SPP response in which the branch cut contribution is negligible except exceedingly close to the source.

For large  $q_z$  compared to  $k$ , (3.26) becomes

$$q_{xp}(q_z) = q_z \sqrt{-\frac{\sigma_{zz}}{\sigma_{xx}}}. \quad (3.28)$$

The SPP direction of propagation on the 2D anisotropic surface is easily determined as  $\tan^{-1}(\frac{q_{xp}}{q_z})$ ,

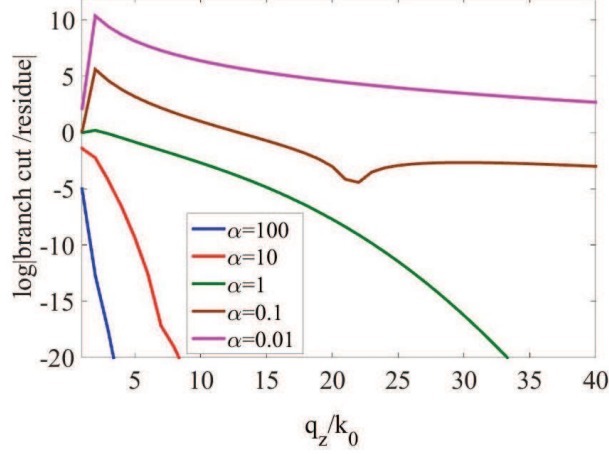


Figure 3.7: Ratio of the branch cut and residue terms in (3.25),  $\sigma_{xx} = \alpha\sigma_0(0.01+i)$ ,  $\sigma_{zz} = 0.1\sigma_{xx}^*$ ,  $\sigma_0 = e^2/4\hbar$ . Source is positioned  $\lambda/50$  above the surface,  $f = 10$  THz, and  $x = 0.2\lambda$ .

and using (3.28) the angle of propagation with respect to the  $z$ -axis is simply

$$\phi = \tan^{-1} \sqrt{-\frac{\sigma''_{zz}}{\sigma''_{xx}}}, \quad (3.29)$$

where  $\sigma'' = \text{Im}(\sigma)$ . Although the conductivities are complex-valued, for the low-loss cases of interest we can estimate the real angle  $\phi$  by only considering their imaginary parts. Therefore, in the anisotropic hyperbolic case the SPP is directed along a specific angle. For the isotropic case ( $\sigma_{xx} = \sigma_{zz}$ ) this does not occur (and (3.29) does not apply), since in this case  $q_{xp}^2 + q_z^2 = q_p^2$ , where  $q_p$  is the radial in-plane wavenumber. If we measure the angle  $\phi$  relative to the positive  $z$ -axis, then at each point in the plane of the surface we have  $x = \rho \sin \phi$ ,  $z = \rho \cos \phi$ ,  $q_{xp} = q_p \sin \phi$  and  $q_z = q_p \cos \phi$ . For a source at the origin,

$$e^{-i\mathbf{q}\cdot(\mathbf{r}-\mathbf{r}')} = e^{-i(q_{xp}x+q_zz)} = e^{-iq_p\rho(\cos^2\phi+\sin^2\phi)} = e^{-iq_p\rho}, \quad (3.30)$$

which  $e^{-iq_p\rho}$  describes a SPP wave that is radially propagating along all directions in the plane of the surface. However, in the anisotropic case for large  $q_z$ ,

$$e^{-i\mathbf{q}\cdot(\mathbf{r}-\mathbf{r}')} = e^{-i(q_{xp}x+q_zz)} = e^{-i(q_z\sqrt{-\frac{\sigma_{zz}}{\sigma_{xx}}}x+q_zz)} = e^{-iq_z\rho(\sqrt{-\frac{\sigma_{zz}}{\sigma_{xx}}}\sin\phi+\cos\phi)}, \quad (3.31)$$

and the maximum of  $(\sqrt{-\frac{\sigma_{zz}}{\sigma_{xx}}}\sin\phi+\cos\phi)$  determines the angle at which the SPP is directed. It can be simply shown that this angle is (3.29). This leads to the conclusion that hyperbolic anisotropy, in contrast to the isotropic case, results in a directed SPP, as expected.

As a function of  $\sigma$ , there are different dispersion scenarios for SPP propagation. The usual elliptic case is obtained when both imaginary parts of the conductivity have the same sign (inductive when  $\text{Im}(\sigma_{xx,zz}) < 0$ , capacitive otherwise). A graphene sheet with dominant intra-band conductivity term

with  $\text{Im}(\sigma_{xx}) = \text{Im}(\sigma_{zz}) < 0$  is a natural example of an elliptic isotropic sheet that can support a TM omni-directional SPP. The hyperbolic case occurs when the sign of the imaginary parts of the conductivity components are different. As discussed later, both a graphene strip metasurface (potentially, metal strips as well) and natural black phosphorus can provide a hyperbolic 2D surface. In this case, as shown in (3.29) and (3.31), energy propagation is focused along specific directions governed by the conductivity components [65].

### 3.3.4 Approximation of the Outer Integral Using Stationary Phase, and Exact Evaluation Using the Continuous Spectrum

Although the SPP field can be evaluated from a numerical 1D integral, (3.23) with (3.27), it is useful to consider other methods of evaluation that are more computationally rapid, and which lead to physical insight into the problem.

### 3.3.5 Stationary Phase Evaluation of the Outer Integral

The “outer” integral (3.23) using (3.27) can be approximated by the well-known method of stationary phase [102]. In particular, an analysis similar to that needed here was performed in [103], where the inner integral is approximated as a residue (ignoring the branch cut contribution, as we do here), and the outer integral is evaluated using SP. Regarding computation of the outer integral, although it seems difficult to show analytically because of the complicated expression (3.26) for the pole  $q_{xp}(q_z)$ , numerical tests show that  $\text{Re}(q_{xp}^2 + q_z^2 - k^2) > 0$  for small values of  $q_z$ . Therefore, no leaky waves are encountered for typical parameter values.

Stationary phase evaluation of (3.23) with (3.27), assuming  $\rho \gg (y + y')$ , results in, to first order,

$$g_{\alpha\beta}^r(\mathbf{r}, \mathbf{r}') \simeq \sqrt{\frac{e^{-i\frac{\pi}{2}}}{2\pi\gamma''(q_s)}} w_{\alpha\beta}^{spp}(q_s) \frac{e^{-p(q_s)(y+y')}}{2p(q_s)} e^{-i\gamma(q_s)} \quad (3.32)$$

where  $w_{\alpha\beta}^{spp}(q_s) = w_{\alpha\beta}^{spp}(q_{xp}(q_s), q_s)$ ,  $p(q_s) = p(q_{xp}(q_s), q_s)$ , and  $\gamma(q_s) = -(q_{xp}(q_s)(x - x') + q_z(z - z'))$ , where  $q_s$  is the root of  $d\gamma/dq_z = 0$ , which can be obtained as the root of a fourth-order polynomial, or via numerical root search. See [103] for a ray-optical interpretation of the SP result in anisotropic media.

Here we provide a comparison between the SP result (3.32) and numerical (real-line) computation of the outer integral (3.23). Figure 3.8 shows the SP result (red) and numerical integration result (blue) for (a)  $\sigma_{xx} = 0.02 + 0.57i$  mS,  $\sigma_{zz} = 0.02 - 0.57i$  mS and (b)  $\sigma_{xx} = 0.003 + 0.25i$  mS,  $\sigma_{zz} = 0.03 - 0.76i$  mS, both using  $\rho = 0.4\lambda$ ,  $\rho/(y + y') = 80$ . It can be seen that excellent agreement is found for the location of the beam angle, although away from the beam maximum there is some disagreement.

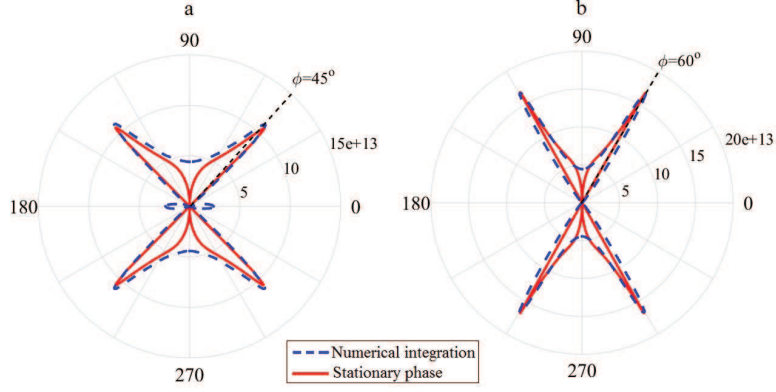


Figure 3.8: The electric field  $E_y$  obtained by stationary phase result (3.32) (red) and numerical integration (3.23) (blue) for (a)  $\sigma_{xx} = 0.02 + 0.57i$  mS,  $\sigma_{zz} = 0.02 - 0.57i$  mS and (b)  $\sigma_{xx} = 0.003 + 0.25i$  mS,  $\sigma_{zz} = 0.03 - 0.76i$  mS,  $\rho = 0.4\lambda$ ,  $\rho/(y + y') = 80$ ,  $f = 10$  THz.

### 3.3.6 Complex-Plane Analysis in the $q_z -$ Plane

Although the SPP field can be evaluated to first order using the SP approximation for  $\rho/(y + y') \gg 1$ , it is useful to consider complex-plane analysis of the “outer” integral over  $q_z$ , which turns out to involve only continuous spectrum. This method is theoretically exact, and is valid for all field and source points. Further, it does not require finding the  $q_z$  root, but does require knowing the  $q_z$ -plane branch points and cuts, which, themselves, lead to considerable physical insight.

The Weierstrass preparation theorem shows that the complex function  $f_{\alpha\beta}^{\text{SPP}}(q_z)$ , (3.27), has no poles, only branch points. Regarding the two complex planes  $q_x - q_z$ , a sufficient condition in order to have a branch point in the  $q_z -$  plane is that [104], [105]

$$D(q_x, q_z) = \frac{\partial}{\partial q_x} D(q_x, q_z) = 0 \quad (3.33)$$

with  $\delta = \frac{\partial}{\partial q_z} D(q_x, q_z) \frac{\partial^2}{\partial q_z^2} D(q_x, q_z) \neq 0$ . Although (3.33) represents a second-order zero of  $D$ , in the  $q_z$ -plane these points are not poles, and are also not necessarily  $q_z$ -plane branch points without the condition  $\delta \neq 0$ . These branch points are associated with modes in the  $q_x$ -plane merging at a certain value of  $q_z$ , forming a second-order zero of  $D$ . Thus, the pair  $(q_x, q_z)$  satisfying (3.33) and  $\delta \neq 0$  represent poles in the  $q_x$  plane and branch points in the  $q_z$  plane (the branch in the  $q_z$  plane controls the merging of poles in the  $q_x$  plane). Another possible branch point in the  $q_z$  plane is associated with the square-root in  $p$ . The fact that a pole in one spectral plane results in a branch point in another spectral plane was recognized in studies of microstrip and other integrated waveguides [95, 96]. It is also worthwhile to note that the asymptotic methods for branch cut evaluation described in [102] do not work here. To use those formulas the branch cut integral must be dominated by the branch point, that is, by the section of the integral in the vicinity of the branch point. This is not the case for the anisotropic problem, where we have found that sections of the branch cut integral far from the branch point can contribute substantially.

### 3.3.7 P-type Branch Point in the $q_z$ -Plane

For the isotropic case,  $p = \sqrt{q^2 - k^2}$  and the p-type branch point occurs at  $q = \pm k$ , resulting in the usual hyperbolic branch cuts in the  $q$ -plane [100]. In this case,  $q_x^2 + q_z^2 = q_p^2$  is a constant and  $q_z = \sqrt{k^2 - q_x^2}$  leads to branch points at  $q_x = \pm k$ . However, for the residue,  $q_p^2 = q_{xp}^2(q_z) + q_z^2$  is a constant in  $q_z$  and so we never have  $q_p = k$  for any  $q_z$ , and so there is no p-type BP in the  $q_z$  - plane for the SPP for the isotropic case. However, for anisotropic media  $q_{xp}^2(q_z) + q_z^2$  is not generally a constant, and so there can be a ‘‘p-type’’ BP in the  $q_z$ -plane, where  $p = \sqrt{q_{xp}^2(q_z) + q_z^2 - k^2} = 0$ , although this will not occur at  $q_z = k$  unless  $q_{xp}(k) = 0$ . In any event, since this branch cut relates to radiation into space, for the SPP we can ignore this contribution to the SPP field.

Introducing the notation that  $(q_x^{(n)}, q_z^{(n)})$  represents the pair of spectral values that satisfy the conditions for a branch point/pole pair, (3.33) and  $\delta \neq 0$ , since the residue term already satisfies  $D(q_{xp}, q_z) = 0$ , we can find branch points in the  $q_z$ -plane from  $\frac{\partial}{\partial q_x} D(q_{xp}(q_z), q_z) = 0$ ,

$$\left( \sigma_{xx} + \frac{ik/\eta}{\sqrt{q_{xp}^2 + q_z^2 - k^2}} \left( 1 + \frac{1}{4}\eta^2 \sigma_{xx} \sigma_{zz} \right) \right) q_{xp}(q_z) = 0. \quad (3.34)$$

As we will show later, these branch points have a significant role in the analysis of the SPP. Because of their importance, we categorize them into two groups, type-0 and type-1 branch points.

### 3.3.8 Type-0 Branch Point in the $q_z$ -Plane

First we define type-0 branch points as those values of  $q_z$  for which  $q_{xp}(q_z) = 0$  in (3.34); i.e., the merging of the forward and backward modes (associated with different signs in the outer square-root in (4.28)) in the  $q_x$ -plane at a certain value of  $q_z$  [105], given by

$$q^{(+0)} = q_z^{\text{TM}} = k \sqrt{1 - \left( \frac{2}{\eta \sigma_{zz}} \right)^2} \quad (3.35)$$

$$q^{(-0)} = q_z^{\text{TE}} = k \sqrt{1 - \left( \frac{\eta \sigma_{xx}}{2} \right)^2} \quad (3.36)$$

such that the pair  $(q_x, q_z) = (0, q^{\text{TM/TE}})$  form a pole-branch-point pair. For  $\sigma_{xx} = \sigma_{zz}$  these are well-known TM and TE SPP wavenumbers, respectively (graphene is an example of such a 2D isotropic layer which can support these modes [16]). Note that for isotropic media, a vertically-polarized current source will produce only TM fields (although a horizontally-polarized source will produce both TE and TM fields even when the sheet is isotropic [100]). For an anisotropic sheet the boundary conditions cannot be satisfied assuming only one type of field.



### 3.3.9 Type-1 Branch Point in the $q_z$ -Plane

Another set of singularities in the  $q_x$ - $q_z$  plane is related to the point in the  $q_z$ -plane where modes  $q_{xp}$  associated with different signs in the inner square-root in (4.28) merge for  $q_{xp} \neq 0$ . These can be obtained by simultaneously solving the equations  $D(q_x, q_z) = 0$  and  $\frac{dD(q_x, q_z)}{dq_x} = 0$ , leading to

$$q_x^{(\pm 1)} = \sqrt{\frac{-k^2}{\delta\sigma} \left( \sigma_{xx} + (\sigma_{zz} \mp 2\sigma_{xx}) \frac{(1 + \frac{1}{4}\eta^2\sigma_{xx}\sigma_{zz})^2}{\eta^2\sigma_{xx}^2} \right)} \quad (3.37)$$

$$q_z^{(\pm 1)} = \sqrt{-(q_x^{(\pm 1)})^2 + k^2 \left( 1 - \frac{(1 + \frac{1}{4}\eta^2\sigma_{xx}\sigma_{zz})^2}{\eta^2\sigma_{xx}^2} \right)} \quad (3.38)$$

where  $\delta\sigma = \sigma_{zz} - \sigma_{xx}$ , such that  $(q_x, q_z) = (q_x^{(\pm 1)}, q_z^{(\pm 1)})$  form a pole-branch-point pair.

### 3.3.10 Branch Cut Analysis in the $q_z$ -Plane

Using the SPP field (3.27) and performing the outer integration, the Green's function is

$$g_{\alpha\beta}^r = \frac{-i}{2\pi} \int_{-\infty}^{+\infty} w'_{\alpha\beta}(q_{xp}, q_z) \frac{e^{-p(y+y')}}{2p} e^{-iq_{xp}(x-x')} e^{-iq_z(z-z')} dq_z. \quad (3.39)$$

Assuming  $(z - z') > 0$ , due to the term  $e^{-iq_z(z-z')}$  the contour can be closed in the lower half plane of the  $q_z$  - plane, leading to

$$g_{\alpha\beta}^r \approx \frac{-i}{2\pi} \int_{bc} w'_{\alpha\beta}(q_{xp}, q_z) \frac{e^{-p(y+y')}}{2p} e^{-iq_{xp}(x-x')} e^{-iq_z(z-z')} dq_z \quad (3.40)$$

where the branch cut integral is over all branch cuts. Also, from the term  $e^{-iq_{xp}(x-x')}$  it is clear that for  $x - x' \geq 0$  then only when  $\text{Im}(q_{xp}) \leq 0$  do we obtain an SPP that decays away from the source. Therefore, we have in the  $q_z$  - plane two Riemann sheets (as mentioned previously, neglecting the  $p$ -type branch point, which would introduce another two sheets; here we simply enforce  $\text{Re}(p) > 0$ ), the top (proper) sheet where  $\text{Im}(q_{xp}) \leq 0$  and the bottom sheet where  $\text{Im}(q_{xp}) \geq 0$ , for  $x - x' \geq 0$ . Those values of  $q_z$  that lead to  $\text{Im}(q_{xp}) = 0$  determine the branch cut trajectory which separates the proper from improper Riemann sheets.

Typically, branch cut trajectories to separate certain Riemann sheets can be analytically determined from the functional dependence of the multi-valued function that defines the branch point. However, for anisotropic surfaces the form of  $q_{xp}$  is too complicated to determine a simple equation for the branch cut for  $\text{Im}(q_{xp}) = 0$ . As an example, Fig. 3.9-a shows the branch cuts for  $\text{Im}(q_{xp}) = 0$  obtained by plotting  $\text{Im}(q_{xp})$  for an array of graphene strips (will be addressed later in this chapter) in the hypothetical lossless case (i.e., ignoring the real parts of the conductivities) at 10 THz. Fig. 3.9-b shows a close-up near the Im axis, and Fig. 3.9-c shows the properly-cut  $q_z$  - plane for the lossless case. It can be seen that for the considered frequency the TM branch point leads to a branch

cut starting at  $q_z^{\text{TM}}$  and going horizontally to infinity, and the TE branch point  $q_z^{\text{TE}}$  and the branch point  $q_z^{(-1)}$  are connected by a branch cut. The branch point  $q_z^{(+1)}$  is on the improper Riemann sheet (not shown).

Insight into the correct branch cut can be obtained from a large  $q_z$  approximation. From (3.28), for a lossy 2D surface  $\sigma_{xx} = \sigma'_{xx} + i\sigma''_{xx}$  and  $\sigma_{zz} = \sigma'_{zz} + i\sigma''_{zz}$  then the branch cut trajectory is along  $q_z$  values such that

$$\text{Im}(iq_z \sqrt{\sigma'_{zz}\sigma'_{xx} + i\sigma''_{zz}\sigma'_{xx} - i\sigma''_{xx}\sigma'_{zz} + \sigma''_{xx}\sigma''_{zz}}) = 0. \quad (3.41)$$

For a lossless surface,  $\sigma'_{xx} = \sigma'_{zz} = 0$ , leading to

$$\text{Im}(iq_z \sqrt{\sigma''_{xx}\sigma''_{zz}}) = 0, \quad (3.42)$$

such that if  $\sigma''_{xx}\sigma''_{zz} > 0$  the BC is along  $\text{Im}(q_z)$ , and if  $\sigma''_{xx}\sigma''_{zz} < 0$  the BC is along  $\text{Re}(q_z)$ , in agreement with the numerically-determined contours.

The branch cut integrals can be viewed as a continuous superposition of modes. The BP  $q_z^{\text{TM}}$  is associated with the pair  $(q_x, q_z) = (0, q_z^{\text{TM}}) = (0, 9.3)k$  for the numerical example considered), and along the branch cut, as  $\text{Re}(q_z)$  increases,  $\text{Re}(q_x) = \text{Re}(q_{xp})$  also increases from zero, and the resulting continuum summation of pair values synthesis the beam. Similar comments apply to the branch cut between  $q_z^{\text{TE}}$  and  $q_z^{-1}$  (between  $q_z = 1.005k$  and  $-3.22ik$  in the numerical example considered).

The lossy case is shown in Fig. 3.10; the branch cut trajectory deflects a bit from the lossless case, but for low-loss surface the lossless BC contour is sufficient.

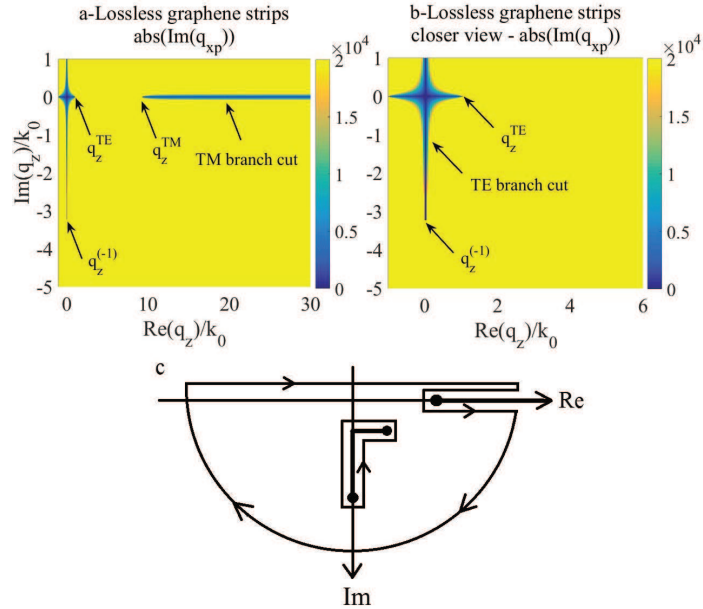


Figure 3.9: a,b: Branch cut contours  $\text{Im}(q_{xp}) = 0$  determined from a plot of the absolute value of  $\text{Im}(q_{xp})$  for a lossless model of a graphene strip array at 10 THz ( $\sigma'_{xx} = \sigma'_{zz} = 0$ ,  $\sigma''_{xx} = 0.57i$  mS,  $\sigma''_{zz} = -0.57i$  mS). The branch point locations are  $q_z^{\text{TE}}/k = 1.005$ ,  $q_z^{\text{TM}}/k = 9.3$ ,  $q_z^{(-1)}/k = -3.22i$ . c. Integration contour in the  $q_z$  - plane showing branch points (dots) and branch cuts (thick lines).

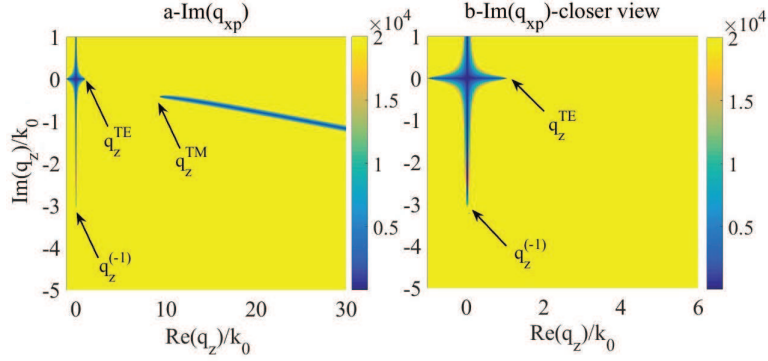


Figure 3.10: Branch cut contours  $\text{Im}(q_{xp}) = 0$  determined from a plot of the absolute value of  $\text{Im}(q_{xp})$  for a lossy model of a graphene strip array at 10 THz with  $\sigma_{xx} = 0.02 + 0.57i$  mS and  $\sigma_{zz} = 0.02 - 0.57i$  mS.

As a common special case, for an inductive isotropic surface such as graphene in the far-infrared,

$$\sigma_{xx} = \sigma_{zz} = \frac{-ie^2 k_B T}{\pi \hbar^2 (\omega - i2\Gamma)} \left( \frac{\mu_c}{k_B T} + 2 \ln \left( 1 + e^{-\frac{\mu_c}{k_B T}} \right) \right). \quad (3.43)$$

Here we consider graphene at  $T = 300$  K,  $\mu_c = 0.5$  eV and  $f = 20$  THz. In this case the TE related branch point is at  $q_z^{\text{TE}} = k(1.0039 + 0.0001i)$ , and so is not implicated in the lower-half-plane closure, consistent with the surface being inductive (no TE mode is supported). Since only TM branch points occur, only a TM mode exists, and the TM related BP occurs at  $q_z^{\text{TM}}/k = (11.3706 - 0.2088i)$ . The two other type-1 branch points move to infinity as the surface becomes isotropic, and therefore the branch cut extends down the entire imaginary axis (therefore for both the isotropic and anisotropic cases there is a branch cut between  $q_z^{\text{TM}}$  and  $q_z^{-1}$ ). Fig. 3.20 shows a surface plot of  $\text{Im}(q_{xp})$  in the  $q_z -$  plane.

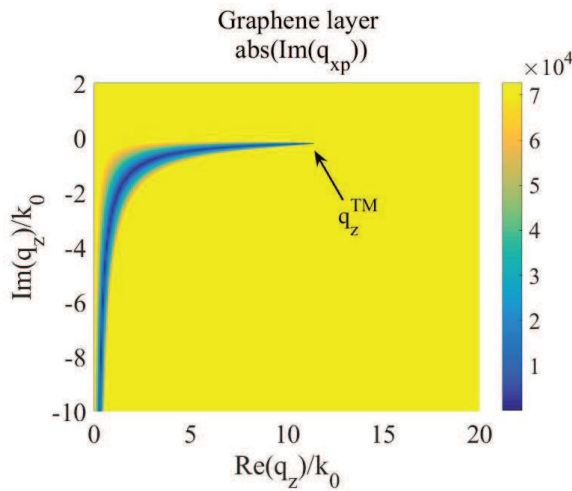


Figure 3.11: Branch cut contour  $\text{Im}(q_{xp}) = 0$  determined from a plot of the absolute value of  $\text{Im}(q_{xp})$  for graphene with  $\mu_c = 0.5$  eV at  $T = 0$  K and  $f = 20$  THz.

For isotropic and inductive graphene only a TM mode can propagate, and so the contribution

is from the TM-related branch point and associated cut, as expected. For the graphene strip array anisotropic case, the hybrid nature of the modes supported by such a surface involve both TE and TM-related branch points, and, in contrast to the isotropic case, three branch points contribute to the field.

### 3.3.11 Conductivity and Its Effect on Branch Points and SPP Confinement

Analytically, it can be shown that both type-1 branch points  $q_z^{(\pm 1)}$  can be connected to a TE or TM branch point, depending on the conductivity value. Two cases are of particular interest, small conductivity values,  $(\text{Im}(\sigma_{xx/zz})\eta)^2 \ll 1$ , and large conductivity values,  $(\text{Im}(\sigma_{xx/zz})\eta)^2 \gg 1$ . For small conductivity values, from (3.35)-(3.36) we have

$$q_z^{TM} = k\sqrt{1 - \left(\frac{2}{\eta\sigma_{zz}}\right)^2} \rightarrow (\eta\sigma_{zz})^2 = \frac{4}{1 - \left(\frac{q_z^{TM}}{k}\right)^2} \quad (3.44)$$

$$q_z^{TE} = k\sqrt{1 - \left(\frac{\eta\sigma_{xx}}{2}\right)^2} \rightarrow \frac{1}{(\eta\sigma_{xx})^2} = \frac{1}{4} \frac{1}{1 - \left(\frac{q_z^{TE}}{k}\right)^2}. \quad (3.45)$$

Making these replacements in (5.10)-(3.38) and using the fact that for small conductivity like in our previous numeric example ( $\sigma_{xx} = 0.02 + 0.57i$  mS and  $\sigma_{zz} = 0.02 - 0.57i$  mS) we have  $(\text{Im}(\sigma_{xx/zz})\eta)^2 \ll 1$ , then  $|q_z^{TM}| \gg k$  and  $|q_z^{TE}| \approx k$ , and so  $|q_z^{TE}|^2 \ll |q_z^{TM}|^2$ , such that

$$q_z^{(\pm 1)} = \frac{k}{2} \sqrt{\frac{1}{1 - \left(\frac{q_z^{TE}}{k}\right)^2} \frac{\sigma_{xx} \mp 2\sigma_{xx}}{\sigma_{zz} - \sigma_{xx}}}. \quad (3.46)$$

Therefore, for small values of  $\sigma_{xx}$  and  $\sigma_{zz}$ , the type-1 branch points are governed by (and associated with) the TE branch point  $q_z^{TE}$ .

For larger values of  $\sigma_{xx}$  and  $\sigma_{zz}$  the situation is different. In this case, for  $(\text{Im}(\sigma_{xx/zz})\eta)^2 \gg 1$  we have  $|q_z^{TM}|^2 \ll |q_z^{TE}|^2$  and it can be shown that an approximate expression for the type-1 branch point is (3.46) with  $q_z^{TM}$  replacing  $q_z^{TE}$ ; the type-1 branch points are associated with the TM related branch point. As the conductivity changes from a small to a large value,  $q_z^{TE}$  and  $q_z^{TM}$  move toward each other and then cross, and eventually interchange roles. Setting (3.35) and (3.36) equal to each other, it can be shown that these type-0 branch points meet at a frequency such that  $\sigma_{xx}\sigma_{zz} = 4/\eta^2$ .

As an example of a large conductivity situation, conductivity tensor components  $\sigma_{xx} = 1.3 + 16.9i$  mS and  $\sigma_{zz} = 0.4 - 9.2i$  mS are attainable using multi-layer graphene to form the strip array. For this set of conductivities the branch points and branch cuts are shown in Fig. 3.12. As can be seen,  $q_z^{TE}$  exceeds  $q_z^{TM}$ , there is a branch cut from  $q_z^{TE}$  to infinity, a branch cut between  $q_z^{TM}$  and  $q_z^{-1}$ , and  $q_z^{-1}$  is connected to  $q_z^{TM}$ .

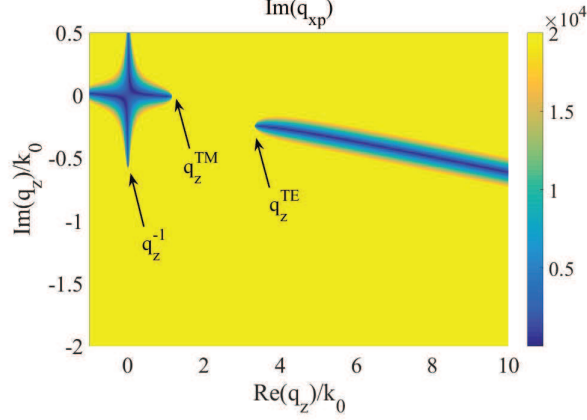


Figure 3.12: Branch cut contours  $\text{Im}(q_{xp}) = 0$  determined from a plot of the absolute value of  $\text{Im}(q_{xp})$  for a lossy model of multi-layer graphene strip at 10 THz,  $\sigma_{xx} = 1.3 + 16.9i$  mS and  $\sigma_{zz} = 0.4 - 9.2i$  mS.

### 3.3.12 Anisotropic Hyperbolic Layer (Graphene Strip Array)

A schematic of an array of graphene strips is shown in Fig. 3.13-a. This densely packed strip surface can act as a physical implementation of a metasurface at terahertz and near infrared frequencies [65, 106]. The dispersion topology of the proposed structure may range from elliptical to hyperbolic as a function of its geometrical and electrical parameters. The in-plane effective conductivity tensor of the proposed structure can be analytically obtained using an effective medium theory as [65]

$$\sigma_{zz}^{\text{eff}} = \sigma \frac{W}{L} \quad \text{and} \quad \sigma_{xx}^{\text{eff}} = \frac{L\sigma\sigma_c}{W\sigma_c + G\sigma}, \quad (3.47)$$

where  $L$  and  $W$  are the periodicity and width of the strips, respectively,  $G = L - W$  is the separation distance between two consecutive strips,  $\sigma$  is graphene conductivity (3.43) and  $\sigma_c = j \frac{\omega\epsilon_0 L}{\pi} \ln(\csc \frac{\pi G}{2L})$  is an equivalent conductivity associated with the near-field coupling between adjacent strips obtained using an electrostatic approach [107]. These effective parameters are valid only when the homogeneity condition  $L \ll \lambda_{\text{SPP}}$  is satisfied, where  $\lambda_{\text{SPP}}$  is the plasmon wavelength in the in-plane direction perpendicular to the strips ( $x$  in this case), thus leading to a homogeneous 2D metasurface. Fig. 3.13-b and c shows  $\sigma_{xx}$  and  $\sigma_{zz}$  in a wide range of frequency for a graphene strip array with graphene parameters  $\tau = 0.35$  ps,  $\mu_c = 0.33$  eV, and geometrical parameters  $W = 59$  nm and  $L = 64$  nm. As can be seen from in Fig. 3.13-b, this structure can exhibit a hyperbolic response, as well as implement a non-hyperbolic although anisotropic surface.

As was discussed, conductivity components  $\sigma_{xx} = 0.02 + 0.57i$  mS and  $\sigma_{zz} = 0.02 - 0.57i$  mS can be realized using an array of graphene strips with  $\mu_c = 0.33$  eV, strip width  $W = 59$  nm, and period  $L = 64$  nm. For this anisotropic hyperbolic surface, Fig. 3.14a shows the electric field  $E_y$ , the dominant field component, computed as a real-line integral (3.39), and as a sum of branch cut integrals (4.102); excellent agreement is found between the two methods (the branch cut integrals

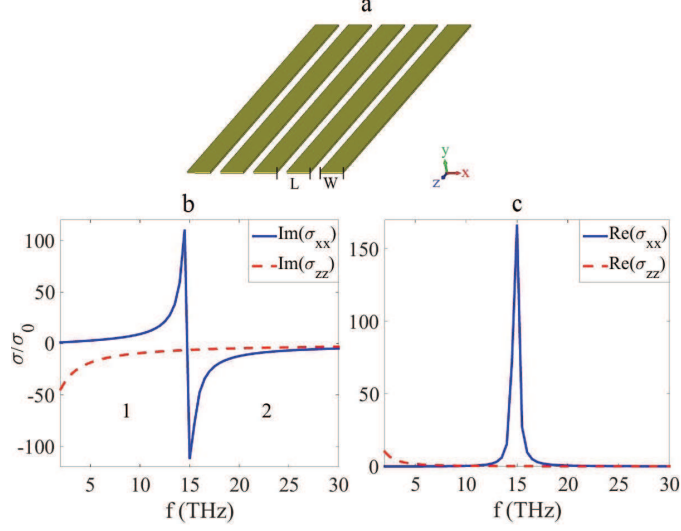


Figure 3.13: a: Array of graphene strips. b: Imaginary parts of  $\sigma_{xx}$  and  $\sigma_{zz}$  and c: real parts of  $\sigma_{xx}$  and  $\sigma_{zz}$  normalized to  $\sigma_0 = e^2/4\hbar$  for a graphene strip array with  $\tau = 0.35$  ps,  $\mu_c = 0.33$  eV,  $W = 59$  nm and  $L = 64$  nm. Region 1 is hyperbolic and region 2 is simply anisotropic

are faster to compute than the brute-force numerical integrals, but no attempt was made to optimize either integration). The branch cuts for this case are shown in Fig. 3.10. Figs. 3.14-b,c show similar agreement for different strip configurations as discussed below.

Although the direction of the beam is electronically controllable via the chemical potential, different combinations of physical parameters of the graphene strip array (width  $W$  and periodicity  $L$ ) can also be used to produce a desired beam. An optimum geometry to produce a beam in a certain direction can be found by tuning all of these parameters simultaneously.

From (3.29), in the hyperbolic regime propagation along a desired direction can be obtained if the tensor conductivity components have the proper ratio. Designing a hyperbolic metasurface to produce a beam in a desired direction (e.g., choosing the strip width and period) can be done by trial-and-error tuning of all geometrical and electrical parameters of the system, but a multi-variable optimization, such as a genetic algorithm (GA) is a good choice for this task [108] [109]. Ideally, the physical layout of the metasurface (graphene strips in the case) should be designed so that the effective (homogenized) conductivity tensor elements are hyperbolic, and have large imaginary part and small real part, since such a surface can support a well-confined, long-range SPP. Here we used the cost function to be minimized as

$$\Psi(L, W, \mu_c, \phi) = \alpha(\text{Re}(\sigma_{xx}) + \text{Re}(\sigma_{zz})) + \frac{\beta}{|\text{Im}(\sigma_{xx})| + |\text{Im}(\sigma_{zz})|} + \gamma \left( \tan^2(\phi) + \frac{\sigma_{zz}}{\sigma_{xx}} \right) \quad (3.48)$$

where  $\sigma_{xx}$  and  $\sigma_{zz}$  are defined in (3.47). The cost function in (3.48) is a multi-objective cost function and the coefficients  $\alpha$ ,  $\beta$  and  $\gamma$  assign a weight (0 to 1) to each objective regarding to its importance. The first term in (3.48) assures a small real part of conductivity, the second term assures a large

imaginary part, and the last term assures the correct ratio for  $\sigma_{zz}$  and  $\sigma_{xx}$  to obtain the SPP beam in desired direction specified by  $\phi$ . It was found that  $\alpha = 0.2$  and  $\beta = \gamma = 0.4$  leads to good results.

The physical strip geometry leading to the beam in Fig. 3.14-a was found in this manner, for a specified beam angle of 45 deg. Note the excellent agreement between desired and obtained beam angle. The chemical potential was then changed to produce the beam at 52 deg., for a fixed geometry. Thus, a significant aspect of using a graphene strip array is its electronic tunability by, e.g., varying the bias to control the chemical potential.

In Fig. 3.14-b a desired beam angle of 60 deg. was sought, and the GA was used to determine the optimized parameters;  $\mu_c = 0.45$  eV,  $W = 56.1$  nm and  $L = 62.4$  nm, such that  $\sigma_{xx} = 0.003 + 0.25i$  mS and  $\sigma_{zz} = 0.03 - 0.76i$  mS, leading to the desired beam. Again, excellent agreement is found between the desired and final beam angles.

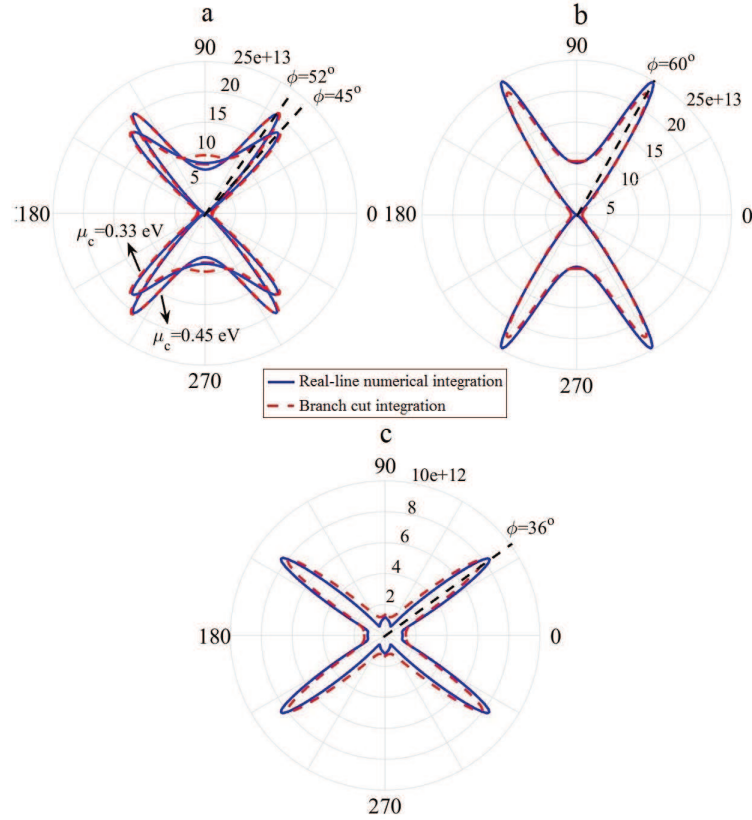


Figure 3.14: Electric field  $E_y$  excited by a  $y$ -directed dipole current above a graphene strip array. a: graphene with  $\mu_c = 0.45$  eV and  $\mu_c = 0.33$  eV,  $W = 59$  nm,  $L = 64$  nm,  $\sigma_{xx} = 0.02 + 0.57i$  mS and  $\sigma_{zz} = 0.02 - 0.57i$  mS. b:  $\mu_c = 0.45$  eV,  $W = 56.1$  nm,  $L = 62.4$  nm,  $\sigma_{xx} = 0.003 + 0.25i$  mS and  $\sigma_{zz} = 0.03 - 0.76i$  mS. c: Strip array with a 5-layer graphene,  $\mu_c = 1$  eV,  $W = 196$  nm and  $L = 200$  nm,  $\sigma_{xx} = 1.3 + 16.9i$  mS and  $\sigma_{zz} = 0.4 - 9.2i$  mS. Blue line is for the integration along the real axis (3.39) and dashed red line is for integration along the branch cuts (4.102).  $f = 10$  THz,  $\rho = 0.2\lambda$ , and  $y = 0.005\lambda$ .

As a final example for the graphene strip array Fig. 3.14-c shows  $E_y$  for the case of multi-layer graphene strips (to increase the conductivity) as discussed in the previous section. By using five layers of graphene with  $\mu_c = 1$  eV,  $W = 196$  nm and  $L = 200$  nm, the conductivities are  $\sigma_{xx} = 1.3 + 16.9i$

mS and  $\sigma_{zz} = 0.4 - 9.2i$  mS. The branch cuts are shown in Fig. 3.12. For this case, (3.29) indicates that the beam should be directed along  $\phi = 36$  deg. Again, excellent agreement is found between the two methods and the position of the beam is along the desired angle.

### 3.3.13 Anisotropic Non-Hyperbolic Layer (Black Phosphorus)

Black phosphorus is an anisotropic monolayer or thin-film material that can support surface plasmons [18]. Fig. 3.15 shows the in-plane conductivity tensor components at two doping levels,  $10 \times 10^{13}/\text{cm}^2$  in Fig. 3.15-a and b and  $5 \times 10^{12}/\text{cm}^2$  in Fig. 3.15-c and d, obtained from a Kubo formula as described in [83]. For a 10 nm BP film, the electronic band gap is approximately 0.5 eV. This accounts for the observed interband absorption along the x polarization, and also characterized by weak interband absorption along z.

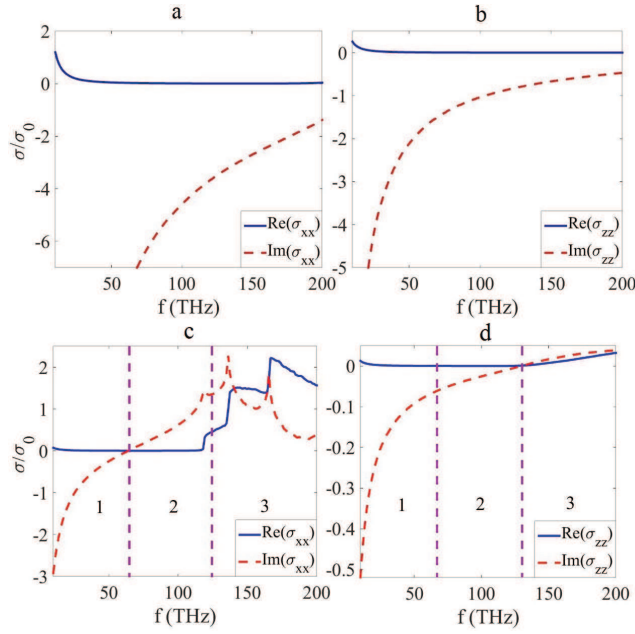


Figure 3.15: a, b. Real and imaginary parts of  $\sigma_{xx}$  and  $\sigma_{zz}$  ( $x$  and  $z$  are in-plane crystal axes of BP, with  $x$  along the small effective mass direction, or commonly called the armchair direction) obtained at doping level  $10 \times 10^{13}/\text{cm}^2$  and c,d.  $5 \times 10^{12}/\text{cm}^2$  normalized to  $\sigma_0 = e^2/4\hbar$  with a 10 nm thickness. Regions 1 and 3 show anisotropic inductive and capacitive responses, respectively, and region 2 shows the hyperbolic regime.  $T=300$  K and damping is 2 meV.

It can be seen that by increasing the doping level, larger conductivity components are attainable but the hyperbolic region is also pushed toward higher frequencies. In Fig. 3.15-a and b black phosphorus is an inductive anisotropic (non-hyperbolic) surface while in Fig. 3.15-c and d regions 1 and 3 show anisotropic inductive and capacitive responses, respectively, and region 2 shows the anisotropic hyperbolic region.

Black phosphorus is a natural material that can be used as a platform to realize an anisotropic surface. Although black phosphorus exhibits a hyperbolic regime, the resulting values of conductivity are rather small (to produce a hyperbolic response the interband conductivity must dominate one



of the conductivity values ( $\sigma_{xx}$  or  $\sigma_{zz}$ ), and the intraband conductivity must dominate the other component, resulting in the required sign difference). Although a hyperbolic SPP can be excited, the residue is not generally the dominant response. Therefore, in order to consider larger values of black phosphorus conductivity, we consider the non-hyperbolic (Drude) regime. A 10 nm thick black phosphorus film with doping level  $10 \times 10^{13}/\text{cm}^2$  has conductivity tensor components  $\sigma_{xx} = 0.0008 - 0.2923i$  mS and  $\sigma_{zz} = 0.0002 - 0.0658i$  mS at  $f = 92.6$  THz. Using (3.35), (3.36) and (3.38), a surface with these conductivity components has  $q_z^{\text{TM}} = k(80.6804 - 0.2114i)$ ,  $q_z^{\text{TE}} \approx k$ , and  $q_z^{(-1)} = k(-0.0300 - 10.3165i)$ .

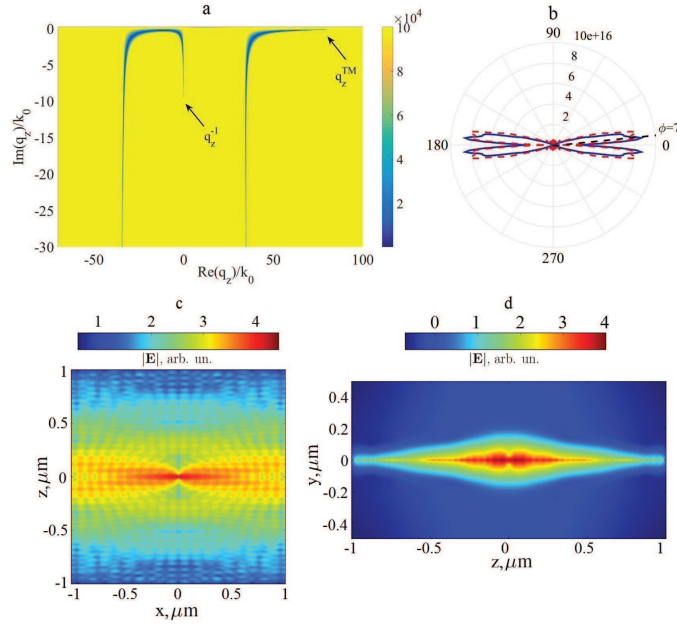


Figure 3.16: a: Branch cut contours for  $\text{Im}(q_{xp}) = 0$  determined from the absolute value of  $\text{Im}(q_{xp})$  in the  $q_z -$  plane. b: Absolute value of  $E_y$  excited by a  $y$ -directed dipole current source above black phosphorus with doping level  $10 \times 10^{13}/\text{cm}^2$  at  $f = 92.6$  THz. The blue line is for the integration along the real axis (3.39) and the dashed red line is for the integration along the branch cuts (4.102).  $\rho = 0.2\lambda$  and  $y = 0.005\lambda$ . c: SPP field in-plane distribution in logarithmic scale calculated by FDTD. d: SPP field vertical variation in logarithmic scale calculated by FDTD.

The imaginary components of the conductivities are negative, so that the surface is not able to support TE modes (the TE branch point is located at the upper half of the  $q_z -$  plane, and so not captured for  $z - z' > 0$ ). The only active branch points are the TM related branch point and  $q_z^{(-1)}$ . Fig. 3.16-a shows the branch points and associated branch cuts in the  $q_z -$  plane. One important difference between branch cuts in this case and in the previous hyperbolic cases is the branch cut trajectory. From (3.42) for the hyperbolic case, because of the condition  $\text{Im}(\sigma_{xx})\text{Im}(\sigma_{zz}) < 0$  the branch cut trajectory was along the real axis, but for the anisotropic non-hyperbolic case we have  $\text{Im}(\sigma_{xx})\text{Im}(\sigma_{zz}) > 0$  and so the trajectory for large  $q_z$  is parallel to the imaginary axis.

As shown in Fig. 3.16-b, this anisotropic non-hyperbolic surface can support a directed SPP, although the beam is directed primarily along one of the coordinate axes. The electric field computed

as a real-line integral (3.39) is in good agreement with the electric field obtained as a sum of branch cut integrals (3.40). Fig. 3.16-c shows the SPP field in logarithmic scale calculated by numerically solving Maxwell's equations using a commercial finite-difference time-domain method (FDTD) from Lumerical solutions [59]. Good agreement with the results obtained by complex plane analysis is observed. Fig. 3.16-d shows the vertical variation of the beam in logarithmic scale calculated by Lumerical, showing strong SPP confinement to the surface. Using the Green's function the attenuation length was found to be  $p = \lambda/12\pi$ .

In the next section we discuss the application of hyperbolic surfaces in generating and controlling entanglement.

### 3.4 Tunable Directed Surface Plasmon-Polariton (SPP) Mediated Entanglement

In this chapter, it has been shown that using a hyperbolic 2D surface, it is possible to launch a narrow-beam surface plasmon-polariton in a specific direction, and the angle of propagation is tunable by changing the components of the conductivity tensor (via, e.g., biasing). The idea is to control and switch entanglement between pairs of (moderately far-separated) quantum dots (QDs); see Fig. 3.17.

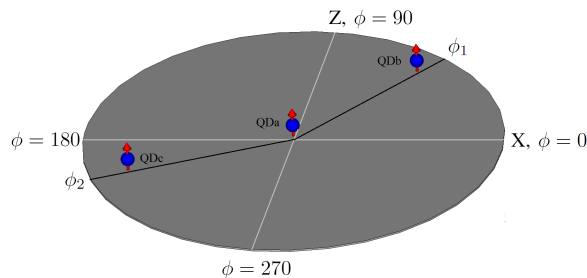


Figure 3.17: A 2D hyperbolic material located in the  $x - z$  plane with conductivity components  $\sigma_{xx}$  and  $\sigma_{zz}$ . Quantum dot 'a' is located at the center, and two other quantum dots are at two different angles. The dipole polarization is along  $y$ , normal to the surface.

The angle of SPP propagation,  $\phi$ , can be controlled by changing the ratio of  $\sigma_{xx}$  and  $\sigma_{zz}$  such that  $(\phi) = \text{atan}^{-1} \sqrt{-\sigma_{zz}/\sigma_{xx}}$ . In Fig. 3.17, QD<sub>a</sub> is located at the center, QD<sub>b</sub> at  $\phi = 50^\circ$  and QD<sub>c</sub> at  $\phi = 235^\circ$ . Using the master equation, the steady state concurrence between pairs of QD<sub>a</sub> and QD<sub>b</sub> or QD<sub>a</sub> and QD<sub>c</sub> has been shown in Fig. 3.18.

In Fig. 3.18, each R corresponds to a specific ratio of conductivity tensor components (that specify the direction of the SPP) such that if we put one quantum dot in the center and the other dot along the direction specified by that R, then we can have maximum steady state concurrence between the pair aligned along that direction. We use a genetic algorithm (GA) optimization, first assuming that the 2D hyperbolic surface is almost lossless, and optimization is done over the imaginary part of the conductivity values.

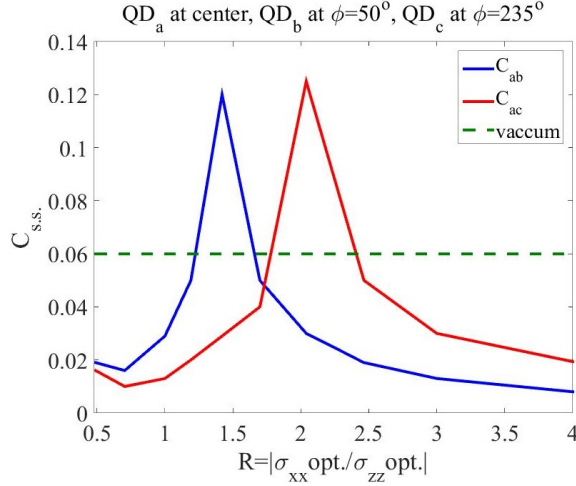


Figure 3.18: Steady-state entanglement for various pairs of QDs. The height of the dots above the hyperbolic surface is  $h = \lambda/60$ , and frequency is 10 THz. The distance between each pair ( $QD_a - QD_b$  and  $QD_a - QD_c$ ) is  $d = \lambda/2$ . Optical dipole moment of the dot at the center is 30 D, and the two other dots have moment 30 D. The dot at the center is illuminated by a pump with intensity  $\Omega_{aa} = 0.35\Gamma_{aa}$ . Solid blue line is the steady state entanglement between pairs  $QD_a$  at center and  $QD_b$  at  $\phi = 50^\circ$ . Solid red is the steady state entanglement between pair  $QD_a$  at the center and  $QD_c$  at  $\phi = 235^\circ$ . Horizontal axis, R, is the ratio of conductivity tensor components that yield these conductivity values.

By changing the ratio of the conductivity tensor components we can rotate the beam, so that we can launch an SPP toward one of the targets (dots). The SPP forms a narrow beam, so that each QD can be separately targeted, creating entangled (linked by beam) or non-entangled (beam in other direction) QD pairs.

Figure 3.19 shows concurrence versus normalized time for the configuration of the dots described in Fig. 3.18.

As can be seen, when the beam links  $QD_a - QD_b$ , we have strong entanglement between  $QD_a$  and  $QD_b$ , while  $QD_c$  is not entangled. When the beam is launched toward  $QD_c$ , then  $QD_b$  is not entangled while  $QD_c$  is entangled to  $QD_a$ .

The conductivity component values corresponding to the ratio  $R = 2$  can be realized using an array of graphene strips. The conductivity values for  $R = 2$  (SPP propagation along  $\phi = 235^\circ$ ) are  $\sigma_{xx} = 0.001 - 2.9i$  mS,  $\sigma_{zz} = 0.001 + 5.9i$  mS. Using an array of 3 layer graphene with  $W = 97$  nm,  $L = 100$  nm,  $\tau = 1$  pS and  $\mu_c = 1.01$  eV it is possible to resemble a surface with  $\sigma_{xx} = 0.01 - 2.60i$  mS,  $\sigma_{zz} = 0.08 + 5.50i$  mS at  $f = 10$  THz, which is very close to the values obtained in previous section for  $R = 2$  (determining the strip grid geometry is also done using a second genetic algorithm). One of the advantages of this surface is that the conductivity values are tunable via the chemical potential. For the geometry mentioned earlier if we change chemical potential to  $\mu_c = 0.8$  eV then we obtain  $\sigma_{xx} = 0.02 - 2.94i$  mS,  $\sigma_{zz} = 0.06 + 4.36i$  mS which leads to SPP propagation along  $\phi = 235^\circ$ .

Figure 3.20-a and b show the SPP propagation, dot positions and driven concurrence between pairs of QDs.

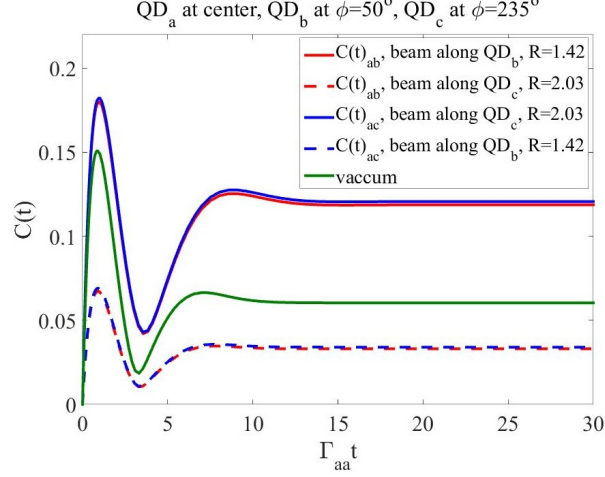


Figure 3.19: Time-evolution of entanglement. The QDs are  $h = \lambda/60$  above the surface, and frequency is 10 THz. The distance between the dots is  $d = \lambda/2$ . Optical dipole moment of the dot at the center is 30 D, and same thing for the other two dots. The dot at the center is illuminated by a pump with  $\Omega_{aa} = 0.35\Gamma_{aa}$ . The ratio  $R = 1.42$  ( $\phi = 50^\circ$ ) corresponds to  $\sigma_{xx} = 0.001 - 3.87i$  mS,  $\sigma_{zz} = 0.0010 + 5.5080i$  mS and  $R = 2$  ( $\phi = 235^\circ$ ) corresponds to  $\sigma_{xx} = 0.001 - 2.9i$  mS,  $\sigma_{zz} = 0.001 + 5.9i$  mS.

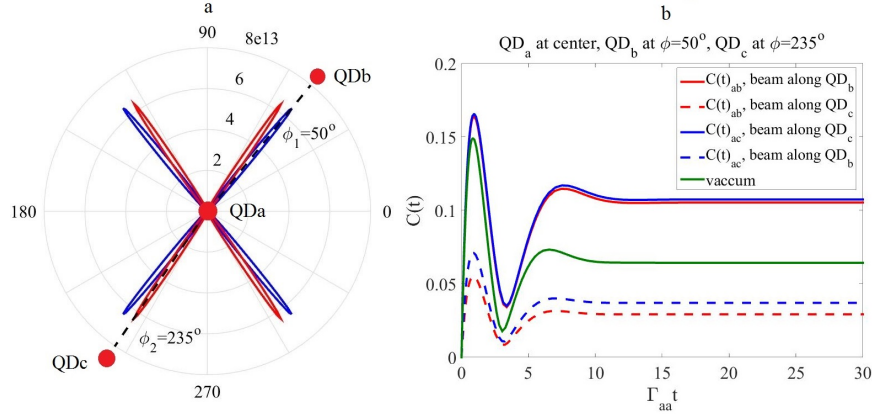


Figure 3.20: SPP propagation due to a dipole located at  $h = \lambda/60$  above the surface made by graphene strips array with  $\tau = 1$  pS,  $W = 97$  nm and  $L = 100$  nm. a: Solid blue for  $\mu_c = 0.8$  eV and solid red is for  $\mu_c = 1.01$  eV. QDs are indicated by red dots. b: Driven concurrence by a pump with intensity  $\Omega = 0.4\Gamma_{aa}$  between pair QD<sub>a</sub>, QD<sub>b</sub> and QD<sub>a</sub>, QD<sub>c</sub> when beam is in a different direction.

### 3.5 Summary

In this chapter we have studied the electromagnetic response of 2D anisotropic and hyperbolic surfaces and developed a method based on complex plane analysis for the efficient computation of electric field excited on such surfaces. A solution in term of electric field Sommerfeld integrals has been obtained for the electromagnetic field due to a vertical dipole current source located in close proximity to the surface. Poles, branch points, and related branch cuts and their relative importance and physical meaning for surface wave propagation have been emphasized. A first-order approximation has also been obtained using the stationary phase method. Examples have been shown for a graphene strip

array and black phosphorus. Also the application of directive SPPs for generating and controlling the entanglement between quantum dots has been investigated.

# Chapter 4

## Photonic Topological Insulators

### 4.1 Review of Theory

#### 4.1.1 Motivation- Backscattering-Immune One-Way SPP Propagation

Surface plasmons polaritons (SPPs) are well-known and long-studied waves that can be guided at the interface between two materials (nominally, for an SPP to exist in an isotropic environment one material has relative permittivity  $\varepsilon = \varepsilon_1 < 0$  and the other has  $\varepsilon = \varepsilon_2 > 0$ , such as an air-plasma (metal) interface). For a wave travelling as  $e^{\pm ikz}$  ( $z$  parallel to the interface), the SPP dispersion relation is

$$k = \frac{\omega}{c} \sqrt{\frac{\varepsilon_1 \varepsilon_2}{\varepsilon_1 + \varepsilon_2}}, \quad (4.1)$$

where  $\varepsilon_\alpha = \varepsilon_\alpha(\omega)$ ,  $\alpha = 1, 2$ . For example, for a simple lossless plasma  $\varepsilon(\omega) = 1 - \omega_p^2/\omega^2$  with  $\omega_p$  being the plasma frequency. Plotting the dispersion equation (Fig. 4.1.a) we see that propagation is reciprocal,  $\omega(-k) = \omega(k)$ , so that forward-propagating ( $k$ ) and backward-travelling ( $-k$ ) waves exist at the same frequency. A source near the surface will excite SPPs travelling in both directions ( $\pm z$ ), and upon encountering a discontinuity an SPP travelling in, say, the  $+z$  direction will undergo both reflection and transmission, again resulting in both forward and backward travelling waves.

Waves can be excited in a single direction using a directive source (e.g., planar Yagi-Uda antenna, or by a circularly-polarized source that couples to the SPPs spin polarization), but upon encountering a discontinuity, partial reflection of the wave will occur since the material itself allows propagation in both directions.

However, if the medium only supports modes that can travel in one direction, say, via non-reciprocity as depicted in Fig. 4.1.b (e.g., via a magnetic-field biased plasma having a tensor permittivity with non-zero off-diagonal elements), then upon encountering a discontinuity an SPP cannot be reflected (back-scattered), as shown in the upper-right insert of the figure. This is a rather remarkable occurrence, and has important applications in waveguiding (e.g., defect-immune waveguides).

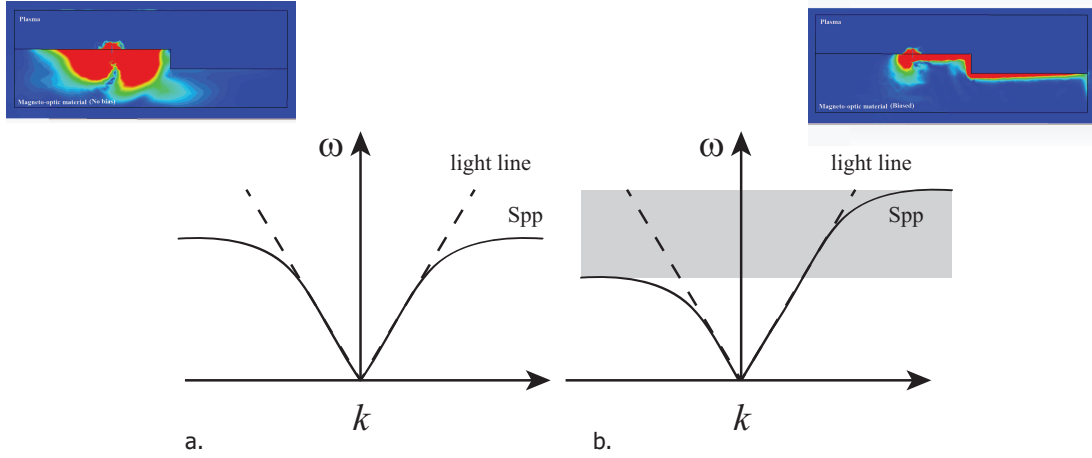


Figure 4.1: a. Dispersion of reciprocal SPP. Upper-left insert shows SPP power flow excited by a vertical dipole source near a step change in height at the interface between a reciprocal medium (below) and a different reciprocal medium (above), b. nonreciprocal SPP; shaded region depicts frequency range of uni-directional propagation. Upper-right insert is the same as upper-left insert, except that the lower medium is now non-reciprocal and we operate in the gap, ensuring one-way propagation.

In general, there will be a range of energies where only propagation in one direction is possible (e.g., in Fig. 4.1.b in the indicated frequency band only forward propagating modes can exist, there are no states with  $-k$ ).

However, the idea of one-way (backscattering-immune) surface-wave propagation is more general than indicated above. In particular, one does not necessarily need a non-reciprocal material. A broad class of materials exist known as photonic topological insulators (PTIs) which have this characteristic, generally supporting Hall/chiral edge states. This class of materials includes biased non-reciprocal magneto-plasmas (more generally, materials with broken time-reversal symmetry), but it also includes time-reversal-invariant materials with broken inversion symmetry. In the latter case, photon states are separated in two ‘spin’ sub-spaces (usually through geometry such as via a hexagonal lattice), and ‘spin-orbit’ coupling is introduced through inversion symmetry-breaking. Here focus on the simplest subclass formed by photonic topological media with a broken time reversal symmetry, sometimes also designated as Chern-type insulators (the analogs of quantum Hall insulators).

On the electronic side, topological insulators (TIs) and quantum Hall edge state materials (which utilize many of the same concepts described here) came first, and, noting the analogy between electronic and optical systems, the first work on PTIs was described in [110] and [20]. The first experimental demonstration of an optical TI was shown in [111], and in various material systems [112], [113], [114], [115], and [116], among others. Understanding the broad field of PTIs necessitates understanding the Berry phase, potential, curvature, and the concept of Chern invariants, which is the

subject of these notes. After an introduction to these concepts, we examine two previous PTI results from the literature, and provide details of the various computations necessary to characterize the materials.

### 4.1.2 Origin of the Berry Phase

Here we derive the Berry phase, following the usual procedure for electronic systems. For a derivation that only considers classical electromagnetics, as well as a more thorough introduction, see [117].

We consider a system described by a Hamiltonian dependent on parameters that vary in time,  $H = H(\mathbf{R})$ , such that  $\mathbf{R} = \mathbf{R}(t) = (R_1(t), R_2(t), R_3(t), \dots)$ . We will consider a path in parameter space  $C$  along which  $\mathbf{R}$  changes. For example,  $\mathbf{R}$  could describe the position of a particle  $(x(t), y(t), z(t))$  and  $C$  could be a path in physical space. However, here we are primarily interested in the case when  $\mathbf{R}(t)$  lives in momentum (reciprocal) space.

The evolution of the system is assumed to be adiabatic, such that the parameters  $\mathbf{R}(t)$  of the Hamiltonian change slowly along path  $C$  in parameter space. The adiabatic theorem states that if a system is initially in the  $n$ th eigenstate of the initial Hamiltonian  $H(\mathbf{R}(0))$ , and the system is moved slowly-enough as  $\mathbf{R}(t)$  changes, it will arrive at the  $n$ th eigenstate of the final Hamiltonian  $H(\mathbf{R}(T))$ . Development of the adiabatic solution below will show how the Berry phase comes about.

We will assume that the time dependent states evolves through an evolution equation

$$i\hbar\partial_t |\Psi(t)\rangle = (H(\mathbf{R}(t))) |\Psi(t)\rangle \quad (4.2)$$

which is typically taken to be the Schrödinger equation, where  $|\Psi(t)\rangle$  is a scalar, but it could also represent the Dirac equation where  $|\Psi(t)\rangle$  is a spinor, and classical Maxwell's equations ( $\hbar = 1$ ), where  $|\Psi(t)\rangle$  is the six-vector of EM fields.

Because of the slow variation of the Hamiltonian parameters we can assume that at every time the instantaneous eigenstates of the Hamiltonian satisfy

$$H(\mathbf{R}) |n(\mathbf{R})\rangle = E_n |n(\mathbf{R})\rangle. \quad (4.3)$$

However, (4.3) does not uniquely determine the function  $|n(\mathbf{R})\rangle$ , since we could include an arbitrary phase factor (gauge choice) that depends on  $\mathbf{R}(t)$ .

To motivate the following derivation, note that if the Hamiltonian is independent of time, then a system that starts out in the  $n$ th eigenstate  $|n\rangle$ , remains in  $n$ th eigenstate but simply pick up a phase factor,

$$|\Psi_n(t)\rangle = |n\rangle e^{-\frac{i}{\hbar} E_n t}. \quad (4.4)$$

So, to represent the evolution of the system with slowly varying Hamiltonian we use a superposition



of these instantaneous eigenvectors, adjusting the phase factor to account for the time variation,

$$|\Psi(t)\rangle = \sum_n a_n(t) e^{-\frac{i}{\hbar} \int_0^t E_n(\mathbf{R}(t')) dt'} |n(\mathbf{R}(t))\rangle = \sum_n a_n(t) e^{i\alpha_n} |n(\mathbf{R}(t))\rangle \quad (4.5)$$

where  $\alpha_n(t) = -\frac{1}{\hbar} \int_0^t E_n(\mathbf{R}(t')) dt'$  is called the dynamical phase. If we substitute this general form of solution in the evolution equation (4.2) we obtain

$$\begin{aligned} i\hbar \sum_n (\partial_t a_n + i a_n \partial_t \alpha_n) e^{i\alpha_n} |n\rangle + i\hbar \sum_n a_n e^{i\alpha_n} |\partial_t n\rangle &= \mathbf{H} |\Psi\rangle \\ i\hbar \sum_n (\partial_t a_n) e^{i\alpha_n} |n\rangle + \sum_n E_n a_n e^{i\alpha_n} |n\rangle + i\hbar \sum_n a_n e^{i\alpha_n} |\partial_t n\rangle &= \mathbf{H} |\Psi\rangle, \end{aligned} \quad (4.6)$$

and taking the inner product of both sides by  $\langle m|$ , yields

$$\partial_t a_m = - \sum_n a_n e^{i(\alpha_n - \alpha_m)} \langle m | \partial_t n \rangle. \quad (4.7)$$

In the adiabatic limit, where excitation to other instantaneous eigenvectors is negligible<sup>1</sup>, the choice of initial state  $|\Psi(t=0)\rangle = |n(\mathbf{R}(0))\rangle$  will imply that  $|a_n(t)| = 1$ ,  $a_m(t) = 0$  for  $m \neq n$ . We then have

$$\begin{aligned} \partial_t a_m &= - \sum_n a_n e^{i(\alpha_n - \alpha_m)} \langle m | \partial_t n \rangle \\ \partial_t a_n &= -a_n \langle n | \partial_t n \rangle \rightarrow a_n = e^{i\gamma_n}; \quad \partial_t \gamma_n = i \langle n | \partial_t n \rangle. \end{aligned} \quad (4.9)$$

Therefore, the adiabatic evolution of the state vector becomes

$$|\Psi(t)\rangle = e^{i\gamma_n} e^{i\alpha_n} |n(\mathbf{R}(t))\rangle. \quad (4.10)$$

---

<sup>1</sup>To prove the statement that the excitation probability of states  $n \neq m$  is small, the time derivative of the energy state equation is  $\partial_t H |n\rangle + H |\partial_t n\rangle = \partial_t E_n |n\rangle + E_n |\partial_t n\rangle$ , where we can set  $\partial_t E_n = 0$  due to slow variation. The inner product with  $\langle m|$  yields  $\langle m | \partial_t n \rangle = \langle m | \partial_t H |n\rangle / (E_m - E_n)$  ( $n \neq m$ ) so we have from (4.7)  $\partial_t a_m = - \sum_n a_n e^{i(\alpha_n - \alpha_m)} \langle m | \partial_t H |n\rangle / (E_m - E_n)$  ( $n \neq m$ ). Choose the initial state to be one of the instantaneous eigenstates  $|\Psi(t=0)\rangle = |n(\mathbf{R}(0))\rangle$ , so  $a_n(t=0) = 1$  and  $a_m(t=0) = 0$  for  $n \neq m$ . Then, for  $n \neq m$  we have  $\partial_t a_m \approx -e^{i(\alpha_n - \alpha_m)} \langle m | \partial_t H |n\rangle / (E_m - E_n)$ . Since the time dependencies of  $\langle m | \partial_t H |n\rangle$  and  $E_n - E_m$  are slow, the most important time dependence will be in the exponential, which can be approximated by  $e^{i(\alpha_n - \alpha_m)} = e^{i(E_m - E_n)t/\hbar}$ . Neglecting the other slow time dependencies then yields

$$\begin{aligned} \partial_t a_m &\approx -e^{i(\alpha_n - \alpha_m)} \langle m | \partial_t H |n\rangle / (E_m - E_n) \\ a_m(t) &= - \int_0^t e^{i(E_m - E_n)t'/\hbar} \frac{\langle m | \partial_t H |n\rangle}{(E_m - E_n)} dt' = \frac{i}{\hbar} \frac{\langle m | \partial_t H |n\rangle}{\omega_{mn}^2} \{e^{i\omega_{mn}t/\hbar} - 1\}, \end{aligned} \quad (4.8)$$

$\omega_{mn} = (E_m - E_n)/\hbar$ , ( $n \neq m$ ). Due to adiabatic approximation we have adopted,  $\langle m | \partial_t H |n\rangle$  is slow compared to the transition frequency  $\omega_{mn} = (E_m - E_n)/\hbar$ . Therefore, the magnitude of the excitation probability to other states  $|a_m(t)|^2$  is small for  $n \neq m$ . For further reading see [118].

We have

$$\begin{aligned}
\gamma_n &= i \int_0^t \langle n(\mathbf{R}(t')) | \frac{\partial}{\partial t} | n(\mathbf{R}(t')) \rangle dt' \\
&= i \int_0^t \langle n(\mathbf{R}(t')) | \frac{\partial}{\partial \mathbf{R}} | n(\mathbf{R}(t')) \rangle \cdot \frac{\partial \mathbf{R}}{\partial t'} dt' \\
&= \int_{R_i}^{R_f} d\mathbf{R} \cdot i \langle n(\mathbf{R}) | \nabla_{\mathbf{R}} | n(\mathbf{R}) \rangle = \int_{R_i}^{R_f} d\mathbf{R} \cdot \mathbf{A}_n(\mathbf{R})
\end{aligned} \tag{4.11}$$

(setting  $\nabla_{\mathbf{R}} = \partial/\partial\mathbf{R}$ ), where  $R_i$  and  $R_f$  are the initial and final values of  $\mathbf{R}(t)$  in parameter space, and where

$$\mathbf{A}_n(\mathbf{R}) = i \langle n(\mathbf{R}) | \nabla_{\mathbf{R}} | n(\mathbf{R}) \rangle = -\text{Im} \langle n(\mathbf{R}) | \nabla_{\mathbf{R}} | n(\mathbf{R}) \rangle \tag{4.12}$$

is called the *Berry vector potential* (also called *the Berry connection* since it connects the state at  $\mathbf{R}$  and the state at  $\mathbf{R} + d\mathbf{R}$ ) and  $\gamma_n$  is called the *Berry phase*.<sup>2</sup>

Eq. (4.11) shows that, in addition to the dynamical phase, the state will acquire an additional phase  $\gamma_n$  during the adiabatic evolution (note that  $\gamma_n$  is real-valued;  $e^{i\gamma_n(t)}$  is a phase, not a decay term<sup>3</sup>). The existence of this phase has been known since the early days of quantum mechanics, but it was thought to be non-observable since a gauge-transformation could remove it. It was Berry who, in 1984, showed that for cyclic variation ( $\mathbf{R}_f = \mathbf{R}_i$ ) the phase is not removable under a gauge transformation[119] (discussed below), and was also observable<sup>4</sup>. This net phase change depends only on the path  $C$  in parameter space that is traversed by  $\mathbf{R}(t)$ , but not on the rate at which it is traversed (assuming the adiabatic hypothesis still holds). It is therefore called a *geometrical phase*, in distinction to the dynamical phase which depends on the elapsed time. This geometric phase has been generalized for non-adiabatic evolution [120].

## Geometric Phase

Geometric phases have a long history, and arise in many branches of physics [121]. They are well-illustrated by considering parallel transport of a vector along a curved surface. To consider an intuitive example, as widely discussed (see, e.g., [122]) and depicted in Fig. 4.2, consider at  $t = 0$  a pendulum at the north pole of a sphere, swinging along a longitude line. If the pendulum is moved along the longitude line to the equator, across the equator some distance, and at  $t = T$  arriving back at the north pole via a different longitude line (and assuming the movement is sufficiently slow, in keeping with the adiabatic assumption), the angle of the pendulum swing with some fixed reference is obviously different from its initial angle (this difference is called the defect angle, which is a mechanical analogue of phase). The defect angle is given by the solid angle  $\Omega$  subtended by the

<sup>2</sup>One can also obtain this result by assuming the existence of this extra phase [119],  $|\Psi(t)\rangle = e^{i\gamma_n} e^{i\alpha_n} |n(\mathbf{R}(t))\rangle$ , and inserting into Schrödinger's equation. Taking the inner product with  $\langle n(\mathbf{R}(t)) |$  and using  $\langle n(\mathbf{R}(t)) | H(\mathbf{R}) | n(\mathbf{R}(t)) \rangle = E_n$  leads to the same result as above.

<sup>3</sup> $\langle n(\mathbf{R}) | \nabla_{\mathbf{R}} | n(\mathbf{R}) \rangle$  can easily be seen to be itself imaginary since  $\langle n(\mathbf{R}) | n(\mathbf{R}) \rangle = 1$ , and so taking a derivative on both sides yields  $\langle n(\mathbf{R}) | \nabla_{\mathbf{R}} | n(\mathbf{R}) \rangle = -\langle n(\mathbf{R}) | \nabla_{\mathbf{R}} | n(\mathbf{R}) \rangle^*$ .

<sup>4</sup>Physically observable quantities must be gauge-independent

path of movement. For example,  $\Omega_{\text{sphere}} = 4\pi$  for a sphere, and so if the longitude lines are 180 degrees apart the subtended angle is  $\Omega_{\text{sphere}}/4 = \pi$ . For the electronic case, moving along a contour in parameter space, the Berry phase is equal to  $s\Omega$ , where  $s$  is the particle spin. Parallel transport along a non-curved surface does not lead to a defect angle, and so we see that a non-zero Berry phase has its origins in the curvature of parameter space. In optics, an optical fiber wound into a

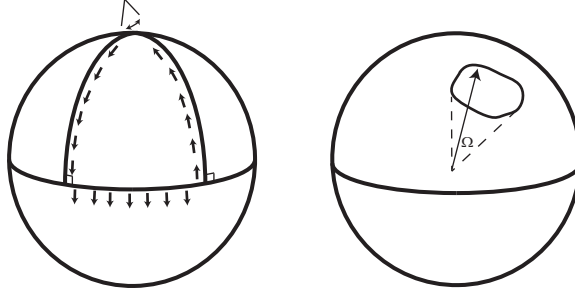


Figure 4.2: a. Parallel transport around a sphere. b. Parallel transport about a closed contour on a sphere and solid angle subtended.

helix has been used to demonstrate Berry phase [123], among other results (see, e.g., [124]). In these cases the momentum is  $\mathbf{p} = \hat{x}p_x + \hat{y}p_y + \hat{z}p_z = \hbar\mathbf{k}$ , where  $\mathbf{k}$  is the propagation vector of the optical wave,  $|\mathbf{k}| = k = 2\pi/\lambda$ . Therefore,  $|\mathbf{p}|^2 = p_x^2 + p_y^2 + p_z^2 = (\hbar k)^2$ , which is a sphere, and so rotation of momentum is equivalent to movement on the surface of a sphere.

When  $\mathbf{R}$  is a real-space parameter, consider an electron in the ground state of an atom. As the atom is slowly moved through a static magnetic field the electron stays in the ground state (adiabatic) but picks up a Berry phase, which is the Aharonov-Bohm phase. An example of  $\mathbf{R}$  as a parameter space is given in Section 4.1.4 for an electron fixed in space but exposed to a time-varying magnetic field  $\mathbf{B}(t)$ . As detailed in the electromagnetic examples below, we will be more interested in the case when the parameter space  $\mathbf{R}$  is momentum space,  $\mathbf{R} = \mathbf{k}$ . In this case, we can simply consider moving through  $\mathbf{k}$ -space without necessitating the time variable, and simply consider  $\gamma_n(\mathbf{k})$ , which will depend on the path taken in  $\mathbf{k}$ -space.

## Gauge

Obviously,  $A_n(\mathbf{R})$  is a gauge dependent quantity. If we make a gauge transformation  $|n(\mathbf{R})\rangle \rightarrow e^{i\xi(\mathbf{R})}|n(\mathbf{R})\rangle$  with  $\xi(\mathbf{R})$  an arbitrary smooth function (this is equivalent to the EM gauge transformation<sup>5</sup>) the Berry potential transforms to  $A_n(\mathbf{R}) \rightarrow A_n(\mathbf{R}) - \nabla_{\mathbf{R}}\xi(\mathbf{R})$ . Consequently, the

<sup>5</sup>In EM, the gauge transform is

$$\Phi'(\mathbf{r}, t) = \Phi(\mathbf{r}, t) - \frac{\partial\chi(\mathbf{r}, t)}{\partial t}, \quad \mathbf{A}'(\mathbf{r}, t) = \mathbf{A}(\mathbf{r}, t) + \nabla\chi(\mathbf{r}, t), \quad (4.13)$$

which leaves the fields

$$\mathbf{E}(\mathbf{r}, t) = -\nabla\Phi(\mathbf{r}, t) - \frac{\partial\mathbf{A}(\mathbf{r}, t)}{\partial t}, \quad \mathbf{B}(\mathbf{r}, t) = \nabla \times \mathbf{A}(\mathbf{r}, t) \quad (4.14)$$

unchanged. Then,

$$i\hbar \frac{d}{dt} |\psi\rangle = \mathbf{H} |\psi\rangle \quad (4.15)$$

additional phase  $\gamma_n$  will be changed by  $\xi(\mathbf{R}_i) - \xi(\mathbf{R}_f)$  after the gauge transformation, where  $\mathbf{R}_i$  and  $\mathbf{R}_f$  are the initial and final points of the path  $C$ . For an arbitrary path one can choose a suitable  $\xi(\mathbf{R})$  such that accumulation of that extra phase term vanishes, and we left only with the dynamical phase. However, by considering a closed path (cyclic evolution of the system)  $C$  where  $\mathbf{R}_f = \mathbf{R}_i$  and noting that the eigenbasis should be single-valued,  $|n(\mathbf{R}_i)\rangle = |n(\mathbf{R}_f)\rangle$ , then  $e^{i\xi(\mathbf{R}_i)} |n(\mathbf{R}_i)\rangle = e^{i\xi(\mathbf{R}_f)} |n(\mathbf{R}_f)\rangle = e^{i\xi(\mathbf{R}_f)} |n(\mathbf{R}_i)\rangle$ , and so  $e^{i\xi(\mathbf{R}_i)} = e^{i\xi(\mathbf{R}_f)}$ . That is, single-valuedness of the eigenbasis means that  $e^{i\xi(\mathbf{R})}$  (but not necessarily  $\xi(\mathbf{R})$ ) must be single-valued, and therefore we must have

$$\xi(\mathbf{R}_i) - \xi(\mathbf{R}_f) = 2\pi m \quad (4.17)$$

where  $m$  is an integer. This shows that  $\gamma_n$  can be only changed by an integer multiple of  $2\pi$  under a gauge transformation using a smooth gauge function; this phase cannot be removed. Note that this holds for  $\text{Dim}(R) > 1$ , so that we have a path integral in (4.11). For a one-parameter space  $R$ , (4.11) becomes a simple integral over a vanishing path; for  $R_f = R_i = R$   $\int_R^R i \langle n(R) | \frac{\partial}{\partial R} | n(R) \rangle dR = 0$ . However, when applied to periodic solids (for which the Berry phase is also called the *Zak phase*, electrons crossing the Brillouin zone can indeed pick up a Berry phase, which persists in 1D because of the periodicity of the Brillouin zone; assuming period  $a$ , when  $k$  sweeps across the BZ due to, say, an applied field, a phase can be acquired since  $\int_{-\pi/a}^{\pi/a} (\cdot) dk = \oint_{-\pi/a}^{\pi/a} (\cdot) dk$ .

As described below, we will only be interested in paths  $C$  that are closed in parameter space, and so we write

$$\gamma_n = \gamma_n(\mathbf{R}) = \oint_C d\mathbf{R} \cdot \mathbf{A}_n(\mathbf{R}). \quad (4.18)$$

In the space of gauge functions  $\xi$  where  $e^{i\xi(\mathbf{R})}$  is single-valued, (4.18) is gauge-dependent (one could say it is gauge-invariant up to factors of  $2\pi$ ). If we restrain the class of gauge functions  $\xi$  to be themselves single-valued, then (4.18) is gauge-independent<sup>6</sup>.

For a two-dimensional periodic material (such as graphene as an electronic example, or a hexagonal array of infinite cylinders as an electromagnetic example),  $C$  is typically the boundary of the first Brillouin zone and  $\mathbf{S}$  is its surface in  $\mathbf{k}$ -space. In this case, the ‘‘cyclic’’ variation forming the closed path  $C$  in  $\mathbf{k}$ -space is the perimeter of the first Brillouin zone.

---

with the Hamiltonian

$$H(\mathbf{r}, t) = \frac{1}{2m} [\hat{\mathbf{p}} + e\mathbf{A}(\mathbf{r}, t)]^2 - e\Phi(\mathbf{r}, t) + V(r),$$

becomes

$$i\hbar \frac{d}{dt} |\psi'\rangle = H' |\psi'\rangle \quad (4.16)$$

where  $|\psi'\rangle = e^{-ie\chi(\mathbf{r}, t)/\hbar} |\psi\rangle$  and

$$H' = \frac{1}{2m} [\hat{\mathbf{p}} + e\mathbf{A}'(\mathbf{r}, t)]^2 - e\Phi'(\mathbf{r}, t) + V(r).$$

Therefore, Schrödinger's equation is invariant under the gauge transformation, and the EM change of gauge is equivalent to a phase change in the wavefunction,  $|\psi'\rangle = e^{-ie\chi(\mathbf{r}, t)/\hbar} |\psi\rangle$ .

<sup>6</sup>This is easily seen since  $\oint_C d\mathbf{R} \cdot \nabla_{\mathbf{R}} \xi(\mathbf{R}) = 0$  for  $\xi$  a smooth, single-valued function.

### 4.1.3 Berry Curvature, Flux, and Tensor, and Chern Number

Eq. (4.18) is an analogy to the equation for magnetic flux  $\Phi_{\text{mag}}$ , in terms of the real-space magnetic field and magnetic vector potential  $\mathbf{A}_{\text{mag}}$  in electromagnetics,

$$\Phi_{\text{mag}} = \int_S d\mathbf{S} \cdot \mathbf{B}(\mathbf{r}) = \oint_C d\mathbf{l} \cdot \mathbf{A}_{\text{mag}}(\mathbf{r}). \quad (4.19)$$

where  $\oint_C d\mathbf{l} \cdot \mathbf{A}_{\text{mag}}(\mathbf{r})$  is also related to the Aharonov-Bohm phase in quantum mechanics. For the magnetic flux density in electromagnetics we have

$$\mathbf{B}(\mathbf{r}) = \nabla_{\mathbf{r}} \times \mathbf{A}_{\text{mag}}(\mathbf{r}). \quad (4.20)$$

By analogy to electromagnetics, when  $2 \leq \dim(\mathbf{R}) \leq 3$  (other dimensional are considered below) a vector wave can be obtained from the Berry vector potential  $\mathbf{A}_n(\mathbf{R})$  as

$$\mathbf{F}_n(\mathbf{R}) = \nabla_{\mathbf{R}} \times \mathbf{A}_n(\mathbf{R}) \quad (4.21)$$

$$= i \nabla_{\mathbf{R}} \times \langle n(\mathbf{R}) | \nabla_{\mathbf{R}} | n(\mathbf{R}) \rangle = i \langle \nabla_{\mathbf{R}} n(\mathbf{R}) | \times | \nabla_{\mathbf{R}} n(\mathbf{R}) \rangle. \quad (4.22)$$

This field is called the *Berry curvature*, and is obviously gauge-independent. It is a geometrical property of the parameter space, and can be viewed as an effective magnetic field in parameter space; just as the motion of a moving charge is perpendicular to the magnetic field ( $\mathbf{F}_B = \mathbf{v} \times \mathbf{B}$ ), i.e., the curvature of the magnetic vector potential, the Berry curvature will induce transverse particle motion (an electronic or optical Hall effect). To continue the analogy, first note that the magnetic flux can also be written as

$$\Phi_{\text{mag}} = \int_S d\mathbf{S} \cdot \mathbf{B}(\mathbf{r}), \quad (4.23)$$

where (4.19) and (4.23) are equal via Stokes' theorem, i.e.,

$$\oint_C d\mathbf{l} \cdot \mathbf{A}_{\text{mag}}(\mathbf{r}) = \int_S d\mathbf{S} \cdot \nabla_{\mathbf{r}} \times \mathbf{A}_{\text{mag}}(\mathbf{r}) = \int_S d\mathbf{S} \cdot \mathbf{B}(\mathbf{r}). \quad (4.24)$$

For Stokes' theorem to hold the fields must be nonsingular on and within the contour  $C$ . Given that magnetic monopoles, which would serve as singularities of the field, do not seem to exist, Stokes' theorem is valid to apply in this case. One can similarly use Stokes' theorem to connect the Berry phase and the Berry curvature,

$$\gamma_n = \oint_C d\mathbf{R} \cdot \mathbf{A}_n(\mathbf{R}) \stackrel{?}{=} \int_S d\mathbf{S} \cdot \mathbf{F}_n(\mathbf{R}) \quad (4.25)$$

where  $C$  and  $S$  are a contour and surface in parameter space, and where the right side could be called the *Berry flux*. However, it must be kept in mind that the relation (4.25) is not always valid, since

for the parameter-space fields  $\mathbf{A}_n(\mathbf{R})$ ,  $\mathbf{F}_n(\mathbf{R})$  singularities can occur, such that Stokes' theorem does not generally hold<sup>7</sup>. Nevertheless, a gauge-independent Berry phase  $\gamma_n$  can be computed from the Berry flux integral,

$$\gamma_n = \int_S d\mathbf{S} \cdot \mathbf{F}_n(\mathbf{R}), \quad (4.27)$$

Stokes' theorem holding modulo  $2\pi$ .

The above form of  $\mathbf{F}_n$  (and of  $\mathbf{A}_n$ ) can be inconvenient for numerical work since it involves derivatives of the state function (the problem this engenders is described below). In the following an alternative tensor formulation is shown, applicable for any dimension parameter space, and which also leads to a more convenient form for numerical computations.

For  $R^\mu$  and  $R^\nu$  elements of  $\mathbf{R}$ , with  $\mu, \nu$  covering all of  $\mathbf{R}$ , then the Berry curvature tensor can be defined as

$$F_{\mu\nu}^n = \frac{\partial}{\partial R^\mu} A_n^\nu - \frac{\partial}{\partial R^\nu} A_n^\mu = i \left[ \left\langle \frac{\partial}{\partial R^\mu} n(\mathbf{R}) \left| \frac{\partial}{\partial R^\nu} n(\mathbf{R}) \right\rangle - \left\langle \frac{\partial}{\partial R^\nu} n(\mathbf{R}) \left| \frac{\partial}{\partial R^\mu} n(\mathbf{R}) \right\rangle \right] \quad (4.28)$$

which serves as a generalization of the vector Berry curvature. We can also write the Berry curvature tensor in terms of the Berry curvature vector; for  $\dim(\mathbf{R}) = 3$

$$F = -\mathbf{F} \times \mathbf{I}_{3 \times 3} = \begin{bmatrix} 0 & F_z & -F_y \\ -F_z & 0 & F_x \\ F_y & -F_x & 0 \end{bmatrix} \quad (4.29)$$

where  $\mathbf{I}_{3 \times 3}$  is the identity. More generally, the Berry curvature tensor  $F_{\mu\nu}^n$  and vector  $\mathbf{F}_n$  are related by  $F_{\mu\nu}^n = \epsilon_{\mu\nu\xi} (\mathbf{F}_n)_\xi$  with  $\epsilon_{\mu\nu\xi}$  the Levi-Civita anti-symmetry tensor.

Importantly, the Berry curvature tensor (4.28) can be also written as a summation over the eigenstates,

$$F_{\mu\nu}^n = i \sum_{n', n' \neq n} \frac{\langle n | \partial H / \partial R^\mu | n' \rangle \langle n' | \partial H / \partial R^\nu | n \rangle - \langle n | \partial H / \partial R^\nu | n' \rangle \langle n' | \partial H / \partial R^\mu | n \rangle}{(E_n - E_{n'})^2}. \quad (4.30)$$

To obtain this result, note that

$$A_n^{\nu,\mu} = i \langle n(\mathbf{R}) | \frac{\partial}{\partial R^{\nu,\mu}} | n(\mathbf{R}) \rangle, \quad \frac{\partial}{\partial R^\alpha} A_n^{\nu,\mu} = i \left\langle \frac{\partial}{\partial R^\alpha} n(\mathbf{R}) \left| \frac{\partial}{\partial R^{\nu,\mu}} n(\mathbf{R}) \right\rangle + i \left\langle n(\mathbf{R}) \left| \frac{\partial}{\partial R^\alpha} \frac{\partial}{\partial R^{\nu,\mu}} n(\mathbf{R}) \right\rangle \right.$$

Inserting into (4.28),

$$F_{\mu\nu}^n = \frac{\partial}{\partial R^\mu} A_n^\nu - \frac{\partial}{\partial R^\nu} A_n^\mu = i \left[ \left\langle \frac{\partial}{\partial R^\mu} n(\mathbf{R}) \left| \frac{\partial}{\partial R^\nu} n(\mathbf{R}) \right\rangle - \left\langle \frac{\partial}{\partial R^\nu} n(\mathbf{R}) \left| \frac{\partial}{\partial R^\mu} n(\mathbf{R}) \right\rangle \right]. \quad (4.31)$$

---

<sup>7</sup>The obstruction to Stokes' theorem

$$D = \frac{1}{\pi} \left[ \oint_C d\mathbf{R} \cdot \mathbf{A}_n(\mathbf{R}) - \int_S d\mathbf{S} \cdot \mathbf{F}_n(\mathbf{R}) \right] \neq 0 \quad (4.26)$$

can lead to a  $\mathbb{Z}_2$  invariant that characterizes the system [125], [126].

Then,

$$H(\mathbf{R}) |n(\mathbf{R})\rangle = E_n(\mathbf{R}) |n(\mathbf{R})\rangle \rightarrow \partial H/\partial \mathbf{R} |n\rangle + H |\partial n/\partial \mathbf{R}\rangle = \partial E_n/\partial \mathbf{R} |n\rangle + E_n |\partial n/\partial \mathbf{R}\rangle$$

and because of the adiabatic assumption we can drop the first term on the right side. By changing the kets to bras and multiplying by  $|n'\rangle$  we obtain

$$\begin{aligned} \langle n | \partial H/\partial \mathbf{R} |n'\rangle + \langle \partial n/\partial \mathbf{R} | H |n'\rangle &= E_n \langle \partial n/\partial \mathbf{R} |n'\rangle \\ \langle n | \partial H/\partial \mathbf{R} |n'\rangle &= (E_n - E_{n'}) \langle \partial n/\partial \mathbf{R} |n'\rangle, \quad n \neq n' \end{aligned} \quad (4.32)$$

from which the result (4.30) follows.

In general, the fact that the wavefunction itself is gauge-dependent, creates an issue in computing  $\mathbf{A}_n$  via (4.18), and therefore  $\mathbf{F}_n$  via (4.22), since for slightly different  $\mathbf{R}$  values a numerical algorithm will generally output eigenstates with unrelated phases, thus prohibiting one from numerically taking the required derivative of the eigenvector unless care is taken to make sure the phases are smooth. However, (4.30) only requires the derivative of the Hamiltonian, and so any numerical phase will disappear in taking the inner product.

Similar manipulations lead to the Berry phase

$$\gamma_n = i \int d\mathbf{S} \cdot \sum_{n', n' \neq n} \frac{\langle n | \nabla_{\mathbf{R}} H |n'\rangle \times \langle n' | \nabla_{\mathbf{R}} H |n\rangle}{(E_n - E_{n'})^2}. \quad (4.33)$$

Although the previous forms depend only on a certain state and its derivative, the forms (4.30) and (4.33) involving summation over  $n' \neq n$  show that the Berry properties can be thought of as resulting from interactions between the  $n$ th state and all other states – it is a global property of the bandstructure.

Equations (4.30) and (4.33) show that the Berry curvature becomes singular if two energy levels  $E_n$  and  $E_{n'}$  are brought together at a certain value of  $\mathbf{R}$ , resulting in the ‘‘Berry monopole.’’ In fact, the adiabatic approximation assumes no degeneracies on the path  $C$ , but degeneracies can occur within the space enclosed by the path.

It is easy to show the conservation law<sup>8</sup>

$$\sum_n F_{\mu\nu}^n = 0, \quad (4.34)$$

which demonstrates, among other things, that the sum over all bands of the Berry curvature is zero.

<sup>8</sup>When we also do a summation over  $n$  then in fact we are taking all of the non-diagonal elements of the operators  $\partial H/\partial R^{\mu,\nu}$  into account. Then, for any states like  $|n\rangle \equiv |a\rangle$ ,  $|n'\rangle \equiv |b\rangle$ ;  $a \neq b$  there are another set of states like  $|n\rangle \equiv |b\rangle$ ,  $|n'\rangle \equiv |a\rangle$ ;  $a \neq b$  such that  $\langle n | \partial H/\partial R^\mu |n'\rangle \langle n' | \partial H/\partial R^\nu |n\rangle |_{(n=a, n'=b)} = \langle a | \partial H/\partial R^\mu |b\rangle \langle b | \partial H/\partial R^\nu |a\rangle$  and  $\langle n | \partial H/\partial R^\nu |n'\rangle \langle n' | \partial H/\partial R^\mu |n\rangle |_{(n=b, n'=a)} = \langle b | \partial H/\partial R^\nu |a\rangle \langle a | \partial H/\partial R^\mu |b\rangle = \langle a | \partial H/\partial R^\mu |b\rangle \langle b | \partial H/\partial R^\nu |a\rangle$  cancel out each other at the numerator.

As discussed later for the photonic case, under time-reversal (TR) and inversion (I) symmetries,

$$\text{TR: } \mathbf{F}(-\mathbf{k}) = -\mathbf{F}(\mathbf{k}) \quad (4.35)$$

$$\text{I: } \mathbf{F}(-\mathbf{k}) = \mathbf{F}(\mathbf{k}) \quad (4.36)$$

$$\text{TR+I: } \mathbf{F}(\mathbf{k}) = \mathbf{0}. \quad (4.37)$$

Therefore, a non-zero Berry curvature will exist when either TR or I are broken.

#### 4.1.4 Chern Number, Bulk-Edge Correspondence, and Topologically Protected Edge States

From elementary electromagnetics, Gauss's law relates the total flux over a closed surface  $S$  to the total charge within the surface,

$$\oint_S \varepsilon_0 \mathbf{E}(\mathbf{r}) \cdot d\mathbf{S} = Q^T = mq, \quad (4.38)$$

where, assuming identical charged particles,  $m$  is the number of particles and  $q$  the charge of each particle (although often approximated as a continuum,  $Q^T$  is quantized). To keep things simple we'll assume a monopole charge of strength  $mq$  located at the origin. The electric field is given by Coulombs law,

$$\mathbf{E} = \left( \frac{mq}{4\pi\varepsilon_0} \right) \frac{\mathbf{r}}{r^3}. \quad (4.39)$$

The analogous magnetic form

$$\oint_S \mathbf{B}(\mathbf{r}, t) \cdot d\mathbf{S} = 0 \quad (4.40)$$

indicates that there are no magnetic monopoles. However, in parameter space the flux integral over a closed manifold of the Berry curvature is quantized in units of  $2\pi$ , indicating the number of Berry monopoles (degeneracies) within the surface,

$$\oint_S d\mathbf{S} \cdot \mathbf{F}_n(\mathbf{R}) = 2\pi m_n = 2\pi C_n \quad (4.41)$$

where  $m_n = C_n$  is an integer for the  $n$ th band known as the *Chern number*. The Chern number can be seen to be the flux associated with a Berry monopole of strength  $2\pi C_n$ , leading to the Berry curvature

$$\mathbf{F}_n = \left( \frac{C_n}{2} \right) \frac{\mathbf{k}}{k^3}. \quad (4.42)$$

The Berry monopole plays the role of source/sink of Berry curvature  $\mathbf{F}$ , just the electric charge monopole  $mq$  servers as a source/sink of electric field  $\mathbf{E} \propto \mathbf{r}/r^3$ . The Chern number can also be



written in terms of the gauge form. For two dimensions, e.g.,  $\mathbf{R} = \mathbf{k} = (k_x, k_y)$ ,

$$C_n = \frac{1}{2\pi} \int_S dk_x dk_y F_{xy}^n = \frac{1}{2\pi} \int_S dk_x dk_y \left( \frac{\partial}{\partial k_x} A_n^y - \frac{\partial}{\partial k_y} A_n^x \right), \quad (4.43)$$

or, from (4.30),

$$C_n = \frac{i}{2\pi} \int_S dk_x dk_y \sum_{n', n' \neq n} \frac{\langle n | \partial H / \partial k_x | n' \rangle \langle n' | \partial H / \partial k_y | n \rangle - \langle n | \partial H / \partial k_y | n' \rangle \langle n' | \partial H / \partial k_x | n \rangle}{(E_n - E_{n'})^2}, \quad (4.44)$$

which is a form used later for computation.

Importantly, the Chern number is topologically invariant, meaning it is unaffected by smooth deformations in the surface that preserve topology (e.g., for a real-space surface, a teacup deforming into a torus). Moreover, the sum  $\sum_n C_n$  over all energies or bands  $n$  is zero (this comes from the curvature conservation equation (4.34)), which plays a role in what is known as bulk-edge correspondence. This is an extremely important point in understanding the most significant aspect of Topological Insulators (TIs), which is backscattering-protected edge propagation. Note that in the presence of TR but with I broken, integration over the entire BZ yields zero Chern number for each band, whereas in the presence of I but with TR broken, the band Chern number will generally be nonzero.

In periodic media (e.g., for electrons, in a crystalline solid, and for photons, EM waves in a photonic crystal), the Berry phase  $\gamma_n$  is a geometric (in parameter space) attribute of the  $n$ th band. The Brillouin zone is equivalent to a torus, forming the closed surface over which the Berry curvature of any non-degenerate band is integrated to compute the Chern number  $C_n$  for that band.

### Example - Two-level systems in parameter space

A common example that demonstrates Berry phase, curvature, and Chern number concepts is cyclic evolution of a two level system [122], such as electronic spin or valley pseudospin. Consider the evolution of spin for an electron at the origin immersed in a magnetic field. Let the tip of the magnetic field vector trace out a closed curve on a sphere of radius  $r = B_0$ ,  $\mathbf{B} = B_0 \hat{\mathbf{r}}(t)$  – in this case the magnetic field itself plays the role of parameter space,  $\mathbf{R} = (B_x, B_y, B_z)$ . The Hamiltonian is the projection of spin onto the magnetic field coordinates,

$$\mathbf{H} = -\boldsymbol{\mu} \cdot \mathbf{B} = -\gamma \mathbf{B} \cdot \mathbf{S}, \quad (4.45)$$

where  $\boldsymbol{\mu}$  is the magnetic moment ( $\boldsymbol{\mu} = \gamma \mathbf{S}$ ),  $\gamma$  is the gyromagnetic ratio ( $\gamma = q_e/2mc$  for orbital electrons,  $\gamma = gq_e/2mc$  where  $g \sim 2$ ),  $\mathbf{S} = (\hbar/2) \boldsymbol{\sigma}$ , and  $\boldsymbol{\sigma} = (\sigma_x, \sigma_y, \sigma_z)$  are the Pauli matrices

$$\sigma_x = \begin{pmatrix} 0 & 1 \\ 1 & 0 \end{pmatrix}, \quad \sigma_y = \begin{pmatrix} 0 & -i \\ i & 0 \end{pmatrix}, \quad \sigma_z = \begin{pmatrix} 1 & 0 \\ 0 & -1 \end{pmatrix}. \quad (4.46)$$

Whereas for magnetic moment due to a current loop the torque  $\mathbf{T} = \boldsymbol{\mu} \times \mathbf{B}$  acts to align  $\boldsymbol{\mu}$  and  $\mathbf{B}$ , for angular momentum and spin the torque causes a precession of  $\boldsymbol{\mu}$  around  $\mathbf{B}$ , with the precession frequency  $\omega_0 = -\gamma\mathbf{B}$ .

Writing the Hamiltonian as  $H = \mathbf{h} \cdot \boldsymbol{\sigma}$ , where  $\mathbf{h} = h\hat{\mathbf{r}}$  with  $h = -\gamma\hbar B_0/2$ ,

$$\sigma_r = h\hat{\mathbf{r}} \cdot \boldsymbol{\sigma} = h \begin{pmatrix} \cos\theta & e^{-i\phi}\sin\theta \\ e^{i\phi}\sin\theta & -\cos\theta \end{pmatrix}. \quad (4.47)$$

Eigenvalues and eigenvectors satisfy  $(h\boldsymbol{\sigma} \cdot \hat{\mathbf{r}})|u\rangle = \lambda|u\rangle$  and are

$$\lambda^+ = +h, \quad |u^+\rangle = \begin{pmatrix} e^{-i\phi}\cos(\theta/2) \\ \sin(\theta/2) \end{pmatrix}, \quad (4.48)$$

$$\lambda^- = -h, \quad |u^-\rangle = \begin{pmatrix} e^{-i\phi}\sin(\theta/2) \\ -\cos(\theta/2) \end{pmatrix}. \quad (4.49)$$

The Berry potential is  $\mathbf{A}^\pm(\mathbf{R}) = i\langle u^\pm | \nabla_{\mathbf{R}} | u^\pm \rangle$  where  $\mathbf{R} = (r, \theta, \phi)$ . Since the gradient is  $\nabla f = \frac{\partial f}{\partial r}\hat{\mathbf{r}} + \frac{1}{r}\frac{\partial f}{\partial\theta}\hat{\boldsymbol{\theta}} + \frac{1}{r\sin\theta}\frac{\partial f}{\partial\phi}\hat{\boldsymbol{\phi}}$ ,

$$A_\theta^- = i\langle u^- | \frac{\partial}{h\partial\theta} | u^- \rangle = 0, \quad A_\theta^+ = i\langle u^+ | \frac{\partial}{h\partial\theta} | u^+ \rangle = 0, \quad (4.50)$$

$$A_\phi^- = i\langle u^- | \frac{1}{h\sin\theta}\frac{\partial}{\partial\phi} | u^- \rangle = \frac{\sin^2\frac{1}{2}\theta}{h\sin\theta}, \quad A_\phi^+ = i\langle u^+ | \frac{1}{h\sin\theta}\frac{\partial}{\partial\phi} | u^+ \rangle = \frac{\cos^2\frac{1}{2}\theta}{h\sin\theta}. \quad (4.51)$$

The Berry curvature is

$$\mathbf{F}^\pm = \frac{1}{h\sin\theta} \left( \frac{\partial}{\partial\theta} (A_\phi^\pm \sin\theta) \right) \hat{\mathbf{h}} = \pm \frac{1}{2} \frac{\mathbf{h}}{h^3}, \quad (4.52)$$

which is the field generated by a monopole (in parameter space) at the origin. Obviously, the Berry curvature has a singularity at  $h = 0$  (i.e.,  $B_0 = 0$ ). This singularity is due to a degeneracy between  $\lambda^+ = h$  and  $\lambda^- = -h$  at the origin of parameter space ( $h = 0$ ); these degeneracy points serve as ‘‘sources’’ (for  $\lambda^-$ , producing monopole strength  $1/2$ ) and ‘‘sinks’’ (for  $\lambda^+$ , producing monopole strength  $-1/2$ ) of Berry curvature (like any monopole). Similar to Gauss’s law, when we integrate around a closed surface containing the monopole we get an integer (here we call it the Chern number). The Chern number is

$$C = \oint_S \mathbf{F} \cdot d\mathbf{S} = \pm \oint_S \frac{1}{2} \frac{\mathbf{h}}{h^3} \cdot \hat{\mathbf{h}} h^2 \sin\theta \, d\theta d\phi = \pm 2\pi = \pm \frac{1}{2} \Omega. \quad (4.53)$$

Given that

$$\gamma_n = \int_S d\mathbf{S} \cdot \mathbf{F}_n(\mathbf{R}), \quad (4.54)$$

the Berry phase can be viewed as  $1/2$  the solid angle subtended by the closed path,

$$\gamma = \pm \int_S \frac{1}{2} \frac{\mathbf{h}}{\hbar^3} \cdot \hat{\mathbf{h}} h^2 \sin \theta \, d\theta d\phi = \pm \frac{1}{2} \int_S \sin \theta \, d\theta d\phi = \pm \frac{1}{2} \Omega. \quad (4.55)$$

In fact, in general the answer is  $s\Omega$ , where  $\Omega$  is the solid angle and  $s$  is the spin.

As a related example, but considering momentum space as the parameter space, consider a two-dimensional material with a hexagonal lattice and two inequivalent Dirac points, such as graphene. The two inequivalent Dirac points lead to two different valleys sufficiently separated in momentum space so that inter-valley transitions can usually be ignored. In the absence of a magnetic field, graphene respects both TR and I symmetry (and, hence, has zero Berry curvature, but poses a Berry phase). The tight-binding Hamiltonian near the  $K$  and  $K'$  valleys has the same form as the magnetic field problem considered above,

$$H = \tau \hbar v_F \mathbf{q}_\tau \cdot \boldsymbol{\sigma}, \quad (4.56)$$

where  $\mathbf{q}_\tau = (q_x, \tau q_y)$  is momentum relative to the degeneracy point,  $\tau = \pm 1$  is the valley index (for the  $K$  and  $K'$  points, respectively), and  $s = \pm 1$  is the conduction and valance band index. In this case the two inequivalent valleys play the role of spin, and so here  $\sigma$  represents pseudospin, not actual spin. In the  $K$  valley conduction band, the projection of pseudospin onto momentum is parallel to momentum, whereas in the valance band it is antiparallel to momentum. In the  $K'$  valley these are reversed.

The eigenvalues and eigenvectors are <sup>9</sup>

$$\lambda^{s,\tau} = s \hbar v_F |\mathbf{q}_\tau|, \quad |u^{s,\tau}\rangle = \frac{1}{\sqrt{2}} \begin{pmatrix} 1 \\ s\tau e^{i\phi_{\mathbf{q}}} \end{pmatrix} e^{i\mathbf{q}_\tau \cdot \mathbf{r}}, \quad (4.58)$$

where  $(q_x + iq_y) = |\mathbf{q}| e^{i\phi_{\mathbf{q}}}$ ,  $\phi_{\mathbf{q}}$  being the angle between  $\mathbf{q}$  and the  $x$ -axis,  $\phi_{\mathbf{q}} = \tan^{-1}(q_y/q_x)$ . Then, since the gradient is  $\nabla f = \frac{\partial f}{\partial q} \hat{\mathbf{q}} + \frac{1}{q} \frac{\partial f}{\partial \phi_{\mathbf{q}}} \hat{\phi}_{\mathbf{q}} + \frac{\partial f}{\partial z} \hat{\mathbf{z}}$ ,

$$A_{\phi_{\mathbf{q}}}^{s,\tau} = i \langle u^{s,\tau} | \frac{1}{q} \frac{\partial}{\partial \phi_{\mathbf{q}}} | u^{s,\tau} \rangle = -\frac{1}{2} \frac{1}{q}, \quad (4.59)$$

and [128]

$$\gamma_n = \oint_C d\mathbf{q} \cdot \mathbf{A}(\mathbf{q}) = \int_0^{2\pi} -\frac{1}{2} \frac{1}{q} q d\phi_{\mathbf{q}} = -\pi. \quad (4.60)$$

The Berry phase of  $\pi$  manifests itself in various ways, including in the suppression of backscattering

---

<sup>9</sup>The often used eigenfunctions

$$|u^{s,\tau}\rangle = \frac{1}{\sqrt{2}} \begin{pmatrix} e^{-i\phi_{\mathbf{q}}/2} \\ s\tau e^{i\phi_{\mathbf{q}}/2} \end{pmatrix} e^{i\mathbf{q}_\tau \cdot \mathbf{r}}, \quad (4.57)$$

are not appropriate since they are not single-valued [127]

and a phase shift in Shubnikov de-Haas (SdH) oscillations [129]. Note, however, that

$$\mathbf{F} = \frac{1}{q} \frac{\partial}{\partial q} (qA_{\phi_{\mathbf{a}}}) \hat{\mathbf{z}} = -\frac{1}{q} \frac{\partial}{\partial q} \left( \frac{1}{2} \right) \hat{\mathbf{z}} = 0, \quad (4.61)$$

so that in (non-gapped) graphene, which has both time-reversal and inversion symmetry, the Berry curvature vanishes.

Finally, let us consider the optical fiber wound into a helix as mentioned previously. For a linearly polarized optical field we have  $(\boldsymbol{\sigma} \cdot \mathbf{k})|u\rangle = \lambda|u\rangle$ , which is the projection of spin (e.g., polarization) onto the direction of momentum. This has the same general form as the magnetic field problem. However, for photons (spin 1), the spin matrices are different and Berry phase is equal to the solid angle,  $\gamma = \Omega$ .

### Bulk-Edge Correspondence

An aspect of Berry curvature that is of immense interest in both electronic and photonic applications is the presence of one-way edge modes that are topologically protected from backscattering. The idea of Hall conductivity in an insulator gives some intuition about the one-way nature of these modes. Consider a finite-sized rectangle of thin material, immersed in a perpendicular magnetic field as depicted in Fig. 4.3. Bound electrons will circulate in response to the applied field, and those near the edge will have their orbits terminated by the edge[133]. The net effect is to have a uni-directional movement of electrons at the edge (orange arrows). The presence of a Hall conductivity (whether due

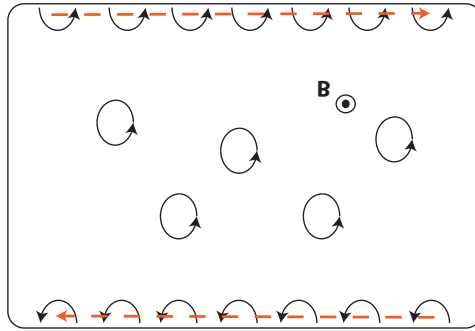


Figure 4.3: Depiction of electron orbits in an insulator in the presence of a magnetic field, and interrupted orbits at the edge.

to a magnetic field in the ordinary manner, or due to non-zero Berry curvature associated with broken TR or I symmetry) will elicit a similar response, although the response is quantized as described above. Thus, the bulk properties of the insulating material will result in a conducting edge state. This happens in both the electronic case, and the photonic case to be described below.

Furthermore, consider that the Chern number and all Berry properties are related to an infinite bulk material, which generates bandstructure. However, in any practical application the material is finite, and has an interface with another medium. Let's consider a planar interface between medium 1

and medium 2. Far from the interface, in each region, particles (electrons, photons) will be governed by the respective Hamiltonians  $H_{1,2}$ . Let's assume that both materials share a common bandgap, and that  $C_{\text{gap},1} = \sum_{n < n_g} C_n^{(1)}$ , the Chern number sum over bands below the gap for material 1, and  $C_{\text{gap},2} = \sum_{n < n_g} C_n^{(2)}$ , the corresponding sum for material 2, differ,  $C_{\text{gap},\Delta} = C_2 - C_1 \neq 0$ . For some parameter value the shared bandgap between the two mediums can close and then reopen. At the closing point there is a degeneracy, and as the gap reopens it can be crossed by a surface mode, as depicted in Fig. 4.4. The edge-modes are circularly-polarized (spin-polarized), and in periodic media are localized to a few lattice constants from the material boundary.

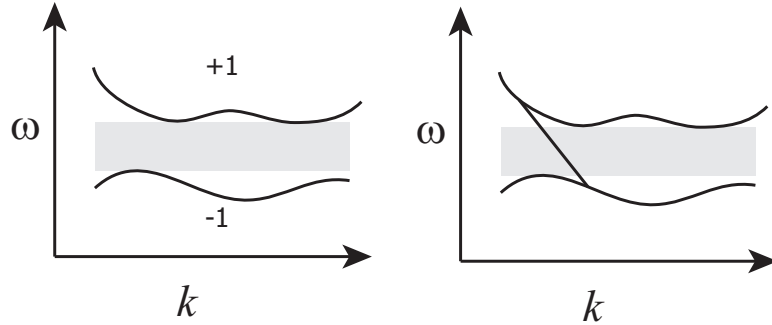


Figure 4.4: Bulk-edge correspondence. Materials with common bandgap and different Chern numbers share an interface where a uni-directional edge state closes the gap.

The existence of the surface/edge state is necessitated by the bulk material characteristics, and so is independent of interface details. Therefore, the interface can possess discontinuities, defects, etc., which will not affect the surface wave. It can also be seen that the fact that the surface/edge states connect different energy levels indicates that they will have a group velocity that has definite sign (i.e., one-directional propagation). Therefore, in summary, the surface states are unidirectional and topologically protected from backscattering.

## 4.2 Electromagnetic Description - Berry quantities for photons

Although the concept of Berry phase is general for any cyclic variation through some parameter space  $\mathbf{R}$ , a primary application is to periodic solid state systems (e.g., electrons in a crystal lattice), although here we are primarily interested in the photonic analogous of those systems, photonic topological insulators (PTIs) for both photonic crystals and for continuum media.

For simplicity in observing the correspondence between Maxwell's equations and the evolution equation (4.2), we first assume lossless and dispersionless materials characterized by dimensionless real-valued parameter  $\bar{\epsilon}$ ,  $\bar{\mu}$ ,  $\bar{\xi}$ ,  $\bar{\varsigma}$ , representing permittivity, permeability and magneto-electric coupling tensors. Although any real material must have frequency dispersion, this simple model allows

a straightforward conversion of various Berry quantities from the electronic to the electromagnetic case. The inclusion of both frequency and spatial dispersion will be discussed later.

In this case, Maxwell's equations are

$$\begin{aligned}\nabla \times \mathbf{E} &= -\mu_0 \bar{\mu} \cdot \frac{\partial \mathbf{H}}{\partial t} - \frac{\bar{\xi}}{c} \cdot \frac{\partial \mathbf{E}}{\partial t} - \mathbf{J}_m \\ \nabla \times \mathbf{H} &= \epsilon_0 \bar{\epsilon} \cdot \frac{\partial \mathbf{E}}{\partial t} + \frac{\bar{\xi}}{c} \cdot \frac{\partial \mathbf{H}}{\partial t} + \mathbf{J}_e.\end{aligned}\quad (4.62)$$

By defining the matrices

$$\begin{aligned}M &= \begin{pmatrix} \epsilon_0 \bar{\epsilon} & \frac{1}{c} \bar{\xi} \\ \frac{1}{c} \bar{\xi} & \mu_0 \bar{\mu} \end{pmatrix}, \quad N = \begin{pmatrix} 0 & i \nabla \times \mathbf{I}_{3 \times 3} \\ -i \nabla \times \mathbf{I}_{3 \times 3} & 0 \end{pmatrix}, \\ f &= \begin{pmatrix} \mathbf{E} \\ \mathbf{H} \end{pmatrix}, \quad g = \begin{pmatrix} \mathbf{D} \\ \mathbf{B} \end{pmatrix} = Mf, \quad J = \begin{pmatrix} \mathbf{J}_e \\ \mathbf{J}_m \end{pmatrix}\end{aligned}\quad (4.63)$$

where  $M$  is Hermitian and real-valued, we can write Maxwell's equations in a compact form [134],

$$N \cdot f = i \left[ \frac{\partial g}{\partial t} + J \right] = i \left[ M \frac{\partial f}{\partial t} + \frac{\partial M}{\partial t} f + J \right]. \quad (4.64)$$

Note that the units of the sub-blocks of  $M$  differ (as do the dimensions of the 6-vectors  $f$  and  $g$ ), and that  $\epsilon$ ,  $\xi$ ,  $\varsigma$ , and  $\mu$  are dimensionless. In the absence of an external excitation ( $J = 0$ ) and assumption of non-dispersive (instantaneous) materials, Maxwell's equations become

$$i \frac{\partial f}{\partial t} = H_{cl} \cdot f \quad (4.65)$$

where  $H_{cl} = M^{-1} \cdot N$ , which has the same form as the evolution equation (4.2) (e.g., the Schrödinger equation) with  $\hbar = 1$ , where the operator  $H_{cl}$  plays the role of a classical Hamiltonian. Because of this similarity between Maxwell's equations and the evolution equation (4.2) it is straightforward to extend the Berry potential concept to electromagnetic energy (photons); rather than, say, electrons acquiring a Berry phase while transversing a path in parameters space, photons will do the same (the polarization of the photon plays the role of particle spin). In this case, we define  $f_n$  as a six-component eigenmode satisfying<sup>10</sup>

$$H_{cl} \cdot f_n = E_n f_n \quad (4.66)$$

where  $E_n = \omega_n$ . Under a suitable inner product (discussed below)  $H_{cl}$  is Hermitian, and assuming the normalization condition  $\langle f_n | f_m \rangle = \delta_{nm}$ , the Berry vector potential has the same form as (4.12)

$$\mathbf{A}_n = i \langle f_n | \nabla_{\mathbf{R}} f_n \rangle. \quad (4.67)$$

<sup>10</sup>In (4.63) and (5.2)  $f$  is real-valued, unlike in the Schrödinger equation where the wavefunction is complex-valued. The eigenfunctions in (4.66)  $f_n$  are complex-valued.

If we assume a photonic crystal (periodic structure),  $f_n$  has the Bloch form  $f_n(\mathbf{r}) = u_n(\mathbf{r}) e^{i\mathbf{k}\mathbf{r}}$ , where  $u_n(\mathbf{r})$  is the periodic Bloch function and  $\mathbf{k}$  is the Bloch wavevector. In this case,  $\nabla_{\mathbf{R}} = \nabla_{\mathbf{k}}$  operates over parameter space  $\mathbf{k} = (k_x, k_y, k_z)$  and

$$\mathbf{A}_n = i \langle u_n | \nabla_{\mathbf{k}} u_n \rangle \quad (4.68)$$

where the inner product is

$$\langle u_n | u_m \rangle = \frac{1}{2} \int_{\text{BZ}} u_n^*(\mathbf{r}) M(\mathbf{r}) u_m(\mathbf{r}) d\mathbf{r}. \quad (4.69)$$

This is the dispersionless special case of the result presented in [20] (see (41) in that reference), generalized to account for magnetoelectric coupling parameters in  $M$ .

The extension to dispersive media (i.e., real materials) would seem difficult since the simple product  $g = Mf$  in (4.63) becomes a convolution in time. However, it is shown in [20] (omitting magnetoelectric parameters, although this can also be included) that the only necessary modification to allow for dispersive materials  $M = M(\omega)$  is to replace  $M$  in (4.69) with  $\partial(\omega M(\omega))/\partial\omega$ , so that

$$\langle u_n | u_m \rangle = \frac{1}{2} \int_{\text{BZ}} u_n^*(\mathbf{r}) \frac{\partial(\omega M(\omega))}{\partial\omega} u_m(\mathbf{r}) d\mathbf{r}. \quad (4.70)$$

The material continuum model will be considered below.

#### 4.2.1 Some electromagnetic material classes that possess non-trivial Chern numbers

Although the field of topological photonic insulators is still being developed, there are several classes of materials and structures which possess topological protection and non-trivial Chern numbers. The approaches to design PTIs can be roughly divided into two categories. The first one relies on breaking of time-reversal symmetry by applying a static magnetic field to a gyromagnetic material [135] or time-harmonic modulation of coupled resonators [136], [137]. Another approach involves time-reversal-invariant metamaterials, where photon states are separated in two ‘spin’ sub-spaces (usually through geometry such as via a hexagonal lattice), and ‘spin-orbit’ coupling is introduced through symmetry-breaking exploring such non-trivial characteristics of metamaterials as chirality, bianisotropy and hyperbolicity [138], [139]. For an electromagnetic standpoint, the most important aspect of a PTI is the presence of surface/edge states that are topologically protected from backscattering (having non-trivial Chern number).

In classical electromagnetics, the fields  $\mathbf{E}$ ,  $\mathbf{D}$ , and  $\mathbf{P}$  are even under time reversal (do not change with time-reversal), whereas  $\mathbf{A}_{\text{mag}}$ ,  $\mathbf{B}$ ,  $\mathbf{H}$ ,  $\mathbf{J}$ , and  $\mathbf{S}$  (Poynting vector) are odd under time reversal

(negated under time reversal). For systems with time-reversal (TR) symmetry,

$$F_{\alpha\beta}^n(\mathbf{k}) = -F_{\alpha\beta}^n(-\mathbf{k}). \quad (4.71)$$

Furthermore, the fields  $\mathbf{B}$  and  $\mathbf{H}$  are even under space inversion, whereas  $\mathbf{E}$ ,  $\mathbf{D}$ ,  $\mathbf{J}$ ,  $\mathbf{P}$ ,  $\mathbf{A}_{\text{mag}}$ , and  $\mathbf{S}$  are odd under spatial inversion. For systems with parity/inversion (I) symmetry,

$$F_{\alpha\beta}^n(\mathbf{k}) = F_{\alpha\beta}^n(-\mathbf{k}), \quad (4.72)$$

so that if both symmetries are present,

$$F_{\alpha\beta}^n(\mathbf{k}) = 0. \quad (4.73)$$

Systems having both spatial-inversion and time-reversal symmetry will exhibit trivial topology in momentum space, so that no one-way edge mode will exist (all bands have  $C_n = 0$ ).

Regarding periodic materials, Dirac (linear) degeneracies will occur for hexagonal lattices, and other lattice types may exhibit other degeneracies (e.g., quadratic degeneracies consisting of double Dirac degeneracies for a cubic lattice [140], [141], but, regardless of degeneracy type, for, e.g., a simple lattice of material cylinders in a host medium, if the cylinders are made of simple isotropic materials have scalar material properties  $\varepsilon$  and  $\mu$ , the system will be both space-inversion and time-reversal symmetric, and all bands will have trivial Chern number.

In the periodic case the degeneracies can be broken in several ways. One way that has been widely studied is to use rods with materials that themselves break TR symmetry [141], or to embed, say, a hexagonal array of nonreciprocal rods into another array of simple rods [142] so that both arrays share a common bandgap. The resulting nonreciprocal structure will generally have bands of non-trivial Chern number, leading to a non-zero gap Chern number. A detailed example is provided below. Large Chern numbers can be achieved by increasing spatial symmetry to result in point degeneracies of higher order (e.g., several co-located Dirac points), and then to, say, introduce TR breaking [143].

Another method to create a nontrivial Chern number is to use simple materials (simple dielectrics and metals), but to break inversion symmetry by deforming the lattice. For example, in [144] simple dielectric rods are used in a hexagonal pattern, resulting in a Dirac degeneracy and trivial Chern number. Slightly deforming the lattice can result in inversion-symmetry breaking, and  $C_{\text{gap}} \neq 0$ . Various other schemes have also been proposed [138], [115].

## 4.2.2 Berry quantities for continuum media

Although the electronic case, and, by analogy, the photonic case, were developed for periodic systems (for which the relations provided in sections 4.1.2 and 4.1.3 hold), it turns out that continuum material models can also lead to nontrivial Chern numbers. The simplest example is of a biased



plasma (magneto-plasma) as considered in Fig. 1, with permittivity tensor

$$\bar{\epsilon} = \begin{pmatrix} \epsilon_{11} & \epsilon_{12} & 0 \\ \epsilon_{21} & \epsilon_{22} & 0 \\ 0 & 0 & \epsilon_{33} \end{pmatrix} \quad (4.74)$$

where typically  $\epsilon_{21} = \epsilon_{12}^*$  and  $\epsilon_{11} = \epsilon_{22} = \epsilon_{33}$  (in the absence of a bias field  $\epsilon_{12} = 0$ , the material is reciprocal, and  $\bar{\epsilon}$  reduces to a scalar). An example involving this type of material is provided below. At the interface between the magneto-plasma and an ordinary (unbiased) plasma, a topologically protected edge mode can exist [132], [130], [131]. In addition, more complicated materials combining hyperbolic and chiral response have been shown to be topologically nontrivial [139].

A continuum material presents a difficulty in that, rather than have a periodic Brillouin zone that is, effectively, a closed surface (equivalent to a torus), providing the surface over which the Chern number can be computed, the momentum-space of an infinite homogeneous material continuum model does not form a closed surface. However, in [132] it is shown that 2D momentum space can be mapped to the Riemann sphere, forming the necessary surface (north and south poles being exceptional points, as discussed below).

Another issue, for both periodic and continuum models, is to account for material dispersion. Following the result in [20] for lossless dispersive local periodic media, in [132] continuum models of dispersive lossless, and possibly wavevector-dependent (nonlocal) materials are considered. The Berry potential is again given by (4.12), with the inner product<sup>11</sup>

$$\langle f_n | f_m \rangle = \frac{1}{2} f_n^* \frac{\partial (\omega M(\omega))}{\partial \omega} f_m. \quad (4.75)$$

### 4.3 Continuum Photonic Example

This example is related to [130] (see also [131]), with Berry quantities and Chern number analysis directly taken from the seminal work [132].

As an example of a nonreciprocal continuous medium, we consider a magnetized plasma in the Voigt configuration (propagation perpendicular to the bias magnetic field  $\mathbf{B}$ ), as depicted in Fig. 4.5.

For a single-component plasma biased with a static magnetic field  $\mathbf{B} = \mathbf{z}B_z$ , the permeability is  $\mu = \mu_0$  and the relative permittivity has the form of a Hermitian antisymmetric tensor,

$$\bar{\epsilon} = \begin{pmatrix} \epsilon_{11} & \epsilon_{12} & 0 \\ \epsilon_{21} & \epsilon_{22} & 0 \\ 0 & 0 & \epsilon_{33} \end{pmatrix} \quad (4.76)$$

---

<sup>11</sup>The most general result in [132] is more complicated, but for a wide range of material classes the simpler result shown here holds.

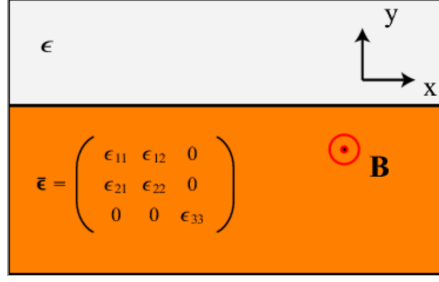


Figure 4.5: Interface between a magnetic-field biased plasma (bottom) and a simple material (top).

where

$$\begin{aligned}\varepsilon_{11} = \varepsilon_{22} &= 1 - \frac{\omega_p^2}{\omega^2 - \omega_c^2}, \quad \varepsilon_{33} = 1 - \frac{\omega_p^2}{\omega^2}, \\ \varepsilon_{12} = -\varepsilon_{21} &= i \frac{-\omega_c \omega_p^2}{\omega(\omega^2 - \omega_c^2)}\end{aligned}\quad (4.77)$$

where the cyclotron frequency is  $\omega_c = (q_e/m_e)B_z$  and the plasma frequency is  $\omega_p^2 = N_e q_e^2 / \varepsilon_0 m_e$ . In the above,  $N_e$  is the free electron density, and  $q_e$  and  $m_e$  are the electron charge and mass, respectively.

We will also consider the material model examined in [132], where  $\varepsilon_{33} = 1$  and

$$\varepsilon_{11} = \varepsilon_{22} = 1 - \frac{\omega_0 \omega_e}{\omega^2 - \omega_0^2}, \quad \varepsilon_{12} = \varepsilon_{21} = i \frac{\omega \omega_e}{\omega^2 - \omega_0^2}, \quad (4.78)$$

where  $|\omega_0|$  is the resonance frequency and  $\omega_e$  determines the resonance strength, with  $\omega_0 \omega_e > 0$ .

For propagation in the  $x - y$  plane,  $\mathbf{k} = (k_x, k_y, 0)$ , the plane wave supported by this medium can be decoupled into TE ( $E_z \neq 0, H_z = 0$ ) and TM ( $E_z = 0, H_z \neq 0$ ) waves. Since there is no magneto-electric coupling  $\bar{\xi} = \bar{\zeta} = 0$ , the dispersion of these modes is

$$k^2 = \frac{\varepsilon_{11}^2 + \varepsilon_{12}^2}{\varepsilon_{11}} \left( \frac{\omega_n}{c} \right)^2, \quad \text{TM mode} \quad (4.79)$$

$$k^2 = \varepsilon_{33} \left( \frac{\omega_n}{c} \right)^2, \quad \text{TE mode} \quad (4.80)$$

such that  $\omega_n$  is the eigenfrequency of each mode. Despite the non-reciprocal nature of the medium itself, in the Voigt configuration the bulk dispersion behavior is reciprocal (an interface will break this reciprocity). The dispersion curves for these material are shown in Fig. 4.6 (the spatial cutoff is described later).

The associated electromagnetic waves envelopes can be obtained by finding the solution  $f = [\mathbf{E}, \mathbf{H}]^T$ , of (4.66),  $N \cdot f = \omega M \cdot f$ , which is

$$\begin{pmatrix} 0 & -\mathbf{k} \times \mathbf{I}_{3 \times 3} \\ \mathbf{k} \times \mathbf{I}_{3 \times 3} & 0 \end{pmatrix} \cdot \begin{pmatrix} \mathbf{E} \\ \mathbf{H} \end{pmatrix} = \begin{pmatrix} \omega \varepsilon_0 \bar{\varepsilon} & 0 \\ 0 & \omega \mu_0 \mathbf{I}_{3 \times 3} \end{pmatrix} \cdot \begin{pmatrix} \mathbf{E} \\ \mathbf{H} \end{pmatrix} \quad (4.81)$$

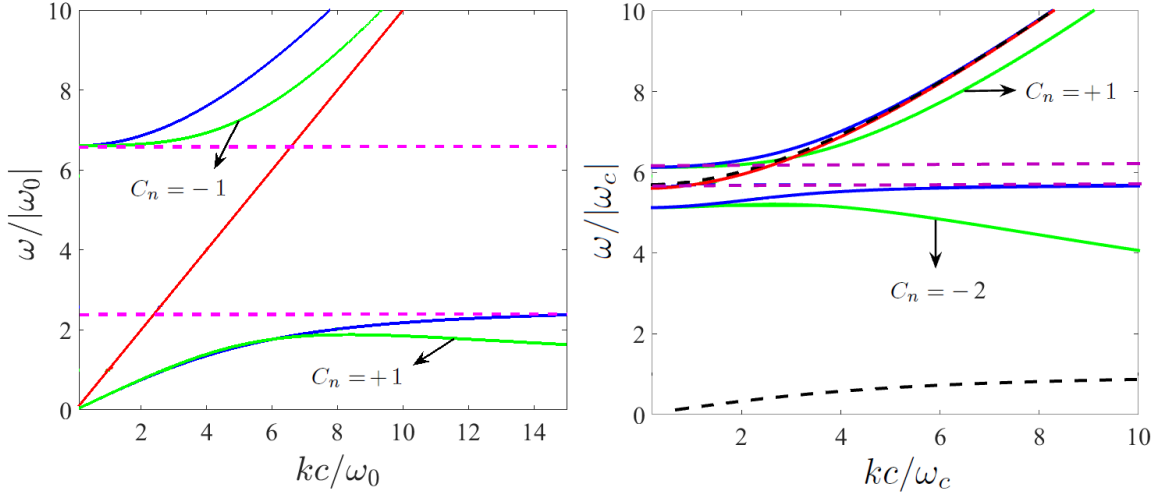


Figure 4.6: Band diagram and Chern numbers (TM modes) for a magneto-optic material; blue: TM mode, no spatial cut-off, green: TM mode, with spatial cut-off, red: TE mode, purple: gap. Left: magneto-optic material (4.78) with  $\omega_e/\omega_0 = 5.6$  and  $k_{\max} = 10$  ( $\omega_0/c$ ), right: magneto-optic material (4.77) with  $\omega_p/2\pi = 9.7$  THz,  $\omega_c/2\pi = 1.73$  THz ( $\omega_p/\omega_c = 5.6$ ), and  $k_{\max} = 10$  ( $\omega_c/c$ ), black: SPP dispersion.

so that

$$\begin{pmatrix} -\mathbf{I}_{3 \times 3} & -\frac{\bar{\epsilon}^{-1}}{\omega \epsilon_0} \cdot \mathbf{k} \times \mathbf{I}_{3 \times 3} \\ \frac{1}{\omega \mu_0} \cdot \mathbf{k} \times \mathbf{I}_{3 \times 3} & -\mathbf{I}_{3 \times 3} \end{pmatrix} \cdot \begin{pmatrix} \mathbf{E} \\ \mathbf{H} \end{pmatrix} = 0. \quad (4.82)$$

With  $\mathbf{H} = \hat{\mathbf{z}} \rightarrow \mathbf{E} = \bar{\epsilon}^{-1} \cdot \frac{\hat{\mathbf{z}} \times \mathbf{k}}{\omega \epsilon_0}$  (TM),  $\mathbf{E} = \hat{\mathbf{z}} \rightarrow \mathbf{H} = \frac{\mathbf{k}}{\omega \mu_0} \times \hat{\mathbf{z}}$  (TE), we have the  $6 \times 1$  vectors

$$\begin{aligned} f_{nk}^{\text{TM}} &= \begin{pmatrix} \bar{\epsilon}^{-1} \cdot \hat{\mathbf{z}} \times \frac{\mathbf{k}}{\epsilon_0 \omega_{nk}} \\ \hat{\mathbf{z}} \end{pmatrix}, \\ f_{nk}^{\text{TE}} &= \begin{pmatrix} \hat{\mathbf{z}} \\ \frac{\mathbf{k}}{\mu_0 \omega_{nk}} \times \hat{\mathbf{z}} \end{pmatrix}. \end{aligned} \quad (4.83)$$

Because the envelopes of the electromagnetic waves in the above equations are not normalized, the Berry potential is computed using

$$\mathbf{A}_{nk} = \frac{\text{Re}\{i f_{nk}^* \cdot \frac{\partial}{\partial \omega} (\omega M_{(\omega)}) \partial_k f_{n,k}\}}{f_{nk}^* \cdot \frac{\partial}{\partial \omega} (\omega M_{(\omega)}) f_{n,k}}. \quad (4.84)$$

Considering the Riemann sphere mapping of the  $k_x - k_y$  plane as detailed in [132], it is possible to write the Chern number associated with  $n$ th eigenmode branch as

$$C_n = \frac{1}{2\pi} \int \mathbf{A}_{n,k=\infty} \cdot d\mathbf{l} - \frac{1}{2\pi} \int \mathbf{A}_{n,k=0^+} \cdot d\mathbf{l} \quad (4.85)$$

where the two line integrals are over infinite and infinitesimal radii (north and south poles of the

Riemann sphere), respectively. If we define  $A_{nk} = \mathbf{A}_{nk} \cdot \hat{\phi}$  then we have

$$C_n = \lim_{k \rightarrow \infty} (A_{n,\phi=0}k) - \lim_{k \rightarrow 0^+} (A_{n,\phi=0}k). \quad (4.86)$$

For a lossless TM-mode in propagating in the  $x - y$  plane we have  $k = k_x \hat{\mathbf{x}} + k_y \hat{\mathbf{y}} = k \cos(\phi) \hat{\mathbf{x}} + k \sin(\phi) \hat{\mathbf{y}}$ . Writing

$$\bar{\epsilon}^{-1} = \begin{pmatrix} \alpha_{11} & \alpha_{12} & 0 \\ \alpha_{21} & \alpha_{22} & 0 \\ 0 & 0 & \alpha_{33} \end{pmatrix} \quad (4.87)$$

we have

$$f_{nk} = \begin{pmatrix} \bar{\epsilon}^{-1} \cdot \hat{\mathbf{z}} \times \frac{\mathbf{k}}{\epsilon_0 \omega_n k} \\ \hat{\mathbf{z}} \end{pmatrix} = \begin{pmatrix} \frac{-\alpha_{11}k_y + \alpha_{12}k_x}{\epsilon_0 \omega_n} \\ \frac{-\alpha_{21}k_y + \alpha_{22}k_x}{\epsilon_0 \omega_n} \\ 0 \\ 0 \\ 0 \\ 1 \end{pmatrix}, \quad \partial_k f_{nk} = \begin{pmatrix} \frac{-\alpha_{11}\hat{y} + \alpha_{12}\hat{x}}{\epsilon_0 \omega_n} \\ \frac{-\alpha_{21}\hat{y} + \alpha_{22}\hat{x}}{\epsilon_0 \omega_n} \\ 0 \\ 0 \\ 0 \\ 0 \end{pmatrix} \quad (4.88)$$

where

$$\alpha_{11} = \frac{\epsilon_{22}}{\epsilon_{11}\epsilon_{22} - \epsilon_{12}\epsilon_{21}}, \quad \alpha_{22} = \frac{\epsilon_{11}}{\epsilon_{11}\epsilon_{22} - \epsilon_{12}\epsilon_{21}}, \quad \alpha_{12} = \frac{-\epsilon_{12}}{\epsilon_{11}\epsilon_{22} - \epsilon_{12}\epsilon_{21}}, \quad \alpha_{21} = \frac{-\epsilon_{21}}{\epsilon_{11}\epsilon_{22} - \epsilon_{12}\epsilon_{21}}, \quad (4.89)$$

such that

$$f_{nk}^* = \frac{1}{\epsilon_0 \omega_n} \begin{pmatrix} (-\alpha_{11}k_y + \alpha_{12}k_x)^* & (-\alpha_{21}k_y + \alpha_{22}k_x)^* & 0 & 0 & 0 & 1 \end{pmatrix}. \quad (4.90)$$

From the frequency derivative of the material response matrix,  $\partial_\omega(\omega M)$ , we have  $\beta_{ij} = \partial_\omega(\omega \epsilon_0 \epsilon_{ij})$ .

So, for the Berry potential we have

$$\mathbf{A}_{nk} = \frac{Re\{i f_{nk}^* \cdot \frac{1}{2} \frac{\partial}{\partial \omega}(\omega M(\omega)) \partial_k f_{n,k}\}}{f_{nk}^* \cdot \frac{1}{2} \frac{\partial}{\partial \omega}(\omega M(\omega)) f_{n,k}} = \frac{Re\{N_x + N_y\}}{D} \quad (4.91)$$

where

$$N_x = \frac{i}{2(\epsilon_0 \omega_n)^2} \{-2\alpha_{11}\alpha_{12}[k_x\beta_{12} + k_y\beta_{11}] + (|\alpha_{11}|^2 + |\alpha_{12}|^2)[k_x\beta_{11} - k_y\beta_{12}]\} \hat{x} \quad (4.92)$$

$$N_y = \frac{i}{2(\epsilon_0 \omega_n)^2} \{2\alpha_{11}\alpha_{12}[k_x\beta_{11} - k_y\beta_{12}] + (|\alpha_{11}|^2 + |\alpha_{12}|^2)[k_x\beta_{12} + k_y\beta_{11}]\} \hat{y}$$

$$D = \frac{|k|^2}{2(\epsilon_0 \omega_n)^2} [ (|\alpha_{11}|^2 + |\alpha_{12}|^2)\beta_{11} - 2\alpha_{11}\alpha_{12}\beta_{12} ] + \frac{\mu_0}{2}. \quad (4.93)$$

Therefore, for the Chern number calculation we obtain

$$A_n = \mathbf{A}_n \cdot \hat{\phi} = \frac{\text{Re}\{N_y \cos(\phi) - N_x \sin(\phi)\}}{D} \quad (4.94)$$

$$A_n(\phi = 0) = \frac{\text{Re}\{N_y(\phi = 0)\}}{D}, \quad N_y(\phi = 0) = \frac{ik}{(\epsilon_0 \omega_n)^2} \{2\alpha_{11}\alpha_{12}\beta_{11} + (|\alpha_{11}|^2 + |\alpha_{12}|^2)\beta_{12}\}$$

$$A_n(\phi = 0)k = \frac{\text{Re}\left(\frac{i|k|^2}{(\epsilon_0 \omega_n)^2} \{2\alpha_{11}\alpha_{12}\beta_{11} + (|\alpha_{11}|^2 + |\alpha_{12}|^2)\beta_{12}\}\right)}{\frac{|k|^2}{(\epsilon_0 \omega_n)^2} [ (|\alpha_{11}|^2 + |\alpha_{12}|^2)\beta_{11} - 2\alpha_{11}\alpha_{12}\beta_{12}] + \mu_0}. \quad (4.95)$$

These expressions are used below in calculating the Chern number from (4.86).

### Chern number calculation as a surface integral over the $k_x - k_y$ plane

From (4.92) the Berry curvature is

$$\begin{aligned} \mathbf{F}_k &= \text{Re}\left\{ \frac{\partial A_x(k_x, k_y)}{\partial k_y} - \frac{\partial A_y(k_x, k_y)}{\partial k_x} \right\} (-\hat{\mathbf{z}}) \\ \mathbf{F}_k &= \text{Re}\left\{ \frac{i\hat{\mathbf{z}}}{D(\epsilon_0 \omega_n)^2} \{2\alpha_{11}\alpha_{12}\beta_{11} + (|\alpha_{11}|^2 + |\alpha_{12}|^2)\beta_{12}\} \right\}. \end{aligned} \quad (4.96)$$

If we consider propagation in  $\mathbf{k}$ -space such that  $k_z = 0$  then the Chern number computed over the infinite surface is

$$\begin{aligned} C &= \frac{1}{2\pi} = \int_{k_x=-\infty}^{k_x=+\infty} \int_{k_y=-\infty}^{k_y=+\infty} dk_x dk_y \cdot \mathbf{F}_k = \frac{1}{2\pi} \int_{\phi=0}^{\phi=2\pi} \int_{k=0}^{k=\infty} k dk d\phi \cdot \mathbf{F}_k \\ C &= (\delta(k))_{k=0}^{k=\infty} = \left( \text{Re}\left\{ \frac{i}{D(\epsilon_0 \omega_n)^2} \frac{1}{2} \{2\alpha_{11}\alpha_{12}\beta_{11} + (|\alpha_{11}|^2 + |\alpha_{12}|^2)\beta_{12}\} \right\} \right)_{k=0}^{k=\infty} \end{aligned} \quad (4.97)$$

which leads to (4.86) with  $\delta(k) = A_n(\phi = 0)k$  in (4.95). Therefore the Chern number computed as an infinite surface integral is the same as computed via the line integral near the north and south poles of the Riemann sphere, as shown in [132].

#### 4.3.1 Low Frequency Band of the TM-Mode, Material Model (4.78)

For material model (4.78), we will denote the lower curve in Fig. 4.6 as the low frequency band of the TM-mode. When  $k \rightarrow \infty$  from the TM-dispersion relation (4.79), then  $\omega_n$  should tend to the zero of  $\epsilon_{11}$ , which is  $\omega_n = \sqrt{\omega_0^2 + \omega_0 \omega_e}$ . Since

$$k^2 = \frac{\epsilon_{11}^2 + \epsilon_{12}^2}{\epsilon_{11}} \left(\frac{\omega_n}{c}\right)^2 = \frac{\omega_0^2 - \omega^2 + 2\omega_0 \omega_e + \omega_e^2}{\omega_0^2 - \omega^2 + \omega_0 \omega_e} \left(\frac{\omega_n}{c}\right)^2, \quad \text{TM mode}, \quad (4.98)$$

in the limit  $k \rightarrow \infty$  we obtain  $\epsilon_{11} = 0$ ,  $\alpha_{11} = 0$  and  $(k/\omega_n)^2 \rightarrow \infty$ . So, for  $A_n(\phi = 0)$  we get

$$A_n(\phi = 0)k = \frac{\text{Re}\frac{i|k|^2}{(\epsilon_0 \omega_n)^2} \{|\alpha_{12}|^2 \beta_{12}\}}{\frac{|k|^2}{(\epsilon_0 \omega_n)^2} \{|\alpha_{12}|^2 \beta_{11}\} + \mu_0} = \frac{\text{Re}\frac{i|k|^2}{(\epsilon_0 \omega_n)^2} \{|\frac{1}{\epsilon_{12}}|^2 \beta_{12}\}}{\frac{|k|^2}{(\epsilon_0 \omega_n)^2} \{|\frac{1}{\epsilon_{12}}|^2 \beta_{11}\} + \mu_0} \quad (4.99)$$

such that

$$\beta_{11} = \epsilon_0(1 + \omega_0\omega_e \frac{\omega_0^2 + \omega^2}{(\omega_0^2 - \omega^2)^2}), \quad \beta_{12} = -i\epsilon_0\omega_e \frac{2\omega\omega_0^2}{(\omega_0^2 - \omega^2)^2}. \quad (4.100)$$

For  $\omega_n = \sqrt{\omega_0^2 + \omega_0\omega_e}$  we have  $\beta_{11} = 2\epsilon_0(1 + \frac{\omega_0}{\omega_e})$  and  $\beta_{12} = -(2\epsilon_0i/\omega_e) \sqrt{\omega_0^2 + \omega_0\omega_e}$ . Finally, taking the limit  $k \rightarrow \infty$ ,

$$\lim_{k \rightarrow \infty} A_n(\phi = 0)k = \frac{\sqrt{\omega_0^2 + \omega_0\omega_e}/\omega_e}{(1 + \frac{\omega_0}{\omega_e})} = \frac{|\omega_0| \sqrt{1 + \frac{\omega_e}{\omega_0}}}{\omega_0(1 + \frac{\omega_e}{\omega_0})} = \frac{\text{sgn}(\omega_0)}{\sqrt{1 + \frac{\omega_e}{\omega_0}}} = \frac{\text{sgn}(\omega_e)}{\sqrt{1 + |\frac{\omega_e}{\omega_0}|}} \quad (4.101)$$

When  $k \rightarrow 0$ , the lower band of TM-mode tends to the light line (which means  $\omega_n \rightarrow 0$ ). Therefore  $\epsilon_{12} = 0$  and  $\beta_{12} = 0$ , which leads to  $\lim_{k \rightarrow 0} A_n(\phi = 0)k = 0$ . Eventually, for Chern number we obtain

$$C_{n=1} = \lim_{k \rightarrow \infty} (A_{n,\phi=0}k) - \lim_{k \rightarrow 0^+} (A_{n,\phi=0}k) = \frac{\text{sgn}(\omega_e)}{\sqrt{1 + |\frac{\omega_e}{\omega_0}|}}. \quad (4.102)$$

The fact that this Chern number is not an integer will be addressed below, and the solution of this issue is a fundamental contribution of [132].

### 4.3.2 High Frequency Band of the TM-Mode, Material Model (4.78)

For material model (4.78), denoting the upper curve in Fig. 4.6) as the high-frequency band, from the dispersion relation (4.79),

$$k^2 = \frac{\omega_0^2 - \omega^2 + 2\omega_0\omega_e + \omega_e^2}{\omega_0^2 - \omega^2 + \omega_0\omega_e} \left(\frac{\omega_n}{c}\right)^2 \rightarrow 0 \quad \text{if } \omega_n = 0, \quad \omega_n = |\omega_0 + \omega_e|. \quad (4.103)$$

If  $\omega_n = 0$ , then

$$\epsilon_{11} = 1 + \frac{\omega_e}{\omega_0}, \quad \epsilon_{12} = 0, \quad \alpha_{11} = \frac{1}{1 + \omega_e/\omega_0}, \quad \alpha_{12} = 0, \quad \beta_{11} = 1 + \omega_e/\omega_0, \quad \beta_{12} = 0, \quad \left(\frac{k}{\omega_n}\right)^2 = \frac{1}{c^2} \left(1 + \frac{\omega_e}{\omega_0}\right)^2 \quad (4.104)$$

so for the numerator of  $A_n(\phi = 0)k$  we have  $2\alpha_{11}\alpha_{12}\beta_{11} + (|\alpha_{11}|^2 + |\alpha_{12}|^2)\beta_{12} = 0$ . Therefore there is no contribution for the eigenfrequency  $\omega_n = 0$  as  $k \rightarrow 0$ . In fact it is obvious that  $\omega_n = 0$  has no contribution because this eigenfrequency as  $k \rightarrow 0$  belongs to the TM low frequency band and it has no effect on the high frequency TM band.

If  $\omega_n = |\omega_0 + \omega_e|$ , it can be shown that

$$\epsilon_{12} = i\epsilon_{11}\text{sgn}(\omega_e), \quad \alpha_{11} = \frac{\epsilon_{11}}{\epsilon_{11}^2 + \epsilon_{12}^2} \rightarrow \infty, \quad \alpha_{12} = \frac{-\epsilon_{12}}{\epsilon_{11}^2 + \epsilon_{12}^2} \rightarrow \infty, \quad \beta_{12} = i\beta_{11}\text{sgn}(\omega_e),$$

$$\left(\frac{k}{\omega_n}\right)^2 = \frac{1}{c^2} \frac{\epsilon_{11}^2 + \epsilon_{12}^2}{\epsilon_{11}} \rightarrow 0 \quad (4.105)$$

and by carefully treating the limit  $\lim_{k \rightarrow 0} A_n(\phi = 0)k$  and considering the fact that for  $\omega_n = |\omega_0 + \omega_e|$

we have  $\epsilon_{11} = (\omega_e^2 + \omega_0\omega_e) / (\omega_e^2 + 2\omega_0\omega_e) > 0$  then it can be shown that

$$\lim_{k \rightarrow 0} A_n(\phi = 0)k = \text{sgn}(\omega_e). \quad (4.106)$$

When  $k \rightarrow \infty$  then the high-frequency mode tends to the light line, so that  $\lim_{k \rightarrow \infty} A_n(\phi = 0)k = 0$ . Eventually for the high frequency TM-band we have

$$C_n = \lim_{k \rightarrow \infty} (A_{n,\phi=0}k) - \lim_{k \rightarrow 0^+} (A_{n,\phi=0}k) = -\text{sgn}(\omega_e). \quad (4.107)$$

### 4.3.3 TE-Mode

Using same procedure as above, it is straightforward to show that for the TE-Mode we have

$$C_n = \lim_{k \rightarrow \infty} (A_{n,\phi=0}k) - \lim_{k \rightarrow 0^+} (A_{n,\phi=0}k) = 0. \quad (4.108)$$

### Material model (4.77)

Considering material model (4.77), from the dispersion equation (4.79),

$$k^2 = \frac{\omega^2(\omega^2 - \omega_c^2) - 2\omega^2\omega_p^2 + \omega_p^4}{\omega^2 - \omega_c^2 - \omega_p^2} \frac{1}{c^2}. \quad (4.109)$$

As  $k \rightarrow \infty$  and regarding Fig. (4.6) we have  $\omega_n \rightarrow \infty$  for the high frequency band, and, for the low frequency band,  $\omega^2 - \omega_c^2 - \omega_p^2 = 0$ , such that  $\omega_n = \sqrt{\omega_c^2 + \omega_p^2}$ .

For the TM mode if  $k \rightarrow 0$  we have

$$\omega^2(\omega^2 - \omega_c^2) - 2\omega^2\omega_p^2 + \omega_p^4 = 0 \rightarrow \begin{cases} \omega_n^2 = \frac{\omega_h^2}{2} \left\{ 1 + \sqrt{1 - 4\left(\frac{\omega_p}{\omega_h}\right)^4} \right\}, & \text{for high frequency TM} \\ \omega_n^2 = \frac{\omega_h^2}{2} \left\{ 1 - \sqrt{1 - 4\left(\frac{\omega_p}{\omega_h}\right)^4} \right\}, & \text{for low frequency TM} \end{cases}$$

where  $\omega_h^2 = \omega_c^2 + 2\omega_p^2$ .

The Chern number is (4.86) with (4.95), and

$$\beta_{11} = 1 + \omega_p^2 \frac{\omega^2 + \omega_c^2}{(\omega^2 - \omega_c^2)^2}, \quad \beta_{12} = 2i\omega_c\omega_p^2 \frac{\omega}{(\omega^2 - \omega_c^2)^2}. \quad (4.110)$$

For the low frequency TM band when  $k \rightarrow \infty$  ( $\omega_n = \sqrt{\omega_c^2 + \omega_p^2}$ ),  $\epsilon_{11} = 0$  and  $\alpha_{11} = 0$ . Therefore,

$$\lim_{k \rightarrow \infty} (A_{n,\phi=0}k) = \text{Re} \left\{ \frac{i\beta_{12}}{\beta_{11}} \right\}_{\omega_n = \sqrt{\omega_c^2 + \omega_p^2}} = -\frac{\text{sgn}(\omega_c)}{\sqrt{1 + \left(\frac{\omega_p}{\omega_c}\right)^2}} \quad (4.111)$$

For the case of  $k \rightarrow 0$ , we have  $\omega_n^2 = \frac{\omega_h^2}{2} \left\{ 1 - \sqrt{1 - 4\left(\frac{\omega_p}{\omega_h}\right)^4} \right\}$  which is the pole of  $\alpha_{11}$  and  $\alpha_{12}$ ,

so  $\alpha_{11} \rightarrow \infty$ ,  $\alpha_{12} \rightarrow \infty$ . Then,

$$\begin{aligned} \lim_{k \rightarrow 0} (A_{n,\phi=0}k) &= \lim_{k \rightarrow 0} \frac{\operatorname{Re}(\frac{i}{(\epsilon_0 c)^2 \alpha_{11}} \{2\alpha_{11}\alpha_{12}\beta_{11} + (|\alpha_{11}|^2 + |\alpha_{12}|^2)\beta_{12}\})}{\frac{1}{(\epsilon_0 c)^2 \alpha_{11}} \{(|\alpha_{11}|^2 + |\alpha_{12}|^2)\beta_{11} - 2\alpha_{11}\alpha_{12}\beta_{12}\} + \mu_0} \\ &= \left\{ \frac{\operatorname{Re}(\frac{i}{(\epsilon_0 c)^2} \{2\frac{\alpha_{12}}{\alpha_{11}}\beta_{11} + (1 + \frac{|\alpha_{12}|^2}{\alpha_{11}^2})\beta_{12}\})}{\frac{1}{(\epsilon_0 c)^2} \{(1 + \frac{|\alpha_{12}|^2}{\alpha_{11}^2})\beta_{11} - 2\frac{\alpha_{12}}{\alpha_{11}}\beta_{12}\}} \right\}_{\omega_n^2 = \frac{\omega_h^2}{2}} \left\{ 1 - \sqrt{1 - 4\left(\frac{\omega_p}{\omega_h}\right)^4} \right\} = 1, \end{aligned} \quad (4.112)$$

and the Chern number of the low frequency band is

$$C_n = -\frac{\operatorname{sgn}(\omega_c)}{\sqrt{1 + \left(\frac{\omega_p}{\omega_c}\right)^2}} - 1. \quad (4.113)$$

For the high frequency band when  $k \rightarrow \infty$  we have  $\omega_n \rightarrow \infty$ ,  $\epsilon_{11} = 1$ ,  $\epsilon_{12} = 0$ ,  $\alpha_{11} = 1$ ,  $\alpha_{12} = 0$  and  $\beta_{12} = 0$ , so  $\lim_{k \rightarrow \infty} (A_{n,\phi=0}k) = 0$  and for the case of  $k \rightarrow 0$  we have  $\omega_n^2 = \frac{\omega_h^2}{2} \left\{ 1 + \sqrt{1 - 4\left(\frac{\omega_p}{\omega_h}\right)^4} \right\}$ , which is a pole of  $\alpha_{11}$  and  $\alpha_{12}$  so  $\alpha_{11} \rightarrow \infty$ ,  $\alpha_{12} \rightarrow \infty$ . Then,

$$\lim_{k \rightarrow 0} (A_{n,\phi=0}k) = \left\{ \frac{\operatorname{Re}(\frac{i}{(\epsilon_0 c)^2} \{2\frac{\alpha_{12}}{\alpha_{11}}\beta_{11} + (1 + \frac{|\alpha_{12}|^2}{\alpha_{11}^2})\beta_{12}\})}{\frac{1}{(\epsilon_0 c)^2} \{(1 + \frac{|\alpha_{12}|^2}{\alpha_{11}^2})\beta_{11} - 2\frac{\alpha_{12}}{\alpha_{11}}\beta_{12}\}} \right\}_{\omega_n^2 = \frac{\omega_h^2}{2}} \left\{ 1 + \sqrt{1 - 4\left(\frac{\omega_p}{\omega_h}\right)^4} \right\} = -1,$$

and so for the high frequency band the Chern number is

$$C_n = 0 - (-1) = 1.$$

It can be seen that generally the Chern number of the high frequency band is an integer, but that of the low frequency TM band is not (as was found for the material model (4.77)). In both material models, when off-diagonal permittivity elements in (4.76) are set to zero, all Chern numbers are  $C_n = 0$ .

#### 4.3.4 Integer Chern Numbers and Wave Vector Cutoff for Magneto-Optic Material Response

The non-integer Chern numbers for the low TM band for both material models, (4.102) and (4.113), arise from the continuum nature of the material [132], associated with the Hamiltonian not being sufficiently well-behaved at infinity (mapped to the north pole of the Riemann sphere). The problem is thoroughly discussed in [132], and here we merely repeat the solution therein. The issue can be solved by introducing a high-frequency spatial cutoff by defining a nonlocal material

$$M_{\text{reg}}(\omega, k) = M_\infty + \frac{1}{1 + k^2/k_{\text{max}}^2} [M(\omega) - M_\infty] \quad (4.114)$$



where  $M_\infty = \lim_{\omega \rightarrow \infty} M(\omega)$ . This material response tends to the local response as  $k_{\max} \rightarrow \infty$ <sup>12</sup> By considering a wave vector cutoff for, e.g., the material model (4.78), the non-local parameters of the material are

$$\epsilon_{11} = \epsilon_{22} = 1 + \frac{1}{1 + k^2/k_{\max}^2} \frac{\omega_0 \omega_e}{\omega_0^2 - \omega^2}, \quad \epsilon_{12} = -\epsilon_{21} = \frac{-i}{1 + k^2/k_{\max}^2} \frac{\omega_e \omega}{\omega_0^2 - \omega^2}, \quad \epsilon_{33} = 1, \quad \mu = \text{diag}\{\mu, \mu, \mu\} \quad (4.116)$$

For the low frequency TM-band we have

$$k^2 = \frac{\omega_0^2 - \omega^2 + 2\gamma\omega_0\omega_e + \gamma^2\omega_e^2}{\omega_0^2 - \omega^2 + \gamma\omega_0\omega_e} \left(\frac{\omega}{c}\right)^2 \quad (4.117)$$

such that  $\gamma = \frac{1}{1 + k^2/k_{\max}^2}$  describes the non-locality. If  $k \rightarrow \infty$  then  $\gamma \rightarrow 0$  and  $\omega_n \rightarrow |\omega_0|$ , which is a zero of  $\epsilon_{11}$  in the limit of  $k \rightarrow \infty$ . Therefore for the case of  $k \rightarrow \infty$  we have

$$\epsilon_{11} = 0, \quad \alpha_{11} = 0, \quad \beta_{11} = \gamma\omega_0\omega_e \frac{2\omega^2}{(\omega_0^2 - \omega^2)^2}, \quad \beta_{12} = -i\gamma\omega_e \frac{2\omega\omega_0^2}{(\omega_0^2 - \omega^2)^2}. \quad (4.118)$$

It can be shown that

$$\lim_{k \rightarrow \infty} A_n(\phi = 0)k = \frac{i|\alpha_{12}|^2\beta_{12}}{|\alpha_{12}|^2\beta_{11}} = \frac{i\beta_{12}}{\beta_{11}} = \frac{\omega_0}{|\omega_0|} = \text{sgn}(\omega_0) = \text{sgn}(\omega_e), \quad (4.119)$$

and for the case that  $k \rightarrow 0$  the low frequency band of the TM-mode tends to the light line and so  $\lim_{k \rightarrow 0} A_n(\phi = 0)k = 0$ . Eventually for the Chern number of the low frequency TM band we obtain

$$C_n = \lim_{k \rightarrow \infty} (A_{n,\phi=0}k) - \lim_{k \rightarrow 0^+} (A_{n,\phi=0}k) = \text{sgn}(\omega_e), \quad (4.120)$$

the desired integer.

For the high frequency TM-band nothing changes from the previous development because the contribution to Chern number comes from  $k \rightarrow 0$ , and in this limit the non-local response turn into local response and the Chern number is the same as previously obtained. So, for high frequency TM-band we have

$$C_n = \lim_{k \rightarrow \infty} (A_{n,\phi=0}k) - \lim_{k \rightarrow 0^+} (A_{n,\phi=0}k) = -\text{sgn}(\omega_e) \quad (4.121)$$

Introducing the wave number cutoff has no effect on the TE-mode because  $\epsilon_{33}$  does not change, and so the Chern number of this mode remains the same as in the previous section ( $C_n = 0$ ).

Therefore, we have Chern numbers  $C_{\text{high}} = \text{sgn}(\omega_e)$  and  $C_{\text{low}} = -\text{sgn}(\omega_e)$  for the higher and lower band, respectively, so that the sum of the Chern numbers is zero. The band dispersion and integer Chern numbers are shown in Fig. 4.6.

<sup>12</sup>Noting the Fourier transform pair

$$\frac{1}{1 + k^2/k_{\max}^2} \leftrightarrow \frac{k_{\max}}{2} e^{-k_{\max}r} \quad (4.115)$$

and as  $k_{\max} \rightarrow \infty$  we have  $\lim_{k_{\max} \rightarrow \infty} \frac{k_{\max}}{2} e^{-k_{\max}r} = \delta(r)$ , which indicates locality.

### Biased Plasma Case

For the material model (4.78), the permittivity tensor components become

$$\epsilon_{11} = \epsilon_{22} = 1 - \gamma \frac{\omega_p^2}{\omega^2 - \omega_c^2}, \quad \epsilon_{12} = -\epsilon_{21} = -i\gamma \frac{\omega_c \omega_p^2}{\omega(\omega^2 - \omega_c^2)} \quad (4.122)$$

such that  $\gamma = 1/(1 + k^2/k_{\max}^2)$ .

For this case, the dispersion equation is

$$k^2 = \frac{\epsilon_{11}(k)^2 + \epsilon_{12}(k)^2}{\epsilon_{11}(k)} \left(\frac{\omega}{c}\right)^2. \quad (4.123)$$

We have  $k \rightarrow \infty$  if  $\epsilon_{11}(k) = 0$  and  $\epsilon_{12}(k) \neq 0$ , or  $\omega_n \rightarrow \infty$ , or  $\omega_n = \omega_c$ . The eigen frequency of the higher TM band is  $\omega_n \rightarrow \infty$  and that of lower frequency band comes from the zero of  $\epsilon_{11}(k)$ ,

$$\epsilon_{11}(k) = 1 - \gamma \frac{\omega_p^2}{\omega^2 - \omega_c^2} = 0 \rightarrow \omega_n = \sqrt{\omega_c^2 + \gamma \omega_p^2}.$$

When  $k \rightarrow \infty$  then  $\gamma \rightarrow 0$  so for the low frequency band the eigenfrequency is  $\omega_n = \lim_{\gamma \rightarrow 0} \sqrt{\omega_c^2 + \gamma \omega_p^2} = |\omega_c|$ .

For  $k \rightarrow \infty$ ,  $\omega_n = |\omega_c|$ , we have  $\epsilon_{11}(k) = 0$ ,  $\alpha_{11}(k) = 0$  and so

$$\lim_{k \rightarrow \infty} (A_{n,\phi=0}k) = \operatorname{Re} \left\{ \frac{i\beta_{12}(k)}{\beta_{11}(k)} \right\}_{\omega_n=|\omega_c|} \quad (4.124)$$

such that  $\beta_{11}(k) = 1 + \gamma \omega_p^2 \frac{\omega^2 + \omega_c^2}{(\omega^2 - \omega_c^2)^2}$ ,  $\beta_{12} = 2i\gamma \omega_c \omega_p^2 \frac{\omega}{(\omega^2 - \omega_c^2)^2}$  so the contribution from  $k \rightarrow \infty$  in low frequency TM band is

$$\lim_{k \rightarrow \infty, \gamma \rightarrow 0} (A_{n,\phi=0}k) = \operatorname{Re} \left\{ \frac{i\beta_{12}(k)}{\beta_{11}(k)} \right\}_{\omega_n=|\omega_c|} = -1. \quad (4.125)$$

For the case of  $k \rightarrow 0$  ( $\gamma \rightarrow 1$ ) and we have same dispersion equation as when there is no wave vector cut-off, and so that limit remains the same as before,  $\lim_{k \rightarrow 0} (A_{n,\phi=0}k) = 1$ . Therefore, for the low frequency band we obtain

$$C_n = -1 - 1 = -2.$$

For the high frequency TM band as  $k \rightarrow \infty$  ( $\gamma \rightarrow 0$ ),  $\lim_{k \rightarrow \infty} (A_{n,\phi=0}k) = 0$  and when  $k \rightarrow 0$  ( $\gamma \rightarrow 1$ ),  $\lim_{k \rightarrow 0} (A_{n,\phi=0}k) = -1$  (as before), and so for the high frequency band the Chern number is

$$C_n = 0 - (-1) = +1.$$

The sum of the Chern numbers is -1. However, in addition to needing a wavenumber cutoff to obtain integer Chern numbers, the continuum model presents another complication. As detailed in [145], to predict edge states in general for continuum media, one should compute Chern numbers for

an "interpolated material response". This means, for example, that to see bulk-edge correspondence for the magnetized plasma and a Drude metal interface, we should define a function  $\epsilon(\tau)$  where  $\tau$  varies from 0 to 1, such that when  $\tau = 0$  we obtain the permittivity of the magnetized plasma, and when  $\tau = 1$  we obtain the Drude metal. Then, one needs to compute the topological numbers for  $\tau = 1^-$  and  $\tau = 0^+$ . With this model, we obtain one additional low frequency band for the magnetized plasma, very near  $\omega = 0$ , having Chern number 1. In this case, all band Chern numbers are integers and sum to zero.

### 4.3.5 Full-Wave Simulation of One-Way Propagation

We first consider a 2D structure. A 2D dipole (i.e., a line source) is at the interface between a simple plasma (upper region) having  $\epsilon = -5$  (this specific value relatively is unimportant; we simply need a negative-permittivity material such as a metal) and a magnetoplasma (lower region) having permittivity (4.77). Fig. 4.7 shows the electric field profile for three cases, unbiased, biased but operating outside the band gap, and biased operating within the bandgap. It can be seen that in the unbiased (reciprocal) case energy flows in both directions, in the biased (non-reciprocal) case operating outside the gap we have one-way propagation but energy can leak into the lower region, and in the biased case operating within the bandgap energy just flows in one direction, is well-contained at the interface, and goes around discontinuities.

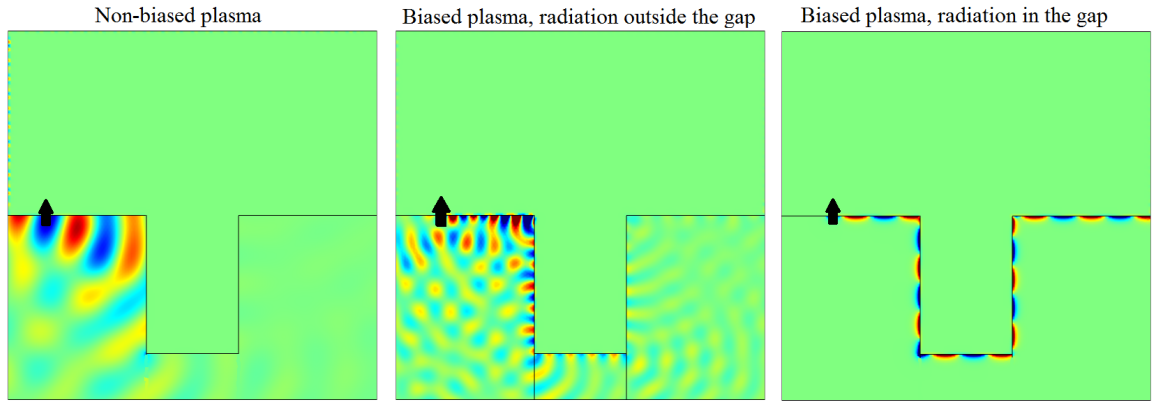


Figure 4.7: Electric field due to a 2D vertical dipole and  $\omega_p/2\pi = 9.7$  THz for three cases: left: unbiased (reciprocal) case that respects TR symmetry,  $\omega_c = 0$ , at 10 THz ( $\lambda = 30\mu$  m), center: biased with  $\omega_c/2\pi = 1.73$  THz at 12 THz, outside of the band gap ( $\omega/\omega_c = 6.93$ ), and right: biased with  $\omega_c/2\pi = 1.73$  THz inside the bandgap at 10 THz, ( $\omega/\omega_c = 5.78$ ).

Fig. 4.8 shows a 3D simulation for a  $420 \times 120 \times 90$   $\mu\text{m}$  rectangular block of magnetoplasma with an  $\epsilon = -5$  plasma on the top surface and vacuum on all other sides: a (top) shows the electric field profile in the reciprocal case,  $\omega_c = 0$ , at 10 THz. Fig. 4.8b (lower) shows the non-reciprocal case at 10 THz (in the bandgap). It can be seen that in the reciprocal case energy flows in both directions, whereas in the non-reciprocal case energy just flows to the right.

Figure 4.9 shows the non-reciprocal case when an obstacle (a half-sphere) is hollowed out of each

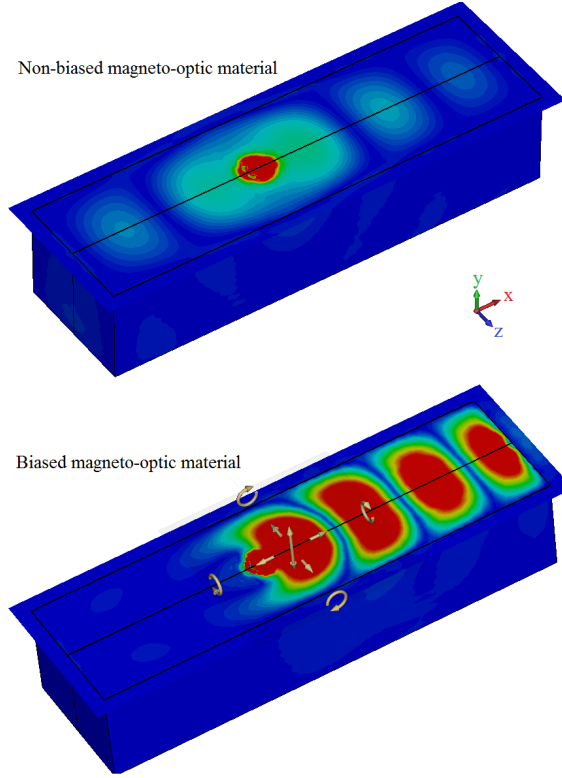


Figure 4.8: Electric field at 10 THz for a 3D vertical dipole at a magnetoplasma–plasma interface (top interface is between the magnetoplasma and the  $\varepsilon = -5$  simple plasma, all other interfaces are between the magnetoplasma and vacuum). Top: unbiased ( $\omega_c = 0$ , reciprocal) case. Bottom: non-reciprocal case when  $\omega_c/2\pi = 1.73$  THz inside the bandgap ( $\omega/\omega_c = 5.78$ ).

material at the interface, forming a spherical vacuum obstacle having radius  $30\mu\text{m}$  ( $1\lambda$ ) in the SPP path. It can be seen that the wave goes past the obstacle without backscattering.

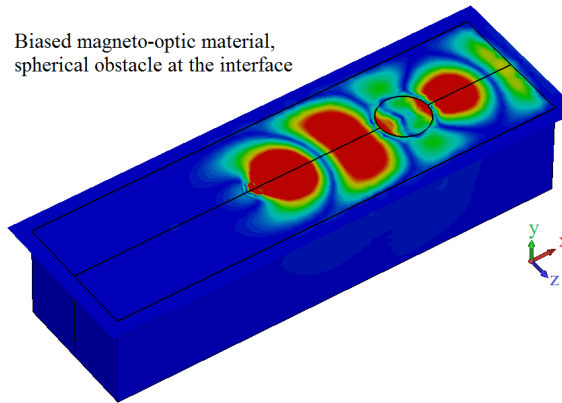


Figure 4.9: Electric field near a magnetoplasma–plasma interface, as in Fig. 4.8, in the non-reciprocal case when a large ( $1\lambda$ ) spherical vacuum obstacle is placed in the SPP path.

Finally, Figs. 4.10 and 4.11 show the power density for the case of an interface with a step discontinuity in height. The step height is  $30\mu\text{m}$  ( $1\lambda$ ). For Fig. 4.10, as in Figs. 4.8 and 4.9, the top interface is with the  $\varepsilon = -5$  simple plasma, all other interfaces are between the magnetoplasma

and vacuum. A vertical dipole source is located on the left side as indicated. Fig. 4.10a shows the side view of the power density in the reciprocal case, and Fig. 4.10b shows the non-reciprocal case. It can be seen that in the reciprocal case energy flows in both directions as well as interacting with and reflecting from the step, whereas in the non-reciprocal case energy just flows to the right, and doesn't scatter off of the step discontinuity. In Fig. 4.11 we surround all sides of the magnetoplasma with  $\varepsilon = -5$  plasma. In this case energy circulates around the entire structure.

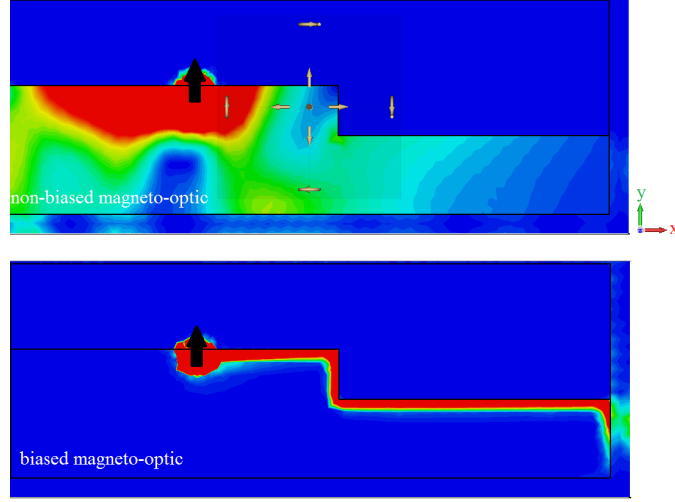


Figure 4.10: Side view of power density due to a vertical point dipole source at the interface between a magnetoplasma–plasma interface (top surface, all other sides interface with vacuum). a. Power density in the reciprocal case. b. Non-reciprocal case.

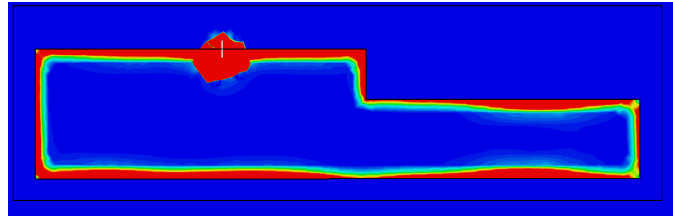


Figure 4.11: Side view of power density due to a vertical point dipole source at the interface between a magnetoplasma–plasma interface. a. Power density in the reciprocal case. b. Non-reciprocal case.

The dispersion relation for the surface mode is [130]

$$\frac{\sqrt{k_x^2 - k_0^2 \varepsilon_s}}{\varepsilon_s} + \frac{\sqrt{k_x^2 - k_0^2 \varepsilon_{eff}}}{\varepsilon_{eff}} = -\frac{\varepsilon_{12} i k_x}{\varepsilon_{11} \varepsilon_{eff}} \quad (4.126)$$

where  $\varepsilon_s$  is the top material permittivity and

$$\varepsilon_{eff} = \frac{\varepsilon_{11}^2 + \varepsilon_{12}^2}{\varepsilon_{11}} \quad (4.127)$$

where  $\varepsilon_{\alpha,\beta}$  are the magnetoplasma permittivity components.

### 4.3.6 Numerical Computation of the Chern Number

In these continuum examples the Chern number can be found analytically. However, often this will not be the case, and numerical methods must be used. As discussed previously, the Berry potential (4.12) and associated Chern computation (4.43) may not be convenient for numerical computations since it involves derivatives of the eigenfunctions, which generally need to be taken numerically. The curvature form (4.30) and associated Chern number (4.44) provide a convenient method, since only the Hamiltonian matrix needs to be differentiated.

In the non-dispersive case the formulation in Section 4.2 suffices, the classical Hamiltonian  $H_{cl} = M^{-1}N$  is Hermitian under the indicated inner product, the eigenvalue problem  $H_{cl} \cdot f_n = \omega_n f_n$  is a standard eigenvalue problem, and the 6-vector of natural modes  $f_n = [\mathbf{E} \ \mathbf{H}]^T$  from (4.66) form a complete set of eigenfunctions. In principle, either the formulation (4.43) or (4.44) can be used to compute the Chern number.

In the dispersive case this does not hold, but, nevertheless, only the natural modes  $f_n$  are needed to compute the Berry curvature (4.68) [132]. However, these modes are not appropriate for the form (4.44), in particular, since the eigenmodes depend on frequency and (4.44) involves terms with different eigenmodes. Furthermore, in the dispersive case the Hamiltonian  $H_{cl} = M^{-1}N$  does not admit a complete set of eigenvectors, which, in principle, is needed in the computation (4.44). Moreover, the 6-vector of natural modes (if one is going to use (4.43)) is not so easily computed in practice, since  $H_{cl}(\omega_n) \cdot f_n = \omega_n f_n$  is a non-standard eigenvalue problem, and eigenvalues would generally need to be found via a root search or similar method.

In [20] (and other works, see, e.g., [146]) the non-standard eigenvalue problem in the dispersive case is avoided by introducing auxiliary variables (additional degrees of freedom), and in [132] this approach is extended to allow for both temporal and spatial dispersion of general linear media. The resulting standard Hermitian eigenvalue problem to be solved is

$$(M_g^{-1} \cdot L) Q = \omega Q, \quad (4.128)$$

where, in block-matrix form (all elements in  $M_g$  and  $L$  are 6x6 blocks),

$$M_g = \begin{pmatrix} M_\infty & \mathbf{0} & \mathbf{0} & \cdots \\ \mathbf{0} & \mathbf{I} & \mathbf{0} & \cdots \\ \mathbf{0} & \mathbf{0} & \mathbf{I} & \cdots \\ \vdots & \vdots & \vdots & \ddots \end{pmatrix}, \quad M_\infty = \lim_{\omega \rightarrow \infty} M(\omega, \mathbf{k}), \quad (4.129)$$

and

$$L = \begin{pmatrix} N + \sum_{\alpha} \text{sgn}(\omega_{p,\alpha}) \mathbf{A}_{\alpha}^2 & |\omega_{p,1}|^{1/2} \mathbf{A}_1 & |\omega_{p,2}|^{1/2} \mathbf{A}_2 & \cdots \\ |\omega_{p,1}|^{1/2} \mathbf{A}_1 & \omega_{p,1} \mathbf{I} & \mathbf{0} & \cdots \\ |\omega_{p,2}|^{1/2} \mathbf{A}_2 & \mathbf{0} & \omega_{p,2} \mathbf{I} & \cdots \\ \vdots & \vdots & \vdots & \ddots \end{pmatrix}, \quad (4.130)$$

$$N = \begin{pmatrix} 0 & -\mathbf{k} \times \mathbf{I}_{3 \times 3} \\ \mathbf{k} \times \mathbf{I}_{3 \times 3} & 0 \end{pmatrix} = \begin{pmatrix} 0 & 0 & 0 & 0 & k_z & -k_y \\ 0 & 0 & 0 & -k_z & 0 & k_x \\ 0 & 0 & 0 & k_y & -k_x & 0 \\ 0 & -k_z & k_y & 0 & 0 & 0 \\ k_z & 0 & -k_x & 0 & 0 & 0 \\ -k_y & k_x & 0 & 0 & 0 & 0 \end{pmatrix}, \quad (4.131)$$

where  $M_g$  and  $L$  are independent of frequency,  $Q = [f \ Q_1 \ Q_2 \ \dots]$  where each element in  $Q$  is 6x1, and  $f$  is defined as before. The elements  $\mathbf{A}_{\alpha}$  are the 6x6 residues of the material matrix,  $\mathbf{A}_{\alpha}^2 = -\text{sgn}(\omega_{p,\alpha}) \text{Res}(M)_{\alpha}$ , and  $\omega_{p,\alpha}$  is the  $\alpha$ th pole of  $M$ . More details are available in [132], and here we focus on the specific material example (4.78) considered above.

Given the permittivity form (4.78), the material matrix has two poles, at  $\omega = \pm\omega_0$ . Therefore,  $L$  is an 18x18 matrix,  $M_g$  is the diagonal matrix  $(\varepsilon_0, \varepsilon_0, \varepsilon_0, \mu_0, \mu_0, \mu_0, 1, 1, 1, \dots, 1)$  and

$$\mathbf{A}_1^2 = \begin{pmatrix} \varepsilon_0 \frac{\omega_e}{2} & -i\varepsilon_0 \frac{\omega_e}{2} & 0 & 0 & 0 & 0 \\ i\varepsilon_0 \frac{\omega_e}{2} & \varepsilon_0 \frac{\omega_e}{2} & 0 & 0 & 0 & 0 \\ 0 & 0 & 0 & 0 & 0 & 0 \\ 0 & 0 & 0 & 0 & 0 & 0 \\ 0 & 0 & 0 & 0 & 0 & 0 \\ 0 & 0 & 0 & 0 & 0 & 0 \end{pmatrix}, \quad \mathbf{A}_2^2 = \begin{pmatrix} \varepsilon_0 \frac{\omega_e}{2} & i\varepsilon_0 \frac{\omega_e}{2} & 0 & 0 & 0 & 0 \\ -i\varepsilon_0 \frac{\omega_e}{2} & \varepsilon_0 \frac{\omega_e}{2} & 0 & 0 & 0 & 0 \\ 0 & 0 & 0 & 0 & 0 & 0 \\ 0 & 0 & 0 & 0 & 0 & 0 \\ 0 & 0 & 0 & 0 & 0 & 0 \\ 0 & 0 & 0 & 0 & 0 & 0 \end{pmatrix}. \quad (4.132)$$

Setting  $k_z = 0$ , the final Hamiltonian matrix is

$$H = M_g^{-1}L = \begin{pmatrix} 0 & -i\omega'_e & 0 & 0 & 0 & -\frac{k'_y}{\varepsilon_0} & -\alpha & i\alpha & 0 & 0 & 0 & 0 & -\alpha & -i\alpha & 0 & 0 & 0 & 0 \\ i\omega'_e & 0 & 0 & 0 & 0 & \frac{k'_x}{\varepsilon_0} & -i\alpha & -\alpha & 0 & 0 & 0 & 0 & i\alpha & -\alpha & 0 & 0 & 0 & 0 \\ 0 & 0 & 0 & \frac{k'_y}{\varepsilon_0} & -\frac{k'_x}{\varepsilon_0} & 0 & 0 & 0 & 0 & 0 & 0 & 0 & 0 & 0 & 0 & 0 & 0 & 0 \\ 0 & 0 & \frac{k'_y}{\mu_0} & 0 & 0 & 0 & 0 & 0 & 0 & 0 & 0 & 0 & 0 & 0 & 0 & 0 & 0 & 0 \\ 0 & 0 & -\frac{k'_x}{\mu_0} & 0 & 0 & 0 & 0 & 0 & 0 & 0 & 0 & 0 & 0 & 0 & 0 & 0 & 0 & 0 \\ -\frac{k'_y}{\mu_0} & \frac{k'_x}{\mu_0} & 0 & 0 & 0 & 0 & 0 & 0 & 0 & 0 & 0 & 0 & 0 & 0 & 0 & 0 & 0 & 0 \\ -\beta & i\beta & 0 & 0 & 0 & 0 & 1 & 0 & 0 & 0 & 0 & 0 & 0 & 0 & 0 & 0 & 0 & 0 \\ -i\beta & -\beta & 0 & 0 & 0 & 0 & 0 & 1 & 0 & 0 & 0 & 0 & 0 & 0 & 0 & 0 & 0 & 0 \\ 0 & 0 & 0 & 0 & 0 & 0 & 0 & 0 & 1 & 0 & 0 & 0 & 0 & 0 & 0 & 0 & 0 & 0 \\ 0 & 0 & 0 & 0 & 0 & 0 & 0 & 0 & 0 & 1 & 0 & 0 & 0 & 0 & 0 & 0 & 0 & 0 \\ 0 & 0 & 0 & 0 & 0 & 0 & 0 & 0 & 0 & 0 & 1 & 0 & 0 & 0 & 0 & 0 & 0 & 0 \\ 0 & 0 & 0 & 0 & 0 & 0 & 0 & 0 & 0 & 0 & 0 & 1 & 0 & 0 & 0 & 0 & 0 & 0 \\ -\beta & -i\beta & 0 & 0 & 0 & 0 & 0 & 0 & 0 & 0 & 0 & 0 & 1 & 0 & 0 & 0 & 0 & 0 \\ i\beta & -\beta & 0 & 0 & 0 & 0 & 0 & 0 & 0 & 0 & 0 & 0 & 0 & 1 & 0 & 0 & 0 & 0 \\ 0 & 0 & 0 & 0 & 0 & 0 & 0 & 0 & 0 & 0 & 0 & 0 & 0 & 0 & 1 & 0 & 0 & 0 \\ 0 & 0 & 0 & 0 & 0 & 0 & 0 & 0 & 0 & 0 & 0 & 0 & 0 & 0 & 0 & 1 & 0 & 0 \\ 0 & 0 & 0 & 0 & 0 & 0 & 0 & 0 & 0 & 0 & 0 & 0 & 0 & 0 & 0 & 0 & 1 & 0 \\ 0 & 0 & 0 & 0 & 0 & 0 & 0 & 0 & 0 & 0 & 0 & 0 & 0 & 0 & 0 & 0 & 0 & 1 \end{pmatrix} \quad (4.133)$$

where  $\alpha = \frac{1}{2}\sqrt{\omega'_e/\varepsilon_0}$ ,  $\beta = \frac{1}{2}\sqrt{\varepsilon_0\omega'_e}$ ,  $\omega'_e = \omega_e/\omega_0$ ,  $k'_{x,y} = k_{x,y}/\omega_0$ .

From (4.133) the eigenvalues and associated eigenvectors can easily be found numerically (or symbolically), and the Chern number computed from (4.44). Of the 18 branches, two are the positive-frequency TM modes and one is the positive-frequency TE mode described previously. In addition to static-like (longitudinal) modes, there are dispersionless dark modes with  $\mathbf{E} = \mathbf{H} = \mathbf{0}$  which don't contribute to the Chern number. For each TM band, the other TM band and, to a lesser extent, the TE band, provide the most important contributions to the Chern number calculation (4.44).

## 4.4 Summary

The properties that quantify PTIs, Berry phase, Berry connection, and Chern number, are typically obtained by making analogies between classical Maxwell's equations and the quantum mechanical Schrodinger equation, writing both in Hamiltonian form which needs a deep knowledge of quantum mechanics. However, the aforementioned quantities are not necessarily quantum in nature, and for photonic systems they can be explained using only classical concepts. In this chapter we have provided a derivation and description of PTI quantities using classical Maxwell's equations, demonstrated how



an electromagnetic mode can acquire Berry phase, and discussed the ramifications of this effect. Based on this classical perspective, we elucidated and evaluated the wave propagation and unidirectional surface waves on the surface of a biased plasma.

## Chapter 5

# Quantum Master Equation for General Non-Reciprocal Inhomogeneous Lossy Medium

### 5.1 Introduction

In this chapter, we first derive a general ME valid for both reciprocal and nonreciprocal, inhomogeneous and lossy environments. This form is valid for 3D, 2D and 1D systems since it is expressed in terms of the electromagnetic Green function. Then, we present concurrence expressions for the unidirectional case. The physical system we will consider is that of two qubits at the interface of a PTI and another (eventually topologically trivial) medium, as depicted in Fig. 5.1, although the development is completely general.

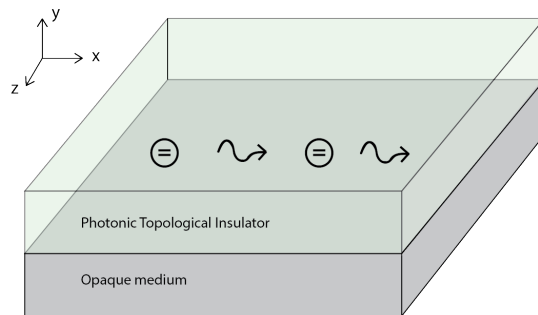


Figure 5.1: Two qubits at the interface of a PTI and topologically trivial medium. The resulting unidirectional SPP provides a strongly non-reciprocal environment for qubit entanglement.

## 5.2 Master Equation for General 3D Nonreciprocal Environments

We consider qubits with transition frequency  $\omega_0$  interacting through a general nonreciprocal environment. For a derivation in the reciprocal case, see [31].

The classical electric field satisfies

$$\left[ \nabla \times \mu^{-1}(\mathbf{r}, \omega) \nabla \times - \frac{\omega^2}{c^2} \varepsilon(\mathbf{r}, \omega) \right] \mathbf{E}(\mathbf{r}, \omega) = i\omega\mu_0 \mathbf{j}_s(\mathbf{r}, \omega), \quad (5.1)$$

where  $c$  is the vacuum speed of light,  $\mu(\mathbf{r}, \omega)$  and  $\varepsilon(\mathbf{r}, \omega)$  are the material permeability and permittivity, and  $\mathbf{j}_s(\mathbf{r}, \omega)$  is the noise current. In this work, we suppose that the medium is non-magnetic,  $\mu(\mathbf{r}, \omega) = \mathbf{I}$ , where  $\mathbf{I}$  is the unit dyad, but that the permittivity is a tensorial quantity. By defining the noise current in terms of polarization as  $\mathbf{j}_s = -i\omega \mathbf{P}_s$ , which is associated with material absorption by the fluctuation-dissipation theorem, the electric field Green tensor is the solution of

$$\left[ \nabla \times \nabla \times - \frac{\omega^2}{c^2} \varepsilon(\mathbf{r}, \omega) \right] \mathbf{G}(\mathbf{r}, \mathbf{r}', \omega) = \mathbf{I} \delta(\mathbf{r}, \mathbf{r}') \quad (5.2)$$

and the electric field is  $\mathbf{E}(\mathbf{r}, \omega) = (\omega^2/c^2 \varepsilon_0) \int_V d\mathbf{r}' \mathbf{G}(\mathbf{r}, \mathbf{r}', \omega) \cdot \mathbf{P}_s(\mathbf{r}', \omega)$ . Following the standard macroscopic canonical quantization [24, 57, 58], the noise polarization can be expressed in term of the bosonic field annihilation operator as [147]

$$\hat{\mathbf{P}}_s(\mathbf{r}, \omega) = -i \sqrt{\frac{\hbar \varepsilon_0}{\pi}} \mathbf{T}(\mathbf{r}, \omega) \cdot \hat{\mathbf{f}}(\mathbf{r}, \omega), \quad (5.3)$$

where

$$\mathbf{T}(\mathbf{r}, \omega) \cdot \mathbf{T}^\dagger(\mathbf{r}, \omega) = \frac{1}{2i} [\varepsilon(\mathbf{r}, \omega) - \varepsilon^\dagger(\mathbf{r}, \omega)], \quad (5.4)$$

and, for the special case of a symmetric permittivity tensor (e.g., a reciprocal medium),  $\mathbf{T}(\mathbf{r}, \omega) = \sqrt{\text{Im} \varepsilon(\mathbf{r}, \omega)}$ . The bosonic field operators  $\hat{\mathbf{f}}(\mathbf{r}, \omega)$  obey the commutation relations  $[\hat{f}_j(\mathbf{r}, \omega), \hat{f}_{j'}^\dagger(\mathbf{r}', \omega')] = \delta_{jj'} \delta(\mathbf{r} - \mathbf{r}') \delta(\omega - \omega')$  and  $[\hat{f}_j(\mathbf{r}, \omega), \hat{f}_{j'}(\mathbf{r}', \omega')] = 0$ . The noise polarization operator generates the electric field operator

$$\hat{\mathbf{E}}(\mathbf{r}, \omega) = i \sqrt{\frac{\hbar}{\pi \varepsilon_0}} \frac{\omega^2}{c^2} \int d\mathbf{r}' \mathbf{G}(\mathbf{r}, \mathbf{r}', \omega) \cdot \mathbf{T}(\mathbf{r}, \omega) \cdot \hat{\mathbf{f}}(\mathbf{r}', \omega), \quad (5.5)$$

where  $\mathbf{G}(\mathbf{r}, \mathbf{r}', \omega)$  is the classical electric field Green tensor. As the details are provided in Appendix I, the nonreciprocal Green tensor has the following useful property [147]

$$2i \frac{\omega^2}{c^2} \int d^3 r'' \mathbf{G}(\mathbf{r}, \mathbf{r}'', \omega) \cdot \mathbf{T}(\mathbf{r}'', \omega) \cdot \mathbf{T}^\dagger(\mathbf{r}'', \omega) \mathbf{G}^*(\mathbf{r}', \mathbf{r}'', \omega) = \mathbf{G}(\mathbf{r}, \mathbf{r}', \omega) - \mathbf{G}^\dagger(\mathbf{r}, \mathbf{r}', \omega). \quad (5.6)$$

Under the dipole approximation, the governing Hamiltonian of a system of qubits (two level atoms)

interacting with the surrounding environment can be written as

$$\mathbf{H} = \int d^3\mathbf{r} \int_0^\infty d\omega \hbar \omega \hat{\mathbf{f}}^\dagger(\mathbf{r}, \omega) \hat{\mathbf{f}}(\mathbf{r}, \omega) + \sum_i \hbar \omega_i \hat{\sigma}_i^\dagger \sigma_i - \sum_i \int_0^\infty d\omega (\hat{\mathbf{d}}_i \cdot \mathbf{E}(\mathbf{r}_i, \omega) + \text{H.c.}), \quad (5.7)$$

where the right side can be decomposed into the reservoir Hamiltonian  $\mathbf{H}_r$  (first term), the qubit Hamiltonian  $\mathbf{H}_s$  (second term), and the interaction Hamiltonian  $\mathbf{H}_{sr}$  (third term). We can modify the total Hamiltonian to include the coherent drive (external laser pump) Hamiltonian  $\mathbf{V}^{AF}$ , given later ((5.22)). We transform to a frame rotating with the laser frequency  $\omega_l$  ( $\mathbf{H} \rightarrow \hat{\mathbf{U}}^\dagger(t) \mathbf{H} \hat{\mathbf{U}}(t)$ ,  $\hat{\mathbf{U}}(t) = e^{-i\omega_l \sum_i \sigma_i^\dagger \sigma_i t}$ ) and write the total density matrix of the qubit system and reservoir according to the Schrödinger equation  $\partial_t \rho_T = -i[\mathbf{H}, \rho_T]/\hbar$ , then we transform to the interaction picture ( $\hat{\mathbf{O}}_I = \hat{\mathbf{U}}^\dagger(t) \mathbf{H} \hat{\mathbf{U}}(t)$ ,  $\hat{\mathbf{U}}(t) = e^{-i(\mathbf{H}_s + \mathbf{H}_r)t/\hbar}$ ) where  $\partial_t \rho_{T,I} = -i[\mathbf{H}_I, \rho_{T,I}]$  with  $\mathbf{H}_I = \mathbf{H}_{sr,I}$ . We integrate to find

$$\rho_{T,I} = \rho_I(0) \mathbf{R}_0 + \frac{-i}{\hbar} \int_0^t dt' [\mathbf{H}_I(t'), \rho_{T,I}(t')] \quad (5.8)$$

where  $\mathbf{R}_0$  is the initial reservoir density matrix. In the interaction picture, by considering  $\Gamma_{ii} \ll \omega$  for optical frequencies we make the rotating wave approximation (RWA) in  $\mathbf{H}_I$  and drop the rapidly varying counter-rotating terms proportional to  $\sigma^\dagger(t') \mathbf{f}^\dagger(\mathbf{r}', \omega) e^{i(\omega_l + \omega)t'}$  and its Hermitian conjugate. The interaction Hamiltonian in the interaction picture reduces to

$$\mathbf{H}_I(t) = - \sum_i \left( \int_0^\infty d\omega \sigma_i^\dagger(t) \mathbf{d}_i \cdot \mathbf{E}(\mathbf{r}_i, \omega) e^{-i(\omega - \omega_l)t} + \text{H.c.} \right) \quad (5.9)$$

To find the system density matrix we insert (5.8) into the interaction picture Schrödinger equation and trace over the reservoir,

$$\begin{aligned} \partial_t \rho_I &= \text{Tr}_R \left\{ \frac{-i}{\hbar} [\mathbf{H}_I, \rho_I(0) \mathbf{R}_{0,I}] \right\} \\ &\quad - \frac{1}{\hbar^2} \int_0^t dt' \text{Tr}_R \{ [\mathbf{H}_I(t), [\mathbf{H}_I(t'), \rho_{T,I}(t')]] \}. \end{aligned} \quad (5.10)$$

Aside from the rotating wave approximation, we apply a number of other approximations to the density matrix to simplify this further (see Appendix II). We first take the mean initial system reservoir coupling to be zero such that  $\text{Tr}_R \{ \frac{-i}{\hbar} [\mathbf{H}_I, \rho_I(0) \mathbf{R}_{0,I}] \} = 0$ . Then we apply the Born approximation, which states that the reservoir will be largely unaffected by its interaction by the system. Next, we assume that the evolution of the density matrix only depends on its current state (Born-Markov approximation). The Born-Markov approximation comes from the assumption that the reservoir relaxation time is much faster than the relaxation time of the system, and so the memory effect of the reservoir can be ignored. Lastly, we make a second Markov approximation, extending the upper limit of the time integral to infinity to produce a fully Markovian equation. With these

simplifications we have

$$\partial_t \rho_I = -\frac{1}{\hbar^2} \int_0^\infty dt' \text{Tr}_R \{ [\mathbf{H}_I(t), [\mathbf{H}_I(t-t'), \rho_I(t) \mathbf{R}_0]] \}. \quad (5.11)$$

We suppose that the atomic transition frequency of the qubits is  $\omega_0$ . Then, for the first term in (5.11) we have

$$\text{Tr}_R \{ \mathbf{H}_I(t) \mathbf{H}_I(t-t') \rho_I(t) \mathbf{R}_0 \} = \sum_{i,j} d_{\alpha i} d_{\beta j} \int_0^\infty d\omega e^{i(\omega_0 - \omega)t'} \sigma_i^\dagger \sigma_j \rho_{T,I} \text{Tr}_R \left( \hat{\mathbf{E}}_\alpha(\mathbf{r}_i, \omega) \hat{\mathbf{E}}_\beta^\dagger(\mathbf{r}_j, \omega) \mathbf{R}_0 \right) \quad (5.12)$$

where

$$\sigma_i = |g_i\rangle \langle e_i|, \quad \sigma_i^\dagger = |e_i\rangle \langle g_i| \quad (5.13)$$

are the atomic lowering/raising operators describing energy level transitions for each qubit, and where it is supposed that one of the qubits is polarized along  $\alpha$  and the other one is polarized along  $\beta$ . Considering (5.5) for the nonreciprocal Green tensor and  $\text{Tr}_R \{ \hat{\mathbf{f}}(r, \omega) \hat{\mathbf{f}}^\dagger(r', \omega') \mathbf{R}_0 \} = (\bar{n}(\omega) + 1) \delta(r - r') \delta(\omega - \omega')$  with zero thermal photon occupation  $\bar{n}(\omega) = 0$ , it can be easily shown that

$$\begin{aligned} \text{Tr}_R \left( \mathbf{E}_\alpha(\mathbf{r}_i, \omega) \mathbf{E}_\beta^\dagger(\mathbf{r}_j, \omega) \mathbf{R}_0 \right) &= \frac{\hbar}{\pi \varepsilon_0} \frac{\omega^4}{c^4} \int d^3 \mathbf{r} \mathbf{G}_{\alpha\gamma}(\mathbf{r}_i, \mathbf{r}, \omega) \left[ \frac{\varepsilon_{\gamma\gamma'}(\mathbf{r}, \omega) - \varepsilon_{\gamma\gamma'}^\dagger(\mathbf{r}, \omega)}{2i} \right] \mathbf{G}_{\gamma'\beta}^*(\mathbf{r}_j, \mathbf{r}, \omega) \\ &= \frac{\hbar}{2i\pi\varepsilon_0} \frac{\omega^2}{c^2} (\mathbf{G}_{\alpha,\beta}(\mathbf{r}_i, \mathbf{r}_j, \omega) - \mathbf{G}_{\beta,\alpha}^*(\mathbf{r}_j, \mathbf{r}_i, \omega)). \end{aligned} \quad (5.14)$$

Thus, we have

$$\begin{aligned} \text{Tr}_R \{ \mathbf{H}_I(t) \mathbf{H}_I(t-t') \rho_I(t) \mathbf{R}_0 \} &= \frac{\hbar}{2i\pi\varepsilon_0 c^2} \sum_{i,j} \sigma_i^\dagger \sigma_j \rho_I(t) \int_0^\infty d\omega e^{i(\omega_0 - \omega)t'} (\mathbf{d}_{\alpha i} \mathbf{G}_{\alpha\beta}(\mathbf{r}_i, \mathbf{r}_j, \omega) \mathbf{d}_{\beta j} - \mathbf{d}_{\beta j} \mathbf{G}_{\beta\alpha}^*(\mathbf{r}_j, \mathbf{r}_i, \omega) \mathbf{d}_{\alpha i}) \\ &\omega^2 d\omega e^{i(\omega_0 - \omega)t'}. \end{aligned} \quad (5.15)$$

Following the same procedure for the second term in (5.11),

$$\begin{aligned} \text{Tr}_R \{ \mathbf{H}_I(t-t') \rho_I(t) \mathbf{R}_0 \mathbf{H}_I(t) \} &= \frac{\hbar}{2i\pi\varepsilon_0 c^2} \sum_{i,j} \sigma_j \rho_I(t) \sigma_i^\dagger \int_0^\infty d\omega e^{i(\omega_0 - \omega)t'} (\mathbf{d}_{\beta i} \mathbf{G}_{\beta\alpha}(\mathbf{r}_i, \mathbf{r}_j, \omega) \mathbf{d}_{\alpha j} - \mathbf{d}_{\alpha j} \mathbf{G}_{\alpha\beta}^*(\mathbf{r}_j, \mathbf{r}_i, \omega) \mathbf{d}_{\beta i}) \\ &\omega^2 d\omega e^{i(\omega_0 - \omega)t'}. \end{aligned} \quad (5.16)$$

Replacing (5.15) and (5.16) in (5.11) and performing the time integral over  $t'$  gives the evolution of the density matrix in the interaction picture, where we have used the Kramers-Kronig relation

$$\begin{aligned} \mathcal{P} \int_{-\infty}^{\infty} \frac{\text{Re} \mathbf{G}_{\alpha\beta}}{\omega - \omega_0} d\omega &= -\pi \text{Im} \mathbf{G}_{\alpha\beta} \\ \mathcal{P} \int_{-\infty}^{\infty} \frac{\text{Im} \mathbf{G}_{\alpha\beta}}{\omega - \omega_0} d\omega &= \pi \text{Re} \mathbf{G}_{\alpha\beta}. \end{aligned} \quad (5.17)$$

Transforming back to the Schrödinger picture, we obtain the master equation for the two-level system dynamics

$$\partial_t \rho_s(t) = -\frac{i}{\hbar} [\mathbf{H}_s + \mathbf{V}^{AF}, \rho_s(t)] + \mathcal{L}\rho(t), \quad (5.18)$$

where

$$\begin{aligned} \mathcal{L}\rho_s(t) = & \sum_i \frac{\Gamma_{ii}(\omega_0)}{2} \left( 2\sigma_i \rho_s(t) \sigma_i^\dagger - \sigma_i^\dagger \sigma_i \rho_s(t) - \rho_s(t) \sigma_i^\dagger \sigma_i \right) \\ & + \sum_{i,j}^{i \neq j} \frac{\Gamma_{ij}(\omega_0)}{2} \left( [\sigma_j \rho_s(t), \sigma_i^\dagger] + [\sigma_i, \rho_s(t) \sigma_j^\dagger] \right) \\ & + \sum_{i,j}^{i \neq j} g_{ij}(\omega_0) \left( [\sigma_j \rho_s(t), -i\sigma_i^\dagger] + [i\sigma_i, \rho_s(t) \sigma_j^\dagger] \right). \end{aligned} \quad (5.19)$$

Equation (5.19) is one of the primary results of this work, and is applicable to both reciprocal and nonreciprocal environments and an arbitrary number of qubits. In (5.19),  $\mathcal{L}$  is the Lindblad superoperator for the general nonreciprocal medium, involving the dissipative decay rate,  $\Gamma_{ij}(\omega_0)$ , and the coherent coupling terms,  $g_{ij}(\omega_0)$ , in terms of the electromagnetic Green dyadic,

$$\begin{aligned} \Gamma_{ij}(\omega_0) &= \frac{2\omega_0^2}{\varepsilon_0 \hbar c^2} \sum_{\alpha, \beta=x,y,z} d_{\alpha i} \text{Im}(\mathbf{G}_{\alpha\beta}(\mathbf{r}_i, \mathbf{r}_j, \omega_0)) d_{\beta j}, \\ g_{ij}(\omega_0) &= \frac{\omega_0^2}{\varepsilon_0 \hbar c^2} \sum_{\alpha, \beta=x,y,z} d_{\alpha i} \text{Re}(\mathbf{G}_{\alpha\beta}(\mathbf{r}_i, \mathbf{r}_j, \omega_0)) d_{\beta j}. \end{aligned} \quad (5.20)$$

The Hamiltonian of the decoupled qubits is

$$\mathbf{H}_s = \sum_i \hbar \Delta \omega_i \sigma_i^\dagger \sigma_i, \quad (5.21)$$

where  $\Delta \omega_i = \omega_0 - \omega_l - \delta_i$ , with  $\delta_i = g_{ii}$  being the Lamb shift and  $\omega_l$  is the laser frequency of an external source. The Lamb shift for optical emitters is in general on the order of a few GHz, therefore the effect of the Lamb-shift for optical frequencies is small ( $\omega_i \sim 10^{15}$  Hz,  $\delta_i \sim 10^9$  Hz), and can be ignored, or assumed to be accounted for in the definition of the transition frequency  $\omega_0$ . In (5.18), the term

$$\mathbf{V}^{AF} = -\hbar \left( \Omega_1 e^{-i\Delta_l t} \sigma_1^\dagger + \Omega_1^* e^{i\Delta_l t} \sigma_1 \right) - \hbar \left( \Omega_2 e^{-i\Delta_l t} \sigma_2^\dagger + \Omega_2^* e^{i\Delta_l t} \sigma_2 \right) \quad (5.22)$$

represents the external coherent drive applied to each qubit at laser frequency  $\omega_l$ . Due to its large amplitude we treat the drive field as a  $c$ -number where  $\Omega_i = \mathbf{d}_i \cdot \mathbf{E}_0^i / \hbar$  is a Rabi frequency and  $\Delta_l = \omega_0 - \omega_l$  is the detuning parameter.

For the reciprocal case where  $\Gamma_{ij} = \Gamma_{ji}$  and  $g_{ij} = g_{ji}$  it can be shown that (5.19) is the well-known reciprocal (bidirectional) master equation [148, 74]. In the reciprocal case, some terms associated with  $g_{ij} = g_{ji}$  cancel each other out and are eliminated from the dissipative term. For example,  $\sigma_i \rho_s(t) \sigma_i^\dagger$ ,  $i \neq j$ , appears in the nonreciprocal case but is absent in the reciprocal case.

For a system of two qubits, (5.19) can be written in the simple form

$$\begin{aligned}
\mathcal{L}\rho_s(t) = & \sum_{j=1,2} \frac{\Gamma_{jj}}{2} \left( 2\sigma_j \rho_s \sigma_j^\dagger - \rho_s \sigma_j^\dagger \sigma_j - \sigma_j^\dagger \sigma_j \rho_s \right) \\
& + \left( \frac{\Gamma_{21}}{2} + ig_{21} \right) \left( \sigma_2 \rho_s \sigma_1^\dagger - \rho_s \sigma_1^\dagger \sigma_2 \right) \\
& + \left( \frac{\Gamma_{21}}{2} - ig_{21} \right) \left( \sigma_1 \rho_s \sigma_2^\dagger - \sigma_2^\dagger \sigma_1 \rho_s \right) \\
& + \left( \frac{\Gamma_{12}}{2} + ig_{12} \right) \left( \sigma_1 \rho_s \sigma_2^\dagger - \rho_s \sigma_2^\dagger \sigma_1 \right) \\
& + \left( \frac{\Gamma_{12}}{2} - ig_{12} \right) \left( \sigma_2 \rho_s \sigma_1^\dagger - \sigma_1^\dagger \sigma_2 \rho_s \right). \tag{5.23}
\end{aligned}$$

A comparison with previous 1D chiral ME formulations is provided in Appendix III.

## 5.3 Robust Entanglement with 3D Non-Reciprocal Photonic Topological Insulator

### 5.3.1 Transient Entanglement: Unidirectional SPP-Assisted Qubit Communication

In this work, all numerical results are computed using the master equation (5.18) with the general 3D Lindblad superoperator (5.19), where the Green tensor for complicated environments is obtained numerically. However, as shown in Appendix IV, if the system of qubits are communicating through a strongly nonreciprocal environment e.g.,  $\mathbf{G}(\mathbf{r}_1, \mathbf{r}_2) = 0$  ( $\Gamma_{12} = g_{12} = 0$ ) and  $\mathbf{G}(\mathbf{r}_2, \mathbf{r}_1) \neq 0$ , then the concurrence (as a measure of entanglement [149]) is

$$\mathcal{C}(t) = 2\sqrt{\frac{\Gamma_{21}^2}{4} + g_{21}^2} t e^{-\Gamma_{11}t} = 2\frac{\omega_0^2 d_y^2}{\hbar \epsilon_0 c^2} |\mathbf{G}_{yy}(\mathbf{r}_2, \mathbf{r}_1, \omega_0)| t e^{-\Gamma_{11}t}, \tag{5.24}$$

where it has been assumed that the qubits are both polarized along the  $y$ -axis. This is the general unidirectional result. Concurrence reaches its maximum value at  $t = 1/\Gamma_{11}$ , such that  $\mathcal{C}_{\max} = 2\sqrt{\tilde{\Gamma}_{12}^2/4 + \tilde{g}_{21}^2}/e$ , where  $\tilde{\Gamma}_{21}$  and  $\tilde{g}_{21}$  are rates normalized by  $\Gamma_{11}$ .

Although the Hamiltonian in nonreciprocal systems is non-Hermitian, it can be seen (Appendix IV) that the density matrix is Hermitian, probability conservation holds ( $\text{Tr}(\rho) = 1$ ), and that diagonal elements of the density operator can be interpreted as population densities, as for Hermitian Hamiltonians.

For two identical qubits interacting through a reciprocal medium,

$$C_{\text{recip}}(t) = \left\{ \frac{1}{4} \left[ e^{-(\Gamma_{11}+\Gamma_{12})t} - e^{-(\Gamma_{11}-\Gamma_{12})t} \right]^2 + e^{-2\Gamma_{11}t} \sin^2(2g_{12}t) \right\}^{1/2} \quad (5.25)$$

One of the main differences between the concurrence in the reciprocal case (5.25), and in the unidirectional case (5.24), is the presence of the sinusoidal term in (5.25). When  $g_{12}$  is strong enough, this sinusoidal term causes oscillations in the transient concurrence related to photons being recycled between the two qubits, with a period that corresponds to the round trip time of the coupled qubits through the reciprocal medium (Rabi oscillations). For the unidirectional case (5.24) Rabi oscillations can not occur.

It was shown in [74] that for qubits coupled to an infinite reciprocal waveguide system, the positions of  $\Gamma_{ij}$  maxima/minima correspond to positions of  $g_{ij}$  minima/maxima (for finite waveguides, see [150]). Thus, in general, coherent and dissipative regimes become dominant at different separations between emitters. It was further shown in [74] that for an infinite reciprocal plasmonic waveguide the best entanglement was obtained when  $\Gamma_{ij}$  was large and  $g_{ij}$  was small (forming the dissipative regime), which forces a restriction on the positioning of the qubits in the reciprocal case. However, in the unidirectional case the qubit positioning is unimportant, as detailed in [151], and the qubits can be anywhere in the coherent or dissipative regimes, which is a practical advantage of these unidirectional systems.

In order to demonstrate this difference between reciprocal and unidirectional systems, we consider two cases of pure dissipative and pure coherent qubit communication for a model system where we simply assign the Green function values. Fig. 5.2 shows that the pure dissipative regime is dominant for the reciprocal case while the dissipative or coherent nature of the qubit communication is unimportant for the unidirectional case.

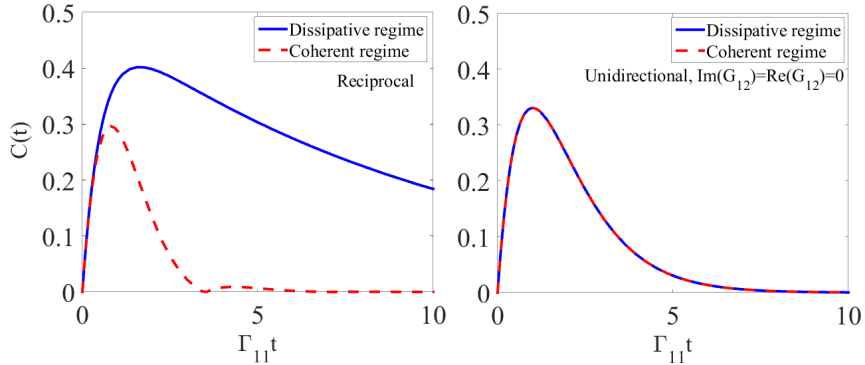


Figure 5.2: Left panel: Concurrence between two qubits for a reciprocal system. For the dissipative regime  $\text{Im}(\mathbf{G}(\mathbf{r}_1, \mathbf{r}_2)) = \text{Im}(\mathbf{G}(\mathbf{r}_2, \mathbf{r}_1)) = 0.9$  and  $\text{Re}(\mathbf{G}(\mathbf{r}_1, \mathbf{r}_2)) = 0$  and for the coherent regime  $\text{Re}(\mathbf{G}(\mathbf{r}_1, \mathbf{r}_2)) = \text{Re}(\mathbf{G}(\mathbf{r}_2, \mathbf{r}_1)) = 0.9$  and  $\text{Im}(\mathbf{G}(\mathbf{r}_1, \mathbf{r}_2)) = 0$ . Right panel: Concurrence between two qubits for a unidirectional system. For the dissipative regime  $\text{Im}(\mathbf{G}(\mathbf{r}_2, \mathbf{r}_1)) = 0.9$ ,  $\text{Re}(\mathbf{G}(\mathbf{r}_2, \mathbf{r}_1)) = 0$  and for the coherent case  $\text{Im}(\mathbf{G}(\mathbf{r}_2, \mathbf{r}_1)) = 0$ ,  $\text{Re}(\mathbf{G}(\mathbf{r}_2, \mathbf{r}_1)) = 0.9$ . In all cases the Green function quantity is normalized by  $\text{Im}(\mathbf{G}(\mathbf{r}_1, \mathbf{r}_1))$ .



A unidirectional SPP can be provided by the interface between a PTI and a topologically-trivial material. When operated in a common bandgap of the two materials (or if the trivial medium is opaque), the SPP is unidirectional, topologically protected from back-scattering, and diffraction-immune, providing an ideal implementation of a strongly nonreciprocal system for qubit interactions. Although here we implement a PTI as a PQHE using a continuum plasma [132]-[152], many other implementations of PTIs are possible, of both PQHE and PQSHE types, and qualitatively would behave in a similar manner.

### 5.3.2 Continuum Photonic Topological Insulator Realization of a Nonreciprocal Surface Plasmon Polariton Environment

We assume a magnetized plasma having the permittivity tensor

$$\underline{\varepsilon} = \begin{bmatrix} \varepsilon_{11} & i\varepsilon_{12} & 0 \\ -i\varepsilon_{12} & \varepsilon_{11} & 0 \\ 0 & 0 & \varepsilon_{33} \end{bmatrix} \quad (5.26)$$

where

$$\begin{aligned} \varepsilon_{11} &= 1 + i\frac{\omega_p^2}{\omega} \left( \frac{\nu - i\omega}{(\nu - i\omega)^2 + \omega_c^2} \right) \\ \varepsilon_{12} &= \frac{\omega_p^2 \omega_c}{\omega((\nu - i\omega)^2 + \omega_c^2)}, \quad \varepsilon_{33} = 1 + i\frac{\omega_p^2}{\omega(\nu - i\omega)}, \end{aligned} \quad (5.27)$$

and where  $\omega_c = (q_e/m_e)B_z$  is the cyclotron frequency ( $B_z$  is the applied bias field),  $\omega_p^2 = N_e q_e^2 / \varepsilon_0 m_e$  is the squared plasma frequency ( $N_e$  is the free electron density and  $q_e$  and  $m_e$  are the electron charge and mass, respectively), and  $\nu$  is the collision frequency. Initially, we set  $\nu = 0$  to focus on the effect of unidirectionality, but later the effect of loss is considered. The magnetized plasma is able to support a bulk TE mode with dispersion  $k_{\text{TE}}^2 = \varepsilon_{33}(\omega/c)^2$  and a bulk TM mode with dispersion  $k_{\text{TM}}^2 = \varepsilon_{\text{eff}}(\omega/c)^2$ , where  $\varepsilon_{\text{eff}} = (\varepsilon_{11}^2 - \varepsilon_{12}^2)/\varepsilon_{11}$  [130]. Both bulk modes are reciprocal. The Chern number of the bulk TE mode is trivial, and so TE modes are not considered further in this work. The Chern numbers of the bulk TM modes are nonzero, and at the interface of the magnetized plasma and a topologically-trivial (simple) medium the gap Chern number is  $C_{\text{gap}} = 1$  [132, 153], indicating the presence of one nonreciprocal, backscattering-immune TM-SPP that crosses the bandgap (bandstructure is shown later, in Fig. 5.4).

### 5.3.3 Entanglement Evaluation in Different Environments

We first consider the behavior of the concurrence for qubits in several different environments, and establish that the best entanglement occurs for a PTI/opaque medium interface. Fig. 5.3a, shows a

comparison of concurrence between four different cases of two qubits interacting through: 1) vacuum, 2) at the interface of a gold half-space and vacuum, 3) at the interface of a magnetized plasma and vacuum, and 4) at the interface of a magnetized plasma and an opaque medium. Here and in the following, the Green function is calculated numerically [154]. The system of qubits were initially

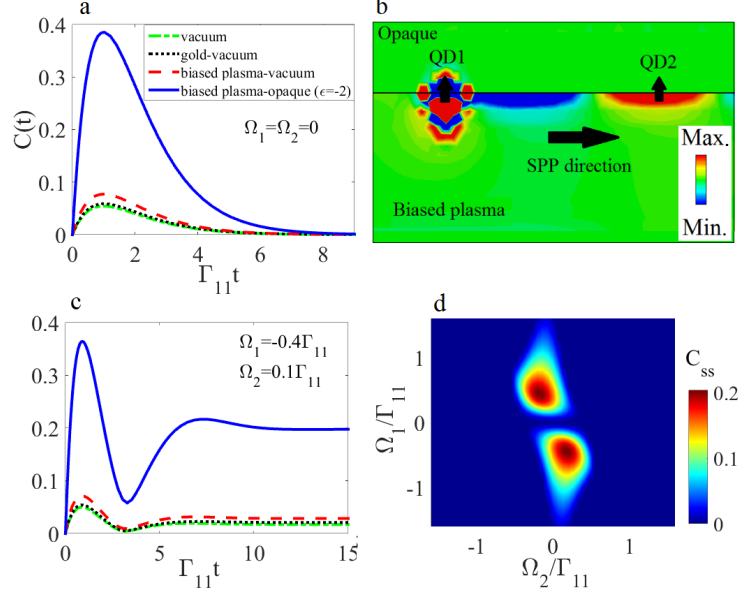


Figure 5.3: a. Transient concurrence for two interacting qubits in different environments; 1) vacuum, 2) at the interface of a gold half-space ( $\varepsilon = -91.6 - 3i$ ) and vacuum, 3) at the interface of a magnetized plasma ( $\omega_p/\omega = 0.95$ ,  $\omega_c/\omega = 0.21$ ) and vacuum, and 4) at the interface of the magnetized plasma and an opaque medium (non-biased plasma with  $\omega_p/\omega = \sqrt{3}$ , such that  $\varepsilon = -2$ ). b. One way SPP at the interface of the biased plasma and the opaque medium at  $\omega/2\pi = 200$  THz. c. Driven concurrence of two qubits in the same environments as in panel a. d. Steady states concurrence versus pumping intensities for the case of the biased plasma and opaque medium interface. The qubit separation is  $2.4 \mu\text{m}$  ( $1.6\lambda_0$ ).

prepared in state  $|4\rangle = |e_1\rangle \otimes |g_2\rangle$ , such that the left qubit is initially in the excited state while the right qubit is in the ground state. It can be seen that the interface between the magnetized plasma and the opaque medium has higher concurrence than the other cases, due to the existence of a strong SPP and the fact that there can be no radiation into either bulk half-space. Thus, in the following, we focus on the magnetized plasma/opaque medium geometry. The poor performance of the gold-vacuum interface is somewhat surprising, since a strong SPP can be excited and the separation is chosen to be in the dissipative regime, which is a best-case scenario for the reciprocal case. Making the gold lossless does not significantly improve the concurrence (results not shown). The problem is primarily due to the lack of lateral confinement of the SPP so the energy of SPP follows along other undesired directions.

Figure 5.3b shows the excited unidirectional SPP at the interface of the magnetized plasma and the opaque medium, demonstrating the unidirectional nature of the SPP, and Fig. 5.3c shows the case of pumped concurrence, where the qubit depopulation is compensated by applying an external

laser source in resonance with the atomic transition frequency. The pump intensity must be chosen carefully, as illustrated in Fig. 5.3d, which shows the steady state concurrence for a wide range of laser intensities (a laser pump can be applied to the qubits via, e.g., a fiber penetrating into the material). It can be seen that the laser intensity can not be too large, otherwise the qubits will interact mostly with the laser. Ideally, the pump should be strong enough to keep the system interacting, but weak enough for the qubit interaction to dominate the dynamics. It is clear from Fig. 5.3d that unequal pumping leads to larger steady state concurrence.

### 5.3.4 Topological Aspect of Entanglement

In this section we briefly show the topological aspect of entanglement in a PTI system. Figure 5.4 shows the reciprocal bulk bands (solid blue) for the biased plasma, and the unidirectional gap-crossing SPP (dashed red) dispersion for a biased-plasma/opaque medium interface, for different values of bias. For  $\omega_c > 0$  the gap Chern number is -1 [132, 153], and there is a positive-traveling SPP ( $v_g = d\omega/dk > 0$ ), topologically-protected against backscattering. At  $\omega_c = 0$  the gap closes, the material becomes topologically-trivial (gap Chern number is 0), and there exists a reciprocal SPP. For  $\omega_c < 0$  the gaps reopens, the gap Chern number is 1, and there is a negative-traveling SPP ( $v_g < 0$ ), topologically-protected against backscattering.

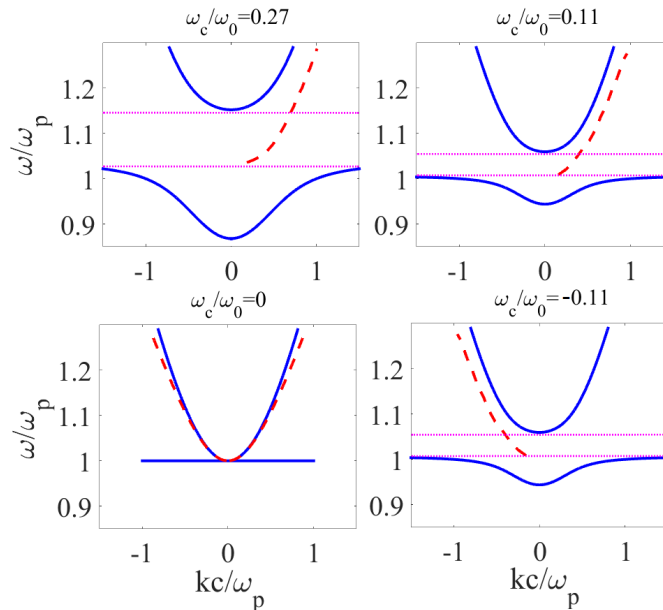


Figure 5.4: Reciprocal bulk bands (solid blue) for the biased plasma ( $\omega_p/\omega = 0.95$ ), and the unidirectional gap-crossing SPP (dashed red) dispersion for a biased-plasma/opaque medium ( $\varepsilon = -2$ ) interface, for different values of bias at  $\omega/2\pi = 200$  THz.

Figure 5.5 shows the concurrence when the left dot has an initial excitation (state  $|4\rangle = |e_1, g_2\rangle$ ). The concurrence is rather insensitive to the bias as long as the topology does not change, however, when the gap closes and reopens the concurrence vanishes.

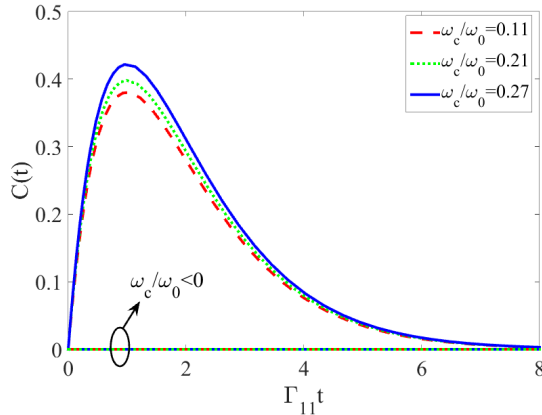


Figure 5.5: Concurrence mediated by a unidirectional SPP at the interface of biased plasma ( $\omega_p/\omega = 0.95$ ) and an opaque medium ( $\varepsilon = -2$ ) when the left dot has an initial excitation (state  $|4\rangle = |e_1, g_2\rangle$ ). For  $\omega_c < 0$ , the same three absolute values are considered as for positive bias, i.e.,  $\omega_c/\omega_0 = -|0.27|, -|0.21|$ , and  $-|0.11|$ . The qubit separation is  $2.4 \mu\text{m}$  ( $1.6\lambda_0$ ).

### 5.3.5 Preserving Entanglement in the Presence of Large Defects

Perhaps the most important aspect of using PTIs for entanglement is the possibility of robust SPPs, topologically-immune to backscattering (and immune to diffraction if operated in the bulk bandgap) in the presence of any arbitrary large obstacle or defect. To examine this, we compare two cases: 1) the interface between an opaque medium and a biased plasma, and 2) the interface between the same opaque medium and an unbiased plasma.

In the nonreciprocal case, this unidirectional and scattering-immune SPP provides the ability to preserve the entangled state of two qubits in plasmonic systems even in the presence of very non-ideal interfaces. Figure 5.6 shows the transient concurrence for the cases of biased/unbiased plasmas with flat and defected interfaces. Although for the flat interface the biased plasma provides better concurrence than the reciprocal (unbiased) case, this could be perhaps altered by adjustment of the two material half-space properties. However, the point is that in the presence of a defect, as shown in the right panel, the reciprocal SPP suffers from a strong reflection at the defect, as expected, whereas the nonreciprocal SPP (biased plasma) detours around the defect, leading to the same concurrence as without the defect.

### 5.3.6 Finite-Width Waveguide

The previous results were for an infinitely-wide interface. In this section we examine the effect of lateral confinement of the SPP [153]. Figure 5.7a shows the finite-width waveguide geometry. In order to efficiently confine the SPP along the propagation axis, the plasma is extended past the interface to form partially-extended sidewalls. Only partial side walls are needed to prevent radiation in space, since the SPP is confined to the vicinity of the interface.

Lateral confinement of the unidirectional SPP improves both the transient and steady state

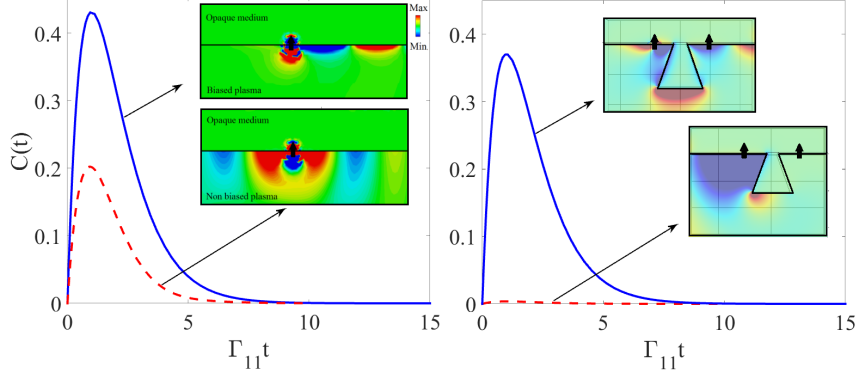


Figure 5.6: Left panel: Transient concurrence of two qubits interacting through a flat interface made of an opaque medium ( $\varepsilon = -2$ ) and both an unbiased plasma ( $\omega_p/\omega = 0.95$ ,  $\omega_c/\omega = 0$ ) and a biased plasma ( $\omega_p/\omega = 0.95$ ,  $\omega_c/\omega = 0.21$ ). Insert shows shows the electric field  $E_y$  excited by a vertical electric dipole. Right panel: Same thing for the case of a defected interface, where the defect contour length is of the order of a free-space wavelength. The system of qubits is initially prepared in the state  $|4\rangle = |e_1, g_2\rangle$ . The qubit separation is  $1.7 \mu\text{m}$  ( $1.13\lambda_0$ ).

(pumped) concurrence. Fig. 5.7b shows the transient and steady state concurrence of two qubits initially prepared in state  $|4\rangle$ . In comparison to Fig. 5.3a, it can be seen that lateral confinement increases both the maximum transient concurrence and the steady state concurrence. Figure 5.7c shows the dynamics of the qubits under external pumping, where  $\rho_{11}$ ,  $\rho_{22}$ ,  $\rho_{33}$ , and  $\rho_{44}$  are the probabilities of finding both qubits to be in ground state, both qubits in the excited state, the first qubit in the ground state and the second qubit in the excited state, and vice versa, respectively. Figure 5.7d shows the steady state concurrence for a wide range of pump values. The behavior is similar to the case of the infinite interface, Fig. 5.3d, except that the range of pump values that result in large steady state concurrence is extended, and the maximum achievable steady state concurrence is larger in the case of the finite-width waveguide.

In Fig. 5.8, qubit concurrence is shown for a finite-width waveguide having a defect which spans the entire waveguide width. It can be seen that the concurrence is minimally affected by the defect. Although not shown, as with Fig. 5.6, in the reciprocal (unbiased) case the defect eliminates the concurrence.

### 5.3.7 Effect of Different Initial State Preparations

An interesting behavior of the concurrence arising from having a unidirectional SPP is that, e.g., if the medium supports only a right going SPP, then the initially excited qubit should be the left qubit, otherwise the qubits remain unentangled, as shown in Fig. 5.9a for the unpumped case  $\Omega_1 = \Omega_2 = 0$ . Figure 5.9b shows the dynamics of the qubits for this unpumped case. It can be seen that  $\rho_{33}$ , which is the probability of finding the right qubit in the excited state and the left qubit in the ground state, starts from 1 and then drops rapidly. However,  $\rho_{44}$ , which is the probability of finding the excitation being in the left qubit with the right qubit in the ground state, is always zero, meaning

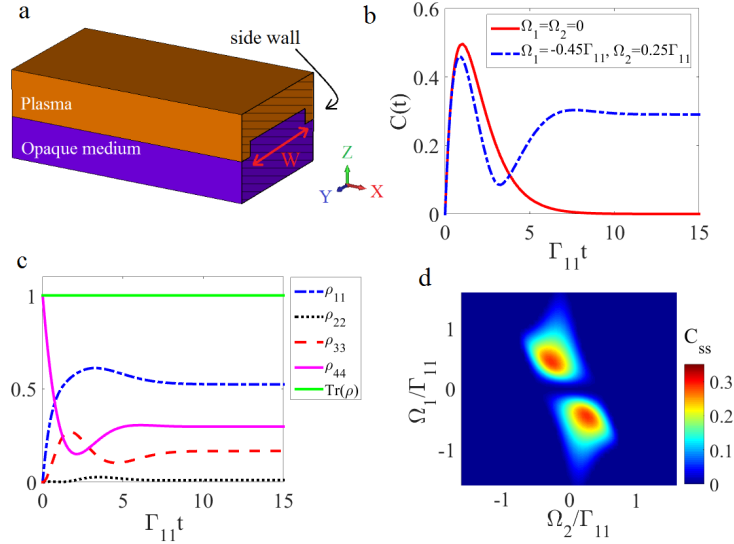


Figure 5.7: a. Finite-width waveguide formed by an opaque medium and biased plasma. b. Transient and driven concurrence of two qubits interacting through the finite-width waveguide. For the biased plasma,  $\omega_p/\omega = 0.95$  and  $\omega_c/\omega = 0.21$ , and for the opaque medium,  $\varepsilon = -2$ . c. Dynamics of the qubits under external pumping. d. Steady state concurrence for different pump values. Waveguide width is  $1.8 \mu\text{m}$  ( $1.2\lambda_0$ ) and qubit separation is  $2.4 \mu\text{m}$  ( $1.6\lambda_0$ )

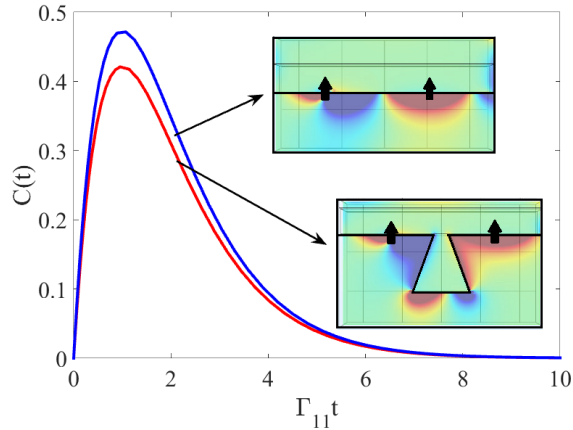


Figure 5.8: Transient concurrence of two qubits interacting in a finite-width waveguide (see Fig. 5.7a) consisting of an opaque medium ( $\varepsilon = -2$ ) and a biased plasma ( $\omega_p/\omega = 0.95$ ,  $\omega_c/\omega = 0.21$ ). The defect contour length is of the order of a free-space wavelength, and spans the width of the waveguide,  $W = 1.8 \mu\text{m}$  ( $1.2\lambda_0$ ). Qubit spacing for the flat interface is  $2.4 \mu\text{m}$  ( $1.6\lambda_0$ ), and for the interface with defect, the line-of-sight spacing is  $2.4 \mu\text{m}$ . The system of qubits is initially prepared in the state  $|4\rangle = |e_1, g_2\rangle$ .

that the excitation lost from the right qubit never gets captured by the left qubit. This behavior is particular to a unidirectional environment, and allows for keeping two qubits disentangled at any qubit separation, even if one of them carries an excitation.

However, by applying an external pump we can achieve non-zero concurrence, as also depicted in Fig. 5.9a. The pump is turned on at  $t = 0$ , and instead of immediately becoming non-zero, the concurrence remains zero for a period of time, then starts raising as a sudden birth in concurrence and

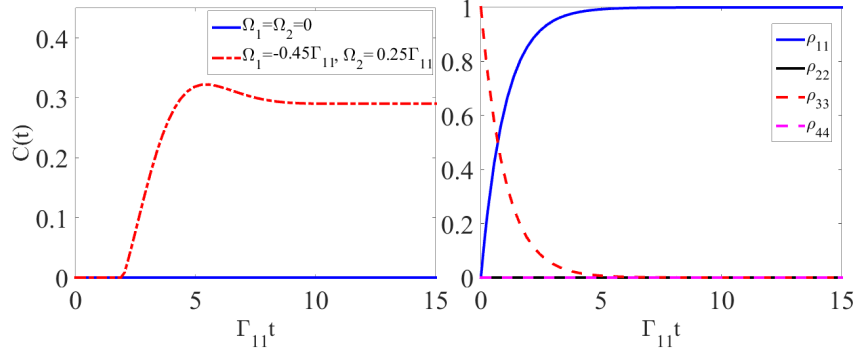


Figure 5.9: Left panel: Transient and driven concurrence for a system of qubits interacting through a right going unidirectional SPP while the initial excitation is in the right qubit. Right panel: Dynamics of the qubit system for the transient case. For the biased plasma  $\omega_p/\omega = 0.95$  and  $\omega_c/\omega = 0.21$ , and for the opaque medium  $\varepsilon = -2$ . The waveguide geometry is shown in Fig. 5.7a, and qubit separation is  $2.4 \mu\text{m}$  ( $1.6\lambda_0$ )

reaches a non-zero steady state value. This delayed sudden-birth is quite different from the pumped reciprocal case.

It is also possible to consider different initial states which can give other possible unidirectional SPP assisted dynamical evolutions. Figure 5.10 shows the case of the initial state being the maximally entangled Bell state  $|\Psi_{\text{Bell}}\rangle = (|1\rangle + |2\rangle)/\sqrt{2}$ . We consider that the qubits are interacting through the

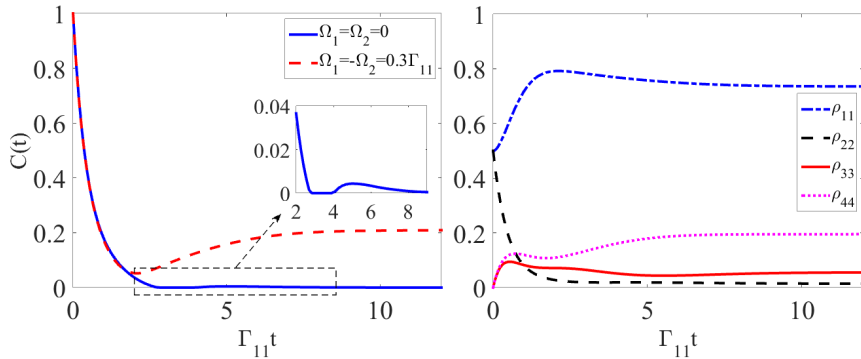


Figure 5.10: Left panel: Transient and driven concurrence for a system of qubits initially prepared in the Bell state. Right panel: Dynamics of the qubits system under external pumping. For the biased plasma,  $\omega_p/\omega = 0.95$  and  $\omega_c/\omega = 0.21$ , and for the opaque medium  $\varepsilon = -2$ . The waveguide geometry is shown in Fig. 5.7a with  $W = 1.8 \mu\text{m}$  ( $1.2\lambda_0$ ), and qubit separation is  $2.4 \mu\text{m}$  ( $1.6\lambda_0$ ).

finite-width waveguide depicted in Fig. 5.7a. Figure 5.10a shows the time evolution of the concurrence for both pumped and non-pumped cases. In contrast to the previous cases, the concurrence starts from one due to the maximum degree of entanglement of the initial Bell state. For the non-pumped case the concurrence diminishes in time as the system becomes disentangled, resulting in a sudden death of entanglement. It remains zero for a period of time, then the entanglement experience a rebirth before decaying exponentially at long times. For the externally pumped case, the concurrence exponentially decays but the qubits do not become completely disentangled. Fig. 5.10b shows the

dynamics of the qubits for the pumped case. The population probabilities  $\rho_{11}$  and  $\rho_{22}$  start from 0.5 due to the Bell state preparation. An interesting behavior in the qubit dynamics is the unequal steady state values  $\rho_{33}$  and  $\rho_{44}$  values under pumping with equal intensities  $|\Omega_1| = |\Omega_2|$  (in the reciprocal case,  $\rho_{33} = \rho_{44}$ ).

### 5.3.8 Lossy Biased Plasma

In a lossy medium the SPP loses power as it propagates along the interface, resulting in weaker qubit entanglement. In order to study the effect of loss, we suppose the qubits are interacting through an infinitely-wide interface as considered in Fig. 5.3, but for three different collision frequencies;  $\nu = 0$ ,  $\nu/2\pi = 270$  MHz and  $\nu/2\pi = 500$  MHz. Qubits are initially prepared in the state  $|4\rangle = |e_1\rangle \otimes |g_2\rangle$ . Figure 5.11, left panel, shows the transient concurrence. Increasing the collision frequency reduces the concurrence, and for collision frequencies greater than 500 MHz loss dominates the system and an entangled state is not achievable for this relatively wide qubit separation of  $1.6\lambda_0$ .

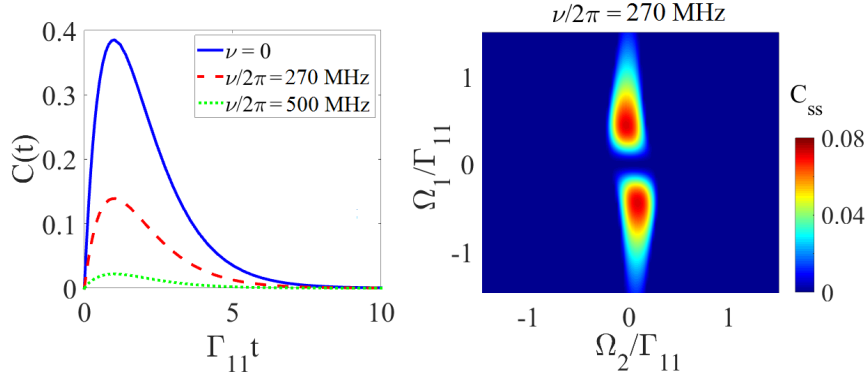


Figure 5.11: Left panel: Transient concurrence of two qubits interacting through an infinite interface between a biased plasma ( $\omega_p/\omega = 0.95$  and  $\omega_c/\omega = 0.21$ ) and an opaque medium ( $\epsilon = -2$ ) for different values of the collision frequency. Right panel: Steady state concurrence for different pump values in the lossy case. Qubit separation is  $2.4 \mu\text{m}$  ( $1.6\lambda_0$ )

The right panel of Fig. 5.11 shows the steady state concurrence of the pumped system, versus pumping intensity. In comparison to the lossless case (Fig. 5.3d), the range of pump intensities that give non-zero steady state concurrence has decreased, and the maximum achievable concurrence value is diminished compared to the lossless case.

## 5.4 Summary

The ability to guide the energy fellow from one quantum dot to another one is a great advantage to achieve highly entangled states. PTIs are able to support unidirectional, backscattering immune surface waves. In this chapter, for the first time, the unidirectional surface wave assisted entanglement using PTIs is investigated. We have studied the spontaneous and pumped entanglement of two level



systems (quantum dots) in the vicinity of a PTIs interface, which supports a unidirectional, back-scattering immune and topologically-protected surface plasmon polariton in the bandgap of the bulk material. We have also derived a master equation for quantum dots interactions in a general three-dimensional, nonreciprocal, inhomogeneous and lossy environment. The environment is represented exactly, via the photonic Green function. The resulting entanglement is shown to be extremely robust to defects occurring in the material system, such that strong entanglement is maintained even if the interface exhibits electrically-large and geometrically sharp discontinuities. We have showed that, alternatively, depending on the initial excitation state, using PTIs allows two quantum dots to remain un-entangled even for very close spacing. Our formulation and results in this work are useful for both fundamental investigations of quantum dynamics in nonreciprocal environments, and technological applications related to entanglement in two-level systems.

# Appendices

## .1 Appendix I: Non-Reciprocal Green Function

The electric field dyadic Green function  $\mathbf{G}(\mathbf{r}, \mathbf{r}', \omega)$  satisfies the following equation

$$\left[ \nabla \times \nabla \times - \frac{\omega^2}{c^2} \boldsymbol{\epsilon}(\mathbf{r}, \omega) \right] \mathbf{G}(\mathbf{r}, \mathbf{r}', \omega) = \mathbf{I} \delta(\mathbf{r} - \mathbf{r}') \quad (28)$$

Let us suppose that the dyadic Green function  $\mathbf{G}(\mathbf{r}, \mathbf{r}', \omega)$  can be accounted as the elements of an operator  $\hat{\mathbf{G}}$  in position basis as

$$\mathbf{G}(\mathbf{r}, \mathbf{r}', \omega) = \langle \mathbf{r} | \hat{\mathbf{G}} | \mathbf{r}' \rangle \quad (29)$$

the matrix elements of the position operator  $\hat{\mathbf{r}}$  are

$$\langle \mathbf{r} | \hat{\mathbf{r}} | \mathbf{r}' \rangle = \mathbf{r} \delta(\mathbf{r} - \mathbf{r}') \quad (30)$$

Let us suppose that the momentum operator is  $\hat{\mathbf{k}}$  where  $\hat{\mathbf{k}} = -i\nabla$  so we can write  $\nabla = i\hat{\mathbf{k}}$ . If we define an operator as

$$\hat{\mathbf{H}} = i\hat{\mathbf{k}} \times i\hat{\mathbf{k}} \times -\frac{\omega^2}{c^2} \boldsymbol{\epsilon} \quad (31)$$

where

$$\langle \mathbf{r} | \hat{\mathbf{I}} | \mathbf{r}' \rangle = \mathbf{I} \delta(\mathbf{r} - \mathbf{r}') \quad (32)$$

is the unit operator, then the Green function equation in 28 corresponds to  $\hat{\mathbf{H}}\hat{\mathbf{G}} = \hat{\mathbf{I}}$ . It follows the equation  $\hat{\mathbf{G}} = \hat{\mathbf{H}}^{-1}$ . After multiplying it from the right by  $\hat{\mathbf{H}}$  we find

$$\hat{\mathbf{G}}\hat{\mathbf{H}} = \hat{\mathbf{I}} \quad (33)$$

The Hermitian conjugate of above equation is

$$\hat{\mathbf{H}}^\dagger \hat{\mathbf{G}}^\dagger = \hat{\mathbf{I}} \quad (34)$$

if we multiply 33 by  $\hat{\mathbf{G}}^\dagger$  from right and 34 by  $\hat{\mathbf{G}}$  from left and subtract them we get

$$\hat{\mathbf{G}} (\hat{\mathbf{H}} - \hat{\mathbf{H}}^\dagger) \hat{\mathbf{G}}^\dagger = \hat{\mathbf{G}}^\dagger - \hat{\mathbf{G}} \quad (35)$$

where

$$\hat{\mathbf{H}} - \hat{\mathbf{H}}^\dagger = i\hat{\mathbf{k}} \times i\hat{\mathbf{k}} \times -\frac{\omega^2}{c^2} \boldsymbol{\epsilon} - i\hat{\mathbf{k}}^\dagger \times i\hat{\mathbf{k}}^\dagger \times +\frac{\omega^2}{c^2} \boldsymbol{\epsilon}^\dagger = -\frac{\omega^2}{c^2} (\boldsymbol{\epsilon} - \boldsymbol{\epsilon}^\dagger) \quad (36)$$

so 35 can be written as

$$\frac{\omega^2}{c^2} \hat{\mathbf{G}} (\boldsymbol{\epsilon} - \boldsymbol{\epsilon}^\dagger) \hat{\mathbf{G}}^\dagger = \hat{\mathbf{G}} - \hat{\mathbf{G}}^\dagger \quad (37)$$

let us define the tensor  $\mathbf{R}$  such that

$$\mathbf{R} = \frac{1}{2i}(\boldsymbol{\epsilon} - \boldsymbol{\epsilon}^\dagger) \quad (38)$$

then in Cartesian components we get

$$2i\frac{\omega^2}{c^2} \sum_{m,m'} \hat{G}_{im} \mathbf{R}_{mm'} \hat{G}_{m'j}^\dagger = \hat{G}_{ij} - \hat{G}_{ji}^\dagger \quad (39)$$

writing above equation in position basis gives

$$2i\frac{\omega^2}{c^2} \int d^3r'' \sum_{m,m'} \langle \mathbf{r} | \hat{G}_{im} | \mathbf{r}'' \rangle \langle \mathbf{r}'' | \mathbf{R}_{mm'} | \mathbf{r}'' \rangle \langle \mathbf{r}'' | \hat{G}_{m'j}^\dagger | \mathbf{r}' \rangle = \langle \mathbf{r} | \hat{G}_{ij} | \mathbf{r}' \rangle - \langle \mathbf{r} | \hat{G}_{ji}^\dagger | \mathbf{r}' \rangle \quad (40)$$

considering the relation

$$\begin{aligned} \langle \mathbf{r}'' | \hat{G}_{m'j}^\dagger | \mathbf{r}' \rangle &= \langle \mathbf{r}' | \hat{G}_{m'j} | \mathbf{r}'' \rangle^* = \mathbf{G}_{m'j}^*(\mathbf{r}', \mathbf{r}'') \\ \langle \mathbf{r} | \hat{G}_{im} | \mathbf{r}'' \rangle &= \mathbf{G}_{im}(\mathbf{r}, \mathbf{r}'') \end{aligned} \quad (41)$$

we get

$$2i\frac{\omega^2}{c^2} \int d^3r'' \sum_{m,m'} \mathbf{G}_{im}(\mathbf{r}, \mathbf{r}'', \omega) \mathbf{R}_{mm'}(\mathbf{r}'', \mathbf{r}'', \omega) \mathbf{G}_{m'j}^*(\mathbf{r}', \mathbf{r}'', \omega) = \mathbf{G}_{ij}(\mathbf{r}, \mathbf{r}') - \mathbf{G}_{ji}^*(\mathbf{r}', \mathbf{r}) \quad (42)$$

in matrix form we have

$$2i\frac{\omega^2}{c^2} \int d^3r'' \mathbf{G}(\mathbf{r}, \mathbf{r}'', \omega) \cdot \mathbf{R}(\mathbf{r}'', \mathbf{r}'', \omega) \cdot \mathbf{G}^*(\mathbf{r}', \mathbf{r}'', \omega) = \mathbf{G}(\mathbf{r}, \mathbf{r}') - \mathbf{G}^\dagger(\mathbf{r}', \mathbf{r}) \quad (43)$$

Above equation is the general non reciprocal form which should be used in density matrix derivation. Now lets consider the reciprocal form with scalar permittivity. In this case the tensor  $\mathbf{R}$  reduces to  $\text{Im}(\epsilon) \mathbf{I}$  with unit dyad  $\mathbf{I}$  and considering the relation  $\mathbf{G}_{ij}(\mathbf{r}, \mathbf{r}') = \mathbf{G}_{ji}(\mathbf{r}', \mathbf{r})$  above equation can be simplified to

$$2i\frac{\omega^2}{c^2} \int d^3r'' \text{Im}(\epsilon(\mathbf{r}'', \omega)) \mathbf{G}(\mathbf{r}, \mathbf{r}'', \omega) \mathbf{G}^*(\mathbf{r}'', \mathbf{r}', \omega) = \mathbf{G}(\mathbf{r}, \mathbf{r}') - \mathbf{G}^*(\mathbf{r}, \mathbf{r}') \quad (44)$$

the right hand side of above equation is  $\mathbf{G}(\mathbf{r}, \mathbf{r}') - \mathbf{G}^*(\mathbf{r}, \mathbf{r}') = 2i\text{Im}\{\mathbf{G}(\mathbf{r}, \mathbf{r}')\}$ , it yields

$$\frac{\omega^2}{c^2} \int d^3r'' \text{Im}(\epsilon(\mathbf{r}'', \omega)) \mathbf{G}(\mathbf{r}, \mathbf{r}'', \omega) \mathbf{G}^*(\mathbf{r}'', \mathbf{r}', \omega) = \text{Im}\{\mathbf{G}(\mathbf{r}, \mathbf{r}')\} \quad (45)$$

which is the usual equation people use.

## .2 Appendix II: Master Equation Approximations

Here we briefly discuss the approximations used in the derivation of the master equation (5.18)-(5.19).

The first approximation made in the derivation is the rotating wave approximation (RWA) where in the interaction picture we drop the rapidly varying counter-rotating terms in  $H_I$ . This approximation is valid for  $\Gamma_{ii} \ll \omega$ . The qubit transition frequency is  $\omega/2\pi = 200$  THz, and we assume a dipole moment  $d = 60$  D. For an interface made of lossless biased plasma,  $\Gamma_{ii}/2\pi \sim 450$  MHz, and for the lossy biased plasma with  $\nu/2\pi = 500$  MHz,  $\Gamma_{ii}/2\pi \sim 2$  GHz. For the non biased plasma-opaque medium interface (interface supporting reciprocal SPP)  $\Gamma_{ii}/2\pi \sim 75$  MHz. In all cases the condition for the validity of the RWA is strongly met.

We also applied the Born-Markov approximation, which comes from the assumption that the reservoir relaxation time,  $\tau_R$ , is much faster than the relaxation time of the qubit system  $\tau_S = 1/\Gamma_{ii}$ . This allows for the expansion of the exact equation of motion for the density matrix up to second order, and makes the quantum master equation local in time. For a nonreciprocal medium the fluctuation-dissipation theorem [147] is

$$\langle P_\alpha(\omega, \mathbf{r}) P_\alpha^\dagger(\omega', \mathbf{r}') \rangle = \frac{\hbar}{4i} (\epsilon(\omega, \mathbf{r}) - \epsilon^\dagger(\omega, \mathbf{r})) N(\omega, T) \delta(\omega - \omega') \delta(\mathbf{r} - \mathbf{r}') \delta_{\alpha\beta}, \quad (46)$$

where  $N(\omega, T) = 2 / (\exp(\hbar\omega/k_B T) - 1)$  for negative frequencies and  $N(\omega, T) = 1 + 2 / (\exp(\hbar\omega/k_B T) - 1)$  for positive frequencies, where  $k_B$  is Boltzmann's constant. Regarding  $\mathbf{E}(\mathbf{r}, \omega) = (\omega^2/c^2\epsilon_0) \int_V d\mathbf{r}' \mathbf{G}(\mathbf{r}, \mathbf{r}', \omega) \cdot \mathbf{P}(\mathbf{r}', \omega)$ , it can be shown that

$$\langle E_\alpha(\mathbf{r}, \omega) E_\alpha^\dagger(\mathbf{r}, \omega) \rangle = k_0^2 \frac{\hbar}{4i\epsilon_0^2} N(\omega, T) (G_{\alpha\alpha}(\mathbf{r}, \mathbf{r}, \omega) - G_{\alpha\alpha}^\dagger(\mathbf{r}, \mathbf{r}, \omega)), \quad (47)$$

which reduces in the reciprocal case to

$$\langle E_\alpha(\mathbf{r}, \omega) E_\alpha^\dagger(\mathbf{r}, \omega) \rangle = \frac{\hbar k_0^2}{2\epsilon_0^2} N(\omega, T) \text{Im}(G_{\alpha\alpha}(\mathbf{r}, \mathbf{r}, \omega)). \quad (48)$$

The bath relaxation time can be estimated by looking at the decay time of the correlation

$$\langle E_\alpha(\mathbf{r}, t) E_\alpha^\dagger(\mathbf{r}, 0) \rangle = \frac{1}{2\pi} \int_{-\infty}^{+\infty} d\omega e^{-i\omega t} \langle E_\alpha(\mathbf{r}, \omega) E_\alpha^\dagger(\mathbf{r}, \omega) \rangle. \quad (49)$$

The Green function consists of homogeneous (vacuum) and scattered terms, and  $\tau_R$  will be dominated by the slower scattered field contribution (for the vacuum term,  $\tau_R(T) = \hbar/\pi k_B T$  [155], so that  $\tau_R(300K) \sim 10$  fs). For the scattered part of the Green function for an interface made of non-biased plasma-opaque medium (interface supporting reciprocal SPP), using the Green function in [156],  $\tau_R \sim 10^{-11}$  s for  $\nu = 500$  MHz and  $\nu = 270$  MHz, whereas  $\tau_S = 1/\Gamma_{ii} \sim 10^{-8}$  s, so that we can ignore the reservoir relaxation time.

### .3 Appendix III: Comparison With Previous 1D Chiral Theory

Here we discuss the relation between the general ME we derived in terms of the exact electromagnetic Green function, resulting, for two qubits, in the Lindblad (5.23), and the 1D phenomenological ME for two level systems coupled to a 1D chiral reservoir presented in [151, 158] (see also [159, 157]). The 1D chiral theory is based on the notion of right and left, defining couplings  $\gamma_{R,L}$ , whereas the theory presented here is based on qubit interactions  $\Gamma_{ij}$ ; note that  $\Gamma_{ij}$  plays the role of a  $\Gamma_{\text{right}}$  if  $x_i > x_j$ , but plays the role of  $\Gamma_{\text{left}}$  if  $x_i < x_j$ . To facilitate the comparison with the 1D chiral theory we will assume two qubits with positions  $x_1$  and  $x_2$ , with  $x_2 > x_1$ . In [151, 158] phenomenological quantities  $\gamma_{iR}, \gamma_{iL}$  for  $i = 1, 2$  are utilized, and setting  $\gamma_{1R} = \gamma_{2R} = \gamma_R$  and  $\gamma_{1L} = \gamma_{2L} = \gamma_L$ , the 1D chiral Lindblad superoperator is

$$\begin{aligned} \mathcal{L}\rho_s(t) = & \sum_{j=1,2} \gamma_j \left( 2\sigma_j \rho_s \sigma_j^\dagger - \rho_s \sigma_j^\dagger \sigma_j - \sigma_j^\dagger \sigma_j \rho_s \right) \\ & + \gamma_R e^{ik_R(x_2-x_1)} \left( \sigma_2 \rho_s \sigma_1^\dagger - \rho_s \sigma_1^\dagger \sigma_2 \right) \\ & + \gamma_R e^{-ik_R(x_2-x_1)} \left( \sigma_1 \rho_s \sigma_2^\dagger - \sigma_2^\dagger \sigma_1 \rho_s \right) \\ & + \gamma_L e^{-ik_L(x_2-x_1)} \left( \sigma_1 \rho_s \sigma_2^\dagger - \rho_s \sigma_2^\dagger \sigma_1 \right) \\ & + \gamma_L e^{ik_L(x_2-x_1)} \left( \sigma_2 \rho_s \sigma_1^\dagger - \sigma_1^\dagger \sigma_2 \rho_s \right), \end{aligned} \quad (50)$$

where  $k_{L,R} = \omega_0/v_{gL,R}$ , with  $v_g$  being the group velocity of the guided photons.

If we assume now a plasmonic environment, the total emission of the source can be divided into several decay channels:  $\Gamma_{11} = \Gamma_r + \Gamma_{\text{nr}} + \Gamma_{\text{SPP}}$ , where  $\Gamma_r$  represents free-space radiation,  $\Gamma_{\text{nr}}$  represents losses in the material (quenching), and  $\Gamma_{\text{SPP}}$  represents excitation of SPPs. Material absorption and radiation do not contribute to strong qubit-qubit interactions, and therefore we are interested in systems with strong decay through the plasmon channel,  $\Gamma_{\text{SPP}}$ , where the fraction of all emissions that are coupled to plasmons is expressed by  $\beta_{ij} = \Gamma_{ij,\text{SPP}}/\Gamma_{11}$ , with  $i \neq j$ .

Assuming a plasmonic environment with a preferred propagation axis, here taken as  $x$ , in order to connect our formulation with previous 1D chiral formulations [151, 158] we introduce a particular 1D plasmonic version of (5.20),

$$\begin{aligned} g_{ij} & \simeq g_{ij,\text{SPP}} = \beta_{ij} \Gamma_{11} e^{-k''_{ij}|x_i-x_j|} \sin [k'_{ij}(x_i - x_j)] \\ \Gamma_{ij} & \simeq \Gamma_{ij,\text{SPP}} \\ & = \begin{cases} (\beta_{12} + \beta_{21}) \Gamma_{11}, & i = j \\ 2\beta_{ij} \Gamma_{11} e^{-k''_{ij}|x_i-x_j|} \cos [k'_{ij}(x_i - x_j)], & i \neq j, \end{cases} \end{aligned} \quad (51)$$

where  $k_{ij} = k_{\text{SPP},ij} = k'_{\text{SPP},ij} + ik''_{\text{SPP},ij}$  are the SPP wavenumbers. In the systems considered here the

bulk modes are reciprocal, whereas the interface SPP is strongly nonreciprocal (unidirectional). Thus, to compare with the 1D chiral ME it is sensible to consider the SPP (nonreciprocal) contribution.

As defined in (51),  $\Gamma_{ij,\text{SPP}}$  is discontinuous at  $x_i = x_j$  in the nonreciprocal case, i.e.,  $\Gamma_{ij,\text{SPP}} = 2\beta_{ij}\Gamma_{11}$  as  $|x_i \rightarrow x_j|$ , whereas at  $x_i = x_j$ ,  $\Gamma_{ij,\text{SPP}} = (\beta_{12} + \beta_{21})\Gamma_{11}$ . As we show below, the SPP contribution in the considered PTI system is indeed discontinuous at  $x_i = x_j$ . However, the exact  $\Gamma_{ij}$ , which contains both the SPP and radiation continuum, is continuous at the source point even in the nonreciprocal case. As another example of this, a 3D analytical Green function for a nonreciprocal bulk medium is provided in [160] (see their Eq. (117)), where  $\Gamma_{ij}$  is also seen to be continuous.

Equating (5.23) in the 1D case (i.e., using (51)) and (50) term by term, the two Lindblad super-operators will be equal if

$$\gamma_j = \frac{\Gamma_{jj}}{2}, \quad (52)$$

$$\gamma_R e^{\pm ik(x_2 - x_1)} = \frac{\Gamma_{21}}{2} \pm ig_{21}, \quad (53)$$

$$\gamma_L e^{\pm ik(x_1 - x_2)} = \frac{\Gamma_{12}}{2} \pm ig_{12}. \quad (54)$$

If we now make the assignments

$$\beta_{21}\Gamma_{11} \rightarrow \gamma_R, \quad \beta_{12}\Gamma_{11} \rightarrow \gamma_L, \quad (55)$$

$$k_{\text{spp},12} \rightarrow \frac{\omega_0}{v_{gL}}, \quad k_{\text{spp},21} \rightarrow \frac{\omega_0}{v_{gR}}, \quad (56)$$

then (52)-(54) are satisfied and (5.23) becomes strictly equal to (50). It is worth stressing that physically the two formulations still differ, since (56) is not exact (phase velocity and group velocity are different quantities). Nonetheless it is interesting to try to connect the phenomenological parameters in the model (50) to the corresponding ones in (5.23), which are obtained in terms of the Green function, and hence can be computed for arbitrary environments.

Using the rates defined in (51), (5.24) reduces to

$$\mathcal{C}^{1\text{D}}(t) = 2\beta_{21}\Gamma_{11}e^{-k''_{\text{spp}}|x_2 - x_1|}te^{-\Gamma_{11}t}, \quad (57)$$

which is distance-independent in the lossless case, as noted in [151] (using (55), (57) is the same as Eq. (6) in [151]).

**Discontinuity of the SPP** Here we show that for the strongly nonreciprocal (unidirectional) case, and for a general nonreciprocal case, near the source point the SPP contribution to the Green function is discontinuous. We also show that for nonreciprocal systems,  $\Gamma_{21} > \Gamma_{11}$  can occur.

To avoid analytical complications of the general 3D case, we first assume a simple 2D model of a  $z$ -directed and  $z$ -invariant magnetic current source located at  $x = 0, y = d$  inside a biased plasma half-space, adjacent to an opaque half-space occupying  $y < 0$ , as depicted in Fig. 12a. The resulting

magnetic field in the plasma is [161, 162]

$$\mathbf{H}_z = \mathbf{H}_z^{\text{inc}} + \frac{A_0}{2\pi} \int_{-\infty}^{+\infty} \frac{1}{2\gamma_p} \mathbf{R}_0 e^{-\gamma_p(y+d)+ik_x x} dk_x, \quad (58)$$

where  $A_0 = i\omega\varepsilon_0\varepsilon_{\text{eff}}\mathbf{I}_m$ , with  $\mathbf{I}_m$  the magnetic current (set to unity) and  $\mathbf{R}_0$  accounts for the interface,

$$\mathbf{R}_0 = \frac{\frac{\gamma_p}{\varepsilon_{\text{eff}}} + \frac{i\varepsilon_{12}}{\varepsilon_{11}} \frac{ik_x}{\varepsilon_{\text{eff}}} - \frac{\gamma_m}{\varepsilon_m}}{\frac{\gamma_p}{\varepsilon_{\text{eff}}} - \frac{i\varepsilon_{12}}{\varepsilon_{11}} \frac{ik_x}{\varepsilon_{\text{eff}}} + \frac{\gamma_m}{\varepsilon_m}}, \quad (59)$$

where  $\gamma_p = \sqrt{k_x^2 - \varepsilon_{\text{eff}}k_0^2}$ ,  $\gamma_m = \sqrt{k_x^2 - \varepsilon_m k_0^2}$  and  $\varepsilon_m$  is the permittivity of the metal (opaque medium). The field in the absence of the interface is

$$\mathbf{H}_z^{\text{inc}} = \frac{A_0}{2\pi} \int_{-\infty}^{+\infty} \frac{1}{2\gamma_p} e^{-\gamma_p|y-d|+ik_x x} dk_x = \frac{A_0}{-4i} \mathbf{H}_0^{(1)}(k_0\sqrt{\varepsilon_{\text{eff}}}\rho) \quad (60)$$

where  $\mathbf{H}_0^{(1)}$  is the Hankel function of the first kind and order zero and  $\rho = \sqrt{x^2 + (y-d)^2}$ . The source-point singularity is contained in  $\text{Im}(\mathbf{H}_0^{(1)})$ , and  $\Gamma \sim \text{Im}(\mathbf{G}_{yy}) \sim \text{Re}(\mathbf{E}_y) \sim \text{Re}(\mathbf{H}_z)$ .

The interface reflection coefficient  $\mathbf{R}_0$ , leading to the scattered field, contains pole singularities at the SPP wavenumbers (e.g., the denominator of  $\mathbf{R}_0$  is the SPP dispersion equation). For  $|\varepsilon_m| \rightarrow \infty$  (perfect conductor), there is one pole at  $k_{\text{spp},x} = \pm k_0\sqrt{\varepsilon_{11}}$  for  $\omega_c \gtrsim 0$ . For  $|\varepsilon_m|$  finite the dispersion equation must be solved numerically, and the plasma may be strongly nonreciprocal, supporting a unidirectional SPP (operating in the bulk bandgap), nonreciprocal, supporting SPPs traveling in opposite directions with unequal wavenumbers (operating above the bulk bandgap), or, in the unbiased (no bandgap) case, reciprocal.

Complex-plane analysis of the magnetic field leads to its evaluation as the sum of a branch cut integral (continuous spectrum) and a discrete residue (SPP) contribution, the latter being

$$\mathbf{H}_z^{\text{res}} = \theta(-x) iA_0 \text{Res}^{(-)} \frac{e^{-\gamma_p^{(-)}(y+d)+ik_{x,\text{SPP}}^{(-)}x}}{2\gamma_p^{(-)}} + \theta(x) iA_0 \text{Res}^{(+)} \frac{e^{-\gamma_p^{(+)}(y+d)+ik_{x,\text{SPP}}^{(+)}x}}{2\gamma_p^{(+)}} \quad (61)$$

where  $\text{Res}^{(\pm)}$  is the residue of  $\mathbf{R}_0$  evaluated at  $k_x = k_{x,\text{SPP}}^{(\pm)}$ , and  $\gamma_p^{(\pm)} = \sqrt{\left(k_{x,\text{SPP}}^{(\pm)}\right)^2 - \varepsilon_{\text{eff}}k_0^2}$ , where  $k_{x,\text{SPP}}^{(\pm)}$  is the SPP pole for  $k_x \gtrsim 0$  (forward propagating or backward propagating), and where  $\theta(x)$  is the Heaviside step function. In the strongly nonreciprocal (unidirectional) case, only one pole is present, leading to only one term in (61).

Figure 12b shows the magnetic field in the bulk bandgap for  $\omega_c > 0$  obtained by numerical evaluation of the Sommerfeld integral (58), and by assuming only the residue component (61) (since we operate in the bulk bandgap and the gap Chern number is  $-1$ , then there is one unidirectional SPP). The opaque medium is topologically-trivial, and is an unbiased plasma having  $\varepsilon = -2$ . As shown in the close-up Fig. 12c, the residue accurately approximates the field except very close to the source, where the real-part of the residue ( $\propto \Gamma_{\text{SPP}}$ ) has an unphysical discontinuity, indicated by



the two black dots. In this case, the radiation continuum compensates for the discontinuity of the residue, such that the real-part of the full Sommerfeld integral ( $\propto \Gamma$ ), is continuous, and the SPP peak is pushed away from the source point.

As a result of the importance of the radiation continuum near the source, at some points  $H_z(x = 0) < H_z(x > 0)$ , so that  $\Gamma_{21}$  exceeds  $\Gamma_{11}$ . Figure 12d shows the unbiased (reciprocal) case for the full Sommerfeld integral, where the field peak occurs at  $x = 0$  and  $\Gamma_{21} < \Gamma_{11}$  at all points. In general, there is a quadrature relationship between the dissipative and coherent rates.

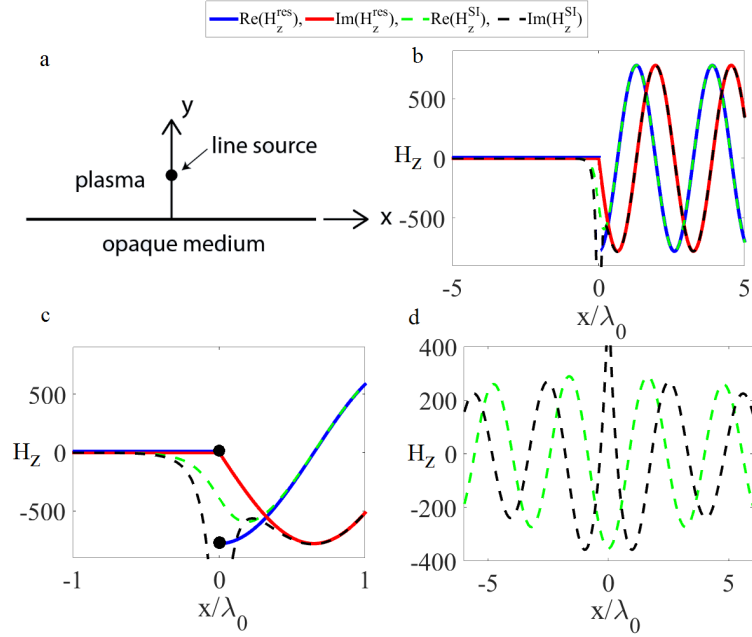


Figure 12: a. Magnetic current source (black dot,  $z$ -directed and  $z$ -invariant) located at  $x = 0, y = d$  inside a biased plasma region, with an opaque half space occupying  $y < 0$ . b. Magnetic field  $H_z(x)$  at the interface of an  $\epsilon = -2$  half-space and a magnetized plasma having  $\omega_p/\omega = 0.95$  and  $\omega_c/\omega = 0.21$ , at  $\omega_0/2\pi = 200$  THz. The magnetic line source is located  $\lambda_0/10$  above the interface in the plasma region, and the field is evaluated at  $(x, y = \lambda_0/10, z = 0)$ . c. Field behavior in the vicinity of the source showing the discontinuity of the residue component. d. Same as (b) for the unbiased (reciprocal) case,  $\omega_c/\omega = 0$ .

Figure 13 shows the magnetic field at a frequency outside the bandgap, where we have two SPPs propagating in opposite directions with unequal wavenumbers. As with the unidirectional case, the residue shows a discontinuity at the source point.

Considering now the 3D case of an electric dipole source at the interface, Fig. 14 shows the dissipative decay and coherent rates (5.20) along the interface, computed using the finite element method (COMSOL, [154]). In this case, it is impossible to separate the discrete and continuum contributions to the field. Fig. 14a,b show the rates for qubits at the interface as a function of qubit separation for two frequencies within the bandgap, and Fig. 14c shows the rates normalized by  $\Gamma_{ii}$  for a fixed separation as a function of height above the interface. It can be seen that, as predicted by the previous analytical 2D model, it occurs that  $\Gamma$  is nearly discontinuous at the source point (the

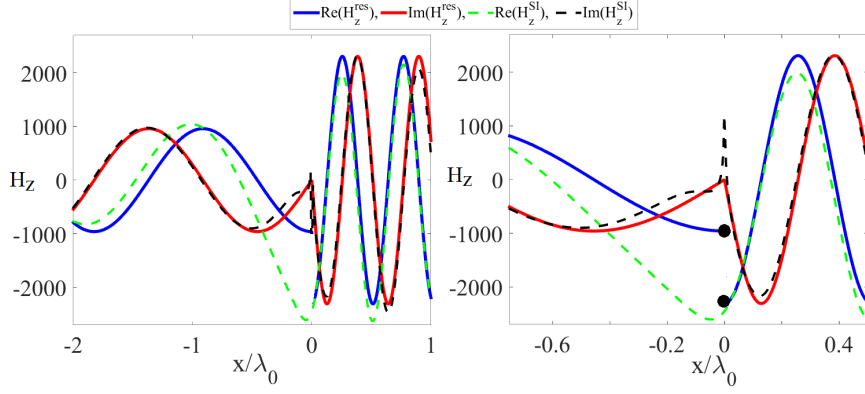


Figure 13: a. Magnetic field  $H_z(x)$  at the interface of an  $\varepsilon = -0.47$  half-space and a magnetized plasma having  $\omega_p/\omega = 0.95$  and  $\omega_c/\omega = 0.20$ , at  $\omega_0/2\pi = 230$  THz. The magnetic line source is located  $\lambda_0/10$  above the interface in the plasma region, and the field is evaluated at  $(x, y = \lambda_0/10, z = 0)$ . b. Field behavior in the vicinity of the source showing the discontinuity of the residue component.

discontinuity of the discrete spectrum is softened by the radiation continuum), and that  $\Gamma_{21} > \Gamma_{11}$  at some points. The coherent rate becomes unbounded at the source due to the well-known divergence of the real part of the Green function.

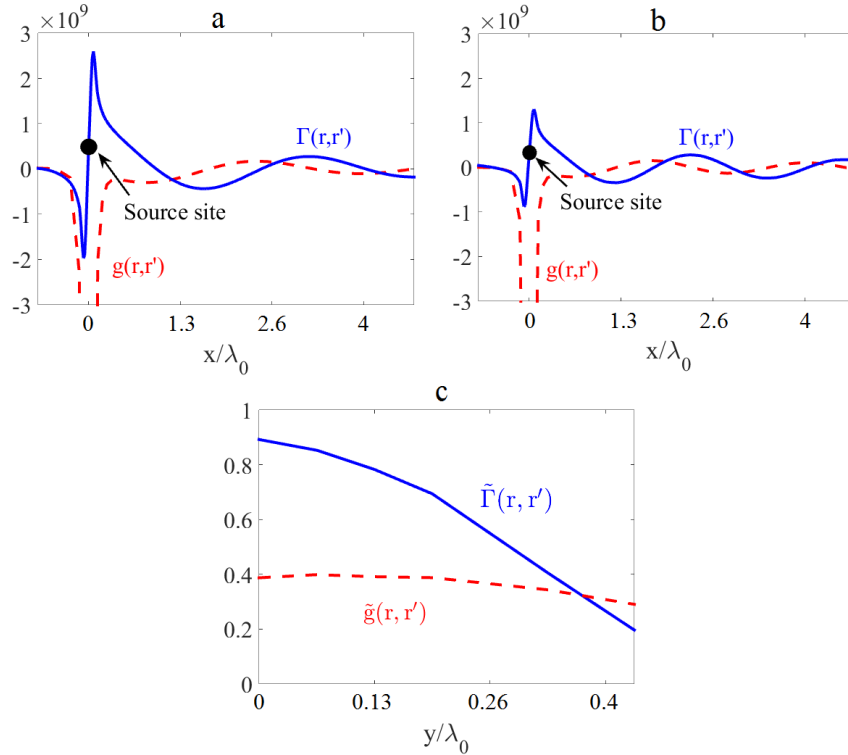


Figure 14: a. Dissipative decay (solid blue) and coherent (dashed red) rates at the interface of a biased plasma ( $\omega_p/\omega = 0.95$ ,  $\omega_c/\omega = 0.21$ ) and an opaque medium ( $\varepsilon = -2$ ) at  $\omega/2\pi = 200$  THz. b. The same as a. but for 207 THz. The black circle demonstrate the point dipole source, and the dipole moment is  $d = 60 D$ . c. The normalized rates as a function of the height of the two qubits above the interface for a fixed separation of  $2.1 \mu\text{m}$ .

## .4 Appendix IV: Concurrence in the Unidirectional Case

In this section we derive the concurrence for a unidirectional system.

Suppose that the system of qubits are communicating through a strongly nonreciprocal environment, so that the communication is strictly unidirectional, such as occurs for SPPs at PTI interfaces. Assuming that  $\mathbf{G}(\mathbf{r}_1, \mathbf{r}_2)$  and  $\mathbf{G}(\mathbf{r}_2, \mathbf{r}_1)$  are the dyadic Green function propagators along two opposite directions, the unidirectionality assumption leads to, e.g.,  $\mathbf{G}(\mathbf{r}_1, \mathbf{r}_2) = 0$  ( $\Gamma_{12} = g_{12} = 0$ ) and  $\mathbf{G}(\mathbf{r}_2, \mathbf{r}_1) \neq 0$ .

Under this unidirectionality assumption, the 3D Lindblad superoperator (5.19) reduces to

$$\begin{aligned} \frac{\partial \rho_s(t)}{\partial t} = & -\frac{i}{\hbar} [\mathbf{H}_s + \mathbf{V}^{AF}, \rho_s(t)] \\ & + \frac{\Gamma_{11}}{2} \left( 2\sigma_1 \rho_s(t) \sigma_1^\dagger - \sigma_1^\dagger \sigma_1 \rho_s(t) - \rho_s(t) \sigma_1^\dagger \sigma_1 \right) \\ & + \frac{\Gamma_{11}}{2} \left( 2\sigma_2 \rho_s(t) \sigma_2^\dagger - \sigma_2^\dagger \sigma_2 \rho_s(t) - \rho_s(t) \sigma_2^\dagger \sigma_2 \right) \\ & + \left( \frac{\Gamma_{21}}{2} + ig_{21} \right) \left( \sigma_2 \rho_s(t) \sigma_1^\dagger - \rho_s(t) \sigma_1^\dagger \sigma_2 \right) \\ & + \left( \frac{\Gamma_{21}}{2} - ig_{21} \right) \left( \sigma_1 \rho_s(t) \sigma_2^\dagger - \sigma_2^\dagger \sigma_1 \rho_s(t) \right) \end{aligned} \quad (62)$$

where it has been assumed that  $\Gamma_{11} = \Gamma_{22}$ .

Defining the basis

$$\begin{aligned} |1\rangle &= |g_1\rangle \otimes |g_2\rangle = |g_1, g_2\rangle, \quad |2\rangle = |e_1\rangle \otimes |e_2\rangle = |e_1, e_2\rangle \\ |3\rangle &= |g_1\rangle \otimes |e_2\rangle = |g_1, e_2\rangle, \quad |4\rangle = |e_1\rangle \otimes |g_2\rangle = |e_1, g_2\rangle \end{aligned} \quad (63)$$

and considering the system of qubits to be initially prepared in the state  $|4\rangle = |e_1\rangle \otimes |g_2\rangle$ , it can be shown that for the non-pumped case the non-zero components of the density matrix in (62) are ( $\rho = \rho_s$ )

$$\begin{aligned} \partial_t \rho_{11} &= \Gamma_{11}(\rho_{33} + \rho_{44}) + \gamma \rho_{34} + \gamma^* \rho_{43} \\ \partial_t \rho_{33} &= -\Gamma_{11} \rho_{33} - \gamma \rho_{34} - \gamma^* \rho_{43} \\ \partial_t \rho_{34} &= -\Gamma_{11} \rho_{34} - \gamma^* \rho_{44} \\ \partial_t \rho_{43} &= -\Gamma_{11} \rho_{43} - \gamma \rho_{44} \\ \partial_t \rho_{44} &= -\Gamma_{11} \rho_{44} \end{aligned} \quad (64)$$

where  $\gamma = \Gamma_{21}/2 + ig_{21}$ . For all times the density matrix is block diagonal. Concurrence for arbitrary materials can be calculated as [149]

$$\mathcal{C} = \max(0, \sqrt{u_1} - \sqrt{u_2} - \sqrt{u_3} - \sqrt{u_4}), \quad (65)$$

where  $u_i$  are arranged in descending order of the eigenvalues of the matrix  $\rho(t)\rho^y(t)$ , where  $\rho^y(t) = \sigma_y \otimes \sigma_y \rho^*(t) \sigma_y \otimes \sigma_y$  is the spin-flip density matrix with  $\sigma_y$  being the Pauli matrix. We have

$$\rho(t)\rho^y(t) = \begin{bmatrix} 0 & 0 & 0 & 0 \\ 0 & 0 & 0 & 0 \\ 0 & 0 & x & y \\ 0 & 0 & z & x \end{bmatrix} \rightarrow \begin{array}{l} u_1 = x + \sqrt{yz} \\ u_2 = x - \sqrt{yz} \\ u_3 = 0 \\ u_4 = 0 \end{array} \quad (66)$$

such that  $x = |\rho_{34}|^2 + \rho_{33}\rho_{44}$ ,  $y = 2\rho_{34}\rho_{33}$  and  $z = 2\rho_{43}\rho_{44}$  and

$$\begin{aligned} \rho_{44}(t) &= e^{-\Gamma_{11}t} \\ \rho_{43}(t) &= -\gamma t e^{-\Gamma_{11}t} \\ \rho_{34}(t) &= -\gamma^* t e^{-\Gamma_{11}t} \\ \rho_{33}(t) &= |\gamma|^2 t^2 e^{-\Gamma_{11}t} \\ \rho_{11}(t) &= 1 - e^{-\Gamma_{11}t} - |\gamma|^2 t^2 e^{-\Gamma_{11}t}, \end{aligned} \quad (67)$$

which leads to (5.24).

## Publications from this thesis in refereed journals

### Journals

1. **Giant interatomic energy-transport amplification with nonreciprocal photonic topological insulators**, Pierre Doyeu, S. Ali Hassani Gangaraj, George W. Hanson, Mauro Antezza, Submitted for Phys. Rev. Letter.
2. **Robust entanglement with 3D nonreciprocal photonic topological insulators**, S. Ali Hassani Gangaraj, George W. Hanson, Mauro Antezza, Phys. Rev. A 95, 063807 (2017).
3. **Berry phase, Berry potential and Chern number for continuous bianisotropic material from a classical electromagnetics perspective**, S. Ali Hassani Gangaraj, George W. Hanson, IEEE journal of multiscale and multiphysics computational techniques, DOI: 10.1109/JMMCT.2017.2654962 (2017).
4. **Directive surface plasmons on tunable two-dimensional hyperbolic metasurfaces and black phosphorus: Green function and complex plane analysis**, S. Ali Hassani Gangaraj, Tony Low, Andrei Nemilentsau, George W. Hanson, IEEE transactions on antennas and propagation, DOI:10.1109/TAP. 2016. 2633900 (2016).
5. **Topologically protected unidirectional surface state in biased ferrites: Duality and application to directional couplers**, S. A. Hassani Gangaraj, George W. Hanson, IEEE antennas and wireless propagation letters, DOI:10.1109/ LAW.2016.2582905 (2016).
6. **The effects of three-dimensional defects on one-way surface plasmon propagation for photonic topological insulators comprised of continuum media**, S. A. Hassani Gangaraj, A. Nemilentsau, George W. Hanson, Scientific Reports 6, 30055, (2016).
7. **Dyadic Green function for dipole excitation of homogenized metasurfaces**, Feng Liang, George W. Hanson, Alexander B. Yakovlev, Giampiero Lovat, Paolo Burghignoli, Rodolfo Araneo, S. A. Hassani Gangaraj, IEEE transactions on antennas and propagation 64 (1), 167-178 (2016).
8. **Transient and steady-state entanglement mediated by three-dimensional plasmonic waveguides**, S. A. Hassani Gangaraj, Andrei Nemilentsau, George W. Hanson, Stephen Hughes, Optics express, Vol. 23, Issue 17, pp. 22330-22346 (2015).
9. **Quantum plasmonic excitation in graphene and loss-insensitive propagation**, George W. Hanson, S. A. Hassani Gangaraj, Changhyoup Lee, Dimitris G. Angelakis, Mark Tame, Phys. Rev. A 92, 013828 (2015).

### Book Chapters

1. **Unidirectional, defect-immune and topologically protected electromagnetic surface waves** , George W. Hanson, S. Ali Hassani Gangaraj, A. Nemilentsau, The World of Applied Electromagnetics: In Appreciation of Magdy Fahmy Iskander, Akhlesh Lakhtakia and Cynthia M. Furse (Editors), Springer Verlag (2017).

## Conferences

1. **Spontaneous qubit entanglement in photonic topological insulator environments** , S. A. Hassani Gangaraj, G. W. Hanson, M. Antezza, Presented in 38th Progress In Electromagnetics Research Symposium, **PIERS**, St Petersburg, Russia, May 2017.
2. **Photonic topological insulator waveguiding from a classical electromagnetics perspective**, S. A. Hassani, G. W. Hanson, Presented in national radio science meeting, **URSI**, 2017, in Boulder, Colorado, January 2017.
3. **Tunable guided surface plasmon-polariton using two dimensional hyperbolic grapheme metasurfaces**, S. A. Hassani, A. Nemilentsau, G. W. Hanson, Presented in national radio science meeting, **URSI**, 2016, in Boulder, Colorado, January 2016.
4. **Plasmon-mediated control of entanglement between two quantum systems**, A. Nemilentsau, S. A. Hassani, G. W. Hanson, S. Hughes, Presented in **META** 2015 in New York, The 6th international conference on metamaterials, photonic crystals and plasmonics.
5. **Control of entanglement of two-level atoms using Grapheme**, Andrei Nemilentsau, S. A. Hassani Gangaraj, George Hanson, Stephen Hughes, Presented in conference on laser and electro-optics, **CLEO** 2015, San Jose, CA, USA, 10-15 May.
6. **Entanglement of Two-Level Atoms Above Graphene**, Andrei Nemilentsau, S. A. Hassani Gangaraj, George Hanson, Stephen Hughes, Presented in **EuCAP** 2015, Lisbon, Portugal 12-17 April.

# Bibliography

- [1] L. Novotny, B.Hecht. Principles of nano-optics, Cambridge Univ. Press, Cambridge (2006).
- [2] Y. Jiang, W. Lu, H. Xu, Z. Dong, T. Cui. A planar electromagnetic black hole based on graphene, *Phy. Lett. A* 376, 1468 (2012).
- [3] Y. Liu, X. Dong, P. Chen. Biological and chemical sensors based on graphene materials, *Chem. Soc. Rev.* 41, 2283 (2012).
- [4] L. Yin et. al, Subwavelength focusing and guiding of surface plasmons, *Nano Lett.* 5, 1399 (2005).
- [5] S. I. Bozhevolnyi et. al, Channel plasmon subwavelength waveguide components including interferometers and ring resonators, *Nature* 440, 508 (2006).
- [6] Z. Jacob, V. M. Shalaev. Plasmonics goes quantum. *Science* 334, 463-464 (2011).
- [7] M. A. Nielsen and I. A. Chuang. Quantum computing and quantum information (Cambridge University Press, Cambridge, England, 2000).
- [8] G. D. Mahan, Many-Particle Physics (Kluwer Academic, New York, 2000).
- [9] R. H. Lehberg. Radiation from an N-atom system. I. general formalism. *Phys. Rev. A* 2, 883 (1970).
- [10] A. Imamoglu, D. D. Awschalom, G. Burkard, D. P. DiVincenzo, D. Loss, M. Sherwin, A. Small. Quantum information processing using quantum dot spins and cavity QED. *Phys. Rev. Lett.* 83, 4204 (1999).
- [11] F. Le Kien, S. Dutta Gupta, K. P. Nayak, and K. Hakuta. Nanofiber-mediated radiative transfer between two distant atoms. *Phys. Rev. A* 72, 063815 (2005).
- [12] S. Hughes. Modified spontaneous emission and qubit entanglement from dipole-coupled quantum dots in a photonic crystal nanocavity. *Phys. Rev. Lett.* 94, 227402 (2005).
- [13] T. Lund-Hansen, S. Stobbe, B. Julsgaard, H. Thyrrerstrup, T. Sunner, M. Kamp, A. Forchel, P. Lodahl. Experimental realization of highly efficient broadband coupling of single quantum dots to a photonic crystal Waveguide. *Phys. Rev. Lett.* 101, 113903 (2008).

- [14] J. Bleuse, J. Claudon, M. Creasey, N. S. Malik, J.-M. Gerard, I. Maksymov, J. P. Hugonin, P. Lalanne. Inhibition, enhancement, and control of spontaneous emission in photonic nanowires. *Phys. Rev. Lett.* 106, 103601 (2011).
- [15] Q. Quan, I. Bulu, M. Loncar. Broadband waveguide QED system on a chip. *Phys. Rev. A* 80, 011810(R) (2009).
- [16] G. W. Hanson. Dyadic Greens functions and guided surface waves for a surface conductivity model of graphene. *J. Appl. Phys.*, vol. 103, No. 6, p. 064302, 2008.
- [17] G. W. Hanson, S. A. Hassani Gangaraj, C. Lee, D. G. Angelakis, M. Tame. Quantum plasmonic excitation in graphene and loss-insensitive propagation. *Phys. Rev. A* 92, 013828, 2015.
- [18] T. Low, R. Roldn, H. Wang, F. Xia, P. Avouris, L. M. Moreno, F. Guinea. Plasmons and screening in monolayer and multilayer black phosphorus. *Phys. Rev. Lett.*, vol. 113, no. 10, p. 106802, 2014.
- [19] L. Lu, J. D. Joannopoulos, M. Soljai. Topological photonics, *Nature Photonics* 8, 821829 (2014).
- [20] F. D. M. Haldane and S. Raghu. Possible realization of directional optical waveguides in photonic crystals with broken time-reversal symmetry. *Phys. Rev. Lett.* 100, 013904 (2008).
- [21] J. Van Bladel. Some remarks on greens dyadic for infinite space. *IRE Transactions on Antennas and Propagation*, 9:533, 1961.
- [22] A.D. Yaghjian. Electric dyadic Greens functions in the source region. *Proc. IEEE*, 68:248, 1980.
- [23] C. Raabe and D-G Welsch. Casimir force acting on magnetodielectric bodies embedded in media. *Phys. Rev. A*, 71:013814, 2005.
- [24] T. Gruner and D. G. Welsch. Green-function approach to the radiationfield quantization for homogeneous and inhomogeneous Kramers-Kronig dielectrics. *Phys. Rev. A.*, 53:1818, 1996.
- [25] S. Scheel, L. Knoll, and D. G. Welsch. QED commutation relations for inhomogeneous Kramers-Kronig dielectrics. *Phys. Rev. A.*, 58:700, 1998.
- [26] S. Scheel, L. Knoll, and D.-G. Welsch. Spontaneous decay of an excited atom in an absorbing dielectric. *Phys. Rev. A*, 60:40944104, Nov 1999.
- [27] H.T. Dung, S.Y. Buhmann, L. Knoll, D.G. Welsch, S. Scheel, and J. Kastel. Electromagnetic-field quantization and spontaneous decay in left-handed media. *Phys. Rev. A*, 68:043816, 2003.
- [28] S. Scheel, L. Knoll, and D. G. Welsch. QED commutation relations for inhomogeneous Kramers-Kronig dielectrics. *Phys. Rev. A.*, 58:700, 1998.



- [29] M. Wubs, L. G. Suttorp, and A. Lagendijk. Multiple-scattering approach to interatomic interactions and superradiance in inhomogeneous dielectrics. *Phys. Rev. A.*, 70:053823, 2004.
- [30] P. Yao and S. Hughes. Macroscopic entanglement and violation of bells inequalities between two spatially separated quantum dots in a planar photonic crystal system. *Opt. Express* 17, 1150511514 (2009)
- [31] G. Angelatos and S. Hughes. Entanglement dynamics and Mollow nonuplets between two coupled quantum dots in a nanowire photonic-crystal system. *Phys. Rev. A* 91, 051803(R) (2015).
- [32] L. Aolita, F. deMelo, L. Davidovich. Open-system dynamics of entanglement: a key issues review. *Rep. Prog. Phys.* 78, 042001 (2015).
- [33] W. K. Wootters. Entanglement of formation of an arbitrary state of two qubits. *Phys. Rev. Lett.* 80, 2245–2248 (1998). *Phys. Rev. A* 89, 042328 (2014).
- [34] K. Życzkowski, P. Horodecki, M. Horodecki, R. Horodecki. Dynamics of quantum entanglement, *Phys. Rev. A* 65, 012101 (2001).
- [35] F. Verstraete, M. M. Wolf, and J. Ignacio Cirac. Quantum computation and quantum-state engineering driven by dissipation, *Nat. Phys.* 5, 633–636 (2009).
- [36] J. T. Barreiro, P. Schindler, O. Guhne, T. Monz, M. Chwalla, C. F. Roos, M. Hennrich, and R. Blatt. Experimental multiparticle entanglement dynamics induced by decoherence. *Nat. Phys.* 6, 943–946 (2010).
- [37] Y. Lin, J. P. Gaebler, F. Reiter, T. R. Tan, R. Bowler, A. S. Sorensen, D. Leibfried, and D. J. Wineland. Dissipative production of a maximally entangled steady state of two quantum bits. *Nature* 504, 415–418 (2013).
- [38] H. Walther, B. T. H. Varcoe, B. G. Englert, T. Becker. Cavity quantum electrodynamics. *Rep. Prog. Phys.* 69, 1325 (2006).
- [39] P. Anger, P. Bharadwaj, L. Novotny. Enhancement and quenching of single-molecule fluorescence. *Phys. Rev. Lett.* 96, 113002 (2006).
- [40] A. V. Akimov, A. Mukherjee, C. L. Yu, D. E. Chang, A. S. Zibrov, P. R. Hemmer, H. Park, M. D. Lukin, Generation of single optical plasmons in metallic nanowires coupled to quantum dots. *Nature* 450, 402–406 (2007).
- [41] A. M. Nemilentsau, G. Y. Slepyan, S. A. Maksimenko, A. Lakhtakia, and S. V. Rotkin. Spontaneous decay of the excited state of an emitter near a finite-length metallic carbon nanotube. *Phys. Rev. B* 82, 235411 (2010).

- [42] E. Forati, G. W. Hanson, and S. Hughes. Graphene as a tunable thz reservoir for shaping the mollow triplet of an artificial atom via plasmonic effects. *Phys. Rev. B* 90, 085414 (2014).
- [43] M. J. Kastoryano, F. Reiter, A. S. Sørensen. Dissipative preparation of entanglement in optical cavities. *Phys. Rev. Lett.* 106, 090502 (2011).
- [44] B. Casabone, A. Stute, K. Friebe, B. Brandstätter, K. Schüppert, R. Blatt, T. E. Northup. Heralded entanglement of two ions in an optical cavity. *Phys. Rev. Lett.* 111, 100505 (2013).
- [45] R. Reimann, W. Alt, T. Kampschulte, T. Macha, L. Ratschbacher, N. Thau, S. Yoon, D. Meschede. Cavity-modified collective rayleigh scattering of two atoms. *Phys. Rev. Lett.* 114, 023601 (2015).
- [46] P. Yao and S. Hughes. Macroscopic entanglement and violation of bell’s inequalities between two spatially separated quantum dots in a planar photonic crystal system. *Opt. Express* 17, 11505–11514 (2009).
- [47] J. Wolters, J. Kabuss, A. Knorr, O. Benson. Deterministic and robust entanglement of nitrogen-vacancy centers using low- $q$  photonic-crystal cavities *Phys. Rev. A* 89, 060303 (2014).
- [48] G. Angelatos and S. Hughes. Entanglement dynamics and multiple Mollow triplets between two coupled quantum dots in a nanowire photonic crystal system. *Phys. Rev. A* 91, 051803(R) (2015).
- [49] M. S. Tame, K. R. McEnery, S. K. Ozdemir, J. Lee, S. A. Maier, M. S. Kim. Quantum plasmonics. *Nat. Phys.* 9, 329–340 (2013).
- [50] J. Xu, M. Al-Amri, Y. Yang, S. Y. Zhu, M. S. Zubairy. Entanglement generation between two atoms via surface modes. *Phys. Rev. A* 84, 032334 (2011).
- [51] A. Gonzalez-Tudela, D. Martin-Cano, E. Moreno, L. Martin-Moreno, C. Tejedor, F. J. Garcia-Vidal. Entanglement of two qubits mediated by one-dimensional plasmonic waveguides. *Phys. Rev. Lett.* 106, 020501 (2011).
- [52] D. Martin-Cano, A. Gonzalez-Tudela, L. Martin-Moreno, F. J. Garcia-Vidal, C. Tejedor, E. Moreno, Dissipation-driven generation of two-qubit entanglement mediated by plasmonic waveguides. *Phys. Rev. B* 84, 235306 (2011).
- [53] D. Dzsotjan, A. S. Sørensen, M. Fleischhauer. Quantum emitters coupled to surface plasmons of a nanowire: A green’s function approach. *Phys. Rev. B* 82, 075427 (2010).
- [54] H. Zheng, H. U. Baranger. Persistent quantum beats and long-distance entanglement from waveguide-mediated interactions. *Phys. Rev. Lett.* 110, 113601 (2013).
- [55] C. Gonzalez-Ballester, E. Moreno, F. J. Garcia-Vidal. Generation, manipulation, and detection of two-qubit entanglement in waveguide QED.

- [56] C. Lee, M. Tame, C. Noh, J. Lim, S. A. Maier, J. Lee, D. G. Angelakis. Robust-to-loss entanglement generation using a quantum plasmonic nanoparticle array. *New Journal of Physics* 15, 083017 (2013).
- [57] H. T. Dung, L. Knöll, D. G. Welsch, Three-dimensional quantization of the electromagnetic field in dispersive and absorbing inhomogeneous dielectrics. *Phys. Rev. A* 57, 3931 (1998).
- [58] H. T. Dung, L. Knöll, D. G. Welsch. Spontaneous decay in the presence of dispersing and absorbing bodies: general theory and application to a spherical cavity. *Phys. Rev. A* 62, 053804 (2000).
- [59] Lumerical Solutions, Inc. <http://www.lumerical.com/tcad-products/fdtd/>.
- [60] D. W. Lynch, W. Hunter. Comments on the optical constants of metals and an introduction to the data for several metals. in *Handbook of Optical Constants of Solids*. E. D. Palik, ed. (Academic Press, 1997), pp. 275 - 367.
- [61] L. Novotny. Effective wavelength scaling for optical antennas. *Phys. Rev. Lett.* 98, 266802 (2007).
- [62] P. B. Johnson, R. W. Christy. Optical constants of noble metals. *Phys. Rev. B* 6, 4370–4379 (1972).
- [63] V. P. Drachev, V. A. Podolskiy, A. V. Kildishev. Hyperbolic metamaterials: new physics behind a classical problem. *Opt. Express* 21, 15048 (2013).
- [64] LM. A. K. Othman, C. Guclu, F. Capolino. Graphene-based tunable hyperbolic metamaterials and enhanced near-field absorption. *Opt. Express* 21, 7614 (2013).
- [65] J. Sebastian Gomez-Diaz, Mykhailo Tymchenko, Andrea Alù. Hyperbolic plasmons and topological transitions over uniaxial metasurfaces. *Phys. Rev. Lett* 114, 233901 (2015).
- [66] V. A. Podolskiy E. E. Narimanov. Strongly anisotropic waveguide as a nonmagnetic left-handed system. *Phys. Rev. B* 71, 201101(R), 2005.
- [67] A. A. Govyadinov V. A. Podolskiy. Metamaterial photonic funnels for subdiffraction light compression and propagation. *Phys. Rev. B* 73, 155108, 2006.
- [68] J. Yao, X. Yang, X. Yin, G. Bartal, X. Zhang. Three dimensional nanometer-scale optical cavities of indefinite medium. *Proc. Nat. Acad. Sci. USA*, vol. 108, pp. 1132711331, 2011.
- [69] E. F. Kuester, M. A. Mohamed, M. Piket-May, C. L. Holloway. Averaged transition conditions for electromagnetic fields at a metafilm. *IEEE Trans. Antennas Propag.* vol. 51, pp. 26412651, Oct. 2003.

- [70] N. Yu, F. Capasso. Flat optics with designer metasurfaces. *Nature Materials* 13, pp. 139150, 2014.
- [71] K. S. Novoselov, D. Jiang, F. Schedin, T. J. Booth, V. V. Khotkevich, S. V. Morozov, A. K. Geim. Two-dimensional atomic crystals. *Proc. Nat. Acad. Sci. USA* 102, pp. 10451-10453, 2005.
- [72] T. Low P. Avouris. Graphene plasmonics for terahertz to mid-infrared applications. *ACS Nano* 8, 1086, 2014.
- [73] F. H. L. Koppens, D. E. Chang, F. J. Garca de Abajo. Graphene plasmonics: a platform for strong lightmatter interactions. *Nano Lett.* 11, 3370, 2011.
- [74] F. Javier Garca de Abajo. Graphene plasmonics: challenges and opportunities. *ACS Photonics* 1, 135, 2014.
- [75] E. Forati, G. W. Hanson, A. B. Yakovlev, A. Al. Planar hyperlens based on a modulated graphene monolayer. *Phys. Rev. B* 89, 081410, 2014.
- [76] D. L. Sounas, H. S. Skulason, H. V. Nguyen, A. Guermoune, M. Siaj, T. Szkopek, C. Caloz. Faraday rotation in magnetically biased graphene at microwave frequencies. *Appl. Phys. Lett.* 102, 191901, 2013.
- [77] A. Vakil, N. Engheta. Transformation optics using graphene. *Science* 332, pp. 1291-1294, 2011.
- [78] A. Morita. Semiconducting black phosphorus. *Appl. Phys. A* 39, pp. 227-242, 1986.
- [79] L. Li, Y. Yu, G. J. Ye, Q. Ge, X. Ou, H. Wu, D. Feng, X. H.Chen, Y. Zhang. Black phosphorus field-effect transistors. *Nat. Nanotechnol.* 9, 372, 2014.
- [80] H. Liu, A. T. Neal, Z. Zhu, D. Tomanek, P. D. Ye. Phosphorene: an unexplored 2D semiconductor with a high hole mobility. *ACS Nano* 8, 4033, 2014.
- [81] F. Xia, H. Wang, Y. Jia. Rediscovering black phosphorus as an anisotropic layered material for optoelectronics and electronics. *Nat. Commun.* 5, 4458, 2014.
- [82] S. P. Koenig, R. A. Doganov, H. Schmidt, A. H. Neto, B. Oezylmaz. Electric field effect in ultrathin black phosphorus. *Appl. Phys. Lett.* 104, 103106, 2014.
- [83] T. Low, A. S. Rodin, A. Carvalho, Y. Jiang, H. Wang, F. Xia, A. H. Castro Neto. Tunable optical properties of multilayer black phosphorus thin films. *Phys. Rev. B* 90, 075434, 2014.
- [84] V. Tran, R. Soklaski, Y. Liang, L. Yang. Layer-controlled band gap and anisotropic excitons in few-layer black phosphorus. *Phys. Rev. B* 89, 235319, 2014.
- [85] J. Qiao, X. Kong, Z.-X. Hu, F. Yang, W. Ji. High-mobility transport anisotropy and linear dichroism in few-layer black phosphorus. *Nature Comm.* 5, 4475, 2014.

- [86] T. Low, M. Engel, M. Steiner, P. Avouris. Origin of photoresponse in black phosphorus photo-transistors. *Phys. Rev. B* 90, 081408, 2014.
- [87] M. Engel, M. Steiner, P. Avouris. Black phosphorus photodetector for multispectral, high-resolution imaging. *Nano letts.* 14, pp. 6414-6417, 2014.
- [88] M. Buscema, D. J. Groenendijk, S. I. Blanter, G. A. Steele, H. S.J. van der Zant, A. Castellanos-Gomez. Fast and broadband photoresponse of few-layer black phosphorus field-effect transistors. *Nano Letts.* 14, pp. 3347-3352, 2014.
- [89] H. Yuan, X. Liu, F. Afshinmanesh, W. Li, G. Xu, J. Sun, B. Lian et al.. Polarization-sensitive broadband photodetector using a black phosphorus vertical pn junction. *Nature Nanotechnology* 10, pp. 707713, 2015.
- [90] N. Youngblood, C. Chen, S. J. Koester, M. Li. Waveguide-integrated black phosphorus photodetector with high responsivity and low dark current. *Nature Photonics* 9, pp. 247252, 2015.
- [91] A. Castellanos-Gomez, L. Vicarelli, E. Prada, J. O. Island, K. L. Narasimha-Acharya, S. I. Blanter, D. J. Groenendijk et al. Isolation and characterization of few-layer black phosphorus. *2D Materials* 1, 025001, 2014.
- [92] O. Y. Yermakov, A. I. Ovcharenko, M. Song, A. A. Bogdanov, I. V. Iorsh, Y. S. Kivshar. Hybrid waves localized at hyperbolic metasurfaces. *Phys. Rev. B* 91, 235423, 2015.
- [93] A. Nemilentsau, T. Low, G. W. Hanson. Anisotropic 2D materials for tunable hyperbolic plasmonics. *Phys. Rev. Lett.* 116, 066804, 2016.
- [94] J. Kong, *Electromagnetic Wave Theory* (Wiley-Interscience, New York, 1986).
- [95] D. C. Chang and E. F. Kuester. An analytic theory for narrow open microstrip. *AEU*, Band 33, Heft 5, pp. 199-206, 1979.
- [96] D. P. Nyquist, J. M. Grimm, D. J. Infante, and H. Braunisch. Classification of the proper propagation-mode spectrum and leaky-wave modes on open planar waveguides. *Electromagnetics*, v. 17, pp. 105-130, 1997.
- [97] L. A. Falkovsky and S. S. Pershoguba. Optical far-infrared properties of a graphene monolayer and multilayer. *Phys. Rev. B* 76, 153410 (2007).
- [98] S. A. Mikhailov and K. Ziegler. New electromagnetic mode in graphene. *Phys. Rev. Lett.* 99, 016803 (2007)
- [99] V. P. Gusynin, S. G. Sharapov, and J. P. Carbotte. Magneto-optical conductivity in graphene. *J. Phys.: Condens. Matter* 19, 026222 (2007)

- [100] A. Ishimaru, *Electromagnetic wave propagation, radiation and scattering* (Prentice Hall, Englewood Cliffs, NJ, 1991).
- [101] F. Liang, A. B. Yakovlev, and G. W. Hanson. Optimum surface plasmon excitation and propagation on conductive two-dimensional materials and thin films. *IEEE Trans. Antennas Propag.*, v. 63, pp. 1765-1774, 2015.
- [102] L. B. Felsen and N. Marcuvitz, *Radiation and Scattering of Waves*, Oxford University Press, 1994.
- [103] H. L. Bertoni and A. Hessel. Ray description for point source excited surface waves in stratified anisotropic media. *Radio Science* 4, 73-81, 1969.
- [104] A. R. Forsyth, *Theory of functions of a complex variable*, Cambridge: University Press, 1893.
- [105] G. W. Hanson and A. B. Yakovlev. An analysis of leaky-wave dispersion phenomena in the vicinity of cutoff using complex frequency plane singularities. *Radio Science*, v. 33, pp. 803-820, July-Aug., 1998.
- [106] O. V. Shapoval, J. S. Gomez-Diaz, J. Perruisseau-Carrier, J. R. Mosig, and A. I. Nosich. Integral equation analysis of plane wave scattering by coplanar graphene-strip gratings in the THz range. *IEEE Trans. Terahertz Sci. Technol.* v. 3, pp. 666-674, 2013.
- [107] C. S. R. Kaipa, A. B. Yakovlev, G. W. Hanson, Y. R. Padooru, F. Medina, and F. Mesa. Enhanced transmission with a graphene-dielectric microstructure at low-terahertz frequencies. *Phys. Rev. B* 85, 245407, 2012.
- [108] Haupt, Randy L. An introduction to genetic algorithms for electromagnetics. *IEEE Antennas and Propagation Magazine*, v. 37, pp. 7-13, April 1995.
- [109] R. L. Haupt, D. H. Werner. *Genetic Algorithms in Electromagnetics*. Hoboken, NJ: Wiley, 2007.
- [110] F. D. M. Haldane and S. Raghu. Possible realization of directional optical waveguides in photonic crystals with broken time-reversal symmetry. *Phys. Rev. Lett.* 100, 013904, Jan. 2008.
- [111] M. C. Rechtsman, J. M. Zeuner, Y. Plotnik, Y. Lumer, D. Podolsky, F. Dreisow, S. Nolte, M. Segev and A. Szameit. Photonic Floquet topological insulators. *Nature* 496, 196200, April 2013.
- [112] M. C. Rechtsman, Y. Plotnik, J. M. Zeuner, D. Song, Z. Chen, A. Szameit, and M. Segev. Topological Creation and Destruction of Edge States in Photonic Graphene. *Phys. rev. Lett.* 111, 103901, 2013.
- [113] M. C. Rechtsman, Y. Plotnik, J. M. Zeuner, D. Song, Z. Chen, A. Szameit, and M. Segev. Topological Creation and Destruction of Edge States in Photonic Graphene. *Phys. rev. Lett.* 111, 103901, 2013.

- [114] Y. Poo, R-X Wu, Z. Lin, Y. Yang, and C. T. Chan. Experimental realization of self-guiding unidirectional electromagnetic edge states. *Phy. Rev. Lett.* 106, 093903, 2011.
- [115] Wen-Jie Chen, Shao-Ji Jiang, Xiao-Dong Chen, Baocheng Zhu, Lei Zhou, Jian-Wen Dong and C. T. Chan. Experimental realization of photonic topological insulator in a uniaxial metacrystal waveguide. *Nature Communications*,5, 5782, December 2014.
- [116] S. A. Skirlo, L. Lu, Y. Igarashi, Q. Yan, J. D. Joannopoulos, and Marin Soljai. Experimental observation of large Chern numbers in photonic crystals. *Phys. Rev. Lett.* 115, 253901, Dec. 2015.
- [117] S. A. Hassani Gangaraj, M. G. Silveirinha, and G. W. Hanson. Berry phase, Berry Potential, and Chern Number for Continuum Bianisotropic Material from a Classical Electromagnetics Perspective. *IEEE Journal on multiscale and multiphysics computational techniques*, to be published 2017.
- [118] Leslie E. Ballentine. *Quantum mechanics: A modern development*. Prentice Hall, New Jersey, 1990.
- [119] M. V. Berry. Quantal phase factors accompanying adiabatic changes. *Proc. R. Soc. Lond. A* 392, 45-57 (1984).
- [120] Y. Aharonov and J. Anandan. Phase change during a cyclic quantum evolution. *Phys. Rev. Lett.* 58, 1593-20 April 1987.
- [121] J. Anandan, J. Christian, and K. Wanelik. Resource Letter GPP-1: Geometric Phases in Physics. *Am. J. Phys.* 65, 180 (1997).
- [122] David J. Griffiths. *Introduction to quantum mechanics*. Prentice Hall, New Jersey, 1995.
- [123] A. Tomita and R. Y. Chiao. Observation of Berry's Topological Phase by Use of an Optical Fiber. *Phys. Rev. Letts.* 57, 937, 1986.
- [124] Q. Xu, L. Chen, M. G. Wood, P. Sun, and R. M. Reano. Electrically tunable optical polarization rotation on a silicon chip using Berrys phase. *Nat. Comm.* DOI: 10.1038/ncomms6337, 2014.
- [125] L. Fu, C. L. Kane, "Time reversal polarization and a Z2 adiabatic spin pump", *Phys. Rev. B*, 74,195312, 2006.
- [126] Mário G. Silveirinha, " $\mathbb{Z}_2$  Topological Index for Homogeneous Continuous Photonic Materials," arXiv:1601.02823, 2016.
- [127] J. Xue. Berry phase and the unconventional quantum Hall effect in graphene. arXiv:1309.6714, 2013.

- [128] T. Ando, T. Nakanishi, and R. Saito. Berry's Phase and Absence of Back Scattering in Carbon Nanotubes. *J. Phy. Soc. Japan*, 67, 2857-2862, 1998.
- [129] A. Young, Y. Zhang, and P. Kim. Experimental Manifestation of Berry Phase in Graphene. in *Physics of Graphene*, H. Aoki, and M S. Dresselhaus (Eds), Springer, 2014.
- [130] Arthur R. Davoyan and Nader Engheta. Theory of wave propagation in magnetized near-zero-epsilon metamaterials: evidence for one-way photonic states and magnetically switched transparency and opacity. *Phys. Rev. Lett.* 111, 257401, December 2013.
- [131] Biao Yang, Mark Lawrence, Wenlong Gao, Qinghua Guo, Shuang Zhang. One-way helical electromagnetic wave propagation supported by magnetized plasma. arXiv:1410.4596 [physics.optics].
- [132] Mário G. Silveirinha. Chern invariants for continuous media. *Phys. Rev. B* 92, 125153, 2015.
- [133] G. Tkachov. *Topological Insulators: The Physics of Spin Helicity in Quantum Transport*. CRC Press, 2015.
- [134] Mário G. Silveirinha and Stanislav I. Maslovski. Exchange of momentum between moving matter induced by the zero-point fluctuations of the electromagnetic field. *Phys. Rev. A* 86, 042118, October 2012.
- [135] Zheng Wang, Yidong Chong, J. D. Joannopoulos and Marin Soljai. Observation of unidirectional backscattering-immune topological electromagnetic states. *Nature* 461, 772-775, Oct. 2009.
- [136] Kejie Fang, Zongfu Yu and Shanhui Fan. Realizing effective magnetic field for photons by controlling the phase of dynamic modulation. *Nature Photonics* 6, 782787 (2012).
- [137] M. Hafezi, S. Mittal, J. Fan, A. Migdall and J. M. Taylor. Imaging topological edge states in silicon photonics. *Nature Photonics* 7, 10011005 (2013).
- [138] Alexander B. Khanikaev, S. Hossein Mousavi, Wang-Kong Tse, Mehdi Kargarian, Allan H. MacDonald and Gennady Shvets. Photonic topological insulators. *Nature Materials* 12, 233239 (2013).
- [139] Wenlong Gao, Mark Lawrence, Biao Yang, Fu Liu, Fengzhou Fang, Benjamin Bri, Jensen Li and Shuang Zhang. Topological photonic phase in chiral hyperbolic metamaterials. *Phys. Rev. Lett.* 114, 037402-22 Jan. 2015.
- [140] Y. D. Chong, Xiao-Gang Wen, and Marin Soljai. Effective theory of quadratic degeneracies. *Phys. Rev. B* 77, 235125, 30 June 2008.
- [141] Zheng Wang, Y. D. Chong, John D. Joannopoulos, and Marin Soljai. Reflection-Free one-way edge modes in a gyromagnetic photonic crystal. *Phys. Rev. Lett.* 100, 013905, January 2008.



- [142] Kejie Fang, Zongfu Yu, and Shanhui Fan. Microscopic theory of photonic one-way edge mode. *Phys. Rev. B* 84, 075477, August 2011.
- [143] Scott A. Skirlo, Ling Lu, and Marin Soljai. Multimode one-way waveguides of large Chern numbers. *Phys. Rev. Lett.* 113, 113904, September 2014.
- [144] Long-Hua Wu and Xiao Hu. Scheme for achieving a topological photonic crystal by using dielectric material. *Phys. Rev. Lett.* 114, 223901, June 2015.
- [145] Mário G. Silveirinha, “Bulk-edge correspondence for topological photonic continua,” *Phys. Rev. B* 94, 205105, 2016.
- [146] A. Raman and S. Fan, “Photonic Band Structure of Dispersive Metamaterials Formulated as a Hermitian Eigenvalue Problem”, *Phys. Rev. Lett.* 104, 087401, 2010.
- [147] S. Y. Buhmann, D. T. Butcher, and S. Scheel. Macroscopic quantum electrodynamics in nonlocal and nonreciprocal media. *New. J. Phys.* 14, 083034 (2012).
- [148] Z. Ficek and R. Tanas. Entangled states and collective nonclassical effects in two-atom systems. *Phys. Rep.* 372, 369 (2002).
- [149] W. K. Wootters. Entanglement of formation and concurrence. *Quantum Information and Computation* 1, 27 (2001).
- [150] S. Ali Hassani Gangaraj, A. Nemilentsau, G. W. Hanson, and S. Hughes. Transient and steady-state entanglement mediated by three-dimensional plasmonic waveguides. *Optics Express*, v. 23, DOI:10.1364/OE.23.022330 (2015).
- [151] C. Gonzalez-Ballesterro, A. Gonzalez-Tudela, F. J. Garcia-Vidal, and E. Moreno. Chiral route to spontaneous entanglement generation. *Phys. Rev. B* 92, 155304 (2015).
- [152] S. A. Hassani Gangaraj, G. W. Hanson. Topologically protected unidirectional surface states in biased ferrites: duality and application to directional couplers. *IEEE Antennas Wireless Propag. Lett.*, DOI: 10.1109/LAWP.2016.2582905 (2016).
- [153] S. A. Hassani Gangaraj, A. Nemilentsau, G. W. Hanson. The effects of three-dimensional defects on one-way surface plasmon propagation for photonic topological insulators comprised of continuum media. *Scientific Reports* 6, 30055 (2016).
- [154] COMSOL Multiphysics v. 5.2. [www.comsol.com](http://www.comsol.com). COMSOL AB, Stockholm, Sweden.
- [155] H-P Breuer and F. Petruccione. *The Theory of Open Quantum Systems*. Oxford University Press (2007).

- [156] J. S. Bagby and D. P. Nyquist. Dyadic Greens functions for integrated electronic and optical circuits. *IEEE Trans. Microwave Theory Tech.* 35, 206-210 (1987).
- [157] T. Ramos, H. Pichler, A. J. Daley, and P. Zoller. Quantum spin dimers from chiral dissipation in cold-atom chains. *Phys. Rev. Letts.* 113, 237203 (2014).
- [158] H. Pichler, T. Ramos, A. J. Daley, and P. Zoller. Quantum optics of chiral spin networks. *Phys. Rev. A* 91, 042116 (2015).
- [159] P. Lodahl, S. Mahmoodian, S. Stobbe, P. Schneeweiss, J. Volz, A. Rauschenbeutel, H. Pichler, P. Zoller. Chiral quantum optics. [arXiv:1608.00446 \[quant-ph\]](https://arxiv.org/abs/1608.00446) (2016).
- [160] A. Lakhtakia and T. G. Mackay. Vector spherical wavefunctions for orthorhombic dielectric-magnetic material with gyrotropic-like magnetoelectric properties. *J. Optics* 41, 201-213 (2012).
- [161] M. G. Silveirinha. Bulk edge correspondence for topological photonic continua. *Phys. Rev. B* 94, 205105 (2016).
- [162] S. R. Seshadri. Excitation of surface waves on a perfectly conducting screen covered with anisotropic plasma. *IRE Trans. Microw. Theory. Techs.* 10, 573-578 (1962).

# Curriculum Vitae

## Name and Address:

S. Ali Hassani Gangaraj

University of Wisconsin-Milwaukee, Department of Electrical Engineering,  
3200 North Cramer Street, Milwaukee, WI 53211 USA

## EDUCATION

**PhD candidate in applied electromagnetics, (Minor: Physics)**, Department of Electrical Engineering and Computer Science, University of Wisconsin-Milwaukee, Milwaukee, United States (January 2014-present), Advisors: Prof. George W. Hanson.

- **Thesis title:** Quantum and classical optics of plasmonic systems and metamaterials
- **Current GPA:** 4/4

**MSc in field and waves**, Department of Electrical Engineering, Iran university of science and technology (IUST), Tehran, Iran (September 2010-September 2012), Advisors: Prof. Majid Tayarani.

- **Thesis Title:** Analysis and design of magnetic anisotropic media and their new applications in microwave devices
- **GPA:**17.02/20. (Ranked 1st among all 15 electrical engineering students in field and waves)

**BSc in electrical engineering-telecommunication**, Department of Electrical Engineering, Iran university of science and technology (IUST), Tehran, Iran, (September 2006-September 2010), Advisors: Prof. Majid Tayarani.

- **Thesis Title:** Band stop waveguide filter by chiral structure in the cross section of waveguide
- **GPA:** 16.57/20. (Ranked 4th among all 40 electrical engineering students in telecommunication)

## RESEARCH INTERESTS

- Mathematical methods in electromagnetics
- Applied electromagnetics
- Metamaterials
- Quantum optics
- Quantum plasmonics, waveguiding structures and entanglement generation
- Photonic topological insulators, one-way plasmonic waveguiding

## RESEARCH EXPERIENCES

- Research and teaching assistant, University of Wisconsin Milwaukee, Milwaukee, Wisconsin, USA. January 2014-Now.
  - worked on surface plasmon polariton (SPP) modes quantization in graphene, building a fully quantum mechanical model for the excitation process.
  - Worked on SPP and its application in entanglement generation in graphene and plasmonic waveguiding structures such as nano rods and groove waveguides.
  - Worked on hyperbolic two-dimensional surfaces (black phosphorus and graphene strip arrays) and investigated their abilities to launch directive SPP..
  - Worked on one-way surface plasmon propagation in photonic topological insulators (PTI) comprised of continuum biased plasma.
  - Worked on quantum optics of PTI medium and their application for entanglement generation.
  - Attended the first annual two-dimensional material summer school, University of Minnesota, Minneapolis, June 2016.
  - Programming in MATLAB, working with several commercial electromagnetic softwares, as well as writing academic manuscripts and reports.
  - Taught several undergraduate level courses.
- Research assistant, Microwave laboratory, Department of Electrical Engineering, Iran university of science and technology, Tehran, Iran. January 2010-December 2014.
  - Studied the wave phenomena and electromagnetic properties of anisotropic media.
  - Designed microwave antenna and waveguiding structure using anisotropic media specially biased ferrites.

- Microwave engineer, Ertebatat Mojbar Shahab CO. Tehran, Iran. September 2012-December 2014.
  - Array antenna and passive microwave waveguiding structure design.
- Project manager, Microwave laboratory, Department of Electrical Engineering, Iran university of science and technology, Tehran, Iran. April 2012-July 2012.
  - Analytical design and numerical simulation of high power strip line ferrite circulator in UHF-Band.
  - Analytical design and numerical simulation of high power waveguide ferrite phase shifter in Ku-Band.
- Technical reviewer.
  - IEEE Transactions on antennas and propagation (TAP).
  - IEEE Antennas and wireless propagation letters (AWPL).
  - Optics express, Optical society of America (OSA).

## JOURNAL PUBLICATION

1. **Giant interatomic energy-transport amplification with nonreciprocal photonic topological insulators**, Pierre Doyeu, S. Ali Hassani Gangaraj, George W. Hanson, Mauro Antezza, Submitted for Phys. Rev. Letter.
2. **Robust entanglement with 3D nonreciprocal photonic topological insulators**, S. Ali Hassani Gangaraj, George W. Hanson, Mauro Antezza, Phys. Rev. A 95, 063807 (2017).
3. **Berry phase, Berry potential and Chern number for continuous bianisotropic material from a classical electromagnetics perspective**, S. Ali Hassani Gangaraj, George W. Hanson, IEEE journal of multiscale and multiphysics computational techniques, DOI: 10.1109/JMMCT.2017.2654962 (2017).
4. **Directive surface plasmons on tunable two-dimensional hyperbolic metasurfaces and black phosphorus: Green function and complex plane analysis**, S. Ali Hassani Gangaraj, Tony Low, Andrei Nemilentsau, George W. Hanson, IEEE transactions on antennas and propagation, DOI:10.1109/TAP. 2016. 2633900 (2016).
5. **Topologically protected unidirectional surface state in biased ferrites: Duality and application to directional couplers**, S. A. Hassani Gangaraj, George W. Hanson, IEEE antennas and wireless propagation letters, DOI:10.1109/ LAMP.2016.2582905 (2016).

6. **The effects of three-dimensional defects on one-way surface plasmon propagation for photonic topological insulators comprised of continuum media**, S. A. Hassani Gangaraj, A. Nemilentsau, George W. Hanson, Scientific Reports 6, 30055, (2016).
7. **Dyadic Green function for dipole excitation of homogenized metasurfaces**, Feng Liang, George W. Hanson, Alexander B. Yakovlev, Giampiero Lovat, Paolo Burghignoli, Rodolfo Araneo, S. A. Hassani Gangaraj, IEEE transactions on antennas and propagation 64 (1), 167-178 (2016).
8. **Transient and steady-state entanglement mediated by three-dimensional plasmonic waveguides**, S. A. Hassani Gangaraj, Andrei Nemilentsau, George W. Hanson, Stephen Hughes, Optics express, Vol. 23, Issue 17, pp. 22330-22346 (2015).
9. **Quantum plasmonic excitation in graphene and loss-insensitive propagation**, George W. Hanson, S. A. Hassani Gangaraj, Changhyoup Lee, Dimitris G. Angelakis, Mark Tame, Phys. Rev. A 92, 013828 (2015).
10. **High-directive patch and dipole antennas using biased grounded ferrite**, S. A. Hassani Gangaraj, M. Tayarani, A. Abdolali, Applied computational electromagnetics society journal, Vol. 27 Issue 10, p779, Oct. (2012).

## BOOK CHAPTERS

1. **Unidirectional, defect-immune and topologically protected electromagnetic surface waves** , George W. Hanson, S. Ali Hassani Gangaraj, A, Nemilentsau, The World of Applied Electromagnetics: In Appreciation of Magdy Fahmy Iskander, Akhlesh Lakhtakia and Cynthia M. Furse (Editors), Springer Verlag (2017).

## ARXIV PREPRINT

1. **Notes on photonic topological insulators and scattering-protected edge states - a brief introduction** , George W. Hanson, S. Ali Hassani Gangaraj, A, Nemilentsau, arXiv:1602.02425v2 (2016).

## CONFERENCE

1. **Spontaneous qubit entanglement in photonic topological insulator environments** , S. A. Hassani Gangaraj, G. W Hanson, M. Antezza, Presented in 38th Progress In Electromagnetics Research Symposium, **PIERS**, St Petersburg, Russia, May 2017.

2. **Photonic topological insulator waveguiding from a classical electromagnetics perspective**, S. A. Hassani, G. W. Hanson, Presented in national radio science meeting, **URSI**, 2017, in Boulder, Colorado, January 2017.
3. **Tunable guided surface plasmon-polariton using two dimensional hyperbolic graphene metasurfaces**, S. A. Hassani, A. Nemilentsau, G. W. Hanson, Presented in national radio science meeting, **URSI**, 2016, in Boulder, Colorado, January 2016.
4. **Plasmon-mediated control of entanglement between two quantum systems**, A. Nemilentsau, S. A. Hassani, G. W. Hanson, S. Hughes, Presented in **META** 2015 in New York, The 6th international conference on metamaterials, photonic crystals and plasmonics.
5. **Control of entanglement of two-level atoms using Grapheme**, Andrei Nemilentsau, S. A. Hassani Gangaraj, George Hanson, Stephen Hughes, Presented in conference on laser and electro-optics, **CLEO** 2015, San Jose, CA, USA, 10-15 May.
6. **Entanglement of Two-Level Atoms Above Graphene**, Andrei Nemilentsau, S. A. Hassani Gangaraj, George Hanson, Stephen Hughes, Presented in **EuCAP** 2015, Lisbon, Portugal 12-17 April.
7. **A Novel Composite Left-Right Handed Structure for Rectangular Waveguide with Its Multi Band Stop and Band Pass Applications**, S. Saravi, S. A. Hassani Gangaraj, M. Tayarani, 21st Iranian conference on electrical engineering **ICEE**, 14-16 May 2013 Publisher: IEEE.
8. **Below/Above Cutoff Dual Metamaterial Band in Cylindrical Media**, S. A. Hassani Gangaraj, M. Tayarani, A. Abdolali, First Iranian conference on electromagnetic engineering, Dec. 26-27, 2012 Tehran, Iran.
9. **A Novel Bandstop Resonator in Waveguide and Its Application for Suppressing the Spurious Responses with New Advantages to Typical Resonators**, S. A. Hassani Gangaraj, M. Tayarani, Progress in electromagnetics research symposium **PIERS** 2011, Suzhou, China, pp 533-537, Sep 12-16.

## HONORS AND AWARDS

- ◇ **USNC-URSI travel fellowship award** to support the participation to the National Radio Science meeting in Boulder, CO, USA, 2017.
- ◇ Awarded **student travel scholarship**, First annual two-dimensional material summer school, University of Minnesota, Minneapolis, June, 2016.

- ◇ **Chancellor's award** , University of Wisconsin-Milwaukee, Milwaukee, Wisconsin, USA, four times between 2014 and present.
- ◇ **Best student presentation award**, M.Sc. seminar course (related to M.Sc. thesis), Iran university of science and tech. (IUST), Tehran, Iran, Jun 2011.
- ◇ **Gold Medal**, physics free competition, Sharif university of technology, Tehran, Iran 2005.
- ◇ **1<sup>st</sup> Rank**, in cumulative GPA, M.Sc., Class of 2010, Iran university of science and technology, Tehran, Iran, 2012.
- ◇ **Honor student**, January 2007 to Jun 2007, September 2009 to Jan 2010 in B.Sc. Class of 2006, Iran university of science and technology, Tehran, Iran.
- ◇ **318<sup>th</sup> Rank**, Nationwide university entrance exam in engineering and applied mathematics, Summer 2006, Among over 200,000 high school students of 2nd region.

## TEACHING EXPERIENCES

### Teaching:

- Microwave measurement and antenna design LAB, Department of Electrical Engineering, Iran university of science and technology, August 2012-Jun 2013.
- Electronics II, Department of Electrical Engineering, University of Wisconsin-Milwaukee, Summer 2014.
- Circuit II, LAB., Department of Electrical Engineering, University of Wisconsin-Milwaukee, Aug. 2014-present.

### Teaching Assistant:

- Circuit I, Department of Electrical Engineering, University of Wisconsin-Milwaukee, August 2014-May 2016.
- Electromagnetics, Department of Electrical Engineering, Iran university of science and technology, January 2010-December 2010.
- Signals and Systems, Department of Electrical Engineering, Iran university of science and technology, September 2010-January 2011.
- Microwave I, Department of Electrical Engineering, Iran university of science and technology, January 2011-Jun 2011.
- Field And Waves, Department of Electrical Engineering, Iran university of science and technology, January 2012-Jun 2012.



## **WORK EXPERIENCES:**

- Microwave engineer intern, “Behsaz Ertebat CO”, May 2009-August 2009.
- Microwave engineer, “Ertebatat Mojbar Shahab CO ”, September 2012-December 2014.

## **COMPUTER SKILLS**

- COMSOL
- CST (Microwave studio)
- HFSS
- MATLAB
- Advanced Design System (Agilent)
- Lumerical (FDTD Solution)

## **LANGUAGE**

- Persian (Native)
- English (With TOEFL and GRE certificates)